UNIVERSITÀ
DI SIENA
1240

Dipartimento di Biotecnologie, Chimica e Farmacia

Dottorato di Ricerca in Chemical and Pharmaceutical Sciences

CICLO XXXVI

Coordinatore: Prof. Maurizio Taddei

Settore Scientifico-Disciplinare: CHIM/08

Strategies to Fight Infective Agents

Dottorando:
Sara Rossi

Signed by: ROSSI SARA
Issuer: Namirial CA Firma Qualificata
Signing time: 08-06-2024 17:46 UTC +02

Tutor:

Prof. Giuseppe Campiani

Anno Accademico: 2023/2024

Abstract

During my PhD project I have been involved in different studies concerning the investigation of different ways to fight infective agents.

In particular the main focus has been the development of inhibitors against the main protease of SARS-CoV-2, in fact, a library of peptide-based inhibitors has been developed, with the aim to accomplish a SAR study that could allow the further development of new antiviral agents with the potential to inhibit the replication not only of SARS-CoV-2 but also of other coronaviruses that have the potential to spillover, or similar viral entities such as enteroviruses. The library of compounds includes 25 new M^{pro} inhibitors which have been designed, synthesized and their inhibitory activity against the main protease of SARS-CoV-2 has been assessed, giving promising outputs. Moreover the most active compounds have been tested in infected VERO E6 cell line.

A further exploration that has been pursued in the context of SARS-CoV-2 M^{pro} inhibition has been the study of a small library of fragments, in order to further expand the knowledge of the active site pocket and explore new accessible scaffolds for the design of small molecule inhibitors against the main protease of SARS-CoV-2. The development of this limited library of compounds is still in progress as well as the biological evaluation of the first compounds that have been synthesized.

The second project in which I have been involved during this PhD project has been the repurposing of in house HDACi with a preventive effect against SARS-CoV-2 infection, based on the knowledge of the entry mechanism of SARS-CoV-2 into the host cells, which is achieved through the binding of the viral particles to the host receptor ACE2, whose expression has been correlated with HDAC modulation. For this reason two selective HDACi developed by the research group have been repurposed for their biological evaluation in terms of prophylactic activity of these compounds towards ACE2-mediated entry coronaviruses. The compounds have thus been synthesized and the biological evaluation is ongoing.

A further study that has been carried out during this PhD project has been the development of monkeypox VP37 inhibitors. In particular, taking inspiration from the approved anti-viral agent tecovirimat, which is an inhibitor of the VP37 protein of monkeypox, a SAR study has been carried out, exploring different moieties for the cap group that interacts with the external surface of the active site and of the linker unit of these compounds. The compounds that have been synthesized so far have been evaluated from a biological point of view, for their inhibitory potency in infected cells, affording promising results,

Finally, among the infective agents with high morbidity and mortality note to mention surely are the *Pseudomonas aeruginosa* acute and chronic infections in patients

affected by cystic fibrosis. During this project, which has been recently published, a family of modulators of the virulence factors within the biofilm of *Pa* has been developed and the evaluation of the inhibition of the biofilm, and the modulation of pyoverdine and pyocyanin has been assessed with promising results, confirming the efficacy of these compounds.

Ringraziamenti

…

Table of contents

CHAPTER 1

INTRODUCTION

CHAPTER 1 – INTRODUCTION

1.1 – Emerging and re-emerging infective agents

In the past, diseases like tuberculosis, polio, smallpox, and diphtheria were widespread and led to significant illness and death. Over the last decades, however, advancements in medicine, improved access to healthcare, and better sanitation have significantly decreased death and illness from these infective pathogens, especially those causing respiratory and diarrheal illnesses, as also confirmed by the fast development of vaccines for the last pandemic COVID-19 [1–5]. Despite these advancements, infectious diseases continue to pose a major challenge in low- and middle-income countries, in which high rates of morbidity and mortality associated to neglected tropical diseases, HIV, tuberculosis, and malaria still persist. Furthermore, the 21st century has seen a consistent threat from new and re-emerging microbial infections. The beginning of a new era has defined, characterized not only by frequent outbreaks of infective agents, but also an escalating growth in bacterial resistance that is leading to high rates of resistant strains such as the ESKAPE pathogens. This growing threat is facilitated by global traveling, climate change, and an increasing interaction between humans and animal reservoirs, as seen with HIV, the 1918 influenza, MERS-CoV, and SARS-CoV-2, West Nile Virus, protozoan neglected diseases such as leishmaniasis [6–8].

The risk of a novel pathogen threatening human health involves several factors, firstly there has to be an initial contact with the animal host, then the pathogen must allow for human-to-human transmission, and its potential for geographical spread must have evolved. Changes in human behavior, such as encroachment into new areas, population growth, agricultural development also in wild-life inhabited territories, wild-life farming, as well as natural habitats destruction, have increased the human-wildlife contact, raising the risk of disease spillover [9,10]. This is exemplified by the Nipah virus outbreak among pig farmers in Malaysia in 1999 identified in numerous species of flying foxes of the family of bats and infections from *Pseudomonas* spp. among poultry workers [11]. In addition to this, changes in human demographics, and sanitary laws such as the discontinuation of smallpox

vaccinations due to the elimination of this virus, have also influenced disease dynamics, potentially facilitating the spread of dormient diseases like monkeypox.

Furthermore, the global landscape is shifting in ways that could allow existing pathogens to develop new traits and spread more widely, exemplified by the worldwide emergence of drug-resistant pathogens and rapid urbanization in developing countries that create fertile ground for the emergence of infectious diseases. Urban areas, in particular, have become hotspots for arboviral diseases transmitted by mosquitoes such as *Aedes aegypti* and *Aedes albopictus* mosquitoes that are well adapted to urban areas, causing insurgence of Dengue, Zika, and Chikungunya viruses, which thrive in densely populated and poor environments [12,13].

In the last years, the World Health Organization (WHO) has highlighted several viral diseases as major global concerns, including MERS, SARS, Ebola, Zika, and Dengue viruses, as well as the infamous disease X. Disease X symbolizes the potential of a global epidemic which could originate from either an unrecognized human infectious pathogen or a known pathogen that has evolved to become more contagious or virulent. This concept was created in order to highlight the possibility of new emerging or re-emerging infectious diseases and establish a new concept of awareness and preparedness which has brought to light the protocols from the R&D Blueprint [14–16].

1.2 – Old and new antimicrobial agents, overview and timeline

In the realm of antiviral medications approved by the Food and Drugs Administration (FDA) and European Medicines Agency (EMA), the majority can be considered small molecules utilized for a range of clinical applications, but also “large” molecules have received approval as antiviral agents which comprehend proteins such as interferons and monoclonal antibodies, peptides and oligonucleotides. These antimicrobial agents comprehend drugs focused on the inhibition of viral cellular processes, and drugs that target mechanisms within the host cells, to be used in combination therapies or as single-agents, the most historically significant have been included in the timeline of Figure 1 [17].

Figure 1 also discloses the parallel timeline of significant antibiotic discoveries, tracing the trajectory from the beginning of the modern “antibiotic era”, raised with pioneers such as Paul Ehrlich and Alexander Fleming, to the most recent antibacterial agents which have gained approval by both FDA and EMA. This timeline highlights drugs that have been milestones in the advancement of antimicrobial treatments, showcasing a range of drug classes with distinct modes of action and tailored uses. This diversity underscores the continuous struggle against bacterial infections and the challenge posed by the evolution of drug-resistant strains [18–21].

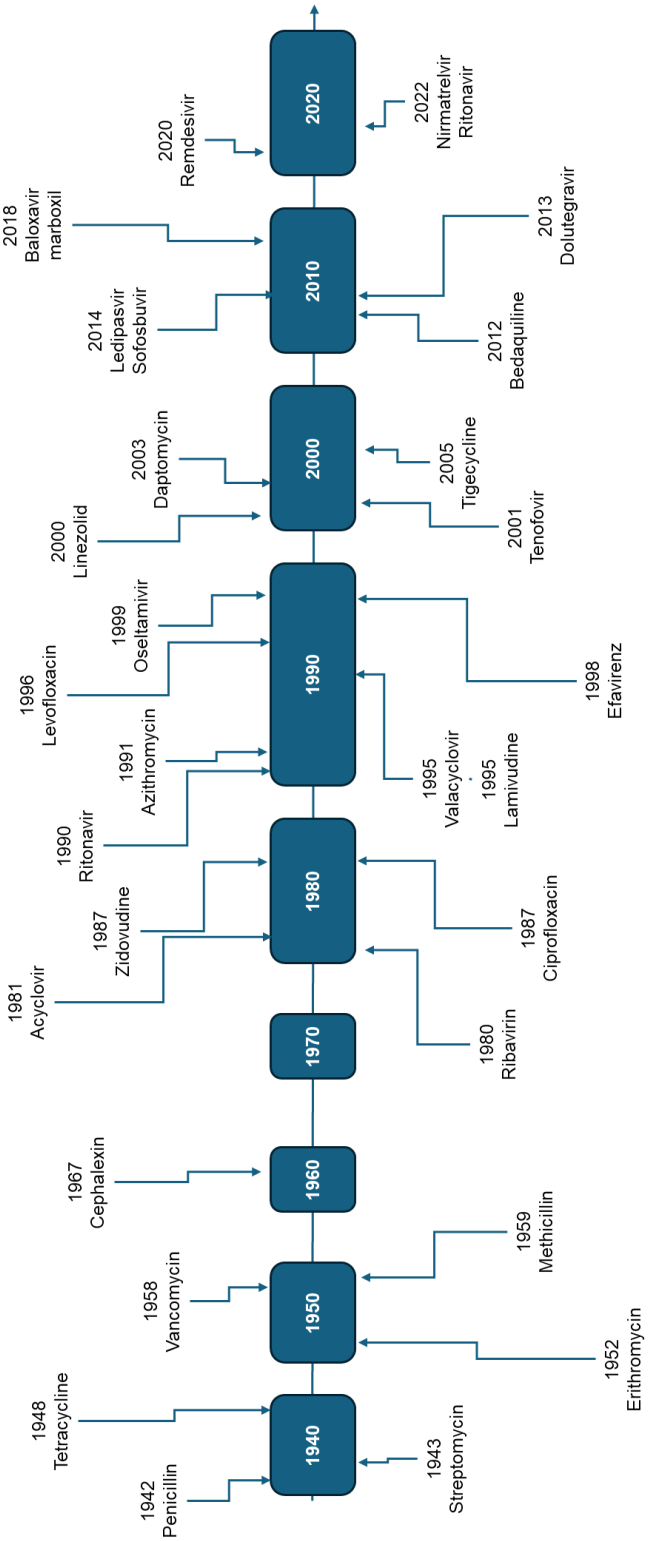

Figure 1: Most important antimicrobial agents that have marked a deep impact in the treatment and management of microbial infections, introducing novel mechanisms of action, or which have paved the way for further developments in antimicrobial therapy.

1.3 – Strategies to fight infective agents

There is no general procedure that can effectively prevent or control microbial infections, despite the time-consuming process of developing various therapeutic strategies such as vaccinations, immunotherapy, and chemotherapy, alone or in combination [22–25]. This largely stems from the unique characteristics and complex interactions that each pathogen, whether it is a virus, bacterium, fungus, or protozoan, shares with its host. The effectiveness of the currently available prevention and treatment therapies notably presents limitations, partly due to the ability for mutation and evolution in both viral and cellular pathogens, challenging the efficacy of existing control measures.

1.3.1 – New anti-viral strategies

Among the classical antiviral strategies pursued by medicinal chemists to fight viral infections, single or combination therapies and split treatments which target viral proteins, host-target therapies and immunotherapies can be found. Monotherapies can be either divided into inhibitors targeting viral proteins, which are the main topic of this PhD thesis, or inhibitors targeting host-cell components involved in the viral life-cycle or replication. Combination therapies work through the association of two or more drugs; the general advantage of this type of therapy lies in its ability to counteract the rapid evolution and adaptability of viruses, identified as quasispecies dynamics [26,27], and there are many clinical evidences of the success of this type of therapy [28]. Another strategy involves the application of the split treatment, which consists in the administration of the therapy into two steps: an induction step and a maintenance step, still for the fast mutation of viruses, allowing to limit the induction of resistant viral strains [29]. Another therapeutic approach able to decrease the chance of resistance selection consists in targeting cellular functions which are pivotal for viral replication, thus avoiding variations in the viral response to the therapy and reducing the likelihood of resistance development. However this kind of strategy has two side-effects which include possible toxic effects derived from the suppression or alteration of host cellular activities, and the selection of viral mutants that are insensitive to the presence of such inhibitor. Bypassing the common antiviral

approaches we can find antiviral strategies that stimulate the host immune system, for example through the use of antibodies or vaccinations. But also a combination of immunotherapy and chemotherapy is possible, this concept has been initially proposed as a strategy for the control of influenza viruses in 1985 [25,30,31].

1.3.2 – New anti-bacterial strategies

In addition to the need for new antiviral agents, the search for new antibacterial strategies is of the utmost importance as well, as increasing antibiotic resistance poses a significant public health challenge in the 21st century. In fact, it's estimated that by 2050, deaths due to antimicrobial resistance could escalate to 10 million annually worldwide. In addition to this the proliferation of major multidrug-resistant (MDR) opportunistic microorganisms, particularly those belonging to the ESKAPE group, underscores this issue. Given that very few novel classes of antibacterial agents have been discovered, the focus has shifted towards innovative approaches to combat bacterial infections. Among these the previously mentioned approach targeting bacterial targets has been amply explored with the approval and the use of many exponents of the penicillin and cephalosporin classes. However, as resistance grows, alternative methods are gaining attention. One such promising method is the use of phages and endolysins, either alone or alongside conventional antibiotics, to target bacterial infections effectively [32,33]. Immunological strategies, including vaccinations and immunomodulators, also represent a pivotal frontline defense against MDR pathogens, eliminating the recurrent need for antibiotics. Moreover vaccines have the added benefit of reducing antimicrobial resistance spread by decreasing both the necessity for antimicrobial treatments and the overall incidence of infections. Finally targeting specific virulence factors, for example targeting the PQS (Pseudomonas quorum sensing) system in *Pseudomonas aeruginosa*, or disrupting secretion systems and toxins can lead to novel anti-infective therapies [34]. Additionally, the exploration of bacterial small regulatory RNAs, which play critical roles in virulence onset, biofilm formation, and antibiotic resistance, presents another innovative strategy. Important to mention, are also the clinical and developmental use of antimicrobial resistance inhibitors, such as β-lactamase and efflux pump

inhibitors, which highlights the ongoing efforts to enhance the effectiveness of existing therapies [35–41].

CHAPTER 2

Design and synthesis of new inhibitors of the main protease of SARS-CoV-2

CHAPTER 2 – Design and synthesis of new inhibitors of the main protease of SARS-CoV-2

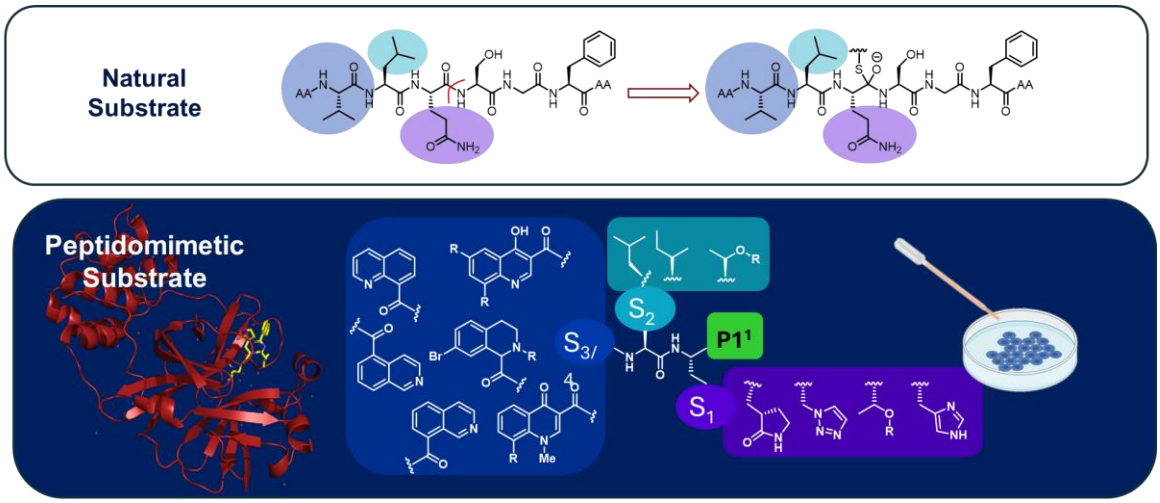

Table of content

Over the past decades, three significant coronavirus outbreaks, all traced back to animal origins, have underscored the urgent need for effective antiviral agents Notably, SARS-CoV-2 has caused a global health and economic crisis, leading researchers to quickly repurpose FDA-approved drugs as an initial response to the pandemic. Concurrently, the necessity to identify new drug targets became evident, driving efforts to design and synthesize novel antiviral agents. Among the most promising targets, the Main protease of SARS-CoV-2 (M^{pro}) has been recognized as a crucial enzyme, pivotal for protein maturation and viral replication. Furthermore, its conservation across other coronaviruses, along with its high amino acidic sequence homology with other zoonotic coronaviruses, makes its inhibition a viable strategy for developing broad-spectrum inhibitors to prevent future spillovers. During this project a new series of peptidomimetic M^{pro} covalent inhibitors has been designed and synthesized, investigating various warheads, including aldehyde, nitrile, and the less commonly used cyanohydrin, the backbone of these inhibitors has been extensively varied as well, incorporating different natural and unnatural amino acids. These compounds have been tested on isolate enzyme and in cell-based assays to confirm their inhibitory potency and selectivity towards M^{pro}, and the most promising showed encouraging activity in micromolar range in infected Vero E6 cells. The binding mode of these peptide-based compounds into the active site of M^{pro} has also

been confirmed through the solved co-crystal structure of one of the tested compounds with the enzyme. These results set the stage for further development of new pan-antiviral inhibitors.

2.1 – Introduction to coronavirus infections

Coronaviruses are a highly diverse family of single-stranded, positive-sense RNA viruses with an enveloped structure [42]. These pathogens are recognized to cause respiratory and gastrointestinal diseases in both humans and animals, ranging from the common cold to more severe conditions such as deadly bronchial pneumonia. These pathogens affect a diverse array of hosts, spanning from humans, to multiple mammal species comprising birds and family pets, thus presenting considerable challenges to public health, animal healthcare, and economic stability [43]. Coronaviruses, classified within the Nidovirales order and the Coronavirineae suborder, are part of the Coronaviridae family. In particular, included within the Orthocoronavirinae subfamily, coronaviruses are divided into four principal groups: α-coronavirus, β-coronavirus, γ-coronavirus, and δ-coronavirus. α-Coronaviruses and β-coronaviruses are known to mainly infect mammals, whereas γ-coronaviruses and δ-coronaviruses may affect a wider range of hosts, including avian species [44]. Until December 2019, only six coronaviruses were known to have the potential to infect humans; these included two α-coronaviruses, specifically HCoV-229E and HCoV-NL63, and four β-coronaviruses, namely HCoV-OC43, HCoV-HKU1, SARS-CoV, and MERS-CoV.

SARS-CoV has marked the first significant coronavirus outbreak, which has occurred between 2002 and 2003, attracting the attention worldwide. This epidemic has caused 8,096 infected individuals, leading to 774 deaths with a mortality rate of approximately 9% [45]. Ten years later, in 2012, a new coronavirus epidemic has emerged, with the infective agent being identified as MERS-CoV due to the primary geographical localization of reported cases. During this second epidemic outbreak the number of reported cases progressed slowly but relentlessly, and in fact many cases were still reported in November 2019, with a total of 2,494 documented cases and 858 deaths, resulting in a mortality rate of 35% [46]. As a matter of fact, in November 2019 another coronavirus with the capability of infecting humans, the predicted pathogen X (later identified as SARS-CoV-2), has been the causative agent for COVID-19 pathology. By July 2020 the global tally had escalated to

13,150,645 confirmed infections and 574,464 deaths, highlighting the critical need for effective antiviral agents [47–49].

In particular, SARS-CoV-2 pandemic has been characterized by the sequential appearance of different variants [50], which arise from the swift evolutionary pace that coronaviruses are characterized by, similarly to other RNA viruses, with changes and mutations occurring over a limited timeframe of months or years, often aligning with their infectivity and ecological dynamics. This evolution is both observable and quantifiable, by tracking down transmission events and changes in environmental factors, including variations in the population of infected individuals, immunity profiles, and human mobility [51]. In comparison to other viruses, coronaviruses present an exceptionally large RNA genome, which is framed by untranslated regions at both 5′ and 3′ ends, which harbor cis-acting secondary RNA structures crucial for the synthesis of RNA. At the 5′ end of the genomic sequence, two extensive open reading frames (ORFs), that group about two-thirds of the genome, can be identified. These ORFs are both capped and polyadenylated and are responsible for the translation of two large polyproteins, pp1a and pp1ab. Specifically, ORF1a and ORF1b encode for the 16 non-structural proteins (nsp), 15 of which compose the viral replication and transcription complex (RTC) [52]. This complex includes a variety of RNA-processing and modifying enzymes, along with an RNA proofreading mechanism that is essential for preserving the integrity of the coronavirus genome. The remaining part of the genome, located at the 3′ end of the sequence, is devoted to the encoding of structural and accessory proteins, leading to the creation of a nested set of subgenomic mRNAs (sg-mRNAs). The accessory proteins of the coronavirus are highly variable showing minimal conservation even within the same species, and are thought to mainly play a role in modifying the host's response to the infection, thus they can be considered the key factors in determining the virus's pathogenicity. Nevertheless, the molecular function of many accessory proteins remains largely unknown owing to the lack of homologies in other coronaviruses or to other known proteins [44,53,54].

2.1.1 – Pandemic and infectivity

2.1.1.1 – Infection onset

For decades, coronaviruses like HCoV-229E and HCoV-OC43 have been recognized for their presence among humans, and as anticipated before they primarily caused mild, seasonal respiratory ailments, and this pattern was echoed with the later identification of HCoV-NL63 and HCoV-HKU1. In strong contrast with these, has been the emergence of SARS-CoV, MERS-CoV, and SARS-CoV-2 in the last twenty years, which have demonstrated a significant pathogenic potential. Genetic analysis of these three coronaviruses highlights that SARS-CoV-2 and SARS-CoV share approximately 79% of their genomic sequences, hinting at a potential shared ancestry. Despite this genetic similarities, SARS-CoV-2 has distinguished from the previous strains for its enhanced transmissibility and a more prolific development of variants compared to its predecessor SARS-CoV [55].

These viruses spread by infecting epithelial cells and pneumocytes in the human respiratory system, including bronchi, lungs, and the upper respiratory tract, though these infections can escalate into critical respiratory conditions, lung and enteric tract damage that pose a high risk to life [56].

Coronavirus infection begins when the virus's spike (S) protein attaches to specific receptors on the surface receptors of host cells, which vary among different coronaviruses. These receptors include human aminopeptidase N (APN) for HCoV-229E [57], angiotensin-converting enzyme 2 (ACE2) for HCoV-NL63, SARS-CoV, and SARS-CoV-2 [58,59], and dipeptidyl peptidase 4 (DPP4) for MERS-CoV [60]. The presence and distribution of these receptors in various tissues plays a critical role in determining the virus's ability to infect different parts of the body and its overall potential to cause disease.

Right after the binding, the virus and the cell membranes merge, initiating the entry phase of the virus into the cell through endocytosis, as described in Figure 2. This process leads to the release of the virus's RNA into the cytoplasm of the host cell, which triggers a detailed and tightly controlled viral gene expression process where it is translated into viral proteins [44,61,62].

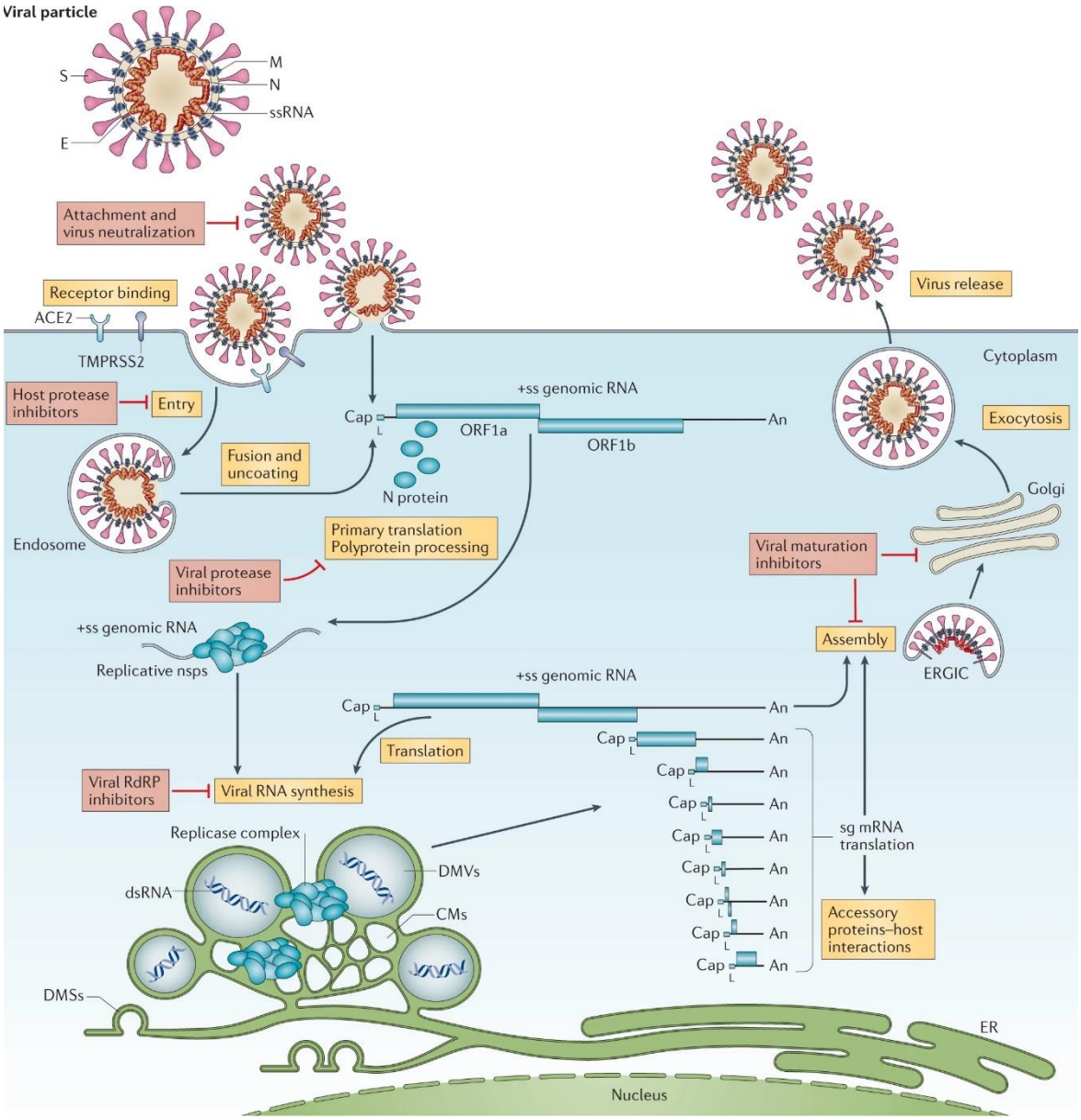

Figure 2: Different steps of coronavirus life cycle, and inhibitors which come in play in the various replication phases [63]

The replication process starts with the genomic RNA translation of ORF1a and ORF1b, leading to the creation of the two large polyproteins, pp1a and pp1ab. These polyproteins are then cleaved into the sixteen non-structural proteins (nsp) through both co-translational and post-translational processes, by the action of the two cysteine proteases, namely nsp3 (papain-like protease or PL^{pro}) and nsp5 (chymotrypsin-like protease CL^{pro}, so-called due to its resemblance to the picornavirus 3C protease or Main protease M^{pro}). The genes for the virus's structural

components, including the S protein, envelope (E) protein, membrane (M) protein, and nucleocapsid (N) protein, are located in the initial 3’ part of the coronavirus genome, with additional genes for accessory proteins interspersed among them. While the specific functions of the structural proteins in virus assembly and release are still under investigation, typically these proteins are involved in the formation and release of new viral particles through the ER-to-Golgi intermediate compartment, allowing the exit from the host cell via exocytosis.

Nsp1's rapid proteolytic release is critical, as it enables the targeting of the host cell translation machinery. Nsp2-16 are crucial for the formation of the viral replication-transcription complex (RTC) and for this reason target host cell components within specific subcellular locations, that are pivotal in directing the replication process. Nsp2 to nsp11 play supportive roles that help maintain the RTC by altering intracellular membranes, evading the immune response, and supplying necessary cofactors for viral replication. Meanwhile, nsp12 to nsp16 are responsible for the virus's key enzymatic activities related to RNA replication, proofreading, and modification [64]. The nsp12 protein, acting as an RNA-dependent RNA polymerase (RdRP) alongside its two cofactors nsp7 and nsp8, drives RNA synthesis, while nsp14 adds a level of fidelity to this process with its 3′–5′ exonuclease activity, enabling RNA proofreading. The virus's mechanism for capping RNA, which is only partially understood, involves nsp10 as a cofactor, nsp13 with its RNA 5′-triphosphatase activity, and nsp14 and nsp16 for N7-methyltransferase and 2′-O-methyltransferase activities, respectively [65].

The viral RTC's formation is a cornerstone of replication, making it a key target for antiviral strategies, but also the M^{pro}, which plays a critical role in nps release, is a particularly promising target since it presents highly specific amino acidic recognition sequence, and compounds that structurally mimic those cleavage sites can specifically target the viral protease with little or no impact on host cellular proteases [44].

2.1.1.2 – Pathogenicity

The initial outbreak of a coronavirus epidemic was traced back to Guangdong province, China, in November 2002, with the SARS-CoV virus responsible for the outbreak, which was eventually contained by July 2003. The primary mode of SARS-CoV transmission was direct physical contact with individuals infected by the virus or through exposure to surfaces (fomites) contaminated with viral particles, including droplets and aerosols emitted by infected persons. This virus targets the epithelial cells of the airways, potentially leading to severe pneumonia known as SARS. Typical symptoms of the infection include fever, dyspnea, and lymphopenia, with some patients also experiencing diarrhea and other gastrointestinal issues, which may be caused by an active viral replication in the intestines and the possibility of fecal-oral transmission routes. Additionally, patients often exhibited prolonged clotting times and increased liver enzyme levels. The virus also infects macrophages and dendritic cells, causing them to release pro-inflammatory cytokines and chemokines, crucial in the progression of the disease[66]. However, the detailed mechanisms driving the pulmonary complications and disease severity have not been fully understood yet. Following the 2002–2003 SARS-CoV epidemic, another coronavirus, MERS-CoV, emerged in Jeddah, Saudi Arabia, in 2012, causing lower respiratory system infections almost identical to those seen with SARS-CoV and with an infectivity comparable to the previous coronavirus infection reported. Also the symptoms closely mirror those of SARS-CoV, with severe cases advancing to acute respiratory distress syndrome, septic shock, failure of multiple organs, and ultimately death. MERS-CoV activates the innate immune response through the interferon I pathway but employs viral proteins to inhibit the IFN and NF-κB signaling pathways, thereby hindering the immune response, thus enhancing viral replication, and increasing the disease's severity.

In December 2019, the novel coronavirus outbreak led to severe pneumonia cases, marking the start of the 21st century's second pandemic, following the swine flu pandemic caused by the Influenza A (H1N1) virus in 2009.

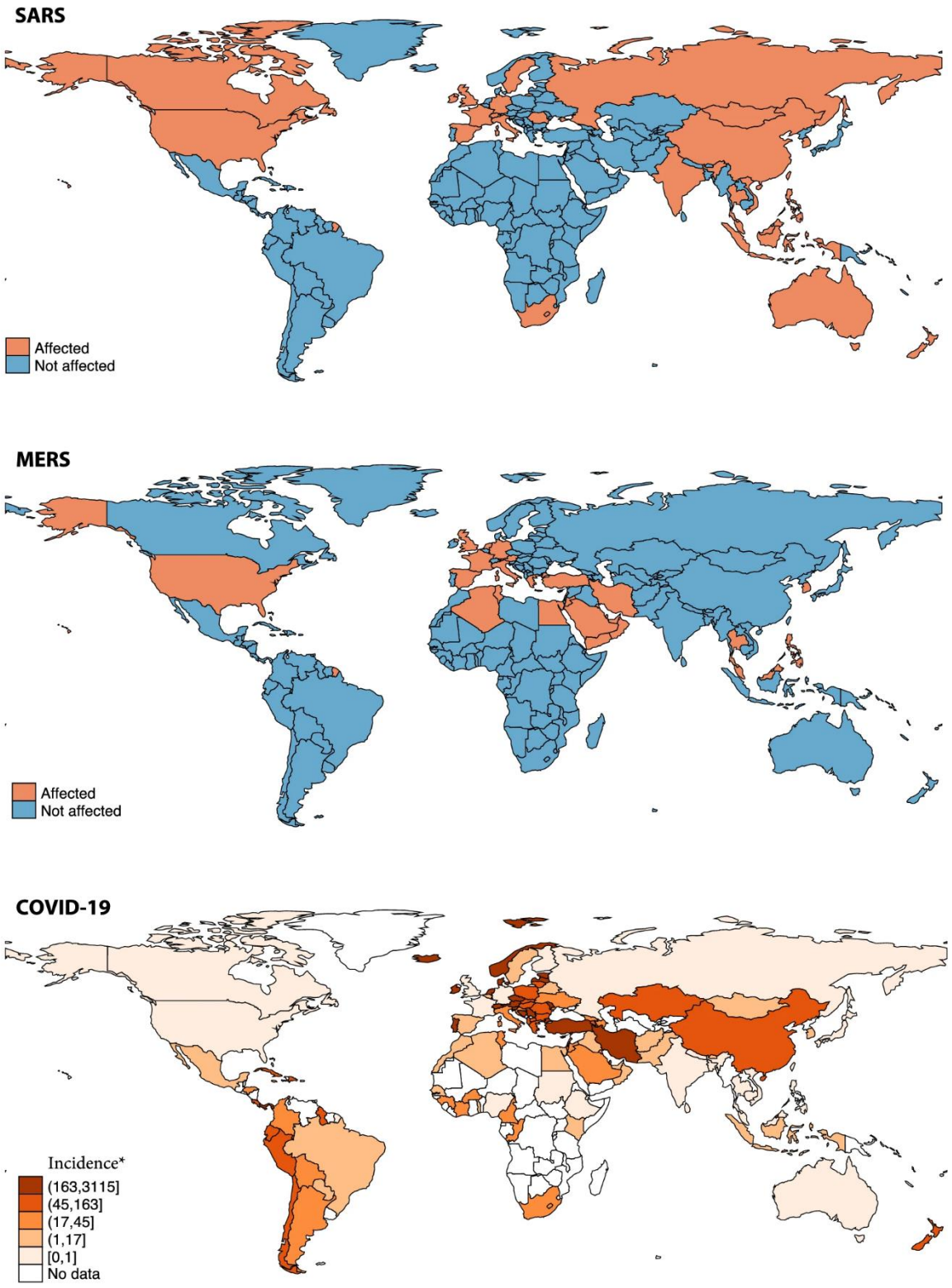

SARS, Severe Acute Respiratory Syndreom; MERS, Mediterranean East Respiratory Syndrome; COVID-19, 2019 coronavirus disease.
* Incidence per 100,000 population within 30 days from the report of the first confirmed case.

Figure 3: Diffusion maps of SARS-CoV, MERS-CoV and SARS-CoV-2[67]

SARS-CoV-2 spreads primarily through respiratory droplets between people and by touching surfaces contaminated with the virus, similarly to its predecessors, SARS-CoV and MERS-CoV [61]. Like the earlier coronaviruses, it can trigger a severe immune response known as "Cytokine Storm Syndrome," characterized by elevated levels of IL-6, MCP-1, VEGF, IL-8, and other analytes, which can lead to pulmonary dysfunction and hypotension [49,68]. Despite the significant health crises sparked by SARS-CoV and MERS-CoV, and the current global challenge posed by SARS-CoV-2, strategies to manage coronavirus infections are still in development, hinging on a more comprehensive understanding of the virus's genetic behavior and interactions with human cells.

Although SARS-CoV and SARS-CoV-2 share similarities in how they enter cells, they differ in their replication efficiency and spread, as visible by the diffusion maps reported in Figure 3. SARS-CoV mainly infects the lower respiratory tract, such as pneumocytes and lung macrophages, where its entry receptor, ACE2, is highly expressed, leading to more severe respiratory symptoms and somewhat contained spread. In contrast, SARS-CoV-2 has a broader replication scope, including the upper respiratory tract, facilitating its efficient transmission. This variation in cell tropism and replication rates between the two viruses may stem from differences in the binding affinities between the spike protein and ACE2 receptor. Other factors, including cellular glycans, integrins, and neuropilin 1, could also influence the phenotypic effects, the distinct behaviors and effects of SARS-CoV compared to SARS-CoV-2 [69,70].

2.1.2 – Zoonoses

The definition of zoonotic diseases includes all those infectious pathologies that naturally transfer from vertebrate animals to human and vice versa, as defined by the World Health Organization in 1951 [71]. Transmission from an infected animal host to humans can occur through direct contact, indirect contact via vectors, whether they are mechanical or biological, or through contaminated inanimate objects. Often, the lifecycle of these diseases may involve multiple vertebrate hosts, sometimes including invertebrates, to complete their infectious cycle. Historically, wildlife has

been a significant reservoir for infectious diseases that humans can contract, and nowadays, zoonotic diseases originating from wildlife represent one of the most significant challenges to public health globally [72]. The consciousness of the importance of wildlife-associated zoonoses is growing, highlighting the urgent need for increased research and attention in this area and while the exact number of zoonotic diseases is not definitively known, it is estimated that out of the 1,415 pathogens known to affect humans, approximately 62% have a zoonotic origin [73].

As aforementioned, a wide array of pathogens, ranging from viruses, bacteria, parasites, to fungi, are responsible for zoonoses. It is estimated that around 80% of all viruses, 50% of bacteria, 40% of fungi, 70% of protozoa, and 95% of helminths that infect humans have zoonotic origins.

The pathways for zoonotic disease transmission varies and can include both direct and indirect interactions with animals or their environments. Among the transmission modalities, consuming contaminated or improperly prepared animal products, such as milk, meat, eggs, and even raw products contaminated with animal waste, can lead to zoonoses [74–76]. Direct exposure to the bodily fluids of infected animals, including pets, or injuries like scratches or bites, as seen with rabies, are also common transmission routes. Additionally, indirect exposure through contact with animal habitats, contaminated objects, or bites from insect vectors like ticks and mosquitoes can result in infection. Certain zoonotic diseases require an intermediate host for transmission to humans, examples comprehend plague, Lyme disease, and West Nile virus infection, which may be transmitted via fleas, ticks, and mosquitoes, respectively [77–79]. Leisure activities that involve close contact with nature, such as camping, hiking, visiting zoos and farms, and various water sports, can also lead to an increase in the risk of coming into contact with zoonotic pathogens. An emerging concern in public health is the rise of antimicrobial resistance among zoonotic pathogens, complicating the treatment and control of these diseases.

The 'One Health' approach emphasizes the need for collaboration among veterinarians, medical researchers, policy makers, and public health experts to effectively address and manage emerging zoonotic diseases. This interdisciplinary

strategy is pivotal for controlling diseases transmitted by various pathogens, including arthropods, bacteria, helminths, protozoans, and viruses, which can lead to severe and sometimes fatal conditions in animals. Additionally, the zoonotic potential of these diseases poses significant risks to human health, underscoring the importance of a unified response [80–84].

The variety of animal species serving as reservoirs for pathogens that cause zoonotic diseases is notably vast, and research into outbreaks of zoonotic diseases has occasionally uncovered unanticipated new animal sources of infection for humans, ranging from wild to domesticated species. Beyond the pathogens that humans share with invertebrates, which act as vectors or intermediate hosts in the transmission of diseases, mammals are the predominant reservoirs for zoonotic pathogens, accounting for approximately 80% of known cases, followed by avian species. Within mammals, the highest number of shared pathogens occurs primarily with artiodactyls, animals often found in close proximity to humans, and only secondarily with rodents, carnivores, and primates.

Recent papers have underscored the camel's role in zoonotic transmission, identifying 19 diseases transmitted by this animal in Iran [85–87], a country where camel breeding is prevalent, and there is significant interaction between camels and humans through farming, as well as the consumption of camel meat and milk. Among the reported zoonotic pathogens are the plague, Q fever, campylobacteriosis, tuberculosis, salmonellosis, rabies, MERS, and toxoplasmosis.

Additionally, birds have been identified as primary carriers of the influenza A virus [88], while pigs, which are susceptible to both avian and mammalian strains of influenza, serve as intermediaries in the viral transmission, allowing for the recombination of these viruses. This process, known as reassortment, leads to the creation of mutant influenza strains that have the pathogenic potential in humans. Wild migratory birds also play a recognized role in spreading zoonotic diseases, either as direct carriers or by transporting infected arthropod vectors, such as in the case of the West Nile virus's introduction to the USA [89]. In addition to these zoonotic intermediates, the rising incidents of zoonotic diseases originating from wildlife, particularly bats,

highlights a global issue [90]. The practice of wildlife farming and trading exacerbates the risk of cross-species virus transmission by placing different species under stressful, cramped conditions; additionally, human activities such as hunting and guano mining increases direct exposure to bat-borne pathogens. These interactions are part of a broader trend of human invasion of wildlife habitats, driven by population growth and escalating demand for natural resources. Bats, belonging to the second most diverse mammalian order with over 1,400 species, harbor a wide variety of coronaviruses, to date, more than 4,800 coronavirus sequences have been identified in bats, representing over 30% of all bat viruses sequenced. Given that only 543 out of approximately 1,435 bat species have been studied for coronavirus presence, the actual diversity of bat coronaviruses is likely much higher. For this reason bats are huge reservoirs for the betacoronavirus lineage, from which several significant public health threats have emerged [91,92].

2.1.2.1 – SARS-CoV-2 as zoonotic pathogen

Since the initial identification of a coronavirus in chickens in the 1930s and the uncovering of the first coronaviruses known to infect humans, HCoV-229E and HCoV-OC43, in the 1960s, significant progress has been made in the field of coronavirus research [93]. The understanding of how coronaviruses replicate and their pathogenicity and infectivity has expanded rapidly, especially following the first outbreak of SARS-CoV in 2002 and MERS-CoV in 2012, highlighting their potential as zoonotic agents with serious implications for human health [44]. However, the origins of SARS-CoV-2 and the specifics of how it was transmitted to humans still remain unclear, despite extensive phylogenetic analysis have been carried out [94].

Since its discovery, extensive research has focused on various animal species to determine potential reservoirs or intermediary hosts for this virus, particularly exploring a wide array of insect-eating bats within the Rhinolophus genus. Notably, SARS-CoV-2-related viruses have been identified in different Rhinolophus species across multiple regions, including *R. shameli* in Cambodia (2010), *R. pusillus* and *R. malayanus* in China (2020 and 2019, respectively), *R. acuminatus* in Thailand (2020), and *R. cornutus* in Japan (2013). However, the bat-borne genome presenting

the highest similarity to that of SARS-CoV-2 is from *R. affinis*, known as RaTG13 (China, 2013), which shares 96.1% of its genomic sequence with SARS-CoV-2.

Since the first transmission of SARS-CoV-2 to humans, it has undergone various mutations and recombination's, with changes that have enhanced its ability to spread or avoid detection by neutralizing antibodies. While the identification of the exact origin of SARS-CoV-2 in bats is a significant aim, a more attainable goal is the identification of the genetic sequences that make up its unique mosaic structure. The spike protein is particularly critical, as it governs the virus's ability to bind to the cellular ACE2 receptor, which is the key for infection and host range so Temman et al. have reported a comparison between the receptor-binding domain of SARS-CoV-2 and that of cave-bats living in northern Laos [95]. The spike sequence of the closest related bat virus, RaTG13, shows limited similarity to SARS-CoV-2, especially in the receptor-binding domain (RBD), with only 11 out of 17 contact amino acids with the human ACE2 (hACE2) receptor being conserved. This results in RaTG13's reduced ability to bind to the hACE2 receptor in comparison to SARS-CoV-2. To date, evidence suggests that SARS-CoV-2 has a limited ability to infect bats and bat cell lines that have been examined. Moreover, no virus closely related to SARS-CoV-2 found in bats has demonstrated the capability to efficiently utilize the hACE2 receptor for the entry into human cells, nor they possess the furin cleavage site linked with enhanced pathogenicity in humans. On the other hand, sarbecoviruses, which are widespread among Rhinolophus bat populations residing in Chinese caves and in near southern regions, present a diverse genetic pool. In particular, in a study conducted in northern Laos, researchers have identified and characterized five sarbecoviruses, which present RBDs that differ from SARS-CoV-2 RBD by only one or two amino acids, exhibiting strong binding to hACE2, and facilitating entry and replication in human cells despite lacking the furin cleavage site. This finding underscores their potential role in the genesis of SARS-CoV-2 and highlights a risk of future direct human transmission, as schematically reported in Figure 4. Among the identified viruses, three in particular, BANAL-52, BANAL-103, and BANAL-236, bear a notable resemblance to SARS-CoV-2 in these specific protein domains, suggesting a close genetic relationship. These discoveries support the theory that

SARS-CoV-2 may have emerged from a combination of genetic sequences present in Rhinolophus bats inhabiting the vast limestone caves of Southeast Asia and South China. The identification of these new viruses highlights that recombination events or the natural selection of mutations that increase the RBD's affinity for hACE2 in an intermediate host, such as pangolins, or in humans post-spillover may have not occurred [96].

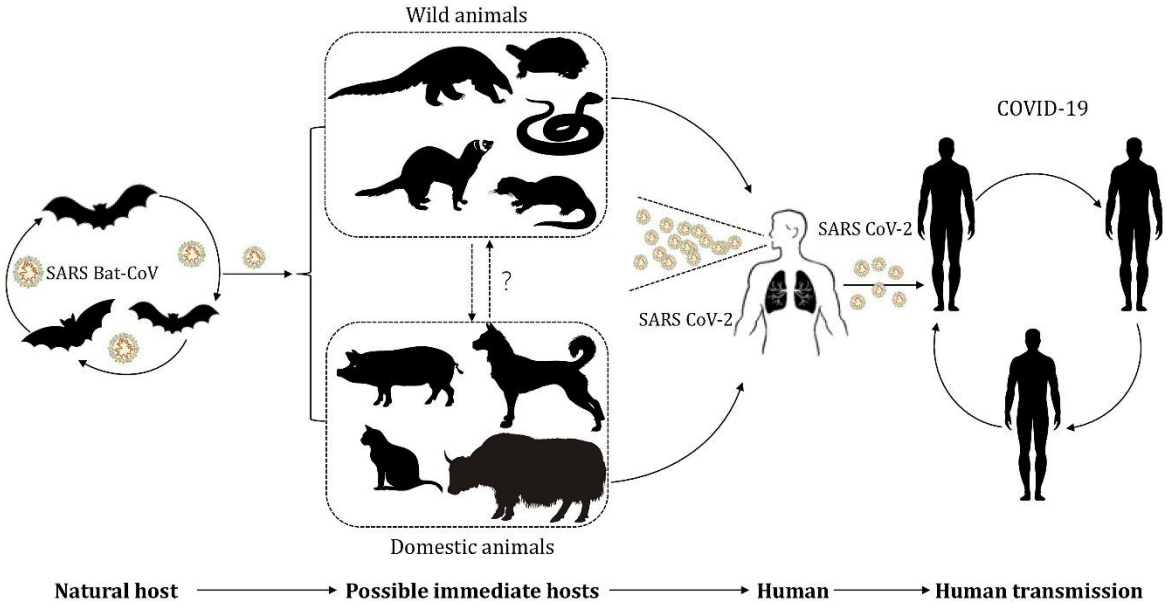

Figure 4: The potential transmission of SARS-CoV-2 between hosts and humans [97].

In a recent study by Pavan et al., they have reported a computational analysis to explore the similarities and differences in the main protease of SARS-CoV-2 compared to those found in the bat coronaviruses from the bats of Northern Laos. This work has a high importance also in perspective of the potential future application new M^{pro} inhibitors as broader spectrum antiviral agents [95]. This work reported a structural comparison that has been performed comparing the crystal structure of SARS-CoV-2's M^{pro} and the homology models of the bat coronavirus proteases RaTG13, identifying two primary structural differences neither one affecting the catalytic site [96]. Specifically, the substitutions that have been identified include a Phe96 in SARS-CoV-2 with a Thr in RaTG13, this latter is the only bat coronavirus with a significant change at this position, which results in fewer hydrophobic contacts without impacting any crucial interactions necessary for the protease's structural

integrity. In fact, this threonine is positioned in a flexible loop, suggesting the structural integrity remains unaffected by this substitution. The second structural difference involves Asn180 in SARS-CoV-2, which does not affect the activity. Moreover just like the reported Phe96 alteration, this change occurs in a solvent-exposed loop, indicating that it's unlikely to compromise the protease's function. Overall, not only the in silico analysis indicates that these structural differences do not lead to significant alterations in the M^{pro} structure, but also that the similarity of the catalytic site between SARS-CoV-2 and these bat coronaviruses supports the continued viability of targeting this protease for the treatment of current and future pandemics, awakening the concept of preparedness [96].

2.2 – Host and viral targets

As mentioned earlier the strategies for fighting viral pathogens may involve a dual approach: directly inhibiting viral components, essential for viral life cycle, or modulating the host's biological pathways that the virus exploits for entry, replication, and evasion of the immune response. These approaches encompass a broad range of targets, which are further going to be analyzed including structural proteins, such as the spike protein critical for cell entry, and non-structural proteins, like the RNA-dependent RNA polymerase (RdRp) and proteases, which are key for viral replication and maturation. In contrast, host targets involve receptors like ACE2 and transmembrane serine protease 2 (TMPRSS2), which facilitate virus entry, and various immune signaling pathways that can be modulated to enhance antiviral defense or mitigate pathological inflammation.

2.2.1 – Spike protein

The S proteins of coronaviruses belong to a homotrimeric class I fusion glycoprotein class, consisting of two distinct functional regions: S1 and S2. The S1 region, visible on the virus surface, includes the receptor-binding domain (RBD), which is critical for attaching to host cell receptors and thus influences the virus's cell tropism and its pathogenic nature. The S2 region, embedded in the membrane, features heptad repeated segments and a fusion peptide that facilitates the merging of viral and host cell membranes through significant structural changes [98].

Following the first severe human coronavirus outbreak, ACE2 was recognized as the crucial receptor for SARS-CoV infection, this has been confirmed also for SARS-CoV-2. In fact, given the substantial genomic and structural resemblance between these two coronaviruses S proteins (with a 76% amino acid identity), ACE2 was once again identified as the entry receptor for SARS-CoV-2. Notably, critical contact residues of SARS-CoV that bind to ACE2 are well-preserved in SARS-CoV-2 and in other related coronaviruses that either engage ACE2 or share similar amino acid characteristics. This was further supported by detailed atomic resolution studies of the SARS-CoV-2 S protein's interaction with ACE2 [99]. However, the bat coronavirus RaTG13, despite being the closest known relative to SARS-CoV-2 based on overall genome sequence (96.2% similarity), retains only one of the six key ACE2-binding amino acids, suggesting that recombination events among SARS-CoVs coexisting in bats likely played a significant role in SARS-CoV-2's development, mirroring the evolutionary path of SARS-CoV [44]. Further attention will be given to the S protein and its host receptors, in chapter 2, with particular reference to the entry process mediated by SARS-CoV-2.

2.2.2 – TMPRSS2

TMPRSS2, found in the human respiratory system it plays a pivotal role in the physiological activation of various proteins through specific amino acidic cleavage, as well as in the pathological dissemination and in the disease development of SARS-CoV and SARS-CoV-2. Importantly, SARS-CoV-2 primarily utilizes TMPRSS2 for cell entry, limiting the roles of CatB and CatL, and it has been shown that blocking TMPRSS2 effectively stops SARS-CoV-2 from infecting lung cell lines and primary lung cells [100]. This evidence underscores the potential of TMPRSS2 inhibitors like camostat mesylate and nafamostat mesylate which are under clinical trials, having already shown significant antiviral effectiveness against SARS-CoV-2 and other coronaviruses in in vitro studies [44].

2.2.3 – RdRP

The RNA-dependent RNA polymerase (RdRP), housed within nsp12, serves as a critical component of the coronavirus replication and transcription complex, making it an attractive target for antiviral drug development [101]. In fact, this enzyme plays an essential role in both the replication of the viral RNA genome and the transcription of sg-RNAs. The catalytic mechanism of RdRP involves the synthesis of a phosphodiester bond between nucleoside triphosphates (NTPs) in a process that requires a primer, where the involved NTP substrates are coordinated by two metal ions held in place by conserved aspartic acid residues. This process exhibits a high degree of conservation, also in the amino acidic regions crucial for nucleotide selection and catalysis [102].

Cryo-electron microscopy has been carried out for SARS-CoV-2 RdRP, the complex structure that includes nsp12 along with its cofactors nsp7 and nsp8 has been captured, displaying the characteristic right-hand shape of viral RdRPs, organized into finger, palm, and thumb subdomains, with the active site featuring seven conserved motifs that create a central cavity for RNA synthesis [103]. The structural design ensures precise coordination of the incoming NTP, RNA template, and primer strand, while the synthesis product's exit through a RNA exit path, highlighting the enzyme's sophisticated functionality [14].

Comparative analysis shows that the RdRPs of SARS-CoV and SARS-CoV-2 share over 95% similarity, with most variations found in the nidovirus RdRP-associated nucleotidyltransferase domain, which has already been identified as a genetic marker, though its functionality still remains to be fully understood. Interesting to note is the possibility of repurposing existing antiviral drugs thanks to the RdRP's structural and functional resemblance to other positive-strand RNA viruses, also thanks to this its pivotal role in the virus life cycle and the lack of a corresponding host cell enzyme, that renders this complex an ideal target for antiviral therapy. For this reason viral polymerase inhibitors, including nucleoside and non-nucleoside inhibitors that interact with allosteric binding sites, form the basis of many antiviral treatments, such as those for HIV and HCV [14]. Among the approved treatments,

remdesivir (RDV) can be identified [104]. As a phosphoramidate, RDV competes with ATP for incorporation by viral RdRPs, leading to delayed chain termination. This mechanism of action has been confirmed for many viruses such as Ebola, Nipah virus, but also SARS-CoV and SARS-CoV-2. Unlike typical nucleoside analogues that immediately halt RNA synthesis upon incorporation, RDV allows for the addition of three more nucleotides before terminating the chain. However, the effectiveness of nucleotide analogues like RDV may be compromised by the exonuclease domain's proofreading activity, part of nsp14, which can remove incorrectly incorporated nucleotides.

2.2.4 – PL^{pro}

PL^{pro}, a cysteine protease in SARS-CoV-2, plays a dual role by cleaving specific sites within the viral polyprotein (at nsp1/2, nsp2/3, and nsp3/4) and hydrolyzing ubiquitin (Ub) and Ub-like protein ISG15 from the lysine ε-amino group of host proteins, a process essential for the innate antiviral response [105]. This action effectively suppresses Ub-dependent immune defenses by inhibiting the production of IFNβ and interfering with IRF3 and NF-κB signaling pathways. Given its crucial functions in viral maturation and immune evasion, PL^{pro} has emerged as a key target for antiviral strategies, allowing the inhibition of virus replication and enhancing the host's immune response.

Sharing 83-86% of its sequence with its SARS-CoV counterpart and exhibiting significant divergence from MERS-CoV PL^{pro} (33% identity), SARS-CoV-2 PL^{pro} presents a characteristic catalytic triad (Cys111-His272-Asp286) that mirrors the active site in SARS-CoV PL^{pro} (Cys112-His273-Asp287). This triad specifically targets the conserved GGXL motif across the cleavage sites of the viral polyprotein. As aforementioned, PL^{pro} can cleave Ub and ISG15, recognizing a GGRL motif, from host proteins, showcasing a structural resemblance to human deubiquitinating enzymes. The enzyme's structure, resembling a right-handed form with the catalytic triad positioned between the thumb and palm subdomains, also features an Ub-binding site at the N-terminus and a zinc-binding fingers region where the four cysteines allow the coordination of the structural zinc ion. Crucial to its activity is the

Trp106 residue in the oxyanion hole, which facilitates the hemi-thioacetal substrate stabilization through a hydrogen bond formed with the indole nitrogen. Another notable aspect of PL^{pro}'s structure is the BL2 loop within the Tyr side chain, that adopts different conformations depending on whether the enzyme is bound to a substrate or to an inhibitor.

Comparative analyses of SARS-CoV-2 PL^{pro} with SARS-CoV's reveal specificity for glycine at the P1−P2 position, while the enzyme accommodates a variety of amino acids at the P3, ranging from basic to hydrophobic types, on the other hand, the S4 subsite prefers hydrophobic residues, especially leucine, though a particular affinity for unnatural residues hTyr and hTyr(Me) over leucine was shown. This specificity underlines the potential for designing inhibitors that could selectively target the PL^{pro} enzyme, offering insights into antiviral drug development [14,106,107].

2.2.5 – ACE2 receptor

ACE2, a type I transmembrane protein, is widely distributed in human tissues, including heart, lungs, kidneys, and intestines. It comprises an N-terminal peptidase domain and a C-terminal domain similar to Collectrin, characteristic of the full-length ACE2 structure. Similarly to SARS-CoV, SARS-CoV-2 exploits the ACE2 receptor for cellular binding and entry through interaction with the viral S protein (detailed mechanism is reported in Chapter 3 of this thesis). Notably, the S protein of SARS-CoV-2 has a significantly higher binding affinity for the ACE2 receptor compared to that of SARS-CoV, potentially up to 20 times greater, which may be the reason for the more efficient human-to-human transmission observed with SARS-CoV-2 [108,109].

2.2.6 – Helicase

SARS-CoV-2 helicase or NSP 13 is a 67 kDa protein that catalyzes the unwinding of the genome, even though the precise role has not been identified yet, it is considered a pivotal component of the viral replication thus affording a promising target. The activity of this enzyme is favored by the complex with NSP12 and works in tandem with the replication-transcription complex previously mentioned [110].

2.3 – M^{pro} as antiviral target

Viral proteases have been successfully targeted to develop a range of approved medications, particularly for chronic infections such as human immunodeficiency virus (HIV) and hepatitis C virus (HCV), targeting the aspartyl protease and the serine protease, respectively [111,112].

M^{pro}, a 33.8 kDa protease plays a crucial role in the life cycle of SARS-CoV and SARS-CoV-2 by cleaving the viral polyprotein to produce the 11 nsps, essential for virus replication. In addition to this it shares a high degree of sequence similarity with SARS-CoV's M^{pro} (96% identical) and exhibits considerable homology with M^{pro} from other coronaviruses (41–51% identity and 73–80% similarity)[113]. Importantly, humans lack an analogous enzyme, rendering it a highly specific target for antiviral intervention. These major reasons confer to M^{pro} a significant role and render this protein a valuable target for antiviral drug development, which has also been amply validated by the approval of Paxlovid in 2022 for COVID-19 treatment [114].

M^{pro} showcases a total of 306 amino acids, and functions as a dimer, as shown in Figure 5. Each monomer of this protease comprises two distinct sections: the N-terminal region, which includes the catalytic dyad, and the C-terminal region, as detailed in Figure 5. The catalytic dyad, crucial for the enzyme's function, is situated within a cleft formed by the juxtaposition of two chymotrypsin-like domains, Domain I (spanning amino acids 8 to 101) and Domain II (encompassing amino acids 102 to 184).

The C-terminal region of SARS-CoV-2 M^{pro}, also known as domain III (spanning amino acids 201–303), is structured into five alpha-helices. These helices create globular folds that are crucial for the stability and functional integrity of M^{pro}'s active dimer form. Additionally, domain III is linked to domain II by a lengthy and flexible loop (covering residues 185–200), which introduces a degree of flexibility to the overall structure. Significantly, the arrangement of the two monomers within the C-terminal domain III forms a near-perpendicular configuration relative to each other. Hence, any alteration in the position of domain III in the dimer can significantly impact its enzymatic function. For instance, in SARS-CoV M^{pro}, the R298A mutation leads

to a 33-degree rotation of domain III. This rotation interferes with dimer formation and diminishes the enzyme's catalytic efficiency. Therefore the destabilization of this dimeric structure makes an interesting strategy at the inhibition of this enzyme [115,116].

The geometry and amino acid composition of the substrate-binding pocket are critical for understanding enzyme activity and guiding the structure-based rational design of small-molecules or peptide-based ligands. Within the substrate-binding pocket of M^{pro}, six sub-pockets are identifiable (S1, S2, S3, S4, S5 and S1'), aligning with the P5 to P1' positions of the natural substrate. Among these, the subsites S1', S1, S2, S3 and S4 are identified as the principal ones, playing a significant role in the enzyme's function and substrate recognition [117,118]. The specificity of the amino acids recognized by the coronavirus M^{pro} at the S1', S1, S2, S3 and S4 subsites is distinct. Notably, S1' serves as a crucial site for the binding of the warhead of covalent inhibitors, in fact, in this position is housed the catalytic dyad composed by Cys145 and His41, where Cys145 acts as a nucleophile, and His41 functions as a proton donor/acceptor, both playing integral roles in the catalysis process, further detailed.

The S1 and S2 subsites within the M^{pro} structure are characterized as deep cavities. At the S1 subsite, a crucial feature is the presence of an oxyanion hole, essential for the protease's function. This oxyanion hole, primarily formed by the backbone nitrogen of Gly143, Ser144, and Cys145, facilitates the formation of hydrogen bonds with peptidomimetic inhibitors. In terms of substrate specificity, the P1 position within the substrate is highly conserved, selectively accommodating a glutamine residue. This specificity is underscored by the consistent hydrogen bonding between the imidazole group of His163 and the side chain of Gln at the S1 subsite rendering it fundamental for a strong binding and biological activity. As a result of numerous studies, the (*S*)-γ-lactam ring has emerged as an optimal mimic of the Gln side chain, confirming its potential for inhibitor design.

The S2 subsite is characterized as a buried hydrophobic cavity capable of accommodating large alkyl or aryl groups, similar to the Leu side chain in the substrate's S1 position. This pocket is encased by a "lid" formed by residues 46−51

of the 310 helix, in particular Met49, three sides delineated by the backbone of residues 186−188 and the side chains of His41, Asp187, and Gln189, while the bottom of this cavity is made up by Met165, completing the structural composition of the S2 pocket.

Among the four main sub-pockets of M^{pro}, sub-pocket 2 has the highest resemblance and conservation when compared to that of MERS-CoV. This similarity is underscored by only two conservative substitutions: Met49 in SARS-CoVs is replaced by Leu49 in MERS-CoV, and Arg188 is swapped for Lys191. Even though a high amino acidic similarity is present, the internal volume of SARS-CoVs' of this sub-pocket, which is 252 $Å^3$, is considerably larger than the corresponding sub-pocket in α-genus coronavirus homologues, like HCoV-NL63 M^{pro}, which has a volume of just 45 $Å^3$ [14,111,115]. Furthermore, the lack of electron density observed in the S2 pocket suggests that ordered water molecules are not present there, this may be caused by the flexible nature of Gln189's side chain that likely plays a role in excluding water from the S2 subsite when the M^{pro} is complexed with various inhibitors. This explains the preference for hydrophobic amino acids for this sub-pocket, notably leucine, which is crucial in the design of peptide-based inhibitors, in addition to various hydrophobic functional groups, including benzene rings and cyclopropyl-methyl.

The S4 subsite is characterized by its shallow hydrophobic nature, forming a slender cavity that typically accommodates smaller amino acids such as Ala, Val, Pro, and Thr.

Having identified the four most important sub-pockets of the active site allows to rationally design inhibitors, small molecules or peptide-based. Focal residues which need to be taken into consideration during the structure-based drug design comprehend Leu27, His41, Met49, Ile51, Tyr54, Phe140, Leu141, Ser144, Cys145, Tyr161, His163, Met165, Glu166, Leu167, His172, Asp187, Thr190, and Ala191, marking them as focal points for enzymatic activity. Among these amino acids, important to note are His163 and Glu166, which play a key role in recognizing the substrate's Gln-P1 position through the engagement in hydrogen bonding. Glu166

from one monomer is thought to interact with the N-finger of both monomers, aiding in the formation of the S1 subsite within the substrate-binding pocket. In fact, as previously mentioned, several studies indicate that mutations in Glu166 can impact the aggregation of dimers. Beyond the catalytic dyad of Cys145 and His41, a catalytic water molecule also participates in the enzymatic activity by helping maintain His41 in its protonated state. This water molecule establishes hydrogen bonds with His41, His164, and Asp187, contributing to the stabilization of their spatial arrangement [55].

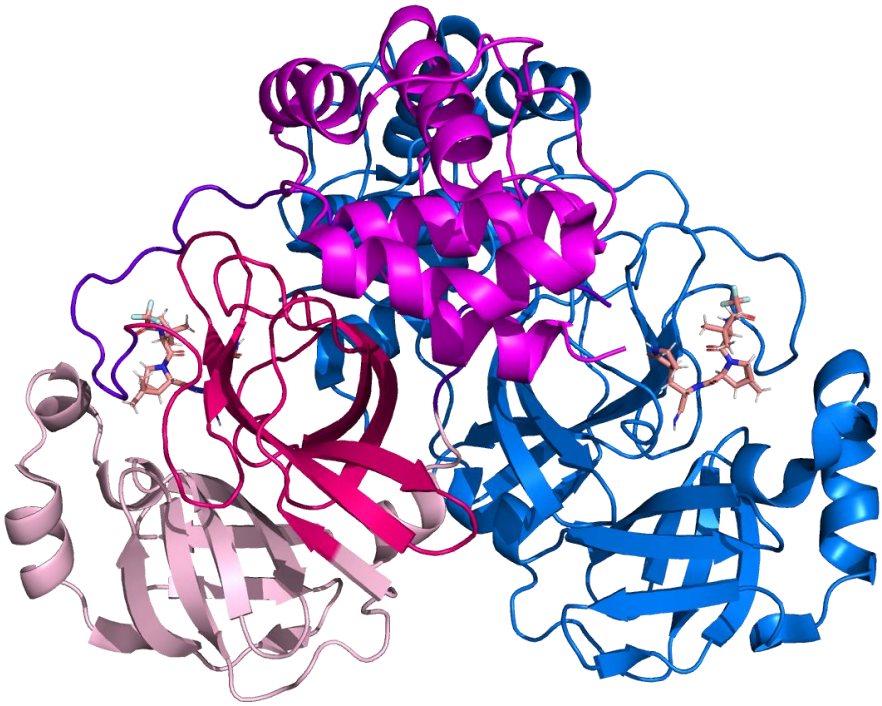

Figure 5: A peptide-based inhibitor co-crystallized with dimeric M^{pro} (PDB 8dz2), the two dimers can be distinguished thanks to the two different colorings, one is represented in blue the other in shades of pink, in particular the three domains can be identified, Domain I light pink, Domain II hot pink and Domain III magenta, while the conjunction flexible loop is colored in purple.

2.3.1 – M^{pro} catalytic cycle

The catalytic mechanism of SARS-CoV-2 M^{pro} differs from the conventional chymotrypsin-like catalytic triad, by employing the Cys145-His41 dyad situated between the S1' and S1 subsites as its active site. This process, which is illustrated

in Figure 6, starts when the imidazole ring of His41 becomes protonated, creating an ionized His41+-Cys145- dyad. This protonation facilitates the activation of Cys145's thiol group, rendering it highly nucleophilic. Consequently, Cys145 attacks the carbonyl carbon of the substrate's scissile bond. Following this nucleophilic attack, the substrate's N-terminal fragment is released, leading to the formation of a thioester bond between the enzyme's sulfhydryl group and the substrate's carbonyl carbon at the cleavage site. The cycle concludes with the hydrolysis of the thioester bond by a water molecule's nucleophilic attack, which releases the substrate's C-terminal fragment and regenerates the free enzyme [55]. It's important to note that the efficiency and specificity of this catalytic process are finely tuned by the structural arrangement and chemical properties of the active site residues. The spatial configuration of His41 and Cys145 within the enzyme's active site is crucial for effective catalysis, ensuring that the nucleophilic attack is both precise and efficient. Additionally, the role of water molecules in the catalytic cycle, specifically their orientation and deprotonation for effective hydrolysis, underscores the importance of the enzyme's hydration shell and the dynamic interaction between the enzyme, substrate, and solvent [119].

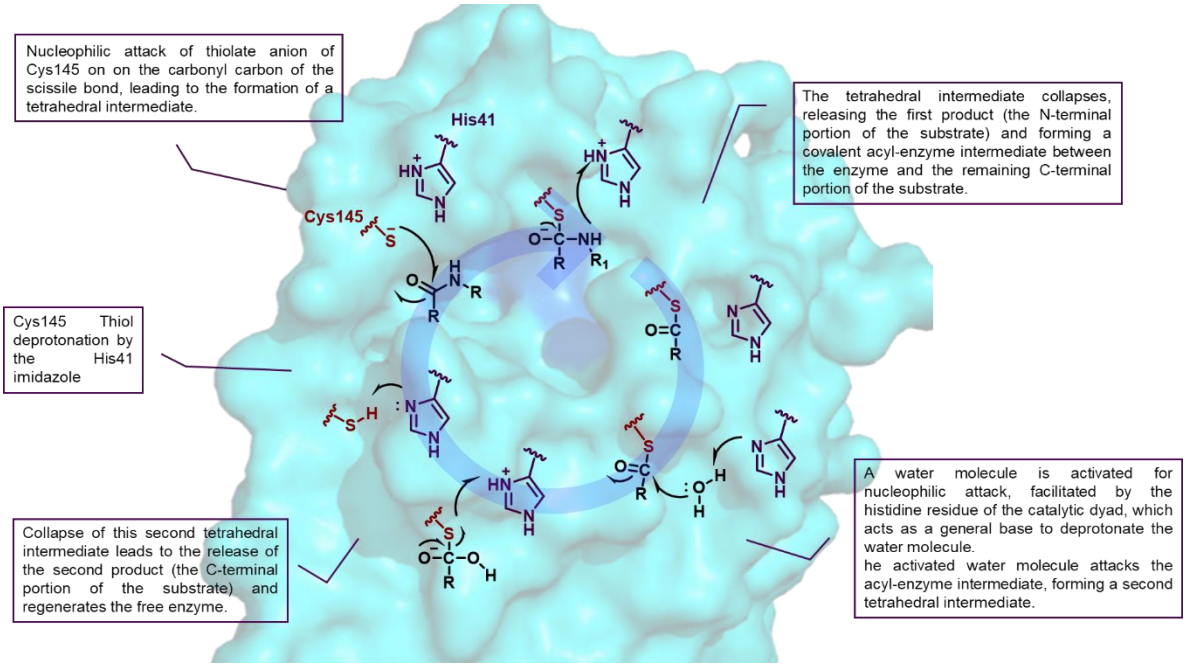

Figure 6: M^{pro} catalytic cycle

2.3.2 – Inhibitors of M^{pro}

As previously highlighted, M^{pro} plays a crucial role in processing the viral polyproteins into mature viral proteins necessary for the virus's replication cycle, and survival. Thus, the design and development of M^{pro} inhibitors represents a strategic approach to interfere with viral replication, offering a promising pathway for the treatment of COVID-19. In terms of structures, M^{pro} inhibitors can be divided into peptide-based inhibitors and non-peptidic small molecules. The action of peptide inhibitors unfolds in a two-step process. Initially, the peptidomimetic compounds bind to M^{pro}, forming a noncovalent complex. Subsequently, the inhibitor's warhead, positioned near the enzyme's catalytic site, undergoes a nucleophilic attack involving the catalytic cysteine, facilitating the formation of a covalent bond ultimately blocking the catalytic activity. These reactive groups predominantly include Michael acceptors, aldehydes, nitriles and various activated ketones. This section aims to explore the diverse landscape of M^{pro} inhibitors, highlighting their mechanisms of action, efficacy, and potential as therapeutic agents against SARS-CoV-2 [114,120].

2.3.2.1 – Peptide-based inhibitors

These inhibitors are characterized by different warheads, which are chemical moieties designed to interact directly with the catalytic cysteine 145 of the active site, thereby blocking its activity. Each type of warhead presents a unique mechanism of action and, consequently a different profile of efficacy, selectivity, and potential side effects.

ALDEHYDES – this group allows the design of covalent inhibitors of the M^{pro}, however their reactivity can lead to chemical instability, off-target effects and toxicities, posing challenges for therapeutic use.

KETONES – this warhead presents a less electrophilic nature, aiming to retain efficacy while minimizing off-target interactions.

α,β-UNSATURATED ESTERS and related MICHAEL ACCEPTORS – this moiety binds through a Michael addition reaction and offers a promising balance of specificity and potency.

NITRILES – this functional group leverages the stability and selectivity of the nitrile group to offer a targeted approach to M^{pro} inhibition.

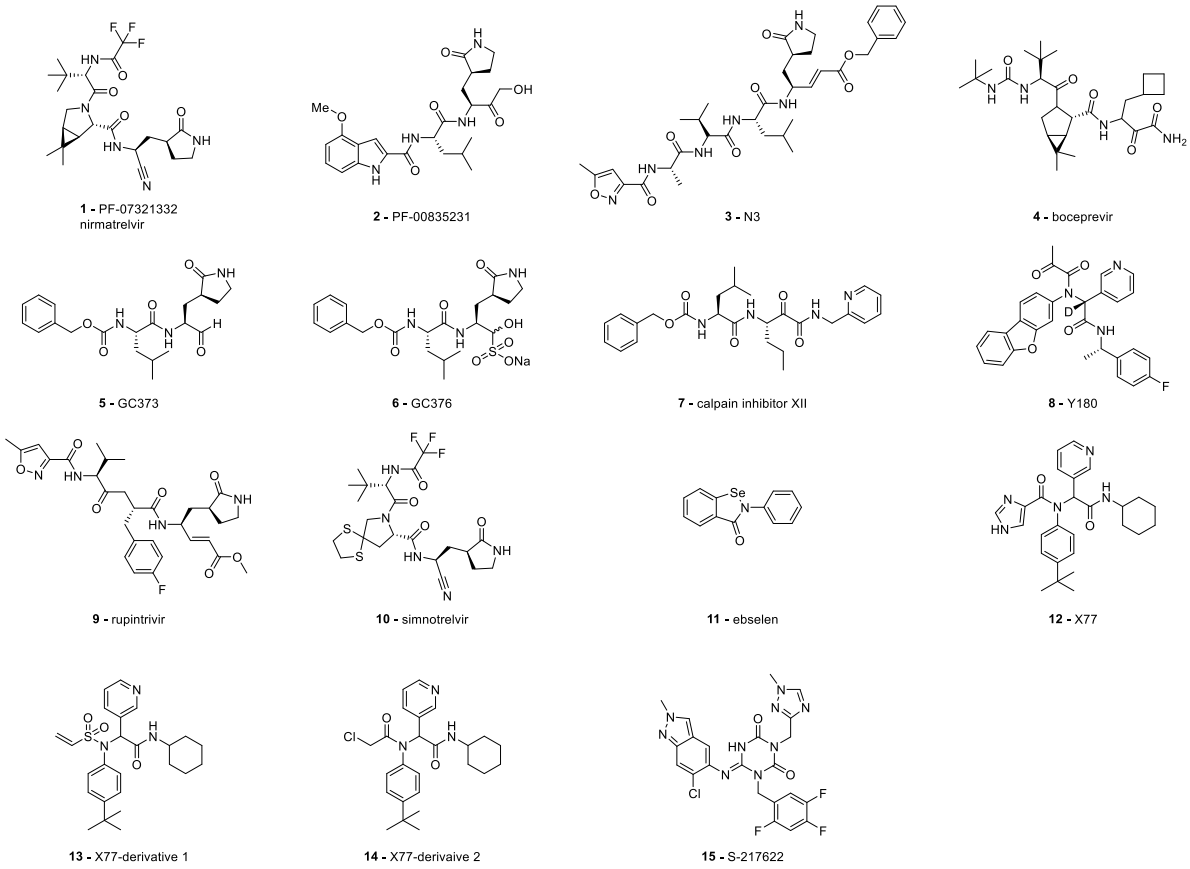

*Figure 7: M^{pro} peptide-based (compounds **1-10**) and non-peptidic small molecule inhibitors (compounds **11-15**)*

PF-00835231 and PF-073221332 or nirmatrelvir

Nirmatrelvir or PF-07321332 (**1**, Figure 7 and X-ray co-crystal structure with M^{pro}, Figure 8, PDB 7z45) [121] has recently been approved by FDA and EMA in combination with ritonavir, for the treatment of COVID-19. An analogue of this inhibitor had been previously designed during the first coronavirus outbreak, and during the last pandemic an improvement of the pharmacokinetic and pharmacodynamic properties led to the design of **1**, giving promising results; successively it has been tested in clinical trials until its final approval in 2022.

In clinical trials, the antiviral combination demonstrated significant efficacy: when administered within five days after symptoms began it decreased the likelihood of COVID-19-related hospitalization or death by 88% when compared to a placebo.

The initial design started from compound PF-00835231 (**2**) [122], which is equipped with a hydroxylmethyl ketone warhead [56] and exhibited potent inhibition against SARS-CoV-2 M^{pro}, with an IC_{50} against the isolate enzyme of 6.9 nM and an EC_{50} in infected cell of 231 nM. It also possess favorable drug properties, and didn't undergo significant metabolic degradation. However, its passive absorption and oral bioavailability were significantly low, consequently, to enhance the pharmacokinetic profiles of a potential antiviral medication, scientists from Pfizer have undertaken various modifications, among which the covalent warhead and further refinement of the compound's side chain architecture.

During the optimization phase, the introduction of benzothiazole and nitrile as covalent warheads notably enhanced oral bioavailability by reducing the number of hydrogen bond donors (HBDs), which are known to diminish oral bioavailability. The strategic use of nitriles to lower the HBD count distinguishes **1** from **2**. Furthermore, to optimize the molecular structure, researchers incorporated a 6,6-dimethyl-3-azabicyclohexane element into the scaffold's side chain, mimicking the folded turn of Leu structure. This adjustment aimed to further minimize HBD presence around the P2/P3 amide linkage, taking inspiration from anti-HCV medication boceprevir.

This refinement has enhanced the passive absorption of **1** in Madin-Darby Canine Kidney-Low Efflux (MECK-LE) cells in comparison to **2**. Successively, the N-terminal indole fragment was modified into a methylsulfonamide group, which established hydrogen bonds with Gln189 and Glu166, and there was a notable improvement across all measures of drug efficacy, in fact, the methylsulfonamide's branched and acyclic structure allows peptidomimetic inhibitors to more effectively occupy the S3 pockets of M^{pro}. However, leveraging the interaction pattern of methylsulfonamide, researchers modified the methylsulfonamide group incorporating a trifluoroacetamide. While this modification may have decreased the antiviral effectiveness of the inhibitor, it had significantly enhanced its oral bioavailability. Ultimately, substituting the benzothiazole moiety with a nitrile group resulted in the clinical candidate **1** reported in Figure 7 (compound **1**). This modification allowed the improvement of pharmacokinetic properties compared to **2**. Specifically, in rat

models, **1**'s oral bioavailability and the fraction of the dose absorbed through the gastrointestinal tract were thirty times greater than those observed for **2**.

Regarding metabolism, both **1** and **2** showed comparable rates of plasma clearance in rat studies (27.2 mL/min/kg vs. 27.0 mL/min/kg, respectively). However, **1** exhibited a rate of NADPH-dependent metabolic clearance in liver microsomes approximately threefold higher than that of **2**, and it was attributed to enhanced first-pass metabolism via CYP3A4 (24.5 µ/min/mg vs. 7.47 µ/min/mg). For this reason **1** has been formulated to be administered alongside ritonavir, a substrate of CYP3A4, to mitigate this effect [55].

Ritonavir lacks direct antiviral effects against SARS-CoV-2 but plays a crucial role by binding to metabolic enzymes. This interaction inhibits the breakdown of **1**, ensuring its stability and effectiveness in targeting the M^{pro} [56].

1 demonstrated a favorable safety profile, showing high specificity across a wide range of human proteins without adverse effects. It also tested negative in genetic toxicity evaluations and the rat micronucleus assay. Additionally, studies on embryo-fetal development, fertility, and early embryonic development in animal models have confirmed the safety profile of nirmatrelvir [113].

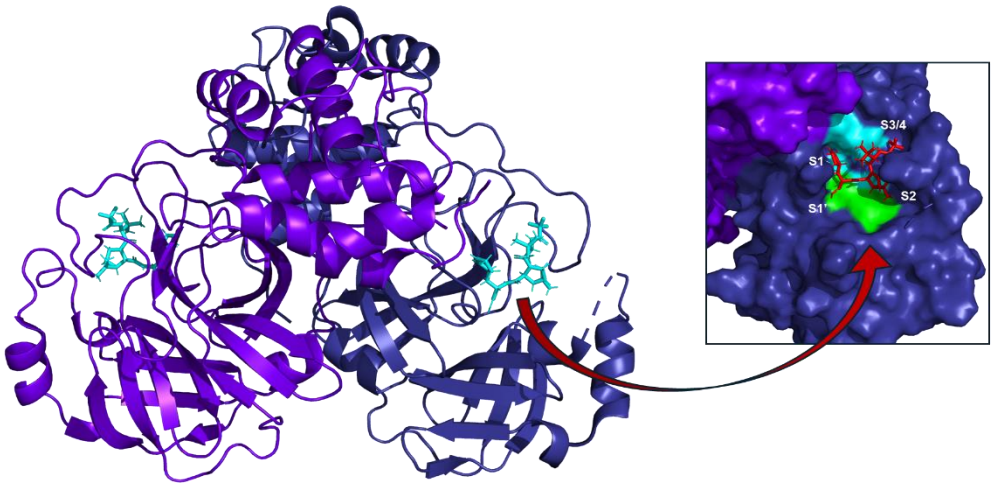

Figure 8: Cristal structure of M^{pro} with nirmatrelvir (PDB7Z45)

N3

The discovery of the SARS-CoV M^{pro} inhibitor N3 (Figure 7, compound **3**) identified through structure-based drug design, demonstrated an inhibitory constant (Ki) of 9.0 μM, demonstrating to possess a good inhibitory potency also against the M^{pro} of SARS-CoV-2 exhibiting an EC_{50} of 16.8 μM [113,123,124]. The first X-ray structure of SARS-CoV-2 M^{pro} has been achieved complexed with N3 (PDB 6LU7 and 7BQY) [125]. This inhibitor has been recognized for its broad-spectrum activity across various coronaviruses, including inhibitory activities noted against SARS-CoV (Ki 9 μM) and MERS-CoV (IC_{50} 0.3 μM).

In particular, N3 effectively occupies the substrate binding sites of M^{pro}, closely mimicking the natural substrate of the enzyme. It engages in a Michael addition reaction with the -SH group of Cys145, forming a covalent bond through the acrylate moiety, thereby securing a strong attachment. The lactam group within N3, mimicking the Gln residue at the P1 position, accomodates into the S1 sub-pocket, interacting with several residues including Phe140, Leu141, Asn142, Glu166, His163, and His172 through multiple hydrogen bonds.

The Leu side chain at the P2 position of N3 engages in hydrophobic interactions within the S2 sub-pocket, bordered by residues such as His41, Met49, Tyr54, Met165, and Asp187, and forms a hydrogen bond with Gln189, while the P3 Val side chain is exposed to solvent, whereas the P4 Ala residue resides within the S4 sub-pocket, interacts with Met165, Leu167, Phe185, Gln192, and Gln189. The terminal oxazole group positioned at the pocket's edge, likely participates in hydrophobic interactions with Pro168, Thr190, and Ala191. Furthermore, the inhibitor's benzyl ester group targets the S1’ sub-pocket, engaging in hydrophobic interactions with Thr24 and Thr25, illustrating the compound's comprehensive engagement with the M^{pro} active site.

Boceprevir

Initially developed for the treatment of hepatitis C virus, boceprevir (**4**, Figure 7), has been identified by various research teams as an inhibitor of SARS-CoV-2 M^{pro}, exhibiting IC_{50} values between 0.95 μM and 8.0 μM. The replacement of the

traditionally utilized lactam ring at the P1 position with a cyclobutyl ring, which is incapable of forming hydrogen bonds at the S1 subsite, is believed to contribute to boceprevir's relatively moderate activity against M^{pro}. Moreover, boceprevir has shown a wide spectrum of anti-viral effects, which include SARS-CoV-2, with EC_{50} values ranging from 1.3 to 19.6 μM. The crystal structure of boceprevir in complex with SARS-CoV-2 M^{pro} has been solved and provides additional information on the binding mode of this compound (PDBs 7BRP,59 6WNP, 7C6S, and 6ZRU) [14,113,126].

GC373 and GC376

GC373 and its prodrug form, GC376 (**5** and **6**, Figure 7), which transforms into its active aldehyde version by shedding the bisulfite group, target the Cys145 of M^{pro} through alkylation. Initially developed for the treatment of feline coronavirus, these compounds have been identified as effective M^{pro} inhibitors, demonstrating submicromolar IC_{50} values. They exhibit robust anti-SARS-CoV-2 capabilities in cellular assays, with EC_{50} values of 1.5 and 0.92 μM, respectively. GC376, in particular, displays a broad-spectrum antiviral activity against various coronaviruses, affecting multiple cysteine proteases from different virus strains with IC_{50} values ranging from 0.72 to 4.35 μM and showing high nanomolar potency against several coronaviruses (TGEV, FIPV, MHV, 229E, and BCV) in cellular models [14,127].

Moreover, two closely related analogs of GC376, differing only in their electrophilic warhead (either an aldehyde or an α-ketoamide), have shown to be effective inhibitors of EV 3C and norovirus 3CL cysteine proteases, as well as replicative agents of various viruses, including human rhinoviruses (HRVs). Despite this, these compounds were found to have limited pharmacokinetics and demonstrated limited efficacy against SARS-CoV-2 in mouse models. Modifications to GC376 have led to derivatives with slightly enhanced enzymatic and cellular efficacy. Importantly, the crystal structure of GC376 in complex with SARS-CoV-2 M^{pro} has been successfully determined, providing valuable insights into its mechanism of action (PDBs 7BRR,59 6WTJ,60 6WTT,56 7C8U, 7C6U, and 7CBT) [113,126,128].

Calpain inhibitor XII

Calpain Inhibitor XII (**7**, Figure 7), characterized by its *n*-propyl P1 side chain, has demonstrated effective inhibition of SARS-CoV-2 M^{pro}, with an IC_{50} value of 0.45 μM against the enzyme and an EC_{50} value of 0.49 μM in VERO E6 cells. Moreover, this compound has shown a broad-spectrum activity against various coronaviruses, including SARS-CoV and SARS-CoV-2 [113,126].

Y180

Compound Y180 (**8**, Figure 7), characterized by a methyl ketone warhead, has been identified as a highly effective inhibitor of SARS-CoV-2 M^{pro}, demonstrating an IC_{50} value of 8.1 nM and advancing through preclinical studies. It showed potent antiviral effects against both the original and the variant strains of SARS-CoV-2, with EC_{50} values ranging from 11.4 to 34.4 nM. Y180 also displayed good oral bioavailability (92.9% in mice), favorable pharmacokinetics (with half-life of 1.42 h), and exhibited no significant toxicity, making it a promising candidate against SARS-CoV-2 in various animal studies [113].

Rupintrivir

Rupintrivir (AG7088) (**9**, Figure 7), known for its strong inhibition of the rhinovirus M^{pro}, demonstrated minimal inhibitory effect on the M^{pro} enzymes of both SARS-CoV and SARS-CoV-2, with IC_{50} values exceeding 68 μM. Despite this, it was effective in suppressing SARS-CoV-2 replication, achieving an EC_{50} of 1.87 μM [113].

Simnotrelvir

The structure-based refinement of boceprevir, has resulted in the discovery of simnotrelvir (**10**, Figure 7). This compound targets SARS-CoV-2 M^{pro} through a covalent bond, characterized by an enthalpy-driven thermodynamic binding. Comprehensive enzymatic tests have established simnotrelvir as a highly effective and selective inhibitor across various coronaviruses with IC_{50} 9 nM, and EC_{50} M^{pro} 34 nM. It has demonstrated capability in inhibiting the replication of SARS-CoV-2 variants in cellular assays. Moreover, simnotrelvir shows promising

pharmacokinetics and safety profiles in both male and female rats and monkeys. It proved to have significant oral efficacy in a male mouse model of SARS-CoV-2 Delta variant infection, notably reducing viral loads in the lungs and completely clearing the virus from the brain [129].

2.3.2.2 – Small molecule inhibitors

Ebselen

Ebselen (**11**, Figure 7), a synthetic organoselenium compound designed to mimic glutathione peroxidase, is recognized for its ability to cross the blood-brain barrier, though it has also been labeled as a pan-assay interference compound (PAIN) due to its capability to bind to the reactive cysteines in a non-selective manner [130]. It exhibits anti-inflammatory, anti-tumor, and antiviral properties, which has led to its approval by the FDA as a novel anti-inflammatory agent. Identified through a comprehensive screening of approximately 10,000 substances, including natural products, FDA-approved drugs, and clinical trial candidates, using fluorescence resonance energy transfer (FRET) analysis, ebselen emerged as one of the most potent inhibitors of M^{pro}, exhibiting an IC_{50} of 0.67 μM. Furthermore, ebselen is notable for its minimal cytotoxicity, with a median lethal dose in rats exceeding 4600 mg/kg, underscoring its safety, which has been affirmed in numerous human clinical trials [131,132].

X77 and its derivatives

Inhibitor X77 (**12**, Figure 7), a non-covalent small molecule targeting SARS-CoV M^{pro}, has been modified to act as a covalent inhibitor against SARS-CoV-2 M^{pro}, thanks to crystallographic analyses, by replacing the imidazole ring with various covalent warheads. These modifications strategically place the warheads close to the catalytic cysteine residue, significantly enhancing the molecule's inhibitory effectiveness. As a result, the potency of the modified compounds, i.e. derivatives **13** and **14**, reported in Figure 7, improved remarkably, achieving IC_{50} values of 0.42 μM and 0.41 μM, respectively [133].

S-217622

On November 22, 2022, Japan sanctioned the use of S-217622 (**15**, Figure 7), a novel non-covalent inhibitor targeting the M^{pro} of SARS-CoV-2. This compound displayed potent inhibitory efficacy with an IC_{50} of 0.13 μM, alongside advantageous drug metabolism and pharmacokinetic properties. It exhibited broad-spectrum antiviral effectiveness against various SARS-CoV-2 mutations and members of the coronavirus family *in vitro*. The drug is characterized by optimal pharmacokinetic and drug metabolism profiles suitable for oral administration, including robust metabolic stability (with 96% stability in human and 88% in rat liver microsomes), high oral bioavailability (97%), and a low rate of clearance (1.70 mL/min/kg in rats), marking it as a promising therapeutic option [134,135].

2.4 – Broad spectrum inhibitors

The M^{pro} of coronaviruses share important structural similarities, as amply discussed in the previous paragraphs, with the main proteases found in enteroviruses (EVs), which are small, non-enveloped (+)-ss-RNA viruses. Specifically, in the genome of EVs, the M^{pro}, is produced from the 3C region, leading to the CoVs protease being referred to as 3C-like. Given the conservation of 3C proteases across various viruses, including enteroviruses, rhinoviruses, and coronaviruses, the pursuit of broad-spectrum antiviral agents is a logical step [136], also confirmed by the dual action of many protease inhibitors reported in literature as inhibitors of both enterovirus and SARS-CoV-2 proteases [137–139]. This cross-viral conservation emphasizes the potential to target common enzymatic functions, presenting a unified approach in the development of antiviral therapies. Such an approach not only streamlines drug development but also expands the arsenal against emerging and existing viral threats, highlighting the strategic importance of identifying and targeting conserved viral components [139,140].

The EVs 3Cprotease ($3C^{pro}$) features a chymotrypsin-like structure, possessing two catalytic domains that resemble domains I and II found in the M^{pro} of coronaviruses, though differently from the M^{pro}, the EV $3C^{pro}$ operates as a monomer, lacking such a domain. Furthermore, the EV $3C^{pro}$ incorporates an acidic residue (Asp/Glu)

alongside the catalytic Cys-His pair, creating a reactive triad, a feature that distinguishes it from the coronaviruses M^{pro}. A pivotal similarity between the M^{pro} of coronaviruses and enteroviruses is their unique and near-absolute preference for glutamine at the P1 position of their substrates. This specific requirement, not found in human proteases, enhances the potential of these viral proteins as targets for the development of inhibitors that are both safe and selective. In addition to this, a comparative analysis between the SARS-CoV M^{pro} and the Coxsackie B $3C^{pro}$ reveals that in EVs, the S2 site is characterized by an open hydrophobic channel bordered by Arg39, Asn69, and Glu71, which create the back wall, with residues 127−132 and His40 forming the side walls, and Val162 making up the base. Despite these structural differences, covalent peptide-based inhibitors designed for these enzymes have shown effectiveness in broadly suppressing both EVs and CoVs replication in cellular models [14].

Furthermore, overlaying the X-ray crystal structures of the main proteases from SARS-CoV-2, SARS-CoV, and MERS-CoV (Figure 9), reveals a significant structural resemblance and conservation of the active site. This similarity could be crucial in creating drugs effective against a broad range of coronaviruses. Indeed, it has facilitated the development of inhibitors targeting SARS-CoV-2's M^{pro}, utilizing the foundation laid by earlier compounds aimed at the main proteases of SARS-CoV or MERS-CoV as in the case of nirmatrelvir [111].

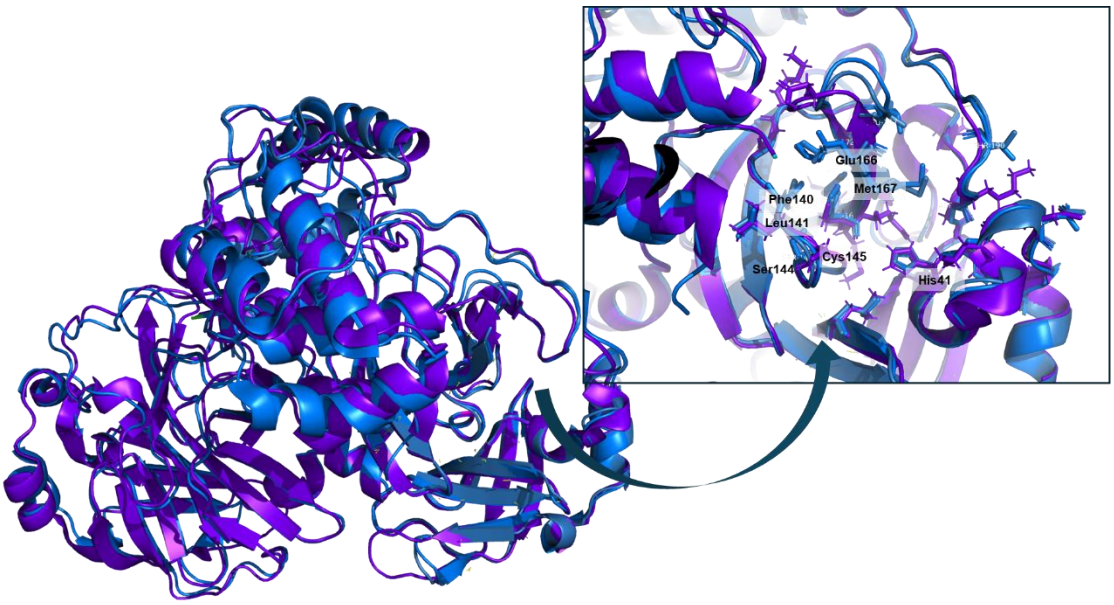

Figure 9: Superimposition of the main protease of SARS-CoV-2 (PDB 7P35, skyblue cartoon), MERS-CoV (PDB 4YLU, purpleblue cartoon) and SARS-CoV (PDB 7ZQW, marineblue cartoon), highlights the high homology among these three proteases, and allows for the design of broad spectrum antiviral agents, the active site pocket has been highlighted and the amino acids involved in the binding have been labeled.

To validate this approach, numerous studies have tested a range of peptide-based inhibitors, previously effective against other RNA viruses like EV71, on the M^{pro} enzymes of SARS-CoV and MERS-CoV, showing the potential for creating broad-spectrum antiviral agents [141].

2.5 – AIM OF THIS STUDY – Design, synthesis and biological evaluation of peptide-based inhibitors of SARS-CoV-2 M^{pro}

2.5.1 – Design of peptide-based inhibitors

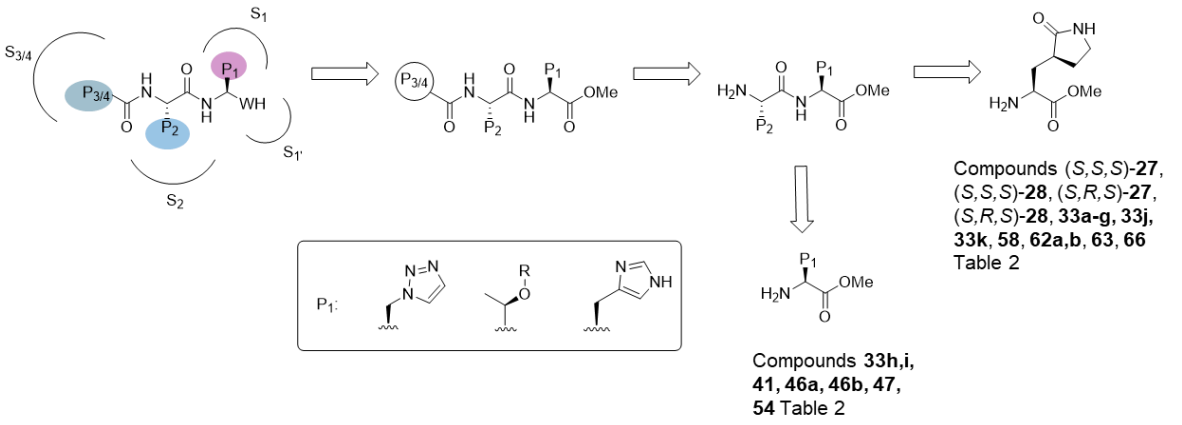

*Figure 10: General structure and retrosynthetic approach for compounds (S,S,S)-**27**, (S,S,S)-**28**, (S,R,S)-**27**, (S,R,S)-**28**, **33a-k**, **41**, **46a,b**, **47**, **54**, **58**, **62a,b**, **63**, **66**. Structures are reported in Table 2,.*

During this PhD a novel series of peptide-based inhibitors has been designed and synthesized (compounds (*S,S,S*)-**27**, (*S,S,S*)-**28**, (*S,R,S*)-**27**, (*S,R,S*)-**28**, **33a-k**, **41**, **46a,b**, **47**, **54**, **58**, **62a,b**, **63**, **66** Table 2), the design of this family of compounds has been carried out taking inspiration from literature data, which has highlighted the most important amino acidic interactions which need to be maintained, and the important features which confer the highest potency to the inhibitors. In particular, as mentioned in the previous paragraph, research studies related to different CoVs clearly indicate that the P1 γ-lactam enhances the inhibitory potency up to 10-fold when compared to the Gln of the natural substrate, probably due to the higher rigidity that reduces the loss of entropy upon binding when compared to the flexible Gln. This feature is a common and well established moiety for this position, and is also present in various cysteine protease inhibitors against different viruses such as norovirus and enteroviruses, thus allowing its exploitation in the design and synthesis of pan-antiviral agents [142–144]. For this reason the majority of the reported compounds of this project presents this important ring in position P1 synthesized (compounds (*S,S,S*)-**27,** (*S,S,S*)-**28,** (*S,R,S*)**27**, (*S,R,S*)-**28**, **33a-k**, **41**, **46a,b**, **47**, **54**, **58**, **62a,b**, **63**, **66** Table 2). Even though, studies demonstrated that sub-pocket S1

can accommodate hydrophobic residues, widening the plethora of substituents that can fit in this position [145]. For what concerns the P2 amino acids, previous studies showed that this position tolerates a wide variety of residues characterized by similar lipophilicity and size to Leu (compounds **1-6**, **9**, **10** Figure 7) [114,133,146], and indeed this residue has been maintained in the majority of the compounds synthesized in this library (compounds (*S,S,S*)-**27**, (*S,S,S*)-**28**, (*S,R,S*)-**27**, (*S,R,S*)-**28**, **33a-g,j,k**, **41**, **46a,b**, **47**, **54**, **58**, **62a**, **66** Table 2) though different protected and non-protected amino acids have been replaced in this position (compounds **33h,l**, **62b**, **63** Table 2). The sub-pockets S3 and S4 of the main protease are less structured and indeed can rearrange upon the binding of distinct P3/P4 residues, thanks to the flexibility of the surface loops. These positions have been amply explored to modulate both potency and drug-like properties of the inhibitors as reported from varies studies (compounds **1-5** Figure 7). Following these properties, we chose to explore different quinoline-derived scaffolds as substituents to reach the S3/4 sub-pocket. These natural scaffolds are privileged structures widely found in natural alkaloids and commonly known for their antiviral and antibiotic properties [147,148].

Furthermore, we explored different electrophilic warheads at position P1'. Specifically, we investigated the potency of the nitrile moiety, and to compare its efficacy, we examined two other distinct warheads: the well-known electrophilic aldehyde and the less explored cyanohydrin moiety, which is present in a number of natural products such as mandelonitrile, cyanohydrin phosphonate, and α-ketoglutarate cyanohydrin (α-kgCN) in animals. More importantly, cyanohydrin derivatives have been used as prescription drugs for treating asthma and proved to possess high potential in cancer chemotherapy. In addition to this many papers report cyanohydrine moiety as an anchoring group for various cysteine protease, including EV71 protease [149]. Comparative studies have been conducted between the reactivity of aldehydes and cyanohydrine moieties as warheads. In fact, despite the significant interests for aldehyde derivatives in modulating important drug targets, and their highly reactive nature, these inhibitors may lead to various issues, such as low selectivity, in further development, mainly due to their high reactivity. Therefore, alternative anchoring functional groups have been amply studied, such

as nitriles which are well-established cysteine protease inhibitors and cyanohydrines which similarly occupy the S1′ pocket and are in close proximity to the protease catalytic center. In fact studies reported that neither −CN nor −OH form a hydrogen bond with the thiol of Cys145. However, because of the electron-withdrawing profile of−OH and −CN, the α-carbon of cyanohydrin exhibits electrophilicity to a certain extent, which forms a noncovalent interaction (2.8 Å) with the thiol. This specific binding element is critical for the cyanohydrin function [149].

2.5.2 – Synthesis of peptide-based inhibitors

2.5.2.1 – Synthesis and optimization of the common intermediate 19

The initial phase of the synthesis of the peptide-based inhibitors (compounds (*S,S,S*)-**27**, (*S,S,S*)-**28**, (*S,R,S*)-**27**, (*S,R,S*)-**28**, **33a-k**, **58**, **62a,b**, **63**, **66**) required the optimization of the synthetic protocol for the preparation of the common building block **19**, inserted at the P1 position. At the beginning of our investigations, various literature sources reported protocols that either lacked reproducibility and feasibility, or were characterized by a high number of low yielding synthetic steps with overall yields ranging from 36% to 60%. Therefore, the primary focus has been the optimization of the overall yield, given the appreciable yields of the protection reaction and of the alkylation reaction our primary focus has been the optimization of the reduction reaction, which was identified as the most limiting step in terms of yields.

For the synthesis of the common intermediate **19** as described in Scheme **1**, an initial protection of the free amine and esterification of the acid moieties of *L*-glutamic acid **16** has been carried out in a one pot reaction, using trimethylsilyl chloride and MeOH, and successively triethylamine and Boc anhydride allowing to obtain the intermediate **17**. The next step has been a stereoselective alkylation, previously reported by Hanessian [150], of the α-carbon using bromoacetonitrile and lithium bis(trimethylsilyl)amide as a base affording the intermediate **18**. For the reduction of

18, two different conditions have been analyzed, specifically a reduction reaction with $NaBH_4$ in presence of catalytic amounts of $CoCl_2$, allowing the selective reduction of the nitrile moiety to primary amine, while the second tested condition has been an hydrogenation reaction. The first attempt of the hydrogenation reaction has been carried out using Pd/C as catalyst with scarce results, so the second attempt has been carried out using Nickel Raney as catalyst. NiRa is an effective catalyst, used in various hydrogenation reactions; it can be found as ready-to-use slurry in water, though the handling of this catalyst can be tricky due to its pyrophoric nature, in fact, it must be kept in wet conditions at all times in order to prevent ignition [151].

The best option resulted to be the hydrogenation in presence of NiRa, so starting from literature data the next step has been the evaluation of the precise conditions for the hydrogenation, entry 2 in Table 1, allowing to obtain an overall yield of 68% in 3 steps.

Entry	Reagent/catalyst	Equivalents or mL	Reaction time	yield
1	$NaBH_4$ + $CoCl_2$	10 eq + 0.6 eq	12 h	54%
2	H_2, Ni/Ra	5mL/0.5mmol of SM	12 h	95%
3	H_2, Recycled Ni/Ra	5mL/0.5mmol of SM	12 h	91%
4	H_2, Ni/Ra	3mL/0.5mmol of SM	12 h	87%
5	H_2, Ni/Ra	1mL/0.5mmol of SM	12 h	82%
6	H_2, Ni/Ra	0.5mL/0.75mmol of SM	12 h	85%

Table 1: Reaction conditions evaluated for the optimization of the hydrogenation reaction reported in scheme 1.

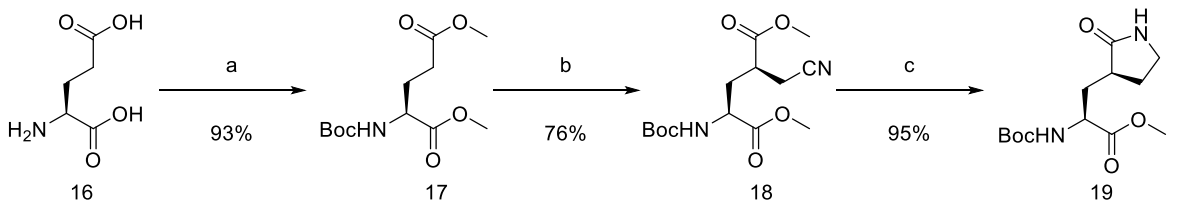

*Scheme 1: Synthesis of the common intermediate **19.** Reagents and conditions: a) I: TMSCl, MeOH, 0 – 25 °C, 12h; II: TEA, Boc_2O 25 °C, 1 h; b) $BrCH_2CN$, LiHMDS, THF, -78 °C, 6h; c) H_2, NiRa, MeOH, 25 °C, 12h.*

2.5.2.2 – Synthesis of target molecules (S,S,S)-27, (S,R,S)-27, (S,S,S)-28, and (S,R,S)-28

The synthesis of the peptide-based compounds has been initially carried out through the synthetic protocol reported for compounds **27** and **28** in Scheme 2. For this synthetic protocol starting from the known intermediate **19** two consecutive deprotection reactions of the Boc-protected amine with trifluoroacetic acid (TFA) and coupling reactions with hexafluorophosphate azabenzotriazole tetramethyl uronium (HATU) in presence of triethylamine (TEA) were carried out. The first coupling reaction has been carried out using Boc-L-leucine allowing to obtain the common intermediate **20**, the second coupling reaction counted two different carboxylates, 8-quinolinecarboxylic acid and 8-chloro-1-methyl-4-oxo-1,4-dihydroquinoline-3-carboxylic acid, the latter has been prepared according to literature [152]. The following reaction step required the hydrolysis of the ester group of **21** and **22** in order to install the nitrile moiety through a 2-steps synthetic protocol. Unfortunately, this step, conducted in the presence of lithium hydroxide 1 M at room temperature, resulted in the racemization of the chiral α-carbon, affording the mixture of diastereomers (*S/R*)-**23** and (*S/R*)-**24**. The following reaction were carried on using the mixture of diastereomers. Accordingly, the acid derivatives were subjected to coupling reactions with NH_4Cl in presence of HATU and TEA to obtain the desired amide derivatives (*S/R*)-**25** and (*S/R*)-**26**. Finally, the amide moiety was dehydrated using trifluoroacetic anhydride (TFAA) and TEA at 0 °C affording the final compounds (*S,S,S*)-**27**, (*S,S,S*)-**28**, (*S,R,S*)-**27** and (*S,R,S*)-**28**. The diastereomers were separated by column chromatography and the isolated compounds (*S,S,S*)-**27**, (*S,S,S*)-**28**, (*S,R,S*)-**27** and (*S,R,S*)-**28** were submitted to biological assay as pure compounds. Stereochemical assignment was confirmed by the stereoselective synthesis of (*S,S,S*)-**27** and (*S,S,S*)-**28** as described in Scheme 3.

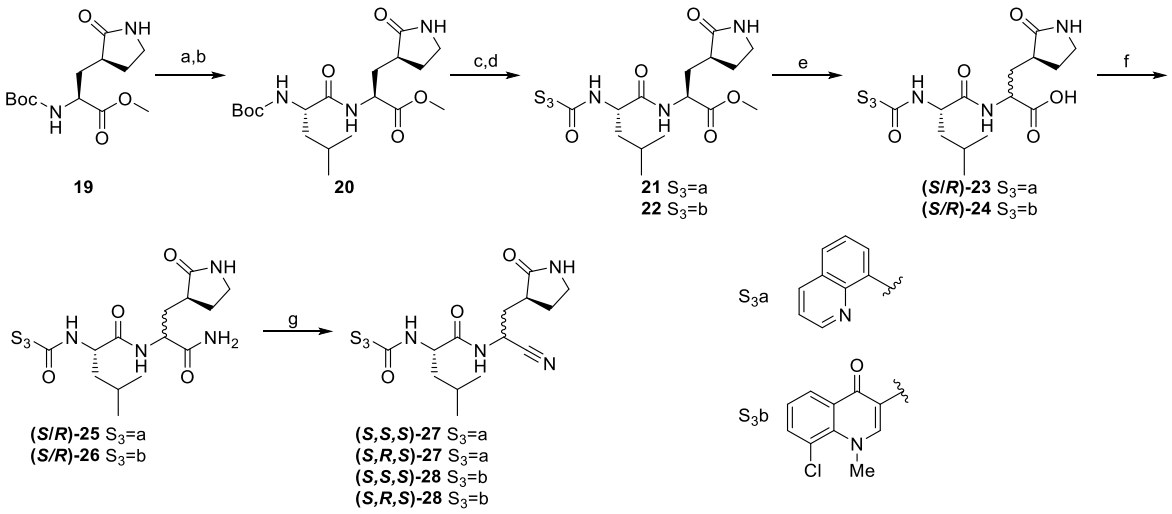

*Scheme 2: Synthesis of compounds (S,S,S)-**27**, (S,R,S)-**27**, (S,S,S)-**28** and (S,R,S)-**28.** Reagents and conditions: a) TFA, DCM, 0 °C, 1 h; b) (tert-butoxycarbonyl)-L-leucine, HATU, TEA, DCM, 0 °C, 4 h; c) TFA, DCM, 0 °C, 1 h; d) quinoline-8-carboxylic acid for derivative **21**, 8-chloro-1-methyl-4-oxo-1,4-dihydroquinoline-3-carboxylic acid for derivative **22**, HATU, TEA, DCM, 0 °C, 4 h; e) LiOH 1 M,THF, 25 °C, 2 h; f) NH_4Cl, HATU, DIPEA, DMF, 25 °C, 5 h; g) TFAA, TEA, THF, 0 °C, 3 h.*

2.5.2.3 – Stereoselective synthesis of compounds (*S,S,S*)-27, (*S,S,S*)-28 and 33a-k

The stereoselective synthesis of final compounds (*S,S,S*)-**27**, (*S,S,S*)-**28**, and **33a-k** is depicted in Scheme 3. In particular, the intermediates **20**, **29** and **30** were obtained by reacting **19** with the corresponding amino acids (Leu for **20**; Thr for **29**; Thr-Bn for **30**). The subsequent deprotection of the amine and coupling reaction with the corresponding quinolone, quinoline, isoquinoline or tetrahydroisoquinoline carboxylic acid derivatives (S_3: d-l) afforded ester intermediates **21**, **22** and **31a-i**. These latter were then converted into the amide intermediates (*S,S,S*)-**25**, (*S,S,S*)-**26** and **32a-i** by treatment with ammonia solution (7N in MeOH). Finally, the target compounds (*S,S,S*)-**27**, (*S,S,S*)-**28a** and **33a-i** were obtained by dehydration of the amides into the nitrile derivatives, which was carried out with TFAA and TEA at 0 °C [153,154]. Finally compounds **33j** and **33k** have been obtained by the formerly prepared target molecules **33f** and **33g** by reduction reaction in presence of Fe powder and deprotection reaction in presence of TFA, respectively.

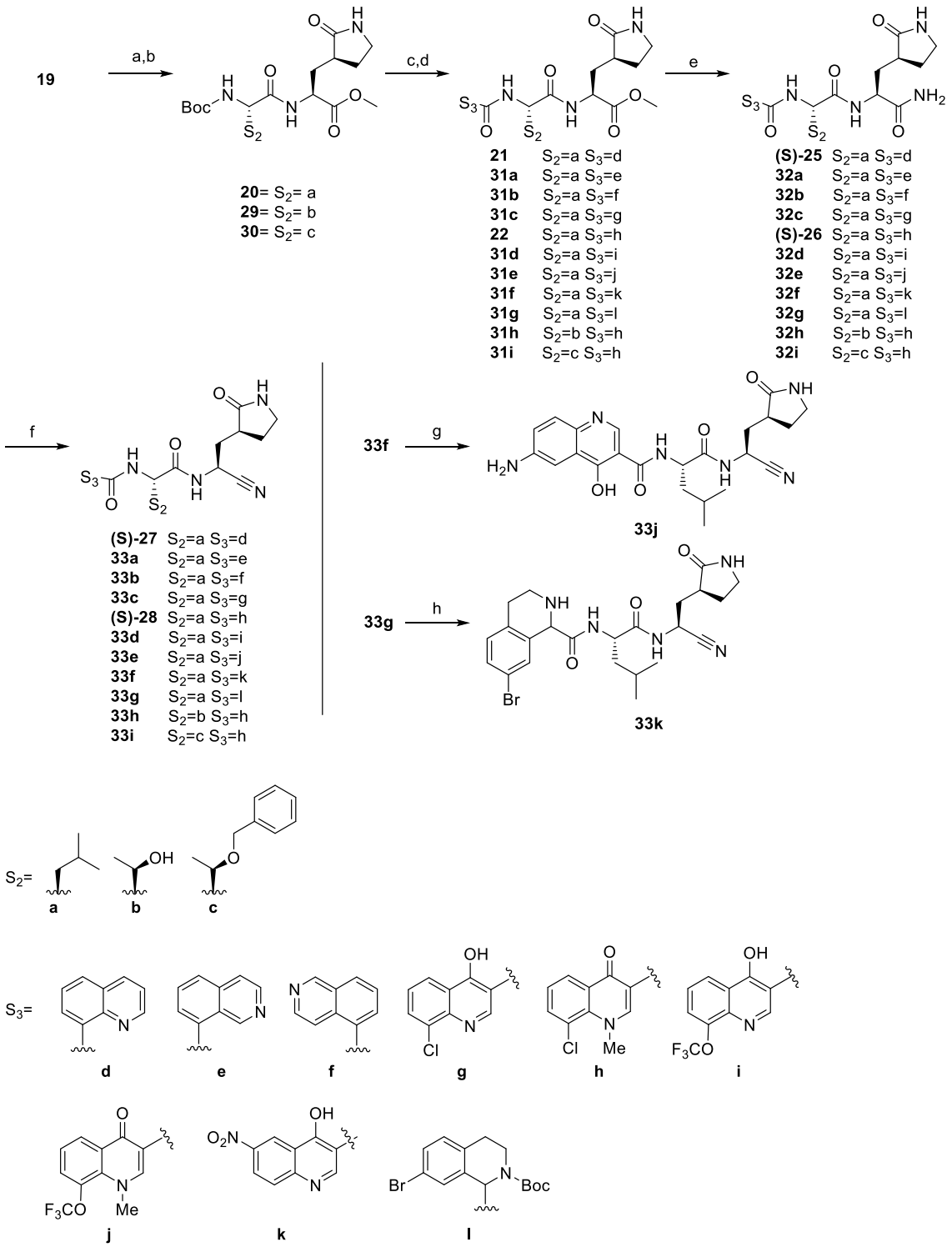

*Scheme 3: Synthesis of compounds (S,S,S)-**27**, (S,S,S)-**28** and **33a-k**. Reagents and conditions: a) TFA, DCM, 0 °C, 1 h; b) (tert-butoxycarbonyl)-L-leucine for derivative **20**, (tert-butoxycarbonyl)-L-threonine for derivative **29**, O-benzyl-N-(tert-butoxycarbonyl)-L-threonine for derivative **30**, HATU, TEA, DCM, 0 °C, 4 h; c) TFA, DCM, 0 °C, 1 h; d) quinoline-8-carboxylic acid for derivative **21**, isoquinoline-8-carboxylic acid for derivative **31a**, isoquinoline-5-carboxylic acid for derivative **31b**, 8-chloro-4-hydroxyquinoline-3-carboxylic acid for derivative*

***31c**, 8-chloro-1-methyl-4-oxo-1,4-dihydroquinoline-3-carboxylic acid for derivative **22**, 4-hydroxy-8-(trifluoromethoxy)quinoline-3-carboxylic acid for derivative **31d**, 1-methyl-4-oxo-8-(trifluoromethoxy)-1,4-dihydroquinoline-3-carboxylic acid for derivative **31e**, 4-hydroxy-6-nitroquinoline-3-carboxylic acid for derivative **31f**, 7-bromo-1,2,3,4-tetrahydroisoquinoline-1-carboxylic acid for derivative **31g**, HATU, TEA, DCM, 0 °C, 4 h; e) ammonia solution (7 N in MeOH), MeOH, rt, 12 h; f) TFAA, TEA, DCM or DMF, 0 °C, 3 h; g) Fe powder, NH_4Cl, $EtOH/H_2O$ (5:1), 55 °C, 30 minutes; h) HCl in MeOH, 0 °C, 1 h.*

2.5.2.4 – Synthesis of compound (*S,S,S*)-41

Synthesis of final compound **41**, bearing a triazole moiety in place of the pyrrolidone ring of (*S,S,S*)-**28**, is reported in Scheme 4. This latter compound was prepared starting from the non-natural amino acid Fmoc-β-azido-Ala-OH (**34**) which was converted into the ester derivative **35** using chlorotrimethylsilane (TMSCl) in MeOH. Successively the triazole intermediate **36** was obtained by a click reaction using trimethylsilylacetylene. The Fmoc protecting group was removed in presence of diethylamine. The intermediate **37** thus obtained was coupled with Boc-L-leucine and successively with 8-chloro-1-methyl-4-oxo-1,4-dihydroquinoline-3-carboxylic acid allowing to obtain the ester intermediate **39**. Ester **39** was then reacted with ammonia solution (7N in MeOH) affording the amide **40**, which underwent dehydration in presence of TFAA and TEA at 0 °C furnishing final compound **41**.

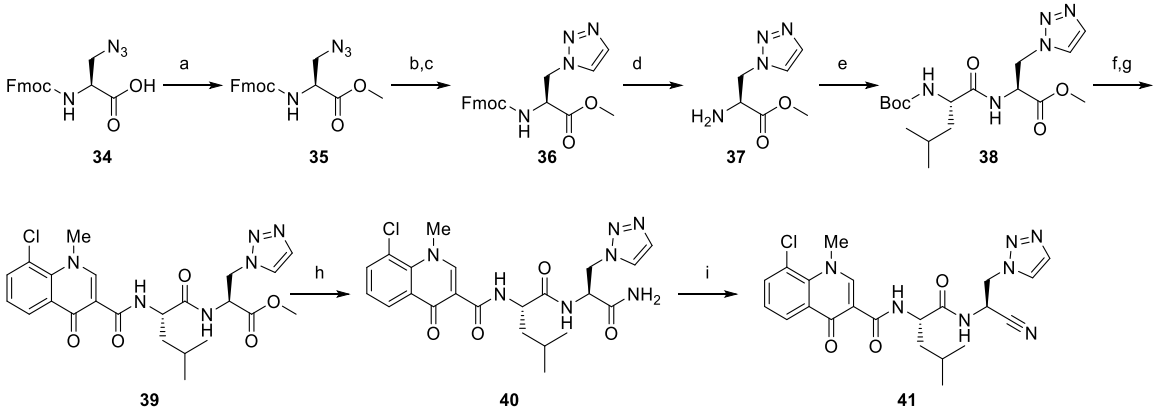

*Scheme 4: Synthesis of compound **41**. Reagents and conditions. a) TMSCl, MeOH, 0-25 °C, 12 h; b-c) trimethylsylilacetylene, sodium ascorbate, CuSO4, t-BuOH/H_2O; TBAF; d) diethylamine, DMF, rt, 1 h; e) (tert-butoxycarbonyl)-L-leucine, HATU, TEA, DCM, 0 °C, 4 h; f) TFA, DCM, 0 °C, 1 h; g) 8-chloro-1-methyl-4-oxo-1,4-dihydroquinoline-3-carboxylic acid, HATU, TEA, DCM, 0 °C 4 h; h) ammonia solution (7 N in MeOH), rt, 12 h; i) TFAA, TEA, THF, 0 °C, 3 h.*

2.5.2.5 – Synthesis of compounds (*S,S,S*)-46a,b and (*S,S,S*)-47

The synthetic procedure to obtain compounds **46a,b** and **47** is shown in Scheme 5. Intermediates **43a,b** were obtained by coupling reaction of (*tert*-butoxycarbonyl)-*L*-leucine (**42**) with methyl L-threoninate for the synthesis of intermediate **43a**, and with methyl *L*-histidinate for the synthesis of intermediate **43b**. Intermediates **43a,b**, after Boc-cleavage, were subjected to coupling reaction with the 8-chloro-1-methyl-4-oxo-1,4-dihydroquinoline-3-carboxylic acid to obtain the ester derivatives **44a,b**. The primary amides **45a,b** were prepared by reacting the ester intermediates **44a,b** with ammonia solution (7N in MeOH), and successively the final compounds **46a,b** were obtained by dehydration of amide intermediates using TFAA and TEA at 0 °C. Final compound **46a** was then converted in the *O*-functionalized compound **47** using *p*-toluenesulfonic acid (PTSA) and 2,3-dihydrofuran.

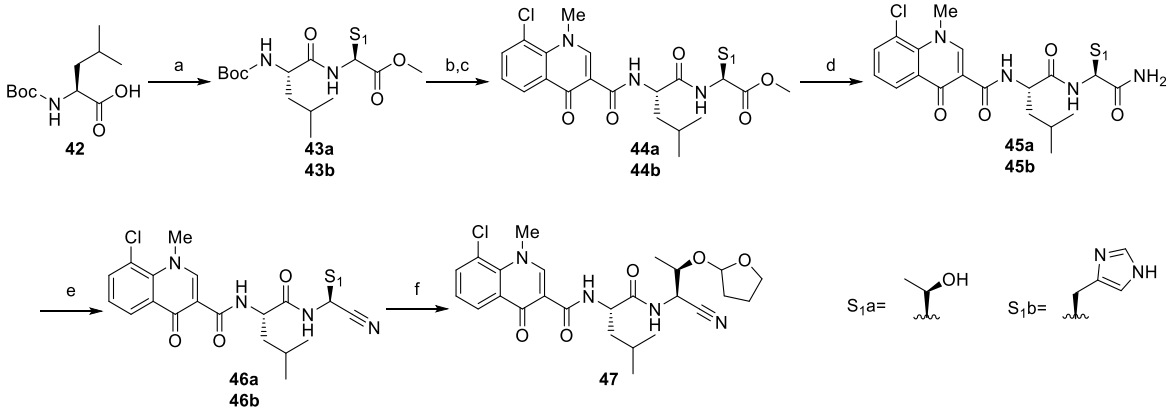

*Scheme 5: Synthesis of compounds **46a,b** and **47**. Reagents and conditions. a) methyl L-threoninate for derivative **43a**, methyl L-histidinate for derivative **43b**, HATU, TEA, DCM, 0 °C, 4 h; b) TFA, DCM, 0 °C, 1 h; c) 8-chloro-1-methyl-4-oxo-1,4-dihydroquinoline-3-carboxylic acid, HATU, TEA, DCM, 0 °C, 4 h; d) ammonia solution (7 N in MeOH), rt, 12 h; e) TFAA, TEA, DCM, 0 °C, 3 h; f) PTSA, DHF, THF, rt, 2 h.*

2.5.2.6 – Synthesis of compound (*S,S,S*)-54

The synthesis of compound **54** has been accomplished as reported in Scheme 6. The natural amino acid L-threonine was initially protected with Boc anhydride to obtain intermediate **49**, suitable for the successive coupling reaction with NH_4Cl furnishing the primary amide **50**. Intermediate **50** was then converted in the protected *O*-TBS derivative **51**, which was subjected to a dehydration reaction of the primary amide using TFAA and TEA at 0 °C affording the nitrile intermediate **52,** which

underwent two successive Boc cleavage and coupling reactions with Boc-L-leucine and the 8-chloro-1-methyl-4-oxo-1,4-dihydroquinoline-3-carboxylic acid respectively, furnishing the target molecule **54**.

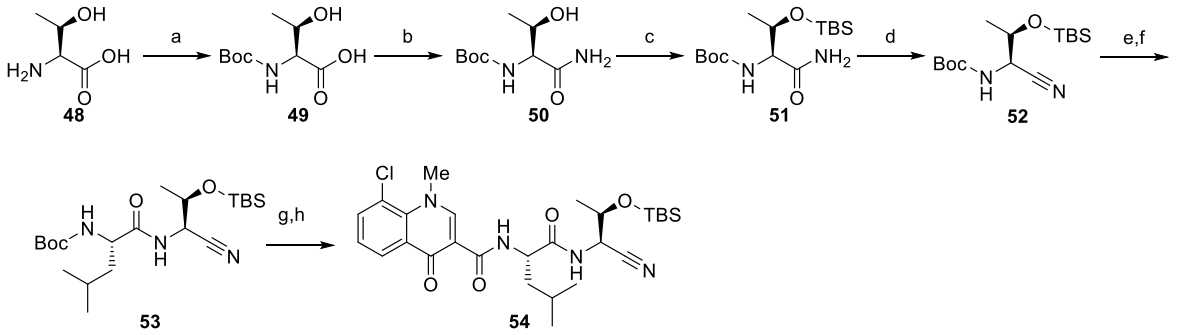

*Scheme 6: Synthesis of compound **54**. Reagents and conditions. a) Boc_2O, TEA, H_2O/Acetone, rt, 3 h; b) NH_4Cl, HATU, DIPEA, DMF, rt, 5 h; c) TBSCl, TEA, DMF, rt, 12 h; d) TFAA, TEA, THF, 0 °C, 3 h; e) TFA, DCM, 0 °C, 1 h; f) (tert-butoxycarbonyl)-L-leucine, HATU, TEA, DCM, 0 °C, 4 h; g) TFA, DCM, 0 °C, 1 h; h) 8-chloro-1-methyl-4-oxo-1,4-dihydroquinoline-3-carboxylic acid, HATU, TEA, DCM, 0 °C, 4 h.*

2.5.2.7 – Synthesis of compound (*S,S,S*)-58

Compound **58** was synthesized as reported in Scheme 7. Intermediate **20** was converted into **55** by an initial Boc cleavage and subsequent coupling reaction with Boc-L-valine. A second deprotection and coupling reaction with 8-chloro-1-methyl-4-oxo-1,4-dihydroquinoline-3-carboxylic acid furnished intermediate **56**, which allowed to obtain the primary amide **57** in presence of ammonia solution (7 N in MeOH). The successive dehydration of the amide furnished the final compound **58**.

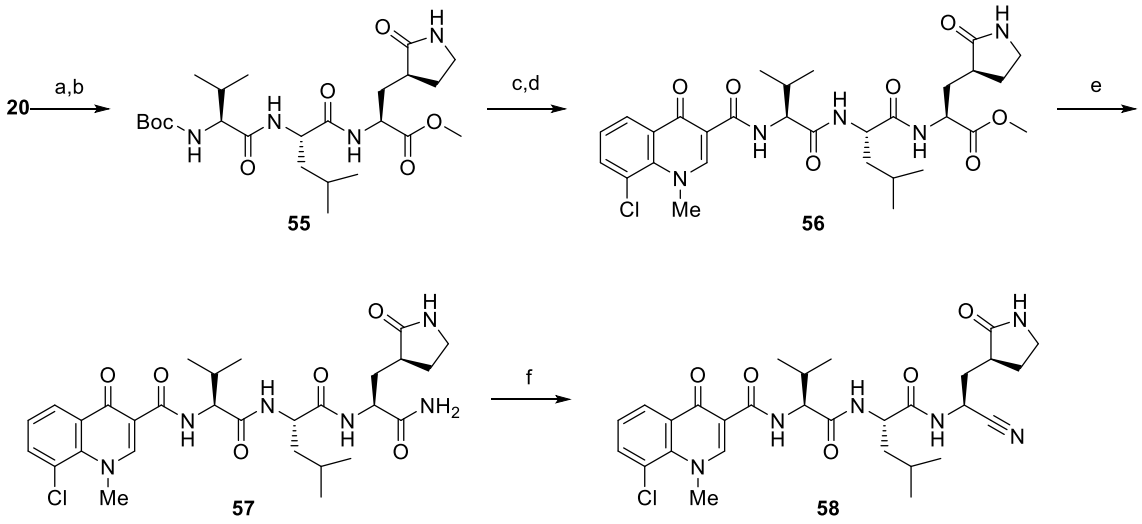

*Scheme 7: Synthesis of compound **58**. Reagents and conditions. a) TFA, DCM, 0 °C, 1 h; b) (tert-butoxycarbonyl)-L-valine, HATU, TEA, DCM, 0 °C, 4 h; c) TFA, DCM, 0 °C, 1 h; d) 8-chloro-1-methyl-4-oxo-1,4-dihydroquinoline-3-carboxylic acid, HATU, TEA, DMF, 0 °C, 6 h; e) ammonia solution (7N in MeOH), MeOH, rt, 20 h; f) TFAA, TEA, DMF, 0 °C, 6 h.*

2.5.2.8 – Synthesis of compounds (*S,S,S*)-62a,b, (*S,S,S*)-63 and (*S,S,S*)-66

The synthesis of compounds **62a,b**, **63** and **66** is reported in Scheme 8. Starting from the common intermediate **19** two consecutive coupling reactions with the appropriate amino acid (Leu **for 20**, Ile for **59**) and 8-quinoline carboxylic acid derivative have been carried out using the same conditions reported previously to obtain intermediates **20** and **59,** and successively the corresponding ester derivatives **60a,b**. The ester intermediates **60a,b** were reduced in presence of $NaBH_4$ in MeOH at rt affording the corresponding alcohol derivatives **61a,b,** which were oxidized using Dess Martin Periodinane (DMP) at 0 °C furnishing the final compounds **62a,b**. The warhead of **62b** was then converted into the cyanohydrin warhead to obtain final compound **63**. Compound **66** was obtained by first converting the ester derivative **20** into the alcohol derivative **64**. Then this latter compound was subjected to amine deprotection and coupling reaction with the 8-chloro-quinolone carboxylic acid to yield the derivative **65**, that was oxidized to target compound **66**.

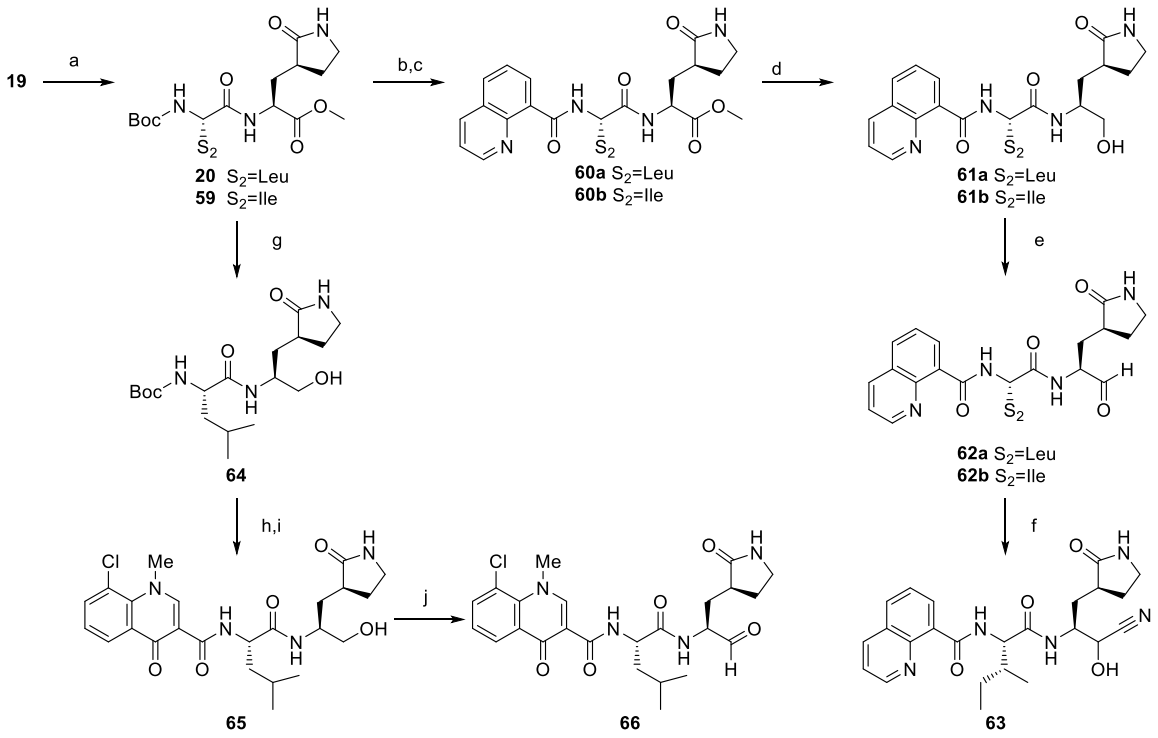

*Scheme 8: Synthesis of compounds **62a-b**, **63** and **66**. Reagents and conditions: a) (tert-butoxycarbonyl)-L-leucine for derivative **20**, (tert-butoxycarbonyl)-L-isoleucine for derivative **59**, HATU, TEA, DCM, 0 °C, 4 h; b) TFA, DCM, 0 °C, 2 h; c) quinoline-8-carboxylic acid, HATU, TEA, DCM, 0 °C, 4 h; d) $NaBH_4$, MeOH, 0-25 °C, 12 h; e) DMP, DCM, 0 °C, 1 h; f) $NaHSO_3$ aq s.s., KCN; g) $NaBH_4$, MeOH, 0-25 °C, 12 h; h) TFA, DCM, 0 °C, 2 h; i) 8-chloro-1-methyl-4-oxo-1,4-dihydroquinoline-3-carboxylic acid, HATU, TEA, DCM, 0 °C, 4 h; j) DMP, DCM, 0 °C, 30 min.*

2.5.3 – Biological evaluation of peptide-based inhibitors

The potential M^{pro} inhibitors synthesized were subjected to biological evaluation thanks to the collaboration with the research group of Professor Maga from the University of Pavia which performed the screening of all the reported compounds against the M^{pro} isolated enzyme furnishing the ID_{50} values; and with the research group of Professor Zazzi from the University of Siena which tested the antiviral activity of the most interesting M^{pro} inhibitors in infected Vero E6 cell lines.

As previously mentioned all the compounds were screened on SARS-CoV-2 M^{pro}, using GC376 (compound **6,** figure 7) as reference inhibitor and positive control, and ID_{50} values have been determined. The compounds have been tested in a fluorescence resonance energy transfer (FRET) biochemical assay in order to

evaluate their inhibitory activity against the isolated SARS-CoV-2 M^{pro} processing a fluorescent substrate. The majority of compounds were able to inhibit the M^{pro} in the micromolar and sub-micromolar range as shown in Table 2. The investigation of portion P4 of the peptide-based inhibitors highlighted the higher inhibitory potency of the 8-chloro-1-methyl-quinolone derivative (*S,S,S*)-**28** when compared to its corresponding 8-chloro-4-hydroxy-quinoline **33c** and to compounds **33d,f** and **33j** bearing differently-substituted quinolines. We investigated two isoquinoline derivatives **33a**,**b** and the 7-bromo-1,2,3,4-tetrahydroisoquinoline derivative **33g** and **33k** which afforded ID_{50} values ranging from 1,28 to 10 μM confirming the higher inhibitory potency of the quinolone derivatives. Encouraged by the promising activity of compound (*S,S,S*)-**28** we investigated positions P2 and P1 replacing the leucine and the pyrrolidine-2-one with different natural and non-natural amino acids affording compounds **33h**, **33i**, **41**, **46a,b** , **47**, **54**, highlighting the importance of leucine or leucine mimetics in position P2 ((*S,S,S*)-**28** *vs* **33h** and **33i**) which interact with the hydrophobic amino acids of sub-pocket S2, and confirming the importance of the γ-lactam in position P1 ((*S,S,S*)-**28** *vs* **41**, **46a,b**, **47** and **54**). Furthermore, the relevance of a precise stereochemistry of the amino acids of these peptidomimetic derivatives has been proved by biological assays of compounds (*S,R,S*)-**27** and (*S,R,S*)-**28** bearing an D-glutamine bioisostere instead of the natural L-glutamine bioisostere, which have resulted in totally inactive compounds. The evaluation of the effect of a longer peptide-based inhibitor has been carried out as well, inserting in position P3 in compound **58** a lipophilic valine causing a slight reduction of the inhibitory activity. Regarding the electrophilic warhead at position P1', we have investigated the nitrile moiety in compounds (*S,S,S)*-**27**, (*S,R,S*)-**27**, (*S,S,S*)-**28** (*S,R,S*)-**28**, **33a-k**, **41**, **46a,b**, **47**, **54** and **58** proving the potency of this electrophilic moiety. In order to compare the efficacy of the nitrile moiety we investigated two other different warheads, such as the well-known electrophilic aldehyde in compounds **62a**,**b** and **66** yielding nanomolar active compounds, and the less explored cyanohydrin moiety in compound **63** which exerted micromolar activity.

Antiviral *in vitro* activity in Vero E6 cells against SARS-CoV-2 has been carried out on Delta variant of the virus (column 3, Table 2), using **GC376** (**6** Table 7) and

nirmatrelvir (**1**, Table 7) as reference compounds and DMSO as negative control. The assays have been carried out in presence of the Pg-P inhibitor CP-100356 at the final concentration of 0.5 μM, which is a non-toxic efflux pump inhibitor. Hit compound (*S,S,S*)-**28** confirmed to be the most active when confronting the IC_{50} values of Table 2, as well as compounds **62a** and **63**.

Further biological evaluation is ongoing, in particular in order to asses the broad spectrum potentiality of these compounds, the two most promising inhibitors will be evaluated in two different cell lines for their inhibitory activity against FCoV and CCov, in order to evaluate their potential as pan-antiviral agents against zoonotic coronaviruses. In addition to this the inhibitory potency against resistant strains of enteroviruses will be assessed.

*Table 2: Biological activities of target compounds (S,S,S)-**27**, (S,S,S)-**28**, (S,R,S)-**27**, (S,R,S)-**28**, **33a-k**, **41**, **46a,b**, **47**, **54**, **58**, **62a,b**, **63**, **66** and reference inhibitors **1** and **6***

Entry		Structure	ID_{50} (μM)[a] or % inhibition at 100 μM[b]	IC_{50} (μM) Plus EI[c] vs Delta[d]	CC_{50} (μM)[e]	SI[f]
1	**27a**	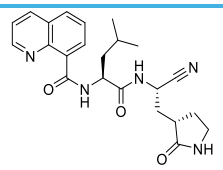	6.57 ± 1.31	1.1± 0.6	81.6	44.1
2	**27b**	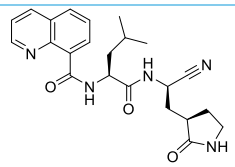	31.2%	n.a.[g]	>200	
3	**28a**	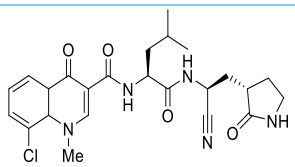	0.56 ± 0.07	1.6± 0.5	>200	187.5
4	**28b**	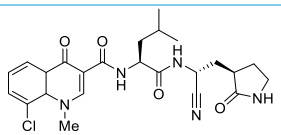	80.8%	n.a.	>200	
5	**33c**	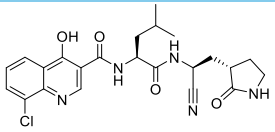	6.0 ±0.67 uM	n.t.[h]	n.t.	

6	**33f**	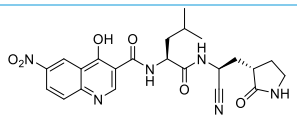	1.065 ±0.19	n.t.	219.2	
7	**33j**	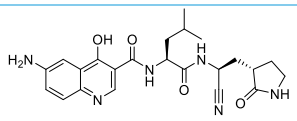	>10uM 83.7%	n.t.	n.t.	
8	**33a**	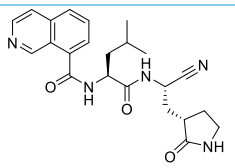	1.284 ±0.20	24.0± 6.5	293.4	12.2
9	**33b**	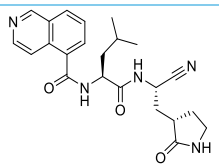	3.38 ± 1.04	n.t.	n.t.	
10	**33g**	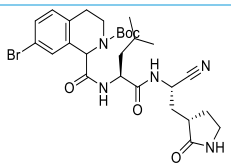	>10 90.12%	n.t.	n.t.	
11	**33k**	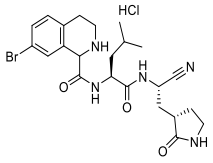	>10	n.t.	n.t.	
12	**33d**	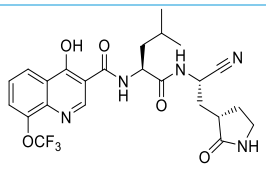	13.85 ±2.14 87.7%	n.t.	n.t.	
13	**33e**	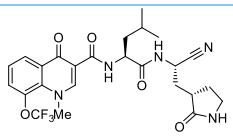	>10 95.2%	n.t.	n.t.	
14	**33h**	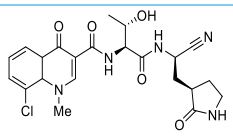	>10 71.0%	n.t.	n.t.	
15	**33i**	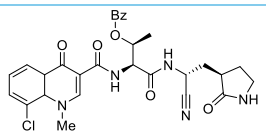	>10 81.5%	n.t.	n.t.	
16	**62a**	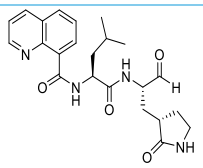	0.435 ±45.08	8.0± 2.5	n.t.	6.6

17	**62b**	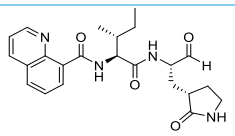	0.51 ± 0.01	n.t.	n.t.	
18	**66**	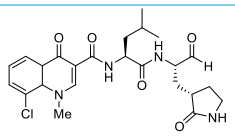	0.65 ± 0,04	n.t.	n.t.	
19	**63**	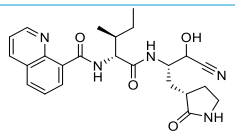	1.81 ±0.53	6.8± 9.5	n.t.	91.6
20	**58**	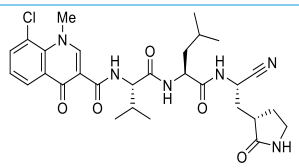	4.246 ±0.28	n.t.	89.2	
21	**41**	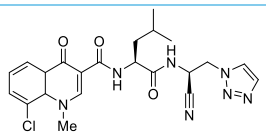	>10 3.8 %	n.t.	n.t.	
22	**46b**	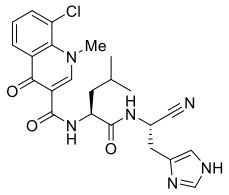	>10	n.t.	n.t.	
23	**46a**	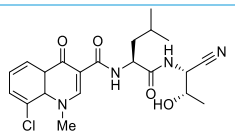	>10 0%	n.t.	n.t.	
24	**54**	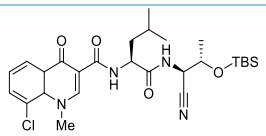	>10 15.2%	n.t.	n.t.	
25	**47**	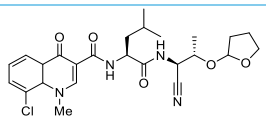	>10	n.t.	n.t.	
26	**GC376 (6)**	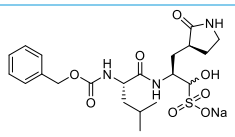	0.138 ± 0.04	0.16 ± 0.1	n.t.	
27	**Nirmatrelvir (1)**	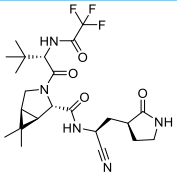		0.05	n.t.	874.8

[a] Compound concentration required to reduce the M^{pro} activity by 50%.

[b] Percentage of enzyme inhibited using a concentration of 100 μM of compound.

[c] P-gp inhibitor (CP-100356) used at the final concentration of 0.5 μM.

[d] Live delta SARS-CoV-2 (EPI_ISL_2840619) virus.

[e] Concentration of compound that causes a cytotoxic effect in 50% of the cells in given population.

[f] SI is the selectivity index calculated as the CC_{50}/EC_{50} ratio.

[g] Not active.

[h] Not tested.

2.7 – Further insights and future explorations

2.7.1 – Design of small molecules inhibitors

Taking inspiration from the experience gained in the design of the peptide-based inhibitors aforementioned and literature data, a limited set of small molecule inhibitors of M^{pro} has been designed. Specifically, these small molecule inhibitors have been designed as an effort towards the development of inhibitors with better drug-like properties and with synthetically accessible scaffolds that could allow a more thorough exploration of the SARs. In particular given the plethora of functional groups which can be accommodated in positions P2 and P3 of the peptide-backbone, a restricted family of fragments has been designed, exploring heteroaromatic and aliphatic cyclic systems, allowing the evaluation of rigid and flexible moieties, nonetheless keeping hydrogen donor portions for specific interactions inside the active site, which can be evaluated through *in silico* studies.

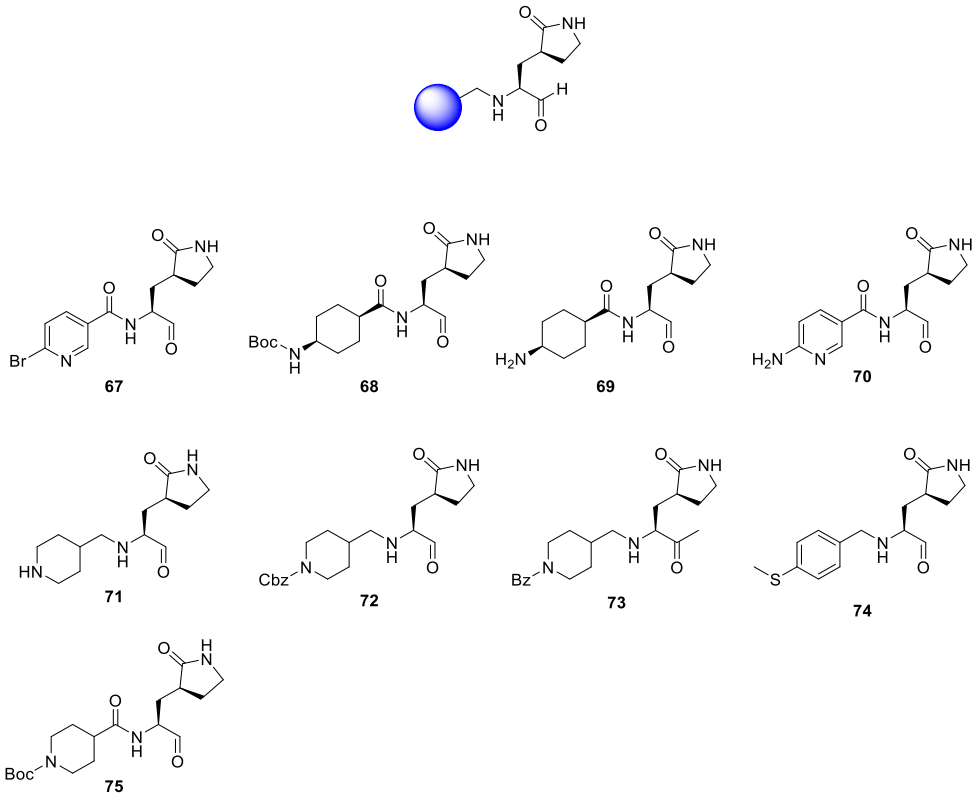

Figure 10: General structure of the small molecule inhibitors, ***67-75***

2.7.2 Synthesis of small molecules fragments

The synthesis of the final compounds **67-69** is reported in Scheme 9. The ester intermediates were obtained through coupling reaction of the common intermediate **19** and the appropriate carboxylic acid, 6-bromonicotinic acid (for derivative **76a**) and (1S,4S)-4-((*tert*-butoxycarbonyl)amino)cyclohexane-1-carboxylic acid (for derivative **76b**). Afterwards the ester intermediates were reduced to the corresponding aldehydic final compounds using DIBAL at low temperatures. To obtain the final compound **69**, compound **68** previously synthesized has been deprotected through an acidic cleavage.

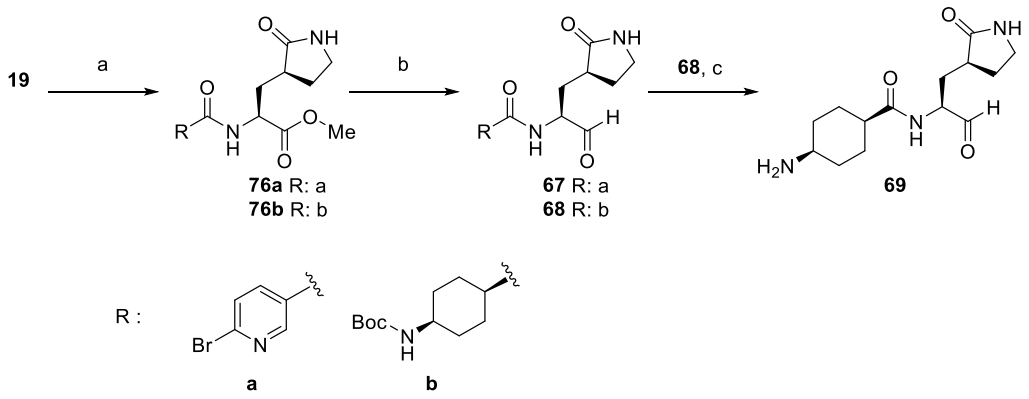

*Scheme 9: Synthesis of compounds **67-69.** Reagents and conditions: a) appropriate carboxylic acid: 6-bromonicotinic acid for derivative **76a** and (1s,4s)-4-((tert-butoxycarbonyl)amino)cyclohexane-1-carboxylic acid for derivative **76b**, HATU, TEA, DCM, 0 °C 3 h; b) DIBAL, DCM, -78 °C, 4 h; c) TFA, DCM, 0 °C, 2h.*

2.7.3 – Biological evaluation

The small library of compounds is under biological evaluation, in particular the compounds will be tested against the M^{pro} of SARS-CoV-2 with the same methodology reported for the previously mentioned peptide-based inhibitors, successively the compounds will be tested in VERO E6 cell line in order to evaluate their inhibitory potency against SARS-CoV-2.

CHAPTER 3

Design and synthesis of HDAC inhibitors for a preventive action against SARS-CoV-2 infection

CHAPTER 3 – Design and synthesis of HDAC inhibitors for a preventive action against SARS-CoV-2 infection

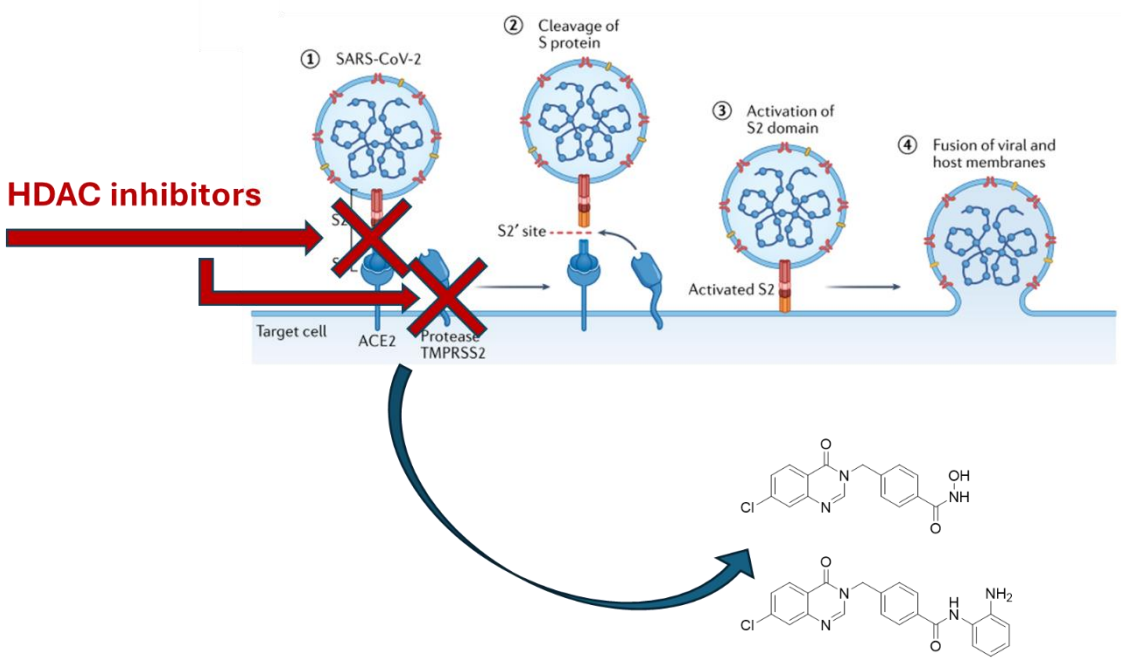

Table of content

The knowledge of the entry mechanism of SARS-CoV-2 into the host cells, gained during the last pandemic has brought to light the complex interconnections between the viral Spike protein and various host targets, among these is note to mention ACE2. This host receptor is pivotal for viral entry, thus rendering its inhibition a promising target for the preventive treatment of this pathogen. In fact, the modulation of expression of ACE2, which can be achieved through HDACi, can allow a reduced viral load into the host cells and a prophylactic action during infection onset. The development of this project was aimed at the identification of HDAC isozymes involved in the modulation of the expression of ACE2 on the cell surface; for this reason two in house repurposed compounds, a selective HDAC1 inhibitor and a selective HDAC6 inhibitor, have been selected and synthesized for further biological evaluation in VERO E6 cells in order to evaluate their prophylactic role during the viral infection.

3.1 – SARS-CoV-2, role of Spike protein and ACE2 receptor in the viral cell entry

The first step of infection onset is the entry of the viral particles into the host cell, this may occur thanks to the S glycoprotein that undergoes specific modifications and conformational changes. The S protein of SARS-CoV-2 exists as a trimer, and the viral genome encodes for many repeated copies which are positioned into the virion membrane giving the “crown-like” conformation, with each monomer composed of two subunits. The S1 subunit presents the RBD, necessary for the recognition and subsequent attachment to the host cell receptor, ACE2, while the S2 subunit facilitates membrane fusion.

The entry process can be divided into 5 steps as depicted in Figure 11. The first step of viral entry, identified as RBD Attachment to ACE2, is mediated by the S1 subunit in which the RBD can adopt either an "up" conformation, that allows the binding to the receptor, or a "down" conformation that impedes the binding. In the "up" conformation, the RBD is exposed and can interact with the ACE2 receptor on the host cell. This binding is a critical determinant for the tropism and infectivity of the virus [42].

At this point, the second step involves the S1 Subunit Shedding which occurs after RBD-ACE2 binding, in which entry glycoproteins of many viruses, including MERS-CoV, are cleaved into two subunits the extracellular unit and the transmembrane unit, this latter exposes the S2 subunit. In the case of SARS-CoV-2 the, proprotein convertase is furin, and it mediates the cleavage in the infected cells [42].

During the third step, the S2 Subunit Activation, the exposed S2 subunit undergoes further conformational changes. In the specific case of SARS-CoV-2 the initial stimuli is the cleavage of an additional internal portion of the S2 subunit, identified as the ‘S2′ site’, which starts with the engagement of ACE2 by the virus [42].

In particular this cleavage can be performed by the TMPRSS2 at the cell surface, or by cathepsin L in the endosomal compartment with the subsequent endocytosis and with the further Release of the Fusion Peptide (step four) and the initiation of the fusion pore formation which inserts itself into the host cell membrane. This step is

crucial for bringing the viral and cellular membranes into close proximity. Following fusion peptide insertion, the last step identified with the Membrane Fusion allows additional conformational rearrangements in S2 which drive the fusion of the viral and cellular membranes. This process involves the formation of a six-helix bundle structure that brings the two membranes together, facilitating the entrance of viral RNA into the host infected cell. Once the viral and cellular membranes have fused, the viral genome is released into the host cell, initiating the viral replication cycle [155–158].

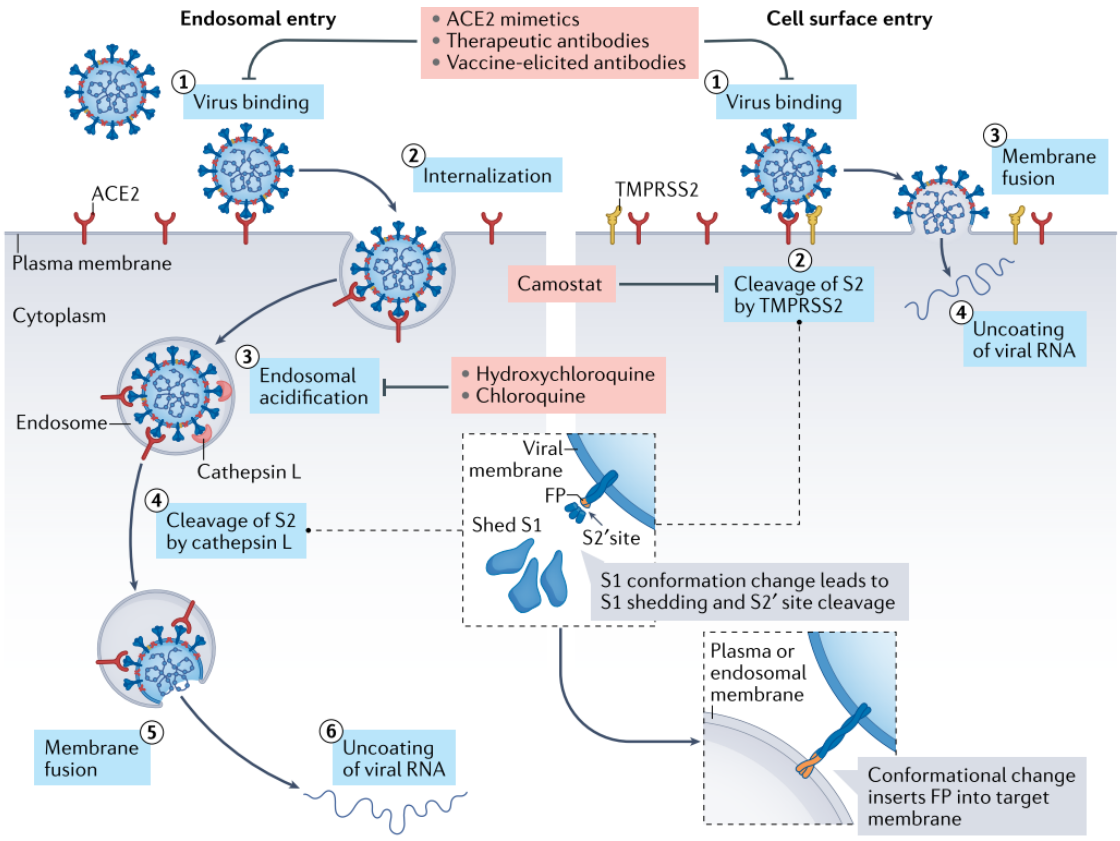

Figure 11: Viral entry into host cells [155]

3.1.1 – Immune response

The interplay between the host immune response and the expression of ACE2 has been identified, and it is suggested ACE2 to be a virus responsive gene, in fact it can either be upregulated by the infection of various viruses or by stimulation of the interferon-mediated cytokine cascade [159].

The cellular response to infection begins when viral pathogen-associated molecular patterns (PAMPs) are detected by pattern recognition receptors (PRRs). This detection triggers a chain of events that comprehend the activation of downstream signaling molecules, such as the adapter proteins MAVS and MyD88, kinases like TBK1 and IKK, and transcription factors including IRF3, NF-κB, and activator protein 1. This complex signaling pathway culminates in the robust production of type I and III interferons (IFN-I and IFN-III) and a general pro-inflammatory cellular stress response. The primary phase of IFN production, essential for countering viral infections like those caused by coronaviruses, involves a positive feedback loop initiated by the activation of PRRs by PAMPs. This loop enhances the interferon response through the production of type I and III interferons (IFN-I and IFN-III), activating signaling pathways via Tyk2 and Jak1 [160]. These pathways lead to the activation of interferon-stimulated genes (ISGs) crucial for antiviral defense, producing proteins that protect against viruses by degrading viral RNA and blocking virus entry. While IFN-I receptors are ubiquitously expressed, enabling a systemic response, IFN-III receptors are localized to epithelial and mucosal barriers, suggesting IFN-III's role in defending entry points like the respiratory and gastrointestinal tracts. In particular SARS-CoV-2, but also many other different viruses, has evolved many redundant mechanisms to evade this IFN-mediated defense by employing proteins that suppress IFN production and signaling, undermining the host's initial immune response, and allowing the virus to establish infection. Specifically, SARS-CoV-2 has developed sophisticated strategies to evade these defenses, notably through proteins like nsp1 and nsp6, which significantly impact IFN production and signaling. This viral evasion highlights the challenge of maintaining a balanced immune response, where as a countermeasure the overproduction of IFNs can contribute to severe COVID-19 outcomes, including cytokine storms and systemic inflammation, leading to tissue damage and potentially life-threatening conditions, like the acute respiratory distress syndrome. Conversely, an initial low level of IFN-I, leading to unchecked viral replication, followed by a later overproduction, contributes to severe inflammation. This paradoxical role of interferons, which can exacerbate disease progression by promoting virus entry into

cells via ACE2 receptors, highlights the intricate interconnection between INF production and ACE-mediated entry [161,162].

3.1.2 –ACE-2 important host target

ACE2 was initially identified in 2000 as a homolog of the ACE receptor, exhibiting 40% identity and 60% similarity with it. The ACE2 protein, made up of 805 amino acids, can be encoded in 6 variant forms via alternative splicing. It features a single extracellular N-terminal domain that houses the active site for catalysis, a membrane-anchoring C-terminal segment, and a HEXXH zinc-binding motif that is highly conserved, and serves as a carboxypeptidase, cleaving single amino acids from the C-terminal ends of its substrates [163].

Studies have shown that under conditions of cellular energy stress, sirtuin 1 (SIRT1) can initiate the transcriptional activation of ACE2 [164]. In a similar manner, apelin treatment was found to restore decreased ACE2 levels in apelin-deficient mice, indicating that apelin positively influences ACE2 expression [165]. This suggests a potential broader impact of apelin on various pathways influenced by ACE2.

Investigations into ACE2 expression, utilizing various experimental models and human transcriptome databases, have identified significant expression levels in the lower respiratory tract, notably in lung type II alveolar cells [166,167]. Given the prevalence of respiratory issues among patients infected with SARS-CoV-2, these observations are understood in the context that SARS-CoV-2 triggers the release of inflammatory cytokines, such as interferons, which can in turn, elevate ACE2 expression, thereby enhancing the virus's ability to infect [161]. Furthermore recent studies have shown ACE2's prevalent expression in several tissues that clarifies why SARS-CoV-2 infection impacts not just the respiratory system but also affects the kidneys, liver, heart, and gastrointestinal tract [168].

ACE2 is also subjected to post-translational modifications and is predominantly found on the cell surface with its N-terminal catalytic domain extending into the extracellular space to interact with various active peptides in the interstitial fluid. The

enzyme is susceptible to proteolytic cleavage by several proteases, including a disintegrin, ADAM10 and ADAM17, as well as the TMPRSS2.

When the S1 subunit of the SARS-CoV-2 Spike protein attaches to the ACE2 receptor, it initiates the cleavage of ACE2 by ADAM17, which results in the generation of a soluble form of ACE2 that maintains its catalytic function, and in fact, inhibitors of ADAM17 have been shown to impede viral entry both in vitro and in animal models, highlighting their critical influence on the infectivity of SARS-CoV-2 and underscoring their potential as targets for developing antiviral treatments.

There are contrasting opinions in whether higher levels of ACE2 offer protection or a higher susceptibility to SARS-CoV-2. In fact, some scientists hypothesize that higher levels of soluble ACE2 might prevent SARS-CoV-2 from attaching to the ACE2 receptors on cell membranes, potentially clarifying why women and children exhibit less susceptibility to the virus. On the opposite front, recent research suggests that elevated sACE2 levels could indicate either an increase in ACE2 expression, or heightened activity of ADAM17, or even both, which might increase the risk of SARS-CoV-2 infection [169].

3.1.3 – HDACi

Epigenetic alterations involve inheritable modifications in the genome that do not affect the DNA sequence itself but can modify DNA accessibility and the structure of chromatin, thereby influencing patterns of gene expression. These type of alterations are exploited through three key mechanisms: DNA methylation, modifications of histone proteins, and positioning of nucleosomes [170–175]. These changes are enzymatically reversible and have significant functions in both normal physiological processes and development of various diseases.

Histone acetylation is characterized by the covalent attachment of an acetyl group to the ε-amino group of lysine residues located on the tails of histone proteins. This process is dynamically regulated by the opposing activities of two types of enzymes: histone acetyltransferases (HATs), which add acetyl groups, and histone deacetylases (HDACs), which remove them [176,177].

Initially recognized as a post-translational modification (PTM) in histones, acetylation has since been discovered as a prevalent PTM also among numerous non-histone proteins [178]. From a biological standpoint, the acetylation of lysine residues leads to the neutralization of their ε-amino group's positive charge, and this modification plays a critical role in the regulation of various cellular processes, including gene transcription, protein folding, and organization of the cytoskeleton.

HDAC enzymes, which are highly conserved across plants, animals, protozoa and fungi, play a crucial role in various biological processes, and most importantly the dysregulation of this mechanism is associated with a variety of diseases, such as cancer, neurological disorders, immune deficiencies, metabolic syndromes, and inflammatory conditions, underscoring its significance for therapeutic intervention [179–183]. In humans, there are 18 identified HDAC enzymes, categorized into four classes based on their similarity to the yeast homologues: Class I (Rpd3-like proteins), Class II (Hda1-like proteins), Class III (Sir2-like proteins, also known as sirtuins), and Class IV. Specifically, Class I includes HDACs 1, 2, 3, and 8; Class II is further divided into Class IIa, comprising HDACs 4, 5, 7, and 9, and Class IIb, including HDACs 6 and 10; Class III encompasses SIRT 1 through 7; and Class IV only consists of HDAC11.

Class I HDAC members are distinguished by their widespread expression across various tissues and their presence in the nucleus (specifically HDACs 1, 2, and 3), while HDAC8 is unique to smooth muscle tissues and is found both in the nucleus and in the cytoplasm. In addition to this, while HDACs 1, 2, and 3 are components of large multiprotein complexes, HDAC8 operates independently of such complexes and exhibits a greater catalytic efficiency on acyl lysine substrates than on acetyl lysine [184].

Enzymes belonging to Class II exhibit a pattern of expression that is highly specific to certain tissues. Specifically, the Class IIa isozymes, namely HDAC 4 and 5, are predominantly found in the brain, heart, and skeletal muscles. On the other hand, HDAC7 is expressed in a broader range of tissues including heart, lungs, placenta, pancreas, skeletal muscles, and thymus. Similarly, HDAC9's expression is mainly

limited to the brain and skeletal muscles. As for the Class IIb isozymes, HDAC6 is observed in the heart, skeletal muscles, and brain, while HDAC10's presence is noted in the liver, spleen, and kidney. Enzymes in Class II possess the unique ability to move between the nucleus and cytoplasm in reaction to specific cellular stimuli. This mobility is facilitated by the presence of signals that direct their nuclear localization and export, or through their co-localization with additional proteins or other HDACs. HDAC6 stands out among the Class IIb enzymes due to its primary cytoplasmic localization and its unique structure, which includes two independently functional catalytic domains and a zinc finger domain that binds to ubiquitin. Additionally to its function as a key histone deacetylase, HDAC6 has an important role also on a variety of cytoplasmic non-histone proteins, such as α-tubulin, cortactin, Ku70, and HSP90. Analyzing the other two important HDAC isozymes, HDAC10 is found both in the nucleus and the cytoplasm, serving as a transcriptional repressor. It is particularly effective as an acetyl polyamine hydrolase, while HDAC11, the only representative of Class IV, is present in various tissues including the brain, heart, kidneys, testis, and skeletal muscles, and is localized within the nucleus [185].

The dysregulated expression of classical HDAC enzymes is closely associated with cancer, often correlating with the severity of the disease and unfavorable prognoses for patients [186–189]. Nonetheless, studies indicate that Class I proteins such as HDAC1, HDAC2, and HDAC3 might play roles in suppressing tumors. In the context of neuropathology, HDAC2 has been implicated in regulating synaptic numbers, plasticity, and the density of dendritic spines. It is also considered a promising target for therapeutic interventions in Alzheimer's disease. Also HDACs 6 and 3 are implicate in a range of processes related to neurodegenerative diseases. In particular, HDAC3 is recognized as a potential target due to its connection with brain-derived neurotrophic factor and elevated levels of hyperphosphorylated tau protein.

In general, HDACs have been documented to play roles in various human pathologies, including the induction of viral silencing, particularly in the case of HIV

infection, as well as in diabetes and immune-related disorders, such as chronic obstructive pulmonary disease [190–192]

In fact, exploring the role of HDACs in viral pathogenic contexts, studies have evaluated the role of HDAC5 which is degraded during Vaccinia virus (VACV) infection and is a restriction factor for VACV and herpes simplex virus type 1 [193]. Further, TMP269 (HDAC IIa inhibitor) can significantly inhibit RABV replication and reduce the viral titers and protein levels of RABV at an early stage in the viral life cycle [194], not to mention the different roles of HDAC6 modulation in various viral infections and hosts immune response [195], and the role of HDACi in HIV latency repression [190,196].

3.1.2.1 – HDAC's ACE-2 MODULATION

The insurgence of COVID-19 has prompted researchers to investigate the infectivity and pathogenicity of SARS-CoV-2. In particular HDACs have been studied for their roles in the described viral pathogenic processes, and their role in influencing the severity of COVID-19 has been established [197]. Specifically, while ACE converts angiotensin I to angiotensin II, ACE2 modifies angiotensin II into the vasodilator angiotensin, acting as a balancing factor in the renin-angiotensin system. HDAC significantly enhances ACE2 surface expression through promoter binding [198], for this reason investigating the epigenetic regulation of these receptors is crucial for developing wide-ranging antiviral treatments against coronaviruses, [199] though ACE2 is not the sole receptor that needs to be investigated, for instance, HCoV-OC43 interacts via aminopeptidase N for viral entry. .

3.2 – AIM OF THIS STUDY – Development of HDACi with a preventive action against SARS-CoV-2 infection

Given the expertise of my research group in the development of HDAC inhibitors, it comes natural to repurpose this knowledge on the development of HDACi focusing on the modulation of expression of ACE2 and TMPRSS for the prevention and reduction of SARS-CoV-2 infection [200]. The development of these inhibitors has focused on the creation of two sets of compounds, one more selective against HDAC6 isozyme and the other more selective towards HDAC1 isoform, in order to evaluate the different inhibition of these two isoforms in the prevention of the viral infection.

3.2.1 – Design of HDACi

The classical pharmacophoric model of the majority of HDACis consists of three essential portions, namely a cap group which interacts with the external surface of the active site, a linker necessary to connect the two contraposing portions and inserted in the hydrophobic substrate binding tunnel, and a zinc binding group (ZBG) which is crucial for the interaction with the metal ion coordinated buried inside the active site. In particular, for this study two compounds from the same library have been repurposed, a selective HDAC1 inhibitor and a selective HDAC6 inhibitor, in addition to a panHDAC inhibitor, SAHA.

The structural features of these compounds comprehend a substituted quinazolinone core which has been selected as the cap group; this privileged scaffold is present in many natural sources and is incorporated in a variety of compounds with an array of biological functions, spanning from anticancer to antimicrobial activity.

For the choice of the linker moiety, the para-substituted benzyl spacer has been selected, since it confers a certain degree of steric hinderance allowing to enhance the selectivity of these inhibitors towards the isoform 6.

Finally, two distinct ZBG have been proposed, an hydroxamic acid which exhibits a higher selectivity against HDAC6, and an o-amino benzamide which displays a more interesting inhibitory activity against HDAC1.

3.2.2 – Synthesis

The synthesis of the final compounds **72** and **73** is reported in Scheme 10. The final compounds have been synthesized starting from the 7-chloroquinazolin-4(3H)-one core [201], that was alkylated with methyl 4-(chloromethyl)benzoate in the presence of potassium carbonate and sodium iodide to obtain the common intermediate **71**. This latter was used for the transformation of the ester moiety in hydroxamic acid using hydroxylamine hydrochloride under basic conditions (**72**). While the final compound **73** was synthesized through an initial hydrolysis of the ester into carboxylic acid derivative, and successively the final benzamide derivative was obtained through coupling reaction in the presence of *o*-phenylendiamine.

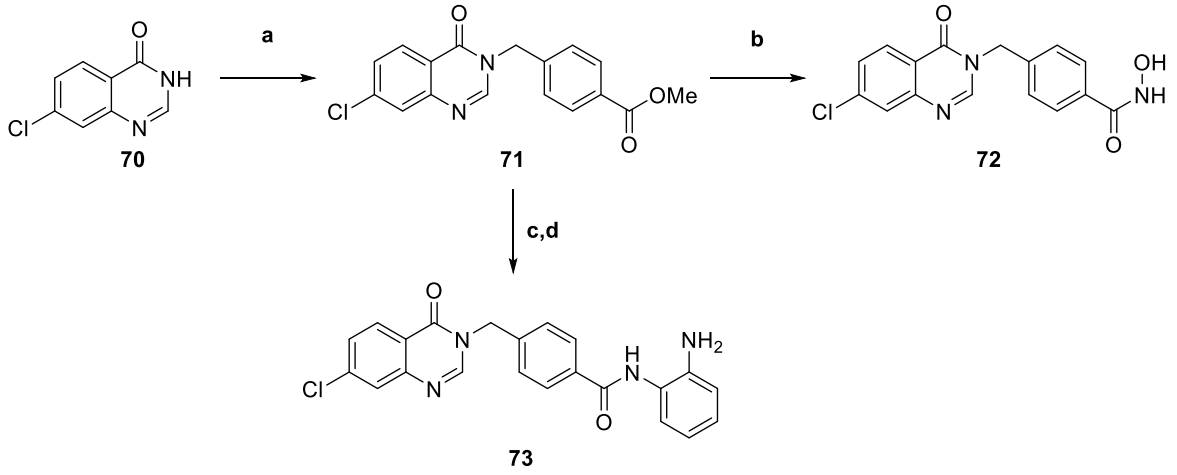

*Scheme 10:Synthesis of compounds **72** and **73**. Reagents and conditions: a) methyl 4-(chloromethyl)benzoate, K_2CO_3, NaI, acetone, 55 °C 12 h; b) $NH_2OH \cdot HCl$, methanolic KOH, MeOH, 25 °C, 12 h; c) NaOH, THF, H_2O, 25 °C, 2 h; d) o-phenylendiamine, HATU, TEA 25 °C, 12 h.*

3.2.3 – Biological evaluation

The two repurposed compounds were evaluated for their ability to inhibit a selected panel of HDAC enzymes as reported in Table 2. For the choice of the isoforms to be tested, different considerations had to be taken into account. As previously described

HDAC1 and HDAC8 belong to class I and are primarily located in the nucleus, playing critical roles in modulating gene expression through the deacetylation of histones and transcriptional regulators, while HDAC8 is uniquely different in its functions and it is the only isoform encoded by a gene on the X chromosome. On the other hand, HDAC6 and HDAC10 are part of class IIB, indicating a different class within the HDAC family, with HDAC6 notably being involved in cytoplasmic activities. The challenge in distinguishing between HDAC6 and HDAC8 arises due to the similarities in their active sites, making it difficult to develop inhibitors that selectively target one over the other. This issue of selectivity among the various HDAC isoforms is a significant consideration in the development of HDAC inhibitors, which are used for therapeutic purposes, including cancer treatment as these were designed for. For this reason the screening process includes different isoforms allowing to identify inhibitors that are selective for class I HDACs to ensure targeted therapeutic effects with minimal off-target effects, though the screening of all the eleven isoforms has proven redundant and not necessary.

The repurposed compounds have been initially evaluated for their inhibitory activity against various HDACs isoforms, namely 1, 6, 8 and 10, *in vitro* in leukemic cells, allowing to establish their selectivity towards HDAC1 and HDAC6 isoforms [202]. In particular, compound **79** is characterized by a hydroxamic acid moiety in the para position exhibiting nanomolar inhibition against HDAC6 (IC_{50} = 9.60 nM) and also an interesting inhibitory activity against HDAC1 (IC_{50} = 890 nM) and HDAC8 (IC_{50} = 707 nM), while compound **80**, which only differs in the ZBG portion, marks an important shift in the selectivity profile. In fact, by modifying the hydroxamic acid to an o-amino benzamide, compound **80** achieved a highly selective inhibition profile with an IC_{50} value of 67 nM against HDAC1. This progression highlights the strategic approach required in designing inhibitors that target specific HDAC isoforms, considering the similarities in their active sites and the therapeutic need for selectivity.

Table 3: Biological evaluation of the repurposed HDACis againsthHDAC1, hHDAC6, hHDAC8 and hHDAC10 [202]

entry		structure	IC_{50} (nM)[a]			
			hHDAC1	hHDAC6	hHDAC8	hHDAC10
1	**72**	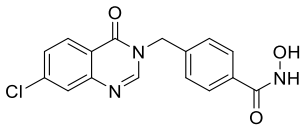	890 ± 61	9.60 ± 0.68	707 ± 44	1116 ± 76
2	**73**	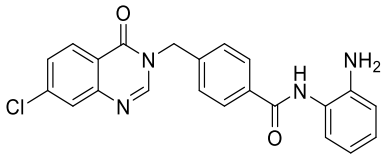	67 ± 4	>10000 (1%)	>10000 (1%)	1149 ± 76

[a] *in vitro* measurements of the HDAC isoforms inhibition profile expressed as IC_{50} value

Further biological studies of these compounds are still ongoing, in particular the preventive action will be assessed by preventive administration of these HDACis to the cell cultures in order to evaluate their capability in preventing the infection.

CHAPTER 4

Design and synthesis of inhibitors of the VP37 enzyme of monkeypox virus

CHAPTER 4 – Design and synthesis of inhibitors of the VP37 enzyme of monkeypox virus

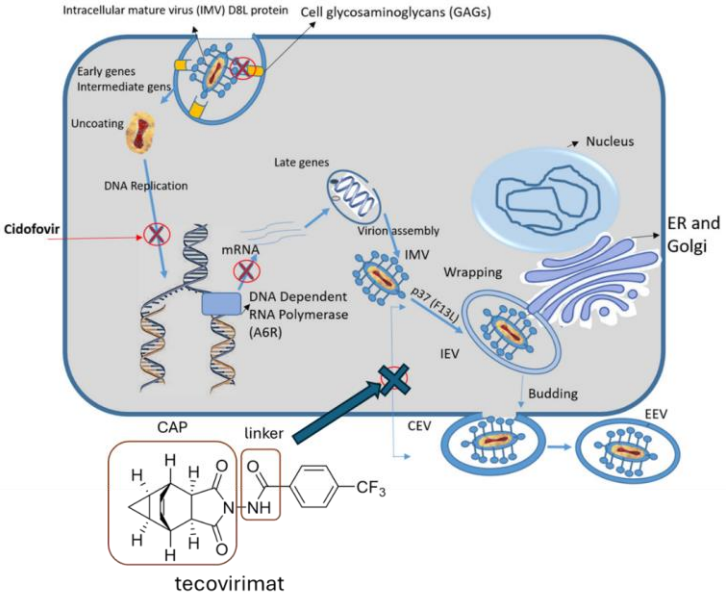

Table of content

Among orthopoxviruses, monkeypox (MPXV) is the most significant pathogen affecting humans, after the global eradication of smallpox has occurred. The recent reported cases worldwide have alarmed researchers, as result of the last COVID-19 pandemic, prompting the research for new anti-viral agents against monkeypox with optimized synthetic protocols and enhanced drug-like properties. Tecovirimat, which has been previously developed for the treatment of smallpox and has proven to be effective against various orthopoxviruses, is the only specifically approved drug for the treatment of MPXV. This drug targets the VP37 (also known as F13L) protein which is pivotal for virion maturation and exit from the host cells, thus allowing for the inhibition of the disease progression. In an effort to develop inhibitors with a more accessible synthetic protocol, and broaden the limited SAR studies, this project has focused on the design and synthesis of a library of tecovirimat analogues, aimed at a thorough exploration of the cap group. The resulting compounds will be tested in phenotypic assays in order to evaluate their inhibitory potency and allow a targeted follow-up SAR study.

4.1 Monkeypox emergence and re-emergence

Before 2022's outbreak, MPXV infections had been endemic to various African nations for decades. Between 1st January 2022 and 7th August 2022, a total of 89 countries reported confirmed MPXV cases, including a small number of deaths, to the World Health Organization [203].

The first reported cases of MPXV affecting humans were sporadically reported in the 1970s across various African nations, though over the last two decades the virus has seen a significant spread throughout the continent. Beginning in May 2022, there was a notable surge in MPXV infections globally (Figures 12 and 13), prompting the WHO to classify the monkeypox epidemic as a worldwide health crisis.

By May 2022, 92 confirmed cases had been reported across 13 countries (including the UK, Australia, Belgium, Canada, France, Germany, Italy, the Netherlands, Portugal, and the USA). These were all regions where the monkeypox virus had not been historically reported yet (Figure 12). On May 24, the United Arab Emirates reported its first case, marking the first occurrence of the infection also in an Arab country [203,204].

In 2022 from January to June, the WHO was notified of 3,413 cases of monkeypox that were confirmed through laboratory testing and one death had been reported, across 50 countries and territories spanning five WHO regions. Of these, the European Region accounted for 2,033 cases, representing 86% of the total confirmed cases. The remaining cases were distributed as follows: the African Region with 73 cases (2%), the Region of the Americas with 381 cases (11%), the Eastern Mediterranean Region with 15 cases (1%), and the Western Pacific Region with 11 cases (1%). Notably, Nigeria reported a single fatality related to monkeypox in 2022 [205,206].

The majority of reported monkeypox cases affected males; these cases are primarily found in urban settings and within specific social and sexual networks. A study conducted by Queen Mary University of London revealed that 98% of the individuals diagnosed with the virus were gay or bisexual men, and 41% were living with HIV [207].

Currently, it remains unclear whether monkeypox transmission occurs specifically through sexual contact or if it primarily spreads via closest physical contact. However, the observed transmission pattern, especially in countries where monkeypox is not endemic, has prompted speculation about whether MPXV has undergone mutations similar to SARS-CoV-2 to enhance human-to-human transmission [208,209].

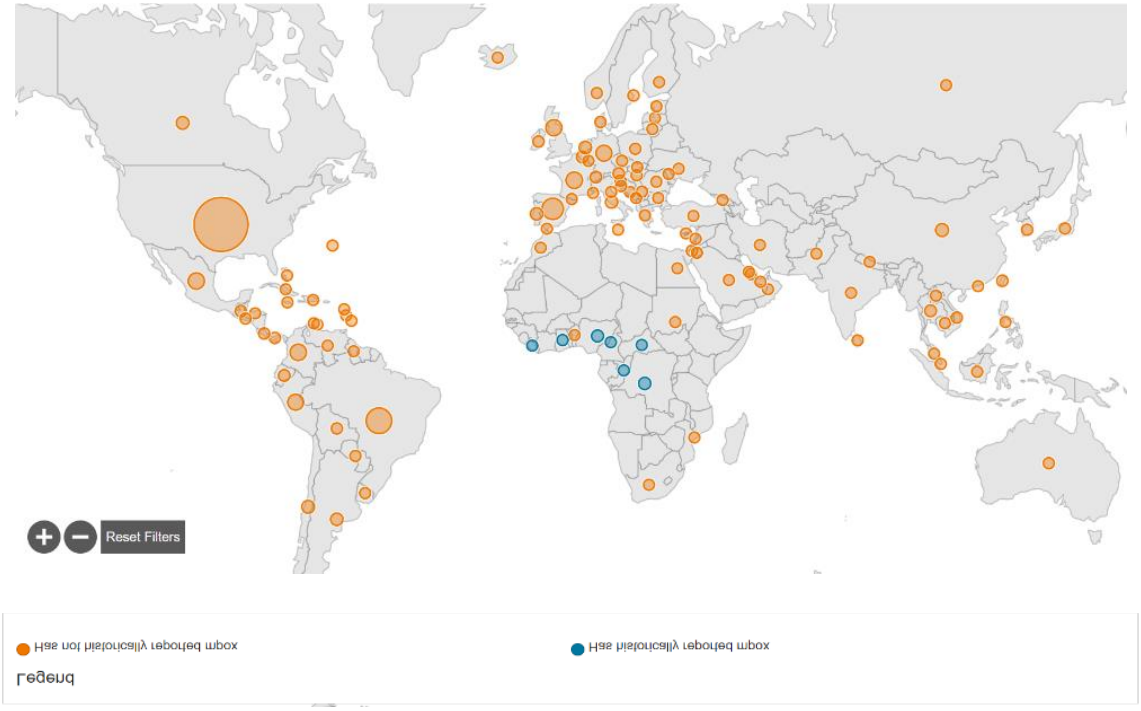

Total confirmed cases	Confirmed cases in locations that have not historically reported MPXV	Confirmed cases in locations that have historically reported MPXV
93,497	91,373	2,124

Figure 12: 2022-2023 Mpox Outbreak Global Map, Data as of 07 Feb 2024 5:30 PM EDT, confirmed cases [210].

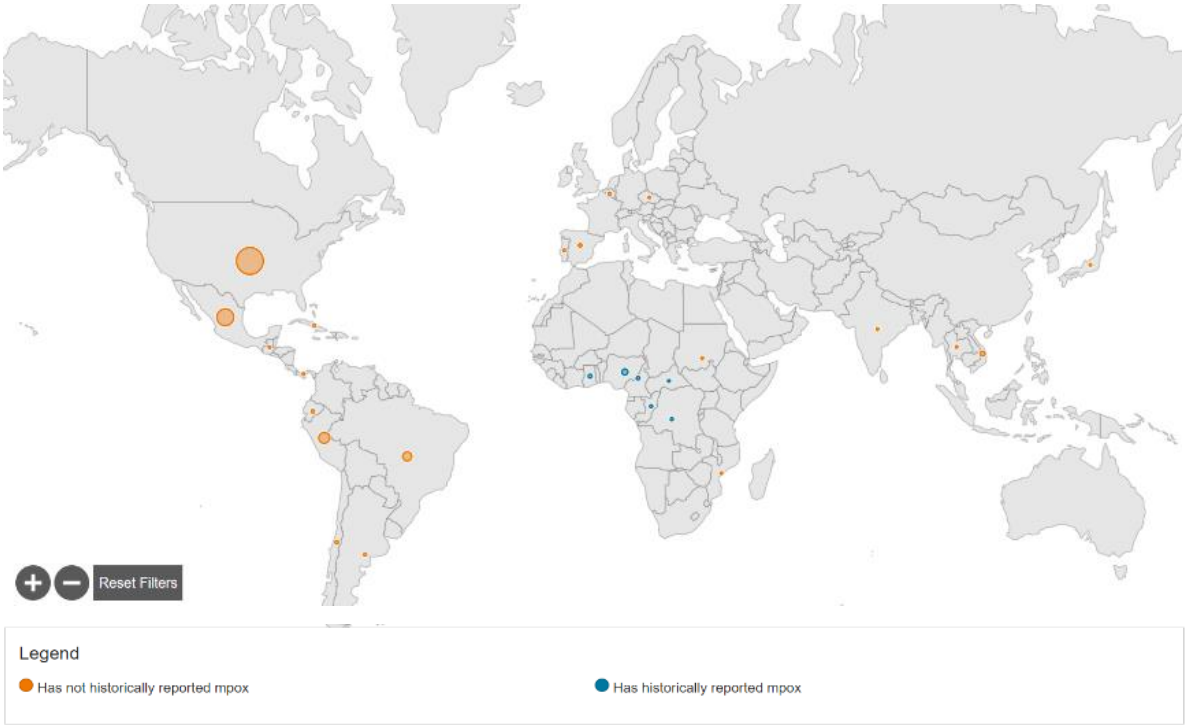

Total confirmed deaths	Confirmed deaths in locations that have not historically reported MPXV	Confirmed cases in locations that have historically reported MPXV
177	156	21

Figure 13: 2022-2023 Mpox Outbreak Global Map, Data as of 07 Feb 2024 5:30 PM EDT, confirmed deaths [210].

4.1.1 Monkeypox

Monkeypox is a zoonotic disease caused by the monkeypox virus, a member of the orthopoxvirus group within the Poxviridae virus family [211]. Genomic analyses classify MPXV into the variola-vaccine complex subtype within the poxvirus family. The virus was named 'monkeypox' due to its initial identification in African monkeys, and its distinctive skin lesions that differ from those caused by the variola virus and other poxviruses [212]. The properties of MPXV fall between those of variola and vaccinia viruses, to which genome homology is the highest, highlighting characteristics that align with other members of the poxvirus family. Morphologically, monkeypox viruses resemble other poxviruses with their brick-shaped structure, measuring approximately 200–250 nm in size. The clinical resemblance between MPXV and smallpox has prompted speculation that MPXV could be an evolutionary precursor

to the variola virus [213]. However, analyses of their genomic sequences, either through restriction enzyme mapping or nucleic acid sequencing, indicate that monkeypox and variola viruses have evolved separately even though alternative studies speculate that the variola virus might be the progenitor of the monkeypox virus, even if they exhibit distinct differences in host specificity and pathogenicity [214].

While the primary natural reservoir of MPXV remains unidentified, it has been shown that a wide range of small rodents, bats, and non-human primates are vulnerable to infection [215]. Other susceptible species include humans, various rodents like squirrels and mice, rabbits, hamsters, porcupines, several non-human primates, black-tailed prairie dogs, African brush-tailed porcupines, rats, and shrews.

Within the Poxviridae family, the orthopoxvirus genus stands out as the most important, comprising viruses that have complex DNA structures and continue to represent a significant biological hazard to human health. In this context, the Monkeypox virus, which is categorized under risk group 3 within the orthopoxvirus genus, boasts one of the larger genomes, spanning approximately 220 Kb. It features a linear double-stranded DNA genome capable of replicating in the cytoplasm, but not within the nucleus, and has a wide host range, typically resulting in only mild infections in humans.

The genome of MPXV is characterized by its linear double-stranded DNA, which is responsible for encoding roughly 223 open reading frames [216]. On the other hand, the variola virus, the causative agent of smallpox, possesses the smallest genome within the orthopoxvirus genus, about 186 Kb, with its transmission restricted exclusively to humans and a notably pathogenic nature. Following the global eradication of smallpox, MPXV has emerged as the most significant orthopoxvirus affecting human health [217].

Infective poxviruses exist in two distinct forms: the intracellular mature virus and the extracellular enveloped virus, each characterized by unique surface glycoproteins and employing different entry methods into cells, with a replication process that is believed to mirror that of other members within the orthopoxvirus genus [218].

The specific receptors facilitating MPXV entry remain uncertain, though it has been proposed that the process varies with the viral strain and the type of host cell, potentially involving a range of surface receptors like chondroitin sulfate or heparan sulfate. For VACV cell entry the surface proteins H3, A27 and D8 are known to play a role in viral attachment, afterwards the penetration occurs via a mechanism involving eleven conserved proteins that assemble into the entry fusion complex [219].

One frequently observed symptom of MPX includes skin lesions, particularly within the oral cavity, which can significantly hinder the ability to eat and drink. Additionally, patients often experience skin hardening, swollen, and pain, ultimately causing the formation of crusts [220].

Right after the first epidermic symptoms, the onset of a febrile phase starts, and this is marked by the parallel progression of skin lesions to a pustular stage. Moreover, throughout the course of the disease, secondary pathogen infections may find their way, including infective bronchopneumonia, typically emerging in a secondary phase in which the primary infection drags-on. In specific cases, septicemia and encephalitis were reported, as well as ocular infections that can lead to complications such as blindness and corneal scarring [221,222].

4.1.2.- Pathogenesis

The clinical outcomes of orthopoxvirus infections, including those caused by variola virus and monkeypox virus (MPXV), are significantly influenced by the virus's entry route and source of infection. The respiratory and oral pathways, through inhalation of droplets or contact with infected fluids, are primary entry points. Initially targeting the mucosal linings of the oral and respiratory tracts, the virus initially infects without symptoms, affecting the epithelium of the airways and surrounding immune cells, including monocytes, macrophages, B cells, and dendritic cells.

The migration of orthopoxviruses to draining lymph nodes, where extensive replication occurs, is a critical, yet unclear, step in the infection process, with lymphoid tissues in the neck and throat regions being primary replication regions [223,224]. This preference for lymphoid tissue is due to the virus targeting cells like

monocytes, macrophages and dendritic cells, leading to lymph node enlargement. Experimental studies in non-human primates have confirmed these findings, showing increased natural killer cell activity in lymph nodes post-MPXV infection. After initial replication, orthopoxviruses spread to distant organs via the lymphohaematogenous route, affecting the spleen and liver before causing a secondary viremia that spreads the virus to the lungs, kidneys, intestines, skin, and other organs. The mechanism of skin infection leading to the development of lesions remains partly unclear, with immune cells such as macrophages and CD3+ T cells surrounding the infectious sites, moreover viral shedding in saliva and feces indicates potential transmission routes. Between the two diverse MPXV clades, clinical symptoms reported are almost the same for the West African and Congo Basin clades, though a clear difference is reported in mortality rates, ranging from 1–3.6% in the West African clade, as opposed to a 10% mortality rate and evidence of human-to-human transmission in the Central African clade [217,225,226].

4.1.3 Vaccines and antiviral compounds

Vaccines

Smallpox vaccines are recognized for their ability to also offer protection against monkeypox through cross-immunity. The FDA has authorized two vaccines for pre-exposure immunization against orthopoxviruses, including monkeypox: ACAM2000, a live, second-generation vaccinia virus vaccine, and JYNNEOS, a third-generation, less virulent vaccine derived from the modified vaccinia Ankara strain [227–229].

Stockpiles of second-generation vaccines like ACAM2000 are widely maintained, however, these vaccines have been linked to rare adverse effects, such as myocarditis and pericarditis, posing increased risks for specific populations, including individuals with eczema or those who are pregnant. Despite these concerns, research has shown the effectiveness of the ACAM2000 smallpox vaccine in generating specific T cell responses to the vaccinia virus. This is evidenced by the detection of activated CD4+ and CD8+ T cell responses at intervals of 1, 3, 6, and 12 months following vaccination.

A number of treatments originally designed for smallpox are also utilized for monkeypox, yet their efficacy against monkeypox largely relies on preclinical findings with minimal clinical validation in human subjects [219]. Furthermore, various molecules approved by the FDA, along with other promising candidates, have been investigated for their potential to inhibit the VP37 protein of MPXV and other orthopoxviruses [230–232], and the computational fragment-based drug design approach has been extensively utilized to develop new potential inhibitors of VP37 [233].

Tecovirimat

Identified in 2002 as an agent against orthopoxviruses, tecovirimat (**81**, Figure 14) is derived from a tetracyclic acylhydrazide [234–236].

Regarding its mechanism of action, it acts by targeting the VP37 membrane protein of MPXV, inhibiting the assembly of virions capable of exiting the cell and thus hindering the virus's ability to spread. In non-human primate models, tecovirimat has shown to ameliorate the symptomatology of monkeypox, although its efficacy diminishes when administered more than five days after the first exposure. Nonetheless, in a small-scale study involving a single monkeypox-infected patient treated with tecovirimat, a reduction in both the duration of viral shedding and the period of illness was observed in comparison to six untreated individuals.

Tecovirimat has received approval from the EMA, FDA, and Health Canada for use against various orthopoxviruses infections. Specifically, FDA has granted approval for its use in treating confirmed cases of smallpox under the Animal Efficacy Rule, which allows for the approval of novel treatments for pathologies for which efficient clinical trials in humans is impractical. Given that smallpox has been globally eradicated, it's impossible to test the effectiveness of antiviral medications against it in human subjects. This special animal regulamentation has been introduced by FDA in 2002, and it has established guidelines for the development of pharmaceutical drugs and biologics, facilitating the approval of products in cases where conducting efficacy trials on humans is either unethical or not feasible [237].

Furthermore, research documented in the literature supports tecovirimat's wide-ranging antiviral effectiveness against OPXV, also validating VP37 as the specific viral target of this inhibitor [238].

NIOCH-14

NIOCH-14 (**82**, Figure 14), a water-insoluble tricyclo-dicarboxylic acid derivative, serves as a precursor to tecovirimat. Once inside the human body, NIOCH-14 undergoes cyclization to yield tecovirimat as its active form.

A study comparing NIOCH-14 and tecovirimat in mouse models infected with MpoxV (V79-1-005) revealed that both drugs exhibited comparable effectiveness after a seven-day treatment period at oral dosages of 30 μg/g and 60 μg/g of mouse body weight, with NIOCH-14 showing slightly superior performance. Furthermore, when NIOCH-14 and tecovirimat were compared in mice infected with the variola virus, both medications significantly reduced the virus levels in the lungs to similar degrees following four days of treatment at an oral dose of 50 μg/g.

In a mice model, NIOCH-14 has demonstrated improved bioavailability at 22.8%, when compared to tecovirimat which stood at 12.1%, with both drugs administered as a single 50 μg/g dose. Additionally, recent research has highlighted NIOCH-14's effectiveness and safety against various orthopoxviruses, with the exception of variola virus, showing a good bioavailability at a dosage of 5 g/kg in experimental animals.

For what concerns its metabolism, NIOCH-14 is rapidly converted in the bloodstream into its primary metabolite, tecovirimat. So in a reported study, the pharmacokinetic properties of NIOCH-14, following a single oral administration of 600 mg, have been evaluated through the measurement of tecovirimat levels in the blood, and after an evaluation it has been noted that a dose of 600 mg of NIOCH-14 corresponds to a 250 mg dose of tecovirimat.

Finally the study of NIOCH-14 mechanism of action has been elucidated, confirming the same previously reported for tecovirimat targeting VP37.

While the clinical studies of this compound are still ongoing with a successfully completed Phase I clinical trial in Russia, and an expected phase II/III clinical trial to be carried out between 2023 and 2024, the expectations that NIOCH-14 could be granted marketing authorization within the same timeframe grow higher.

Tecovirimat and NIOCH-14 share similarities in both their chemical structures and modes of action, in addition to this, recent literature has highlighted the potential of adamantane derivatives in the search for VP37 inhibitors, and the creation of new molecules based on the adamantane structure. Additionally, the exploration has extended to other bicyclic capping groups, including derivatives of camphor and fenchone, alongside an analysis of the tail structure common to inhibitors [239–242].

IMCBH

In 1969, IMCBH (**83,** Figure 14) was identified for its ability to specifically obstruct the replication and release of vaccinia virus it is derived from isonicotinohydrazide, and acts as an inhibitor of the F13L gene/VP37P in orthopoxviruses, blocking their secondary envelopment and the formation of extracellular enveloped virions in a manner akin to tecovirimat [243].

Unfortunately while IMCBH showed activity in in vitro experiments, it failed to offer protective effects in mouse and rabbit models.

Cidofovir

Cidofovir (**84**, Figure 14), which is the pharmacologically active component of brincidofovir is an antiviral medication primarily used to treat cytomegalovirus infections in immunocompromised patients, showcasing its broad antiviral properties. The drug functions by inhibiting viral DNA polymerase, a key enzyme necessary for viral replication. Despite its efficacy, the clinical use of cidofovir is significantly hampered by its nephrotoxic effects, necessitating careful monitoring of kidney function during treatment. Additionally, cidofovir requires dosing adjustments in patients with renal impairment to mitigate the risk of further kidney damage [243,244].

Brincidofovir

Brincidofovir (**85**, Figure 14) which is the prodrug of cidofovir, approved by FDA but not by EMA, acts as an inhibitor of the DNA polymerase utilized by orthopoxviruses for DNA replication. It has demonstrated effectiveness in models using prairie dogs and mice for monkeypox studies. Despite its potential benefits, the clinical application of brincidofovir is closely monitored due to concerns about its side effects, particularly those affecting liver function. Ongoing research aims to balance its antiviral efficacy with its safety profile, highlighting the need for careful patient selection and monitoring during treatment [244].

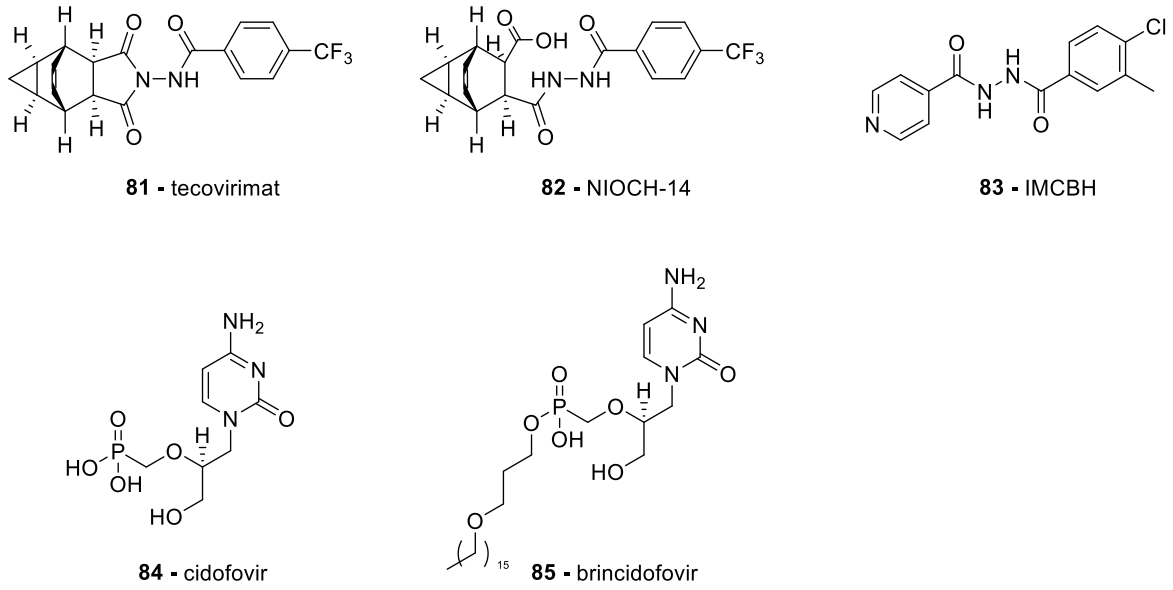

Figure 14: Known MPXV inhibitors

4.2 – VP37 as viral target

VP37, coded in the F13L ORF, is the dominant protein in the vaccinia virus extracellular envelope, and it plays a pivotal role in envelope acquisition, viral egress, and transmission [245]. This protein shows a high degree of conservation across the orthopoxvirus genus, and its SPV homologue, known as P42, shares 54% identity with VP37 and among poxviruses it shows the closest resemblance (73% identity) to the analogous protein in myxoma virus. It consists of 372 amino acids, and is synthesized during the later stages of infection. It is directed to membranes derived

from the Golgi apparatus, where it becomes part of the virion through a process of wrapping. Therefore, VP37 is found in the enveloped variants of the virus but not within the intracellular mature virus acting as a peripheral membrane protein, coating the inner side of the viral envelope. The absence of the VP37 gene disrupts the virus's envelopment, effectively halting the formation of extracellular virus and preventing the transmission of the virus from cell to cell.

Moreover, the absence of virus envelopment also inhibits virus-induced actions such as the formation of actin tails and the fusion of cells at acidic pH levels. Recent studies also indicate enzymatic functions associated with lipid metabolism of VP37 and analysis of the amino acidic sequence has revealed patterns characteristic of the phospholipase D superfamily, confirmed by the phospholipase activities which are important for function [246]. In fact, without it, the virus's ability to form the envelop is compromised, leading to a significant decrease in viral particle production and resulting in a substantially weakened virus in mouse models. The effective localization within the cell and the functionality this enzyme relies on the palmitoylation of Cys185 and Cys186. Additionally, the presence of a functional phospholipase D motif, HKD, is crucial for its activity. VP37 also features a YW motif, which is known to bind with the cellular factor TIP47, involved in the generation of late endosome transport vesicles. Altering this motif interferes with the VP37-TIP47 interaction. In addition, also B5R protein plays a crucial role in the formation of enveloped virions; it is a type I glycoprotein of 42 kDa with transmembrane properties, that includes a significant extracellular domain and a short cytoplasmic tail and undergoes palmitoylation. Without B5R, the virus's ability to wrap is diminished, leading to the production of fewer EEV particles and resulting in a less virulent virus. Studies have shown that B5R and VP37 not only localize together within the cell but also interact with each other.

Notably, the E353K mutation within the VP37 protein is present in all MPXV genomes from 2022. This specific mutation was not found in the most recent common ancestor within a previous clade, although it was detected in a single genome from the 2018 outbreak.

4.3 AIM OF THIS STUDY – Development of simplified analogues of tecovirimat

The aim of this project has been the design of derivatives of tecovirimat with a more chemically tractable chemical structure with respect to the parent drug in order to extend the structure-activity relationships and find more potent antiviral agents against monkeypox and related viruses.

4.3.1 Design of new inhibitors

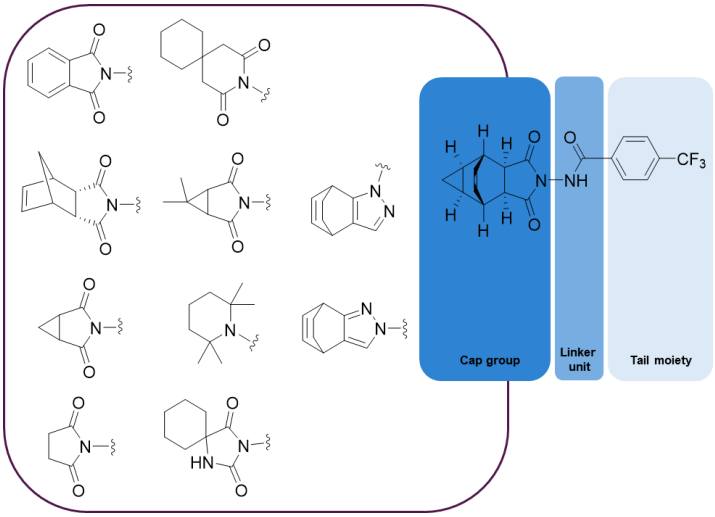

Figure 15: Inhibitors general structure and cap exploration

Tecovirimat can be structurally divided into three different sections, a cap group, a linker unit and a tail moiety, in particular this project has been focused on the exploration of different cyclic portions in order to expand the limited known SARs for the design of new VP37 inhibitors. The compounds here reported fall into a bigger library in which various heteroaromatic and bicyclic groups have been explored in substitution of the hexahydro-4,6-ethenocyclopropa-isoindole-dione which presents synthetic issues. In particular, compounds **89a-d, 98, 113** and **115** were prepared to evaluate different bicyclic rings such as the symmetric 3-azabicyclo[3.1.0]hexane-2,4-dione, the 6,6-dimethyl-3-azabicyclo[3.1.0]hexane-2,4-dione, a more hindered trycyclic system, and a more rigid bicyclic indazole-derivative. Compound **93** was in turn prepared in order to evaluate the importance of the presence of the carbonyl functionalities of the imide group, substituting it with a hindered and lipophilic tetramethylpiperidine system. Finally spiro-hydantoins **105a,b** and spiro derivative

101 have been designed in order to evaluate hindered aliphatic systems replacing the tecovirimat classical bicyclic ring. As a further exploration of the SAR during this project the linker moiety has been exploited through compounds **98** and **106**.

4.3.2 Synthetic protocols of tecovirimat analogues

The synthesis of compounds **89a-d** are reported in Scheme 11. The commercially available 4-(trifluoromethyl)benzoic acid **86**, was subjected to esterification reaction with ethanol in acidic conditions allowing the preparation of the ester intermediate **87**. Successively the ester intermediate underwent to amminolysis reaction with hydrazine in ethanol in order to obtain the benzohydrazide derivative **88**. This intermediate was once again subjected to aminolysis with the appropriate cyclic anhydride allowing the preparation the final compounds **89a-d**.

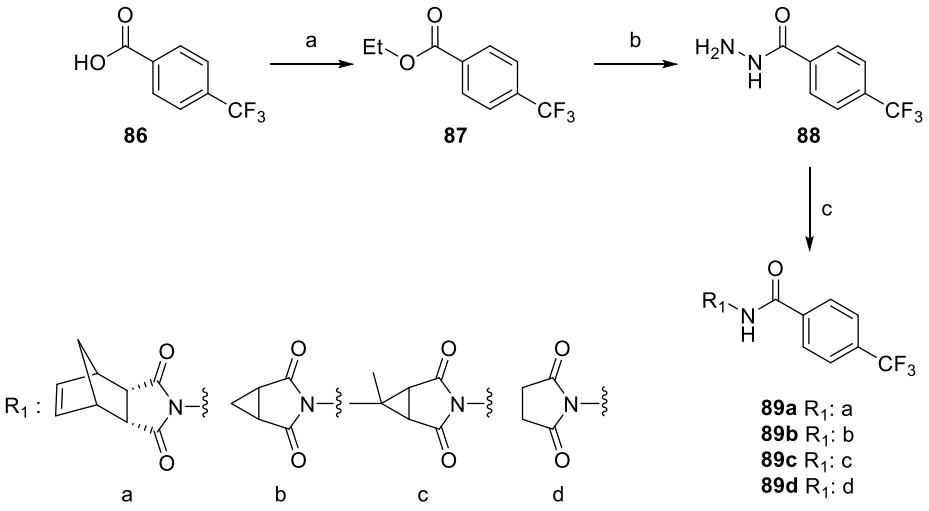

*Scheme 11: Synthesis of compounds **89a-d**. Reagents and conditions: a) H_2SO_4, EtOH, 70 °C, 18h; b) NH_2NH_2, EtOH, 70 °C, 12 h; c) (3aR,4R,7S,7aS)-3a,4,7,7a-tetrahydro-4,7-methanoisobenzofuran-1,3-dione for derivative **89a**, 3-oxabicyclo[3.1.0]hexane-2,4-dione for derivative **89b**, 6,6-dimethyl-3-oxabicyclo[3.1.0]hexane-2,4-dione for derivative **89c**, dihydrofuran-2,5-dione for derivative **89d**, pTSA, toluene, 90 °C, 12h.*

The final compound **93** has been synthesized according to the synthetic protocol reported in Scheme 12. The tetramethylpiperidine (**90**) was converted into the nitroso derivative **91** by the slow addition of sodium nitrite in a cold, acetic acid and acetic anhydride, solution of the starting piperidine. Then the nitroso derivative was

reduced by reaction with Zn powder to the corresponding hydrazine **92** which was alkylated with the commercially available p-trifluoromethyl benzoyl chloride furnishing the final compound **93.**

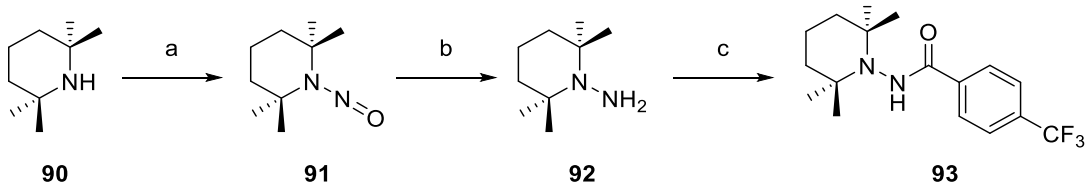

*Scheme 12: Synthesis of compound **93**. Reagents and conditions: .a) AcOH/Ac2O, NaNO2, 0 °C, 72 h; b) AcOH,/H2O, Zn powder, 0 °C, 4 h; c) TEA, 4-(trifluoromethyl)benzoyl chloride, DCM, 0 °C, 12 h.*

The synthesis of compound **96** is reported in Scheme 13. The ethyl 4-(trifluoromethyl)benzoate **94** was converted into the corresponding hydrazido-derivative with hydrazine hydrate at high temperature. Afterwards the hydrazido-intermediate **95** was reacted with phtalic anhydride in xylene at high temperature furnishing the desired compound **96**.

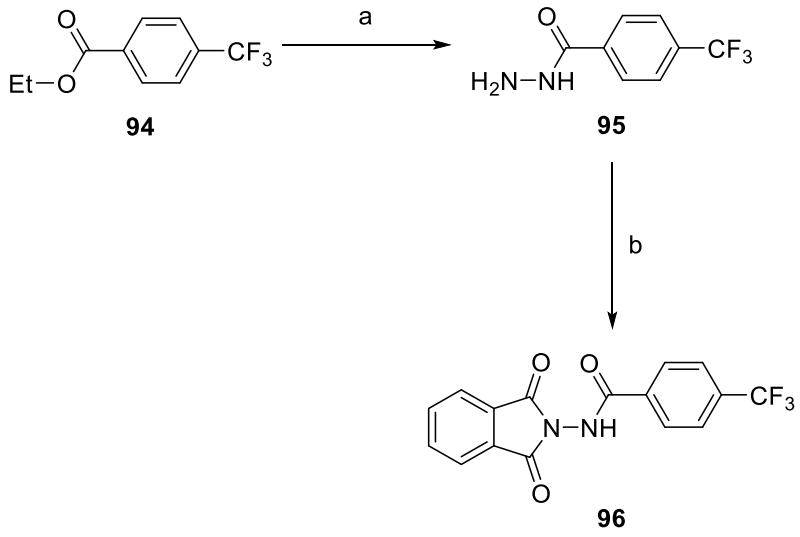

*Scheme 13: Synthesis of compound **96**. Reagents and conditions: a) NH2NH2.H2O, EtOH, 80 °C, 12 h; b) phtalic anhydride, xylene, 110 °C, 12h.*

The preparation of the desired compound **98** is reported in Scheme 14. The reaction was carried out in the presence of 4-(trifluoromethyl)benzoic acid, EDC and TEA, allowing the formation of target molecule **98**.

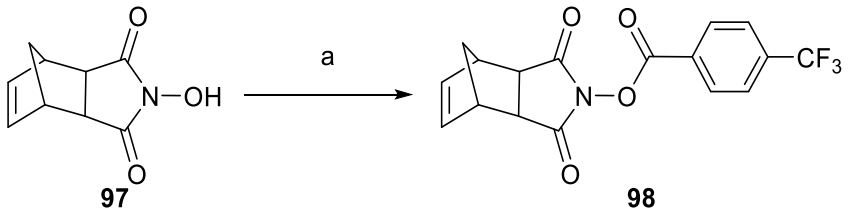

*Scheme 14: Synthesis of compound **98**. Reagents and conditions: a) 4-(trifluoromethyl)benzoic acid, EDC.HCl, TEA, DMF, 25 °C, 5h.*

For the preparation for target molecule **101**, reported in Scheme 15, compound **99** was initially alkylated with hydroxylamine-*O*-sulfonic acid (HOSA) in the presence of NaH in anhydrous DMF furnishing the amino-intermediate **100**. This latter was subjected to coupling reaction with 4-(trifluoromethyl)benzoic acid allowing the preparation of the target molecule **101**.

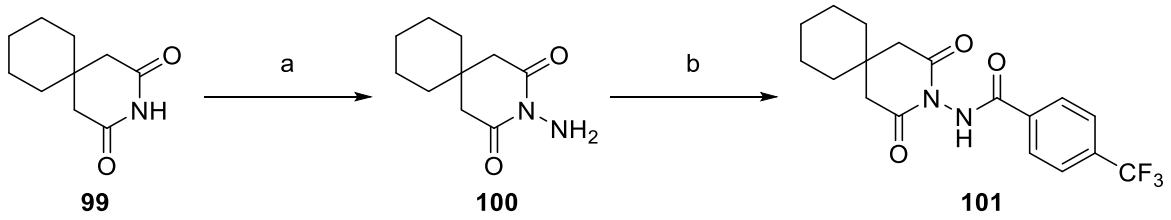

*Scheme 15: Synthesis of compound **101**. Reagents and conditions: a) HOSA, NaH, 25 °C-100°C, 4 h; b) 4-(trifluoromethyl)benzoic acid, HATU, NMM, 25 °C, 5 h.*

For the synthesis of compounds **105** and **106**, which is reported in Scheme16, the initial step has been the formation of the hydantoin, starting from the commercially available cyclohexanone (**102**) this was subjected to MW irradiation in the presence of $(NH_4)_2CO_3$ and KCN affording the cyclic intermediates **103**. Then, intermediate **103** was reacted with hydrazine hydrate to generate the amino-hydantoine derivative **104**, which allowed the formation of the target molecule (**105**) through coupling reaction with 4-(trifluoromethyl)benzoic acid. On the contrary, compound **106** was prepared through direct coupling reaction between 4-(trifluoromethyl)benzoic acid and the intermediate **103** in the presence of HATU as coupling reagent and NMM as a base.

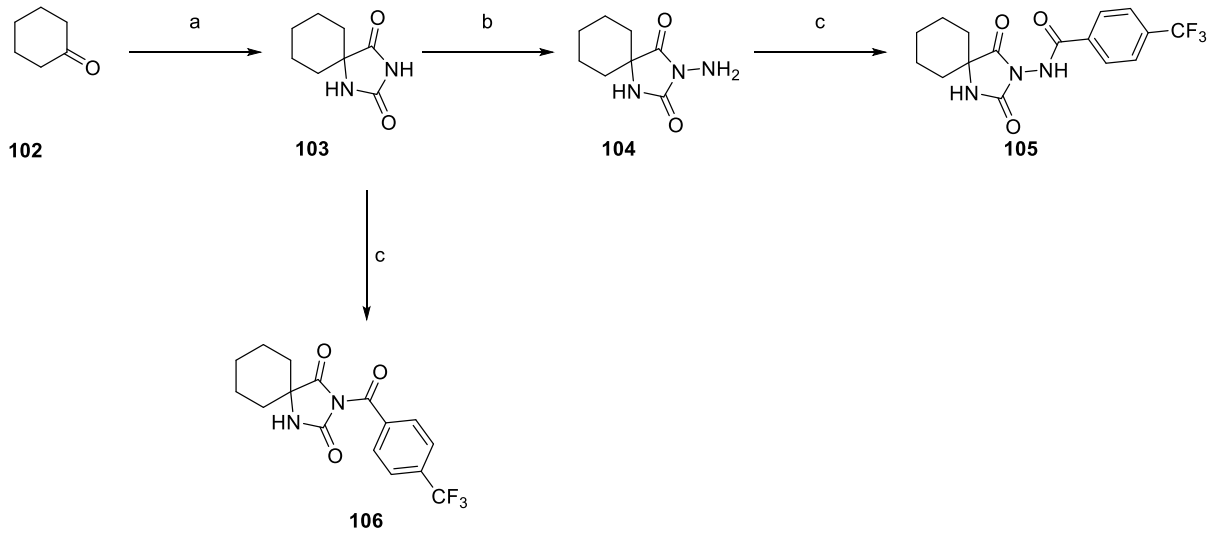

*Scheme 16: Synthesis of compounds **105** and **106**. Reagents and conditions: a) $(NH_4)_2CO_3$, KCN, MeOH/H_2O, MW ir, 10 min; b) $NH_2NH_2.H_2O$, 100 °C, 1 h; c) 4-(trifluoromethyl)benzoic acid, HATU, NMM, DMF, 25 °C, 6 h.*

The synthesis of the final compounds **113** and **115** is reported in Scheme 17. The initial step is a Diels-Alder cycloaddition reaction between the (1Z,3Z)-cycloocta-1,3-diene and 2-chloroacrylonitrile at high temperature allowing to obtain intermediate **108** which has been directly reacted with KOH to furnish compound **109.** This latter was then alkylated in the presence of ethylformate furnishing the aldehydic derivative **110**, which was cyclized in the presence of hydrazine hydrate, to obtain the pyrazole derivative **111**. The alkylation of **111**, in presence of monochloramine and NaH, furnished two regioisomers (**112** and **114**), which have been separated through SiO_2 chromatography. Finally the pure pyrazole derivatives **112** and **114** have been reacted in coupling reaction conditions in the presence of 4-(trifluoromethyl)benzoic acid furnishing the target compounds **113** and **115**.

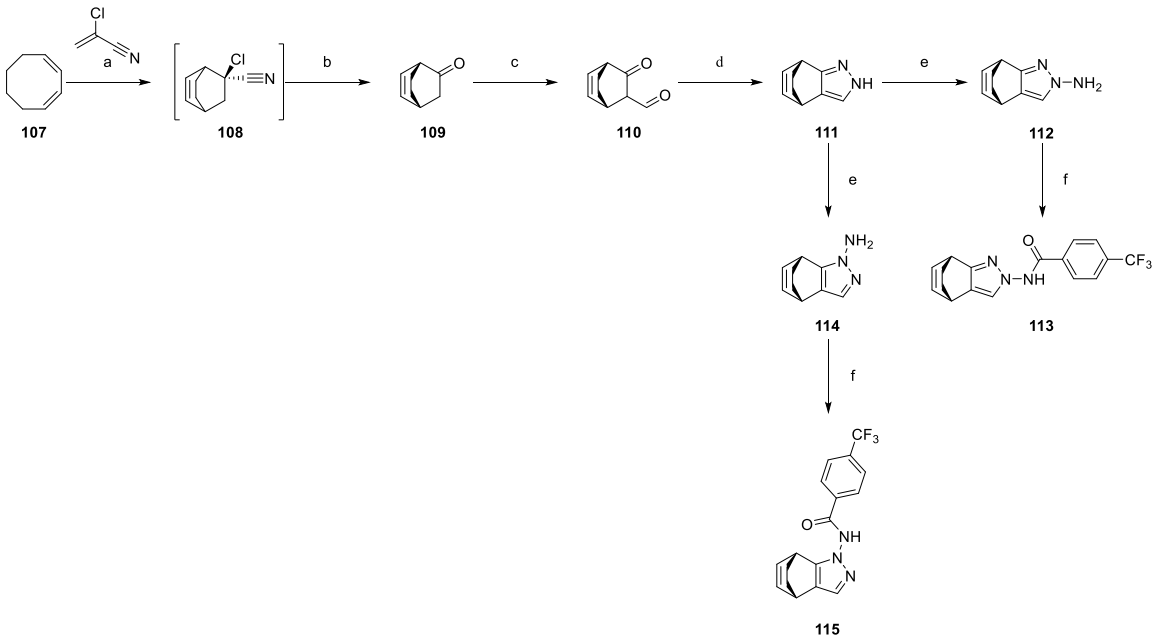

*Scheme 17: Synthesis of compounds **113** and **115**. Reagents and conditions: a) 2-chloroacrylonitrile, HQ, toluene, 80 °C, 12 h; b) KOH, DMSO, 25 °C, 48 h; c) NaH, EtOH, ethylformate, THF, 25 °C, 12 h; d) $NH_2NH_2.H_2O$, MeOH, 25 °C, 12 h; e) NaH, freshly prepared NH_2Cl, DMF, 25 °C, 12 h; f) 4-(trifluoromethyl)benzoic acid, HATU, NMM, DMF, 25 °C, 12 h.*

4.3.3 Biological evaluation

The biological evaluation of the synthesized compounds is still undergoing, though interesting results have been already assessed. In particular the compounds have been tested in a phenotypic assay, allowing to evaluate the percentage of viability of the infected cells and thus allowing to calculate the IC_{50} values which have been reported in Table 4. Different bicyclic systems **89a-d**, **96**, **98**, **113** and **115** have been taken into consideration as valuable replacements for the cap group of tecovirimat. In particular, compounds **113** and **115** have shown promise, thus confirming the necessity for hindered cap portions of the inhibitor, though a more complete view will be achieved after the final results of the bicyclic systems of compounds **89a-c**. In addition to this three differently hampered spiro-derivatives **101**, **105** have been developed, affording optimal results, conversely to compound **93** which has confirmed the necessity of the carbonyl functionalities of the imide group. Finally, the linker moiety has been explored in compounds **98** and **106**, which have resulted in inactive compounds, thus confirming the necessity of an amidic linker moiety connected to the cap group.

*Table 4: Biological evaluation of novel MPXV VP37 inhibitors **89a-d**, **93**, **96**, **98**, **101**, **105**, **106**, **113** and **115** and reference compound **81***

Entry		structure	IC_{50} (µM) [a]
1	**89a**	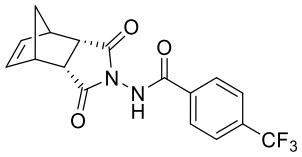	n.t.[b]
2	**89b**	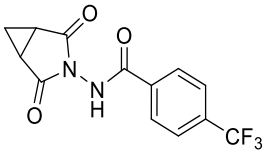	n.t.
3	**89c**	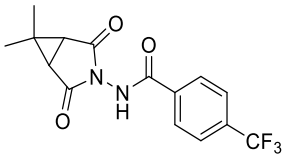	n.t.
4	**89d**	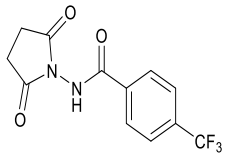	n.a. [c]
5	**93**	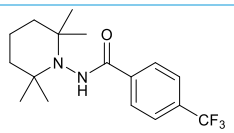	n.a.
6	**96**	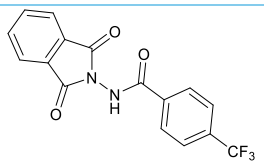	n.a.
7	**98**	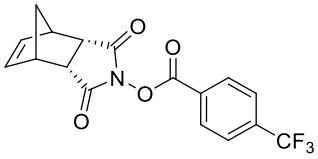	n.a.
8	**101**	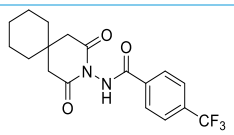	0,31
9	**105**	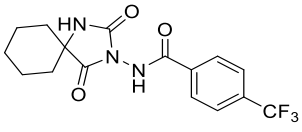	0,31

10	**106**	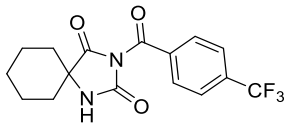	n.a.
11	**113**	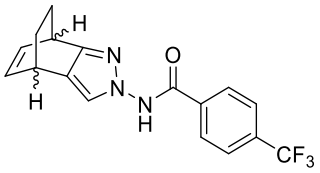	0,31
12	**115**	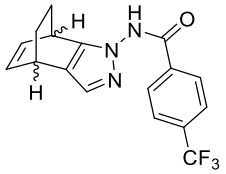	0,31
13	tecovirimat	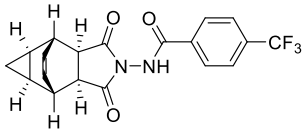	0,35

[a] concentration of compound necessary for the inhibition of the cytopathic effect caused by the virus.

[b] not tested.

[c] not active.

CHAPTER 5

Synthesis of modulators of virulence factors necessary for the formation and maintenance of the biofilm structure of *Pseudomonas aeruginosa*

CHAPTER 5 – Synthesis of modulators of virulence factors necessary for the formation and maintenance of the biofilm structure of Pseudomonas aeruginosa

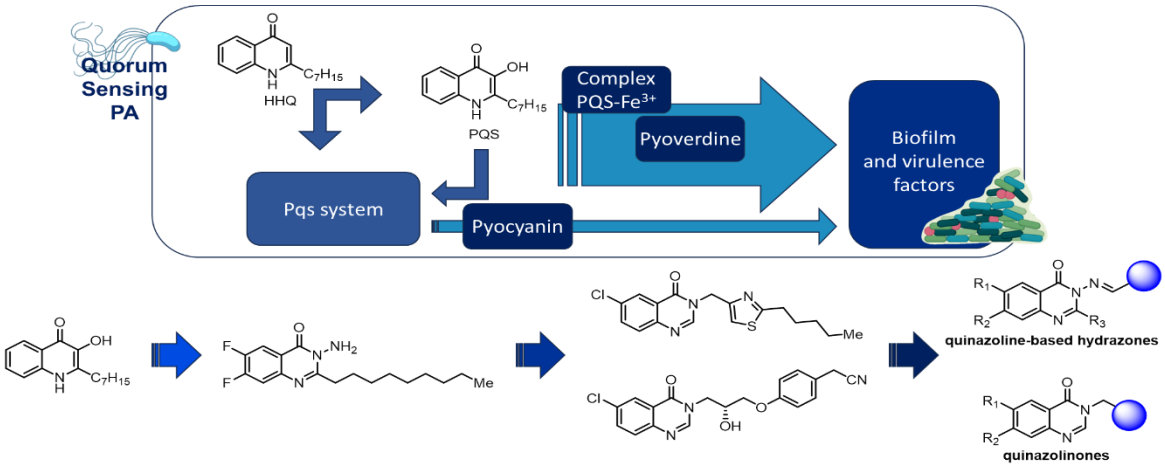

Table of Content

ESKAPE pathogens pose a growing threat for the present and future population, being difficult to manage and eradicate in fragile and immunocompromised patients, in hospital-related settings as well as retirement homes. Among the ESCAPE pathogens, *Pseudomonas aeuruginosa* (PA), is notoriously resistant to multiple drugs, making it one of the most demanding to treat. PA can cause challenging infections in patients affected by cancer, cystic fibrosis or immunocompromised, due to its high mutability and capability to form biofilms which render the eradication even more arduous. In this context, virulence factors modulators emerge as promising strategies avoiding the insurgence of resistance mutations, which commonly occur with the continuous use of antibiotics, thus allowing to reduce the pathogenicity. Pyocyanin (PCN) and pyoverdine (PVD) are two virulence factors important for the pathogenicity of PA, whose production is modulated by the Pqs system, which also controls biofilm production. New quinazolin-4(3H)-one-based modulators have been designed and synthesized, and their biological evaluation has been carried out in two different PA strains responsible for the acute and chronic infection in cystic fibrosis-affected patients proving to reduce biofilm and virulence factors production, confirming to be a valuable resource in fighting PA nosocomial infections.

5.1 ESKAPE pathogens

Pathogens classified under the acronym ESKAPE, include *Enterococcus faecium*, *Staphylococcus aureus*, *Klebsiella pneumoniae*, *Acinetobacter baumannii*, *Pseudomonas aeruginosa*, and *Enterobacter* species, that have developed resistance to antimicrobial treatments and pose a significant threat to global health [247].

The acquisition of antimicrobial resistance genes by ESKAPE pathogens has limited the available treatment options for severe infections, leading to heightened disease burdens and increased mortality rates due to unsuccessful treatments; this situation underscores the need for a unified worldwide effort to monitor antimicrobial resistance. In 2018, WHO has identified pathogens with antimicrobial resistance (AMR) as an emerging threat to global health [248,249]. As of now, there's a lack of a comprehensive global system for AMR monitoring, however, existing data suggest that in the United States alone, over 2 million infections attributable to AMR occur annually, resulting in approximately 29,000 deaths and incurring health care costs exceeding $4.7 billion. Annually in Europe, AMR contributes to more than 33,000 fatalities and 874,000 disability-adjusted life years, stemming from both hospital-acquired and community-acquired infections. These AMR infections lead to direct and indirect expenses amounting to $1.5 billion [250,251]. In developing countries, where estimates of economic losses are lacking, infectious diseases continue to be the primary cause of mortality, and the situation is exacerbated by the rise of new infectious diseases and the resurgence of known ones.

AMR genes are naturally present in the environment, since antibiotic usage has favored the selection of these AMR genes, and the absence of quick diagnostic tools for detecting bacterial pathogens in healthcare settings frequently leads to the unwarranted prescription of broad-spectrum antibiotics.

In particular, in an effort to prioritize and steer the research and development of new antibiotics, the WHO released a list in February 2017 identifying pathogens that critically require new antimicrobial treatments, with the ESKAPE pathogens being tagged with a 'priority status' for new drug development.

These pathogens are notably responsible for severe infections, especially in children, as well as in those with weakened immune systems, and other critically ill patients [252]. ESKAPE pathogens have evolved resistance to a wide array of antibiotics, including oxazolidinones, lipopeptides, macrolides, fluoroquinolones, tetracyclines, β-lactams, combinations of β-lactam and β-lactamase inhibitors, as well as last-resort antibiotics such as carbapenems, glycopeptides, and the less preferred polymyxins. This resistance has emerged through genetic mutations and the acquisition of mobile genetic elements.

5.1.1 – ESKAPE pathogens mechanisms of resistance

The common occurrence of ESKAPE pathogens in healthcare environments explains the diversity of AMR mechanisms identified in these bacteria that have led to a higher prevalence of these resistant species in nosocomial infections [249,253]. The most relevant resistance alterations can be grouped into four categories:

(i) inactivation or modification of the antimicrobial agent,
(ii) alterations in the bacterial target sites,
(iii) decreased antibiotic penetration or accumulation within bacterial cells, and
(iv) biofilm formation by the bacteria.

This section will delve into the key AMR factors that have enabled the persistence and proliferation of ESKAPE pathogens in contemporary healthcare settings [254].

5.1.1.1 - Antibiotic Inactivation/Alteration

A prevalent AMR strategy among ESKAPE pathogens is the synthesis of enzymes capable of permanently inactivating or modifying antibiotics. This tactic is especially common in Gram-negative bacteria and includes enzymes that either (i) dismantle the antibiotic's active site, such as the hydrolysis of the β-lactam ring by β-lactamases, or (ii) chemically alter the drug's critical structural components, preventing it from binding to bacterial targets, for instance, aminoglycoside-modifying enzymes that alter hydroxyl or amino groups.

β-Lactamase enzymes were discovered shortly after penicillin was isolated and purified, and to date, over 2,600 distinct β-lactamases have been identified, conferring resistance to various β-lactam antibiotics such as penicillins, cephalosporins, monobactams, and carbapenems. Among Gram-negative ESKAPE pathogens, β-lactamases represent a critical resistance mechanism. In fact, these enzymes are localized in the periplasm, where they deactivate β-lactam antibiotics before they can interact with the penicillin-binding proteins (PBPs) in the cell wall.

A typical categorization of β-lactamases follows the Ambler classification, [255–257] which is divided in four classes depending on their amino acidic sequence, and on the catalytic residues in the active site; in particular classes A, C, and D present a serine residue that mediates the hydrolysis of the lactam rings, meanwhile class B is a metalloenzyme which requires a zinc ion for the catalytic activity.

5.1.1.2 - Target Site Modifications

ESKAPE pathogens also commonly exhibit AMR by altering the target sites of antibiotics, which diminishes their binding affinity or outright prevents their attachment. These adaptations involve:

(i) modifications to target enzymes, for example in methicillin-resistant *Staphylococcus aures*
(ii) changes to ribosomal binding sites, typical of *S. aureus* and *Enterococcus* species
(iii) alterations in cell wall precursor components, particularly critical among Gram-positive ESKAPE pathogens

5.1.1.3 - Reduced Antibiotic Penetration and Accumulation Mutations

These type of alterations result in the reduction, modulation, activity, or complete elimination of outer membrane protein channels (porins) and are also key factors in antimicrobial resistance among Gram-negative ESKAPE pathogens. Additionally, the role of bacterial efflux pumps, which actively eject antibiotics from the cell, is significantly implicated in contributing to AMR [258].

5.1.1.4 – A critical Survival Strategy: Biofilms

Beyond the traditional mechanisms of AMR, the role of biofilm formation in reducing the efficacy of antimicrobial treatments has gained recognition.

Biofilms, which are complex communities of microbes adhering to surfaces and enveloped in an extracellular matrix, exhibit significantly greater resistance to antimicrobial agents compared to their free-floating, planktonic counterparts [259,260].

Biofilms are particularly significant in persistent infections, including those caused by *P. aeruginosa* in cystic fibrosis patients' airways and device-related infections by *S. aureus* and *A. baumannii*. The diminished effectiveness of antibiotics against cells within biofilms is believed to result from a combination of factors. These include the specific species and genetic characteristics of the bacteria, the type of antimicrobial agent involved, the biofilm's stage of growth, and the surrounding environmental conditions.

5.1.2 Pseudomonas aeruginosa

P. aeruginosa, an opportunistic bacterium that is rod-shaped and Gram-negative, thrives in various environments [261,262]. Although it can cause opportunistic infections such as pneumonia, wound infections, and urinary tract infections in humans without cystic fibrosis (CF), infections of healthy lungs by this pathogen are not common. The bacterium is prevalent in water bodies and is often linked to severe respiratory conditions in individuals with compromised immune systems, and it accounts for around 10% of hospital-acquired infections. Moreover, there's a growing recognition of its role in infections acquired outside hospital settings.

The genetic versatility and adaptability of *P. aeruginosa*, can be attributed to an extensive set of regulatory genes that make up more than 8% of its 6-Mb genome, and that is crucial for its chronic persistence in hosts and resistance to antibiotics [263]. Additionally this pathogen naturally exhibits resistance to a broad spectrum of antimicrobial agents and has developed resistance to various antibiotic classes. As previously described, *P. aeruginosa* presents natural resistance to numerous antibiotics, stemming from a combination of inherent resistance mechanisms and

those acquired from other microorganisms. Numerous studies have analyzed the antibiotic resistance of *P. aeruginosa*, revealing alarming findings, reported in Figure 16 [264]. Specifically, collected data have indicated that the cephems class exhibit the highest levels of resistance, posing significant treatment challenges in CF patients. On the other hand, colistin, a member of the polymyxins class, has shown the lowest resistance rates among the antibiotic classes examined, suggesting that colistin may be a viable treatment option, while within the penicillin category, piperacillin and ticarcillin each exhibited resistance rates of 35%. However, from 1979 to 2021, resistance to both piperacillin and ticarcillin significantly declined, possibly reflecting their reduced usage in recent times. In contrast, within the cephems category, cefotaxime showed the highest resistance, highlighting the importance of cautious application of this antibiotic. Furthermore, resistance to cefotaxime has sharply increased over time, suggesting a need for restricting its use. Carbapenems, which include imipenem, meropenem, and doripenem, represent another class of antibiotics, among which doripenem exhibited the highest resistance rate of 39%, while meropenem showed the lowest at 29%. However, a detailed analysis over time revealed an increasing trend in meropenem resistance, potentially due to its more frequent use in recent years; thus, its application needs careful management. Within the aminoglycoside category, gentamicin faced the highest resistance (52%), whereas tobramycin had the lowest (24%). Additionally, a subgroup analysis by year highlighted a rising resistance trend in tobramycin, distinct from other aminoglycosides, suggesting a need to restrict its use in treating *P. aeruginosa* infections in CF, particularly in Italy where it has the highest resistance rate of 55%. Among the fluoroquinolones, ofloxacin exhibited the greatest resistance of 51%. In recent years, there has been a rise in the use of intravenous colistin for treating *P. aeruginosa* infections in CF patients, and although *P. aeruginosa* shows a high susceptibility to colistin, hesitancy exists regarding its use due to the associated risks of neurotoxicity and nephrotoxicity in treating respiratory infections caused by it in CF patients [265–267]. The most relevant mechanisms of resistance of *P. aeruginosa*, include: heightened activity of efflux pumps, reduced permeability of the outer membrane, and acquisition or mutation of resistance genes. These genes produce

proteins that regulate the passive movement of antibiotics through the outer membrane. Similar to *A. baumannii*, *P. aeruginosa* has been found to possess all four major classes of β-lactamases (Classes A, B, C, and D). Additionally, *P. aeruginosa* can develop resistance through mutations that result in the overproduction of AmpC β-lactamases. Even so ceftazidime and cefepime, which are part of the third and fourth generations of cephalosporins respectively, are broad-spectrum antibiotics still effective against *P. aeruginosa.* When talking about aminoglycosides, also in this case resistance is facilitated by the presence of plasmid-mediated aminoglycoside-modifying enzymes, which reduce the drugs' ability to bind effectively to bacterial cells. For treating MDR *P. aeruginosa*, a regimen often includes colistin paired with another active agent, such as imipenem, piperacillin, aztreonam, ceftazidime, or ciprofloxacin. Moreover, combinations of fosfomycin with aminoglycosides, cephalosporins, or penicillins have been effective in addressing drug resistance in P*. aeruginosa* [8,268].

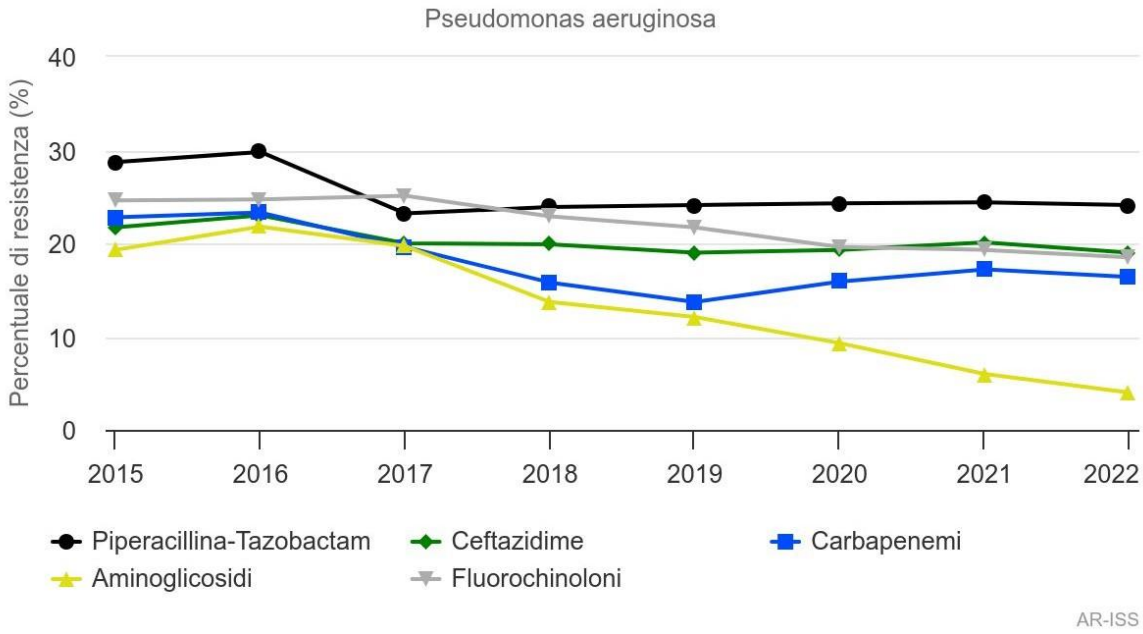

Figure 16: Annual Percentage of antibiotic resistance of Pseudomonas aeruginosa [269]

5.1.3 Cystic fibrosis

Cystic fibrosis (CF) represents the predominant autosomal recessive genetic condition among Caucasian populations, with *P. aeruginosa* being the leading cause

of chronic infections in individuals with CF [270–272]. The disease stems from mutations in the CF transmembrane conductance regulator (CFTR) gene, which plays a critical role in the transport of chloride ions across the apical surfaces of epithelial cells. Thus, a deficiency in CFTR disrupts normal chloride ion transport and enhances sodium absorption through the epithelial sodium channel, causing the airway surface liquid to become dehydrated. This results in thick, sticky mucopurulent secretions that are challenging to expel. The consequent dehydration of the airway surface liquid (ASL) triggers several detrimental changes in the airways, such as reduced effectiveness of mucociliary clearance, decreased pH, and weakened antimicrobial defense and immune responses. The impaired movement of cilia leads to an inability to expel mucus from the lungs effectively. Concurrently, the excessive production of alginate promotes the development of dense biofilms, marking the transition of *P. aeruginosa* from a non-mucoid to a mucoid, biofilm-forming state. This transformation plays a crucial role in enabling *P. aeruginosa* to establish chronic infections. The acidic conditions prevalent in the airways of CF patients causes incorrect folding of the mucins' carbohydrate side chains and as a consequence their capacity to adhere to foreign particles is undermined, instead their affinity for the cell-bound mucins MUC1 and MUC4 increases. Such binding effectively anchors the mucus layer to the epithelial surface, thereby obstructing the process of mucociliary clearance [273,274].

The reduced pH levels are linked to changes in O-glycosylation and sulfation of airway mucins, a consequence of alkalized cellular compartments in CF. This alteration in sputum O-glycosylation enhances the capacity of bacterial pathogens to adhere to and colonize the respiratory tract of the host. *P. aeruginosa*, in particular, has a tendency to bind to a sialoglycoprotein, suggesting that CFTR dysfunction may lead to an increased colonization of the CF airways by this pathogen. The acidic conditions also cause a delay in the apoptosis of neutrophils and suppress the production of IFN-γ by T helper 1 (Th1) cells. The recruitment of neutrophils decreases the oxygen levels in airway mucus due to their high consumption of O_2. This consumption is part of the process for generating superoxide and nitric oxide by polymorphonuclear leukocytes.

5.2 Biofilm

The process of pathogenesis is intricate and operates on multiple levels, incorporating diverse factors that culminate in a successful infection of the host. Despite variations in the strategies and components utilized by pathogens, a consistent pattern emerges. In fact, bacterial entities collaborate to establish their presence within the host by forming robust adhesion bonds both among themselves and with the host tissues [275].

The process of biofilm development can be broken down into four key phases (Figure 17) undertaken by the bacterial community: 1) initial attachment, 2) microcolony establishment, 3) biofilm expansion and maturation, and 4) detachment and dispersal [276].

5.2.1 – Adehesion

The initial and critical stage in establishing a durable biofilm is the adherence to a surface. Targeting this early phase, which is influenced by a range of factors such as surface charge, roughness, hydrophobicity, stiffness, topography, and bacterial movement, with a variety of physical and chemical strategies, has been demonstrated to be effective [276].

5.2.2 – Microcolony formation

After adhering to the surface, bacterial cells multiply and organize into structured micro-colonies, enveloped in an extracellular matrix composed of polysaccharides, proteins, lipids, and nucleic acids. This matrix plays a crucial role in shaping the biofilm's architecture and the microenvironment surrounding the bacterial cells, influencing factors like hydrophobicity, mechanical strength, electrical charge, porosity, moisture levels, and the availability of vital nutrients. Notably, this stage also sees the formation of gradients of oxygen, hydrogen, and nutrients, which establish varied microenvironmental conditions within the biofilm [276].

5.2.3 – Biofilm maturation and dispersal

The maturation of a biofilm is initiated by the build-up of extracellular polymeric substances and extracellular DNA, alongside the development of channels for nutrient exchange and waste removal, changes in ionic concentrations, and, critically, the activation of quorum-sensing signals. During this phase, it's observed that genes linked to the development of flagella are suppressed, which aligns with the necessity for creating a stable biofilm structure. Specific components of the extracellular polymeric substances (EPS), such as Psl, Pel (which are polysaccharides involved in the formation and stability, but also structural integrity of the biofilm matrix), alginate, eDNA, and various protein elements, are known to fulfill distinct functions in the formation and maturation of Pseudomonas biofilms [276].

5.2.4 – Colonization and invasion

To successfully colonize, pathogens need to navigate the constantly changing physiological conditions of the host environment, including temperature, pH, and the presence of various substances. ESKAPE pathogens are known to infect the gut and lead to conditions such as bacteremia, oral infections, wound infections, and urinary tract infections. As pathogens begin to proliferate at the host site, they initiate the production of virulence factors, particularly toxins and enzymes, aimed at neutralizing the host's immune defenses and causing damage to the host. The release of extracellular enzymes and toxins to harm host tissue is a common strategy to facilitate this invasion process. Subsequently, evading the host's immune response becomes a critical phase in sustaining the infection [276].

Various mechanisms, such as different capsular serotypes, peptidoglycan, teichoic acid, and protein A, enable bacteria to evade the host's humoral and cellular innate defenses by deceiving and suppressing them. Alkaline protease, as encoded by the aprA gene, and elastase, encoded by the lasB gene, contribute to immune evasion by cleaving immunoglobulins, inactivating components of the complement system, and neutralizing several cytokines, including TNF, IFN, IL-1, and IL-6. Additionally, bacteria enhance their survival and virulence capabilities by engaging in horizontal

gene transfer. This ability has strengthened bacteria that were not initially endowed with certain virulence factors, presenting a formidable challenge to the opposing forces. In addition to this, bacterial colonies perpetually seek necessary resources, among which free iron is crucial. Iron is a vital mineral required by bacterial pathogens for various functions, including respiration and metabolism [277,278]. The demand for iron by bacteria is significant, making its acquisition a critical step for their survival within the host, but it also serves as a cofactor for numerous enzymatic activities in the human body, being integral to metalloprotein heme complexes like hemoglobin, myoglobin, catalases, cytochromes, and in the formation of Fe-S clusters in aconitase. During periods of iron scarcity, immune cells, including macrophages, act as iron transporters, helping to maintain iron homeostasis. Consequently, there exists a vigorous competition for iron between pathogens and their host, with bacteria evolving a variety of strategies to extract iron from their surroundings.

Key elements such as the bacterial capsule, aggregation substances, pili, and fimbriae have been identified as contributing factors to biofilm formation. Specifically, the capsule plays a crucial role in protecting bacteria from adverse conditions such as varying pH levels, temperature fluctuations, ultraviolet radiation, antibiotics, and nutrient scarcity. It serves as a physical barrier and creates a cohesive microenvironment, thus supporting the bacteria's survival and metabolic activity. It's important to highlight that the successful initiation of an infection usually involves the synergistic action of multiple virulence factors.

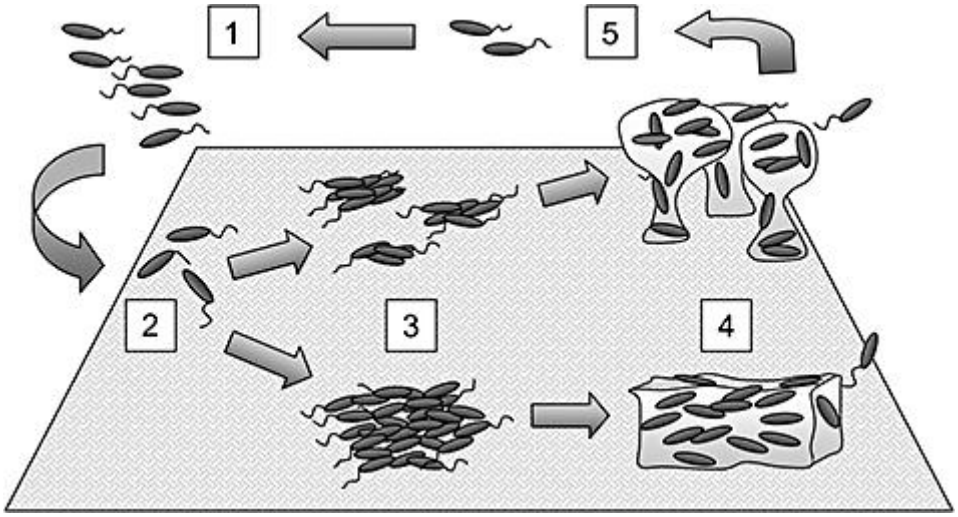

Figure 17: Biofilm formation: Planktonic cells (stage 1). Attachment onto a solid surface (stage 2). Microcolonies formation under QS-controlled rhamnolipid production (stage 3). Developing of flat uniform biofilm (stage 4). Cells detachment and disperse from the biofilm resuming the planktonic mode of growth (stage 5) [279]

5.2.5 Biofilm modulation and the quorum sensing system

The regulation and preservation of the established biofilm are governed by the quorum sensing system, a sophisticated mechanism that allows bacterial communities to communicate and coordinate their actions for an effective colonization of the host. In *P. aeruginosa*, various quorum-sensing systems have been identified, such as the LasI–LasR system, RhlI–RhlR system, Pseudomonas Quinolone System, and the IQS system.

Specifically, the LasI–LasR system operates through the activation of LasR–OdDHL and RhlR–BHL complexes, which enhance their own expression by binding directly to the promoter regions of the las/rhl genes, and play a crucial role in regulating biofilm formation, exotoxins production, and the hydrogen cyanide synthesis [280]. This system is also known to affect the expression of degradative enzymes, including elastase, LasA protease, and alkaline protease.

In contrast, the RhlI–RhlR system as well as the IQS system are linked to the production of enzymes and compounds such as rhamnolipids, PCN, and elastase, playing roles also in the creation of hydrogen cyanide and biofilm development.

Lastly, the Pseudomonas Quinolone System specifically influences the expression of PCN and rhamnolipids, showcasing the diverse regulatory functions of different quorum-sensing systems in *P. aeruginosa* [280,281].

Beyond its role in promoting bacterial virulence and biofilm development, the action of quorum-sensing molecules extends also to interactions between the host and the pathogen as well.

A recent study highlighted the significant role of 2-aminoacetophenone in disrupting the host's autophagic and lipid biosynthesis pathways in *P. aeruginosa* infections. The increased survival and persistence of *P. aeruginosa* have been linked to the downregulation of genes involved in autophagy (such as Unc-51-like autophagy activating kinase 1 (ULK1) and Beclin1) and a key gene in lipid synthesis [stearoyl-CoA desaturase 1 (Scd1)]. This finding underscores the complex strategies employed by *P. aeruginosa* to manipulate host cellular processes to its advantage [282].

Another study demonstrated that inhibiting the LasR system in *P. aeruginosa* significantly reduces the bacterium's capacity to form biofilms and produce PCN, rhamnolipids, and elastin. Further investigations through gene knockout experiments showed that LasI mutants exhibited a marked decrease in biofilm formation, adhesion to surfaces, and swarming motility. These findings highlight the critical role of the LasR quorum-sensing system in regulating the pathogenic behaviors of *P. aeruginosa* [283] also in CF affected patients [284].

Quorum sensing plays a pivotal role in the regulation of virulence factors, making it a crucial target in combating the virulent characteristics of ESKAPE pathogens. Quorum Sensing inhibitors have been effective in disrupting the bacterial communication network, effectively blocking their ability to communicate. This interference with bacterial communication has been beneficial in weakening the collective strength of bacterial communities, impairing their capacity to form biofilms, and to express virulence factors associated with infection. This strategy has enhanced the effectiveness of antibiotics and immune cells in dealing with individual bacterial agents. It's noteworthy that while most interventions apply selective

pressure on the bacterial population, potentially leading to resistance, Quorum Sensing Inhibitors do not exert this kind of selective pressure. A competition study by Gerdt et al. highlighted that the disruption of quorum-sensing signals in QSI-sensitive bacteria, coupled with their mechanisms for outcompeting the rare QSI-resistant strains, naturally limits the proliferation of resistance against QSIs, particularly those targeting the quorum sensing receptor functions. This indicates a promising avenue for controlling bacterial virulence without accelerating the development of antibiotic resistance [276]. In fact, transitioning into a biofilm growth mode prompts significant phenotypic transformations in the sessile bacteria, including enhanced gene expression related to efflux pumps, cell wall components, and peptidoglycan production [285].

Among the virulence factors which promote and modulate the formation of biofilm noteworthy is PCN, this is a redox-active phenazine compound secreted by *P. aeruginosa* through the Type II secretion system is recognized for imparting a blue-greenish hue to the colonies of this bacterium in culture. This secondary metabolite is closely linked to the severity of disease and the deterioration of lung function, attributed to its capacity to generate free radicals and incite pro-inflammatory responses. By increasing the levels of intracellular ROS and hydrogen peroxide, PCN induces oxidative stress, which can damage key cellular components, including those involved in the cell cycle, various enzymes, and DNA, ultimately leading to cell lysis. Moreover, it impedes ciiary motion, disrupts epithelial integrity, and amplifies mucus secretion within the respiratory tract, all of which are factors that facilitate lung colonization. Furthermore, this phenazine enhances the production of IL-8 by alveolar macrophages, resulting in an increased influx of neutrophils, thereby contributing to the inflammatory response in the lungs.

Other important virulence factors comprehend pyoverdine and pyochelin which are produced to satisfy the bacterial iron needs. These are siderophores, which are specialized molecules designed to sequester iron from the environment. In addition to producing its own siderophores, the bacterium is capable of taking up xenosiderophores (siderophores produced by other organisms), and absorbing

heme molecules directly from the host's hemoproteins through two distinct systems, Has and Phu. Iron (Fe^{3+}) which is crucial for the growth and virulence of bacteria, becomes scarce in the host environment due to its low solubility and sequestration by host iron-binding proteins like transferrin and lactoferrin. Pyochelin (PCH) a siderophore with a salicylate base, exhibits a lower affinity for iron compared to pyoverdine (PVD), which has a peptide-based structure and is recognized as the primary siderophore. Given that producing PVD requires significant energy, *Pseudomonas aeruginosa* typically opts to synthesize PCH first. Only when the iron availability drops significantly does the bacterium switch to producing PVD, reflecting a strategic adaptation to efficiently manage its energy resources while ensuring access to essential iron nutrients. [278].

P. aeruginosa synthesizes a variety of alkyl-4(1H)-quinolones, among which 2-heptyl-hydroxy-1H-quinolin-4-one (PQS) (**117**, Figure 18) and its precursor, 2-heptyl-4(1H)-quinolone (HHQ) (**116**, Figure 18), are the most prominently associated with QS, which have been the starting point for the design of the modulators for this project. The synthesis of these compounds is carried out by enzymes encoded by the pqsABCDE, phnAB, and pqsH gene clusters. Both PQS and HHQ interact with their specific regulator protein, PqsR, playing crucial roles in the bacterial communication and virulence regulatory network. The Pqs system is also crucial for the release of extracellular DNA important for the formation of stable and mature biofilms, highlighting its significance in the pathogenicity and persistence of *P. aeruginosa*.

It has been demonstrated that the Minimum Inhibitory Concentrations of various antibiotics can increase by 10 to 1000 times when bacteria are organized within biofilms, and this resistance enhancement is of significant concern, particularly in the context of MDR *P. aeruginosa*. In fact as previously reported research findings indicate that strains of *P. aeruginosa* producing biofilms have a notably lower susceptibility to antibiotics, in contrast, non-biofilm-producing strains exhibited higher sensitivity rates. This correlation between biofilm production and increased antimicrobial resistance is not exclusive to *P. aeruginosa* but has also been observed

in other bacterial species, highlighting the broad challenge biofilms pose to treating bacterial infections effectively [285].

5.3 AIM OF THIS STUDY – Design and synthesis of modulators of virulence factors within the biofilm of PA

The focus of this project was to counteract the pathogenicity and resistance of *P. aeruginosa* by modulating key proteins involved in its quorum sensing system, thus allowing the modulation of its virulence factors. In particular, as previously mentioned by targeting the QS system, we can disrupt the bacterial community's ability to regulate the expression of genes involved in pathogenicity and biofilm formation. This disruption reduces the bacteria's virulence and its ability to form biofilms, thereby making it more susceptible to antibiotic treatment and clearance by the host's immune system. Given that *P. aeruginosa* infections, particularly in the lungs of CF patients, can be extremely difficult to treat due to biofilm formation and antibiotic resistance, targeting QS represents a novel and potentially effective approach to control these infections. As aforementioned, the QS system is regulated by various proteins, among which we can find the PqsR protein that is auto-regulated by internal alkyl quinolone signals as HHQ and PQS (**116, 117** Figure 18). Previous studies have shown the bioisosteric potential of the quinazolin-4(3H)-one-core [286–288] for the development of Pqs system modulators (**118-120** Figure 18), which has been further exploited in this project. In particular, the quinazolinone core has been decorated in positions $R_{1,2}$ with different halogen atoms (-Cl, -Br, -F), the linker unit has been exploited with rigid or flexible moieties through the design of aromatic hydrazones or N-benzyl substituted quinazolinones. Finally, various aromatic and heteroaromatic residues have been explored (general scaffolds of the novel quinazolinone derivatives **I, II** Figure 18).

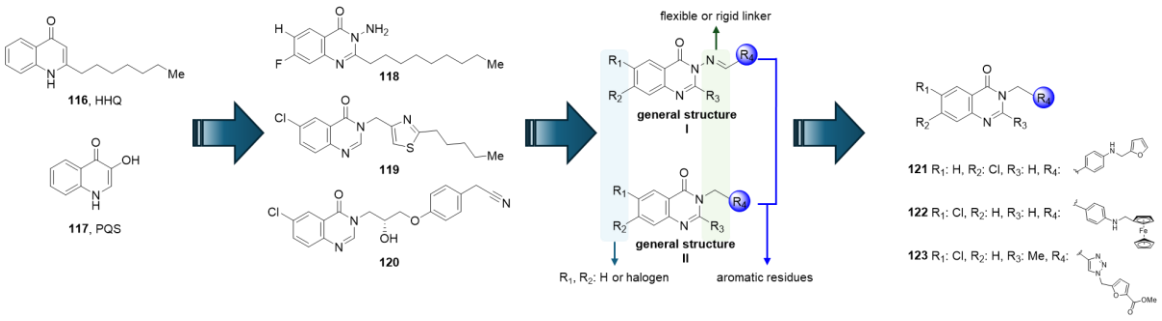

*Figure 18: HHQ and PQS quinolone signals **116, 117**, known PQS system modulators **118-120**, design of new modulators **121, 122, 123**.*

5.3.1 Synthesis of biofilm modulators

The synthesis of quinazolin-4(3H)-one compounds **121**, **122** and **123** was realized starting from the corresponding halo-anthranilic acids **124a,b** as reported in Scheme 18. For the synthesis of the final compounds **121** and **122**, the anthranilic acids were first converted into the lactams **125a,b**, which were alkylated in presence of 4-nitrobenzyl chloride to obtain **126a,b**; which in turn were reduced to anilines **127a,b**. Finally, through reductive amination conditions, anilines **128a,b** were converted into the final compounds **121** and **122** by reaction with the corresponding aldehydes furfural and ferrocene-2-carboxaldehyde, respectively. For the synthesis of lactone **130**, the anthranilic acid derivative were heated under reflux in acetic anhydride, afterward the quinazolin-4(3H)-one intermediate **130** was converted into the corresponding lactam **131** after heating in the presence of ammonium hydroxide in ethanol. The intermediate **131** was then treated with propargyl chloride to obtain the (prop-2-yn-1-yl)quinazolin-4(3H)-one **132**, which was finally reacted with freshly prepared methyl 5-(azidomethyl)furan-2-carboxylate to obtain the title compound **123**.

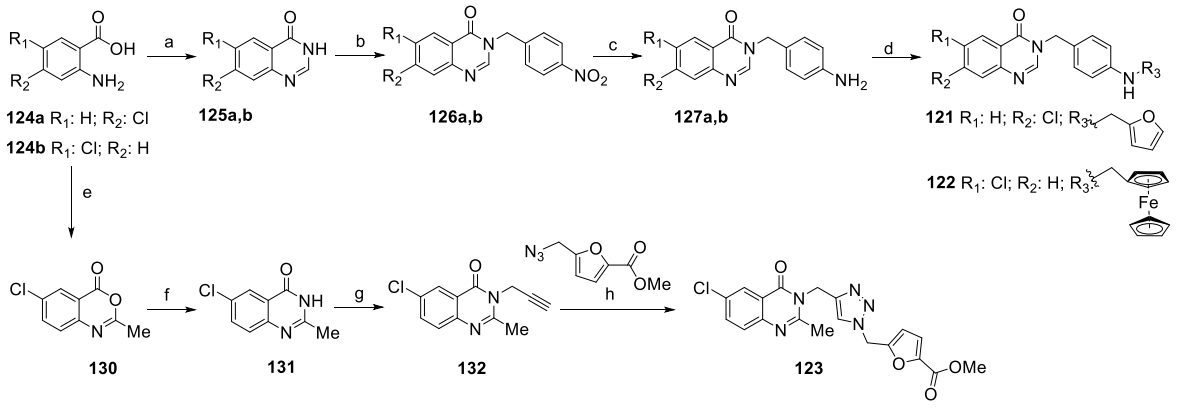

*Scheme 18: Synthesis of compounds **121,122** and **123**. Reagents and conditions: a) formamide, 150 °C, 20 h; b) 4-nitrobenzyl chloride, K_2CO_3, NaI, acetone, 50 °C, 24 h; c) Fe powder, NH_4Cl s.s., EtOH, 70 °C, 2 h; d) i-furfural for derivative **121**, ferrocene-2-carboxaldehyde for derivative **122**, CH_3COOH, MeOH, 50 °C, 12 h, ii-$NaBH_3CN$, 25 °C, 2 h, e) $(CH_3CO)_2O$, 140 °C, 2 h; f) NH_4OH (33% water solution), EtOH, 80 °C, 15 h; g) propargyl chloride, KtBuO, dry DMF, 25 °C, 24 h; h) methyl 5-(azidomethyl)furan-2-carboxylate, sodium ascorbate, CuSO4, t-BuOH/H_2O (1:1), 25 °C, 72 h.*

5.3.2 Biological evaluation

Among the three synthesized compounds two have already been evaluated from a biological point of view and results have been recently published in collaboration with the research group of Professor Bonaventura [201]. The evaluation has been conducted in two different strains of cystic fibroses, the acute strain BJ3525 and the chronic strain RP73 which mimics the chronic form of CF. For clarity the results reported in Figures 20-23 show the results achieved as a whole, in order to better elucidate the meaningfulness of the data. Compounds **121** and **122** have been highlighted, and are reported in the charts as **11b** and **11d**, respectively. The assays revealed that, while biofilm reduction was not significantly achieved (Figure 20) with the two tested compounds that have been reported in this thesis, though there was a notable impact on the production of PCN and PVD for both of the herein synthesized compounds, among the others (Figures 21 and 22). The production of these pigments were markedly suppressed by compound **11b** (**121**) displaying an almost complete inhibition of PCN formation in the RP73 strain. Additionally, compound **11b** (**121**) significantly reduced PVD production in the same strain, showcasing its potential as an effective anti-virulence agent. Finally, in Figure 23 the cytotoxic potential of each compounds has been reported, in particular, MTS tetrazolium-based colorimetric assay has reported a non-toxic effect for all the compounds of the series, rather than compounds **4** and **11d** which resulted toxic reducing viability of 92.3% and 16.1% respectively, when compare to the untreated control cells.

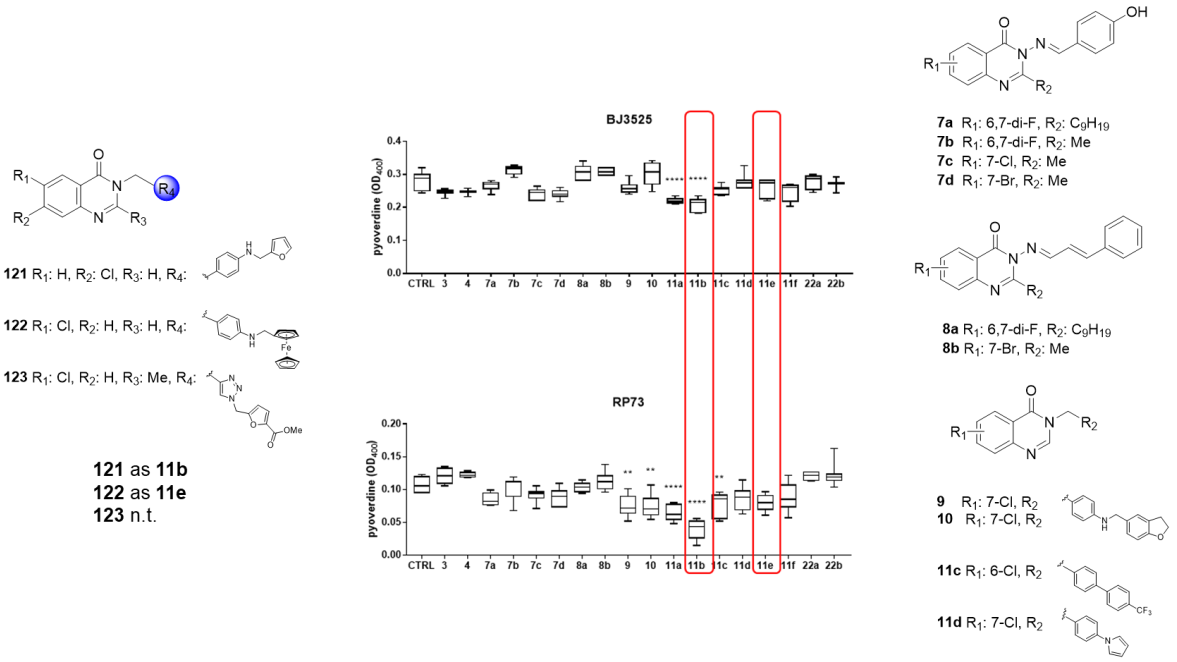

*Figure 19: In vitro activity compounds **3**, **4**, **7a-d**, **8a-b**, **9**, **10**, **11a-f** (**11b** as **121** and **11e** as **122** of this thesis), 22a-b against biofilm formation by RP73 and BJ3525 PA strains. All molecules were tested at 50 µM under «CF-like» conditions (ASM, 5% CO_2, pH 6.8). Results are shown as box and whisker: the ends of the whiskers represent the minima and the maxima of all the data; the box always extends from the 5th to 95th percentiles, while the line in the middle of the box is plotted at the median. Statistical significance at ordinary one-way ANOVA + Holm-Sidak's multiple comparisons test: * p<0.05, ** p<0.01, *** p<0.001, and **** p<0.0001 compared to unexposed sample (control, CTRL).*

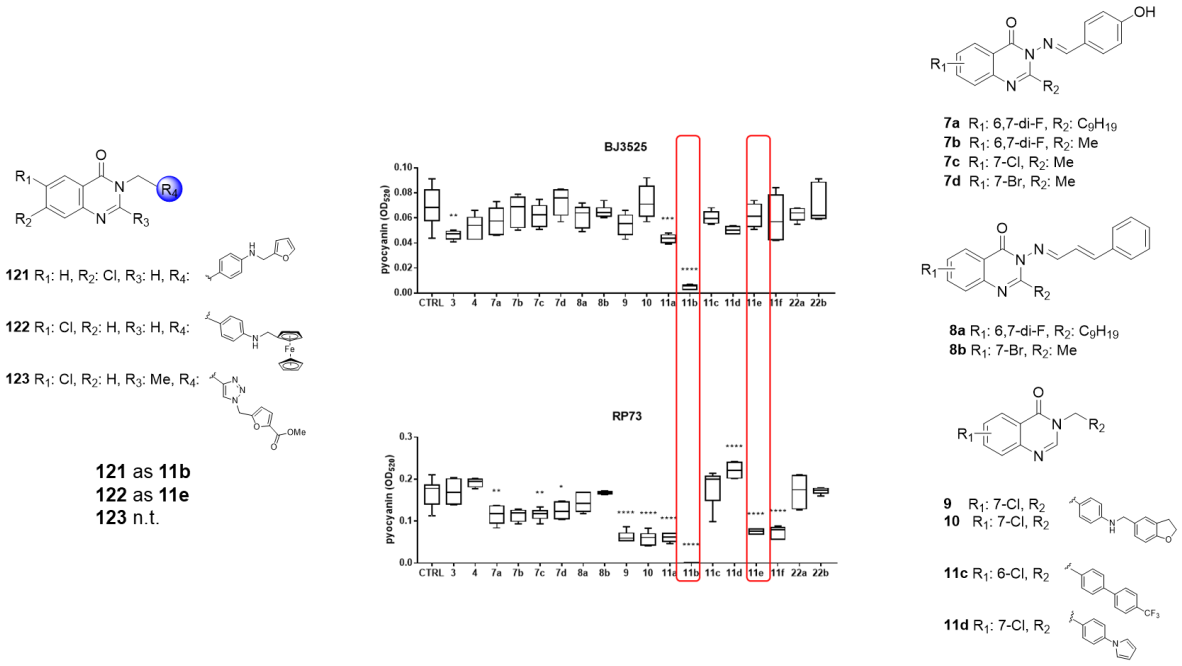

Figure 20: In vitro effect of compounds ***3***, ***4***, ***7a-d***, ***8a-b***, ***9***, ***10***, ***11a-f*** *(****11b*** *as* ***121*** *and* ***11e*** *as* ***122*** *of this thesis), 22a-b against PCN production by BJ3525 and RP73 PA strains. All compounds were tested at 50 µM in LB medium under an aerobic atmosphere. Results are shown as box and whisker: the ends of the whiskers represent the minima and the maxima of all the data; the box always extends from the 5th to 95th percentiles, while the line in the middle of the box is plotted at the median. Statistical significance at ordinary one-way ANOVA + Tukey's multiple comparisons test: * p<0.05, ** p<0.01, *** p<0.001, and **** p<0.0001 compared to unexposed sample (control, CTRL).*

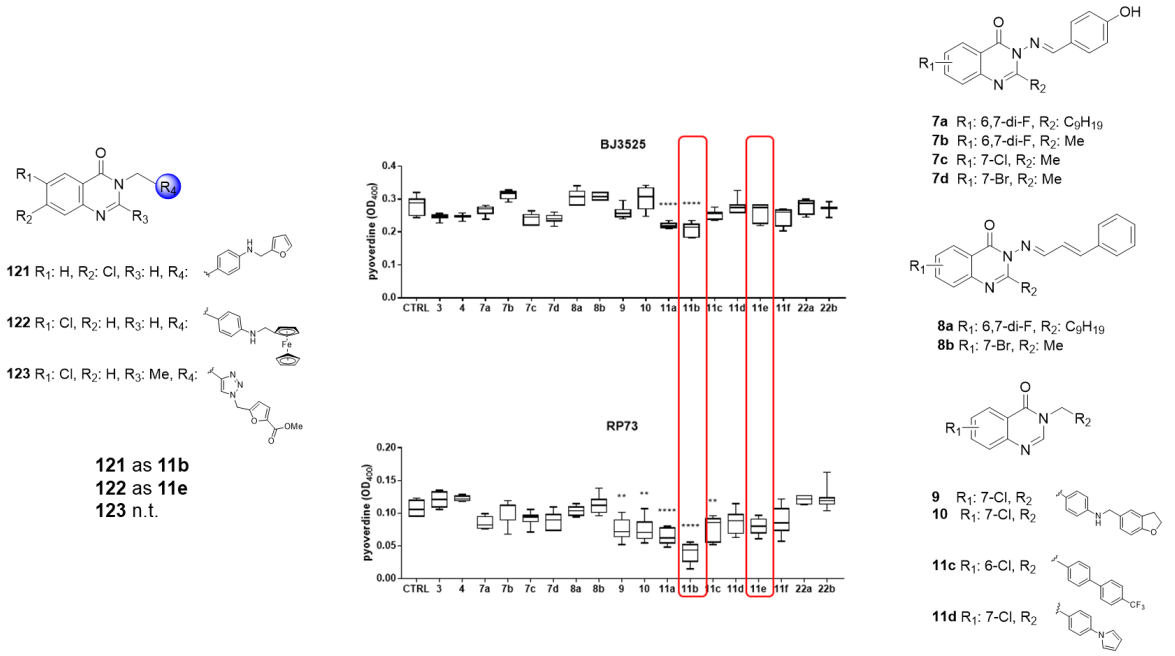

*Figure 21: In vitro effect of compounds **3**, **4**, **7a-d**, **8a-b**, **9**, **10**, **11a-f** (**11b** as **121** and **11e** as **122** of this thesis), 22a-b against PVD production by BJ3525 and RP73 PA strains. All compounds were tested at 50 µM in LB medium under an aerobic atmosphere. Results are shown as box and whisker: the ends of the whiskers represent the minima and the maxima of all the data; the box always extends from the 5th to 95th percentiles, while the line in the middle of the box is plotted at the median. Statistical significance at ordinary one-way ANOVA + Tukey's multiple comparisons test: ** p<0.01, and **** p<0.0001 compared to unexposed sample (control, CTRL)*

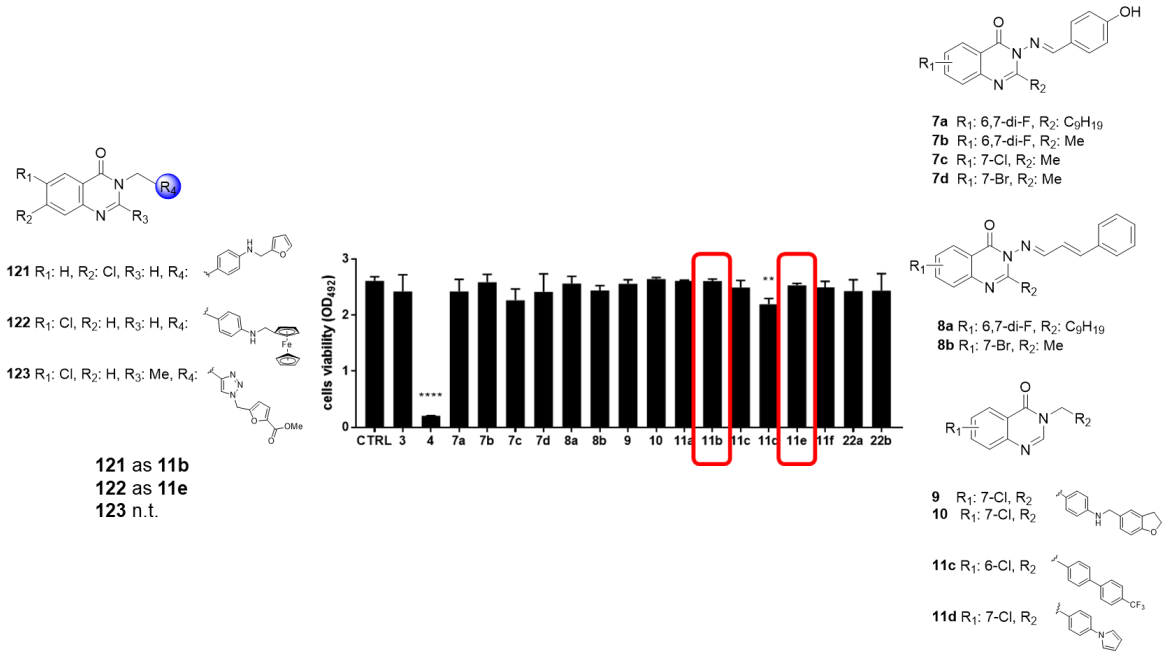

*Figure 22: In vitro cytotoxicity of **3**, **4**, **7a-d**, **8a-b**, **9**, **10**, **11a-f** (**11b** as **121** and **11e** as **122** of this thesis), 22a-b compounds against IB3-1 cells. IB3-1 monolayers were exposed for 24 h to each compound at 50 μM. The cell viability was then measured by an MTS tetrazolium-based colorimetric assay and expressed as mean + SD absorbance at 492 nm. Statistical significance at one-way ANOVA + Holm–Sidak's multiple comparisons post-test: ** p<0.01, and **** p<0.0001 vs. untreated cells (control, CTRL).*

CHAPTER 6

Conclusions

CHAPTER 6 – CONCLUSIONS

Infective agents are considered the culprits of most of the pathologies affecting patients worldwide, with a high morbidity and mortality, and a global burden that affects many aspects of the economic and social sphere [250,251,289]. This reality has emerged with even more strength in the last years due to the last SARS-CoV-2 pandemic, but also the outburst of MPXV and the high bacterial resistance that has emerged in hospital settings have highlighted the urgency for the development of new anti-microbials.

The aim of this thesis has been the investigation of different ways to fight infective agents.

In particular the PhD project that has been accomplished, during three years, has mainly focused on the development of inhibitors against the main protease of SARS-CoV-2, in this context a library of peptide based inhibitors has been designed and synthesized. This library of compounds has the aim to accomplish a SAR study that could allow the further development of new antiviral agents with the potential to inhibit the replication not only of SARS-CoV-2 but also of other coronaviruses that have the potential to spillover, or similar viral entities such as enteroviruses. In this sense 25 new M^{pro} inhibitors have been designed, synthesized and their biological potential has been assessed. In particular, these compounds have been initially evaluated for their inhibitory activity against the main protease of SARS-CoV-2 giving promising outputs. Successively the most active compounds have been tested in infected VERO E6 cell line, some of which have confirmed the positive results achieved on isolate enzymes, highlighting the potential of these pharmacological tools, which could pave the way for new pan-antiviral agents.

Future studies include the synthetic exploration of a difluorostatone warhead in place of those reported in this thesis. As demonstrated in our recent compoutational study, compounds incorporating this bifunctional electrophilic moiety could engage with residues at both the prime and nonprime subsites of the enzyme [290]. Synthetic studies are currently ongoing in our laboratories.

Given the natural evolution in drug discovery, in obtaining compounds synthetically accessible with simplified scaffolds and improved drug-like properties, the next step has been the study of a small library of fragments, in order to further expand the knowledge of the active site pocket and explore new accessible scaffolds for the design of small molecule inhibitors against the main protease of SARS-CoV-2. The development of this limited library of compounds is still in progress as well as the biological evaluation of the first compounds that have been synthesized. Hopefully this study could allow the development of new small molecules with improved pharmacokinetic and pharmacodynamic properties addressing the need for new cores and small molecules achievable in the context of pharmaceutical companies.

In line with the expertise of the research group in the development of HDAC inhibitors to fight rare diseases and infective agents, the second focus that has been pursued during this PhD project has been the repurposing of in house HDACi with a preventive effect against SARS-CoV-2 infection. In particular, this project is based on the knowledge, that has been gained after the emergence of the last coronavirus outbreaks, of the entry mechanism of SARS-CoV-2 into the host cells, which is achieved through the binding of the viral particles to the host receptor ACE2. Studies, in fact, have demonstrated the mechanism and interplay between the spike protein of coronaviruses and ACE2 receptor. In addition to this, many papers have proved the epigenetic modulation in the expression of ACE2 receptor, thus pinpointing the opportunity of modulating the entry of SARS-CoV-2 inside the host cells by HDACis, hence preventing the infection onset. In this context two selective HDACi developed by my research group, a selective HDAC1 inhibitor and a selective HDAC6 inhibitor have been identified for their biological evaluation in terms of prophylactic activity of these compounds towards ACE2-mediated entry coronaviruses. The compounds have thus been synthesized and the biological evaluation is ongoing. This project could open new prospects for the treatment of coronaviruses infections, allowing a preventive treatment in case of close contacts in the context of future epidemics or spillovers.

Still in terms of antiviral agents a further study that has been carried out during this PhD project has been the development of monkeypox VP37 inhibitors, given the urgency that has aroused in the last years of new cases worldwide that have assumed the notion of epidemic with potential to evolve in pandemic as declared by the authorities. In particular, taking inspiration from the approved anti-viral agent tecovirimat, which is an inhibitor of the VP37 protein of monkeypox, a SAR study has been carried out, exploring different moieties for the cap group that interacts with the external surface of the active site and of the linker unit of these compounds. This library of compounds has thus been designed and synthesized, though further exploration of these portions is still ongoing. The compounds that have been synthesized so far have been evaluated from a biological point of view, for their inhibitory potency in infected cells, affording promising results, and thus suggesting a path towards the design of more potent anti-viral agents against different orthopoxviruses.

Finally, among the infective agents with high morbidity and mortality note to mention surely are the *Pseudomonas aeruginosa* acute and chronic infections in patients affected by cystic fibrosis. This genetic disorder is the ideal condition for the biofilm formation and colonization of sensitive and resistant strains of Pa, which pose life-threatening risks in immunocompromised and hospitalized patients. In addition to this, it is important to mention the high rate of resistance and mutations that we commonly encounter in these patients, rendering even more difficult the eradication of this pathogen, not to mention the abuse of antibiotics that has been carried out in the last years, vanishing their inhibitory potency. New therapeutic treatments have been explored to face the insurgence of resistant strains and gain back the efficacy of antibiotics, noteworthy are the biofilm modulators. In this context many biofilm modulators have been designed taking inspiration from the structures of the quorum sensing signals (HHQ and PQS), allowing to design potent modulators of the quorum sensing system, thus allowing the modulation of biofilm formation but also of important virulence factors such as PCN and PVD. This project, which has been recently published [201], has involved the synthesis of a new family of modulators of the virulence factors within the biofilm of Pa have been developed and their biological

evaluation has been carried out, highlighting the potential of this strategy. In particular, the evaluation of the inhibition of the biofilm, and the modulation of PVD and PCN has been assessed with promising results, confirming the efficacy of these compounds, and opening the door for further exploration of this interesting strategy.

CHAPTER 7

Experimental section

CHAPTER 7 – EXPERIMENTAL SECTION

7.1- EXPERIMENTAL M^{PRO} SARS-CoV-2 Inhibitors

7.1.1 General

All the reagents used were commercially available and purchased from Merck (Milan, Italy). Reaction progress was monitored by TLC using silica gel 60 F254 (0.040−0.063 mm) with detection by UV (254 nm). ^{1}H NMR and ^{13}C NMR spectra were recorded on a Varian 300 MHz spectrometer or Bruker 400 MHz spectrometer using the residual signal of the deuterated solvent as the internal standard. Splitting patterns are described as singlet (s), doublet (d), triplet (t), quartet (q); the value of chemical shifts (δ) is given in ppm, and coupling constants (*J*) are given in hertz (Hz). Electrospray ionization mass spectrometry (ESI-MS) spectra were performed by an Agilent 1100 series LC/MSD spectrometer. Yields refer to purified products and are not optimized. All the target compounds that have been analyzed for purity requirements and all compounds present purity higher than 95%.

7.1.2 – Optimized synthesis of common intermediate (19)

Dimethyl (*tert*-butoxycarbonyl)-*L*-glutamate (17)

To a suspension of *L*-glutamic acid **16** (2000 mg, 1 eq) in MeOH (54 mL) cooled at 0 °C, trimethylsilyl chloride (6501 mg, 4,4 eq) has been added dropwise. The reaction mixture was allowed to reach room temperature and stirred for 12 h, then TEA (8938 mg, 6,5 eq) and di-*tert*-butyl dicarbonate (3263 mg, 1,1 eq) in MeOH (4 mL) were slowly added. After 1 h, the mixture was concentrated and the solid was filtered on paper filter and washed with Et_2O (3 x 10 mL), the filtrate was concentrated under reduced pressure and purified by column cromatography (petroleum ether/ethyl acetate (PetEt/EtOAc) 3:1) to furnish dimethyl (*tert*-butoxycarbonyl)-*L*-glutamate as a pale yellow oil (3635 mg, 98% yield).
Spectroscopic data are in agreement with those reported in literature [143].

Dimethyl (2*S*,4*R*)-2-((*tert*-butoxycarbonyl)amino)-4-(cyanomethyl)pentanedioate (18)

In a two-necked flask and under N_2 atmosphere lithium bis(trimethylsilyl)amide (1M in THF) (7,98 mmol, 2,2 eq) was added in dry THF (4 mL), the solution was cooled at -78 °C, then a solution of **17** in THF (4 mL) was slowly added and the mixture was stirred for 1 h at -78 °C. Afterwards, $BrCH_2CN$ (435,7 mg, 1 eq) was slowly dropped and the mixture was stirred for additional 2 h at the same temperature. A solution of pre-cooled MeOH (8 mL) was then slowly added and the mixture was stirred for 30 minutes, then a mixture of AcOH/THF (1:6, 7 mL) precooled a -78 °C was added to the reaction and the mixture was additionally stirred for 30 minutes. After this time the reaction was allowed to reach 20 °C and poured in brine (20 mL). The organic phase was separated and the aqueous phase was additionally extracted with Et_2O (3 x 10 mL), then the combined organic phase was dried over anhydrous Na_2SO_4, filtered and concentrated under vacuum. The crude product was purified by column chromatography (PetEt/EtOAc 5:1) affording the target compound as a colorless oil (1014 mg, 89%).
Spectroscopic data are in agreement with those reported in literature [143].

Methyl (*S*)-2-((*tert*-butoxycarbonyl)amino)-3-((*S*)-2-oxopyrrolidin-3-yl)propanoate (19)

Particular attention needs to be given to this procedure, since Raney-Ni is a pyrophoric reagent, and needs to be handled carefully.
Raney-Ni (50 wt% in H_2O) was washed with MeOH (3 x 5 mL) prior to use. A suspension of Ra-Ni in MeOH (10 mL) was saturated with H_2 for 30 minutes. Then a solution of **18** (300 mg, 1 eq) in MeOH under N_2 atmosphere was slowly added to the reaction mixture. The mixture was stirred under H_2 atmosphere until completion of the reaction (17 h), monitored by TLC. The solid residue was filtered off on paper filter, and washed with MeOH (3 x 5 mL). The organic phase was concentrated under reduced pressure, then ethyl acetate was added (5 mL) and the organic phase was washed with $NaHCO_3$ *s.s.*, dried over anhydrous Na_2SO_4, filtered and concentrated under vacuum. The crude compound was purified by column chromatography (ethyl acetate) affording a colorless oil (260 mg, 96%).
Spectroscopic data are in agreement with those reported in literature [143].

7.1.3 – Synthetic protocol for the synthesis of target molecules 27a-b and 28a-b

<u>General procedure (I) for Boc-cleavage</u> exemplified with compound methyl (*S*)-2-amino-3-((*S*)-2-oxopyrrolidin-3-yl)propanoate

The protected compound **19** (360 mg, 1 eq) was dissolved in DCM (12 mL, 0,1 M) and cooled at 0 °C, then TFA (3,7 mL, 40 eq) was slowly added. The mixture was stirred at 0 °C until completion of the reaction monitored by TLC (30 min), then the solvent and TFA were removed under high vacuum, with the help of the azeotropic mixture Et_2O/DCM (1:1, 2x10 mL).

The crude product was directly used in the next step with no further purification.

ESI-MS *m/z* 187 [M+H]+, 209 [M+Na]+

<u>General procedure (II) for the coupling reaction</u> exemplified with compound methyl (*S*)-2-((*S*)-2-((*tert*-butoxycarbonyl)amino)-4-methylpentanamido)-3-((*S*)-2-oxopyrrolidin-3-yl)propanoate (20)

In a two-necked oven dried round bottom flask, under N_2 atmosphere, (*tert*-butoxycarbonyl)-*L*-leucine (118 mg, 1 eq) was solubilized in anhydrous DCM (2 mL, 0,15 M), the mixture was cooled at 0 °C, then HATU (293 mg, 1,5 eq) and TEA (0,20 mL, 3 eq) were added. The mixture was stirred for 30 min, then a solution of the amine **19** (100 mg, 1,05 eq) in DCM (1,5 mL, 0,15 M) and TEA (0,15mL, 2 eq) was slowly added. The reaction mixture was stirred a 0 °C for 4 h, then after completion of the reaction, checked by TLC, a saturated aqueous solution of NH_4Cl (4mL) was added to the reaction mixture, and the resulting aqueous phase was extracted with DCM (3 x 3 mL). The organic phases were combined, dried over anhydrous Na_2SO_4, filtered and concentrated under reduced pressure. The crude mixture was purified by column chromatography with DCM/MeOH (20:1) yielding a pale yellow oil 187 mg (87% yield).

Spectroscopic data are in agreement with those previously reported [143].

Methyl (*S*)-2-((*S*)-4-methyl-2-(quinolin-8-ylamino)pentanamido)-3-((*S*)-2-oxopyrrolidin-3-yl)propanoate (21)

Compound **21** has been prepared following general procedures (I-II) for Boc-cleavage and coupling reaction, using quinoline-8-carboxylic acid as the appropriate carboxylic acid. The mixture has been purified by SiO_2 column chromatography using as elution mixture $CHCl_3$/MeOH (40:1), yielding a colorless oil (36% yield).

ESI-MS *m/z* 455 $[M+H]^+$, 477 $[M+Na]^+$

^1H NMR (300 MHz, $CDCl_3$) δ 11.66 (dd, J = 42.4, 7.7 Hz, 1H), 8.98 – 8.88 (m, 1H), 8.73 (ddd, *J* = 7.3, 3.9, 1.4 Hz, 1H), 8.29 – 8.20 (m, 1H), 8.02 (d, *J* = 7.3 Hz, 1H), 7.97 – 7.88 (m, 1H), 7.62 (td, *J* = 7.7, 4.3 Hz, 1H), 7.47 (ddd, *J* = 8.3, 4.2, 2.0 Hz, 1H), 6.89 (s, 1H), 5.01 – 4.70 (m, 1H), 4.52 (ddd, *J* = 11.1, 7.3, 3.6 Hz, 1H), 4.19 – 4.03 (m, 1H), 3.67 (d, *J* = 5.5 Hz, 3H), 3.38 – 3.09 (m, 2H), 2.50 – 2.16 (m, 2H), 1.98 – 1.47 (m, 4H), 1.32 – 1.17 (m, 1H), 1.05 – 0.89 (m, 6H).

Methyl 2-((*S*)-2-(8-chloro-1-methyl-4-oxo-1,4-dihydroquinoline-3-carboxamido)-4-methylpentanamido)-3-((*S*)-2-oxopyrrolidin-3-yl)propanoate (22)

Compound **22** has been prepared following general procedures (I-II) for Boc-cleavage and coupling reaction, using 8-chloro-1-methyl-4-oxo-1,4-dihydroquinoline-3-carboxylic acid as the appropriate carboxylic acid. The mixture has been purified by SiO_2 column chromatography using as elution mixture $CHCl_3$/MeOH (40:1), yielding a colorless oil (42% yield).

ESI-MS *m/z* 520 $[M+H]^+$, 542 $[M+Na]^+$

^1H NMR (300 MHz, $CDCl_3$) δ 10.01 (dd, *J* = 15.9, 7.4 Hz, 1H), 8.58 – 8.51 (m, 1H), 8.36 – 8.19 (m, 1H), 7.92 (s, 1H), 7.82 (t, *J* = 8.6 Hz, 1H), 7.56 (dtd, *J* = 9.2, 7.5, 1.4 Hz, 1H), 7.28 – 7.16 (m, 1H), 4.62 (dt, *J* = 11.2, 7.6 Hz, 1H), 4.51 (ddd, *J* = 11.1, 7.6, 3.9 Hz, 1H), 4.25 (s, 3H), 3.63 (s, 3H), 3.23 (dd, *J* = 15.6, 6.1 Hz, 2H), 2.45 – 2.09 (m, 3H), 1.84 – 1.59 (m, 5H), 0.93 – 0.78 (m, 6H).

2-((*S*)-4-Methyl-2-(quinoline-8-carboxamido)pentanamido)-3-((*S*)-2-oxopyrrolidin-3-yl)propanoic acid ((*S,S,S*) and (*S,R,S*)-23)

In a round bottom flask the ester intermediate **21** (190 mg, 1 eq) was solubilized in THF (5,2 mL, 0,08M), then an aqueous solution of LiOH 1M (4,2 mL) was slowly added and the resulting reaction mixture was stirred at 25 °C for 6 h. After this time the pH of the reaction mixture was adjusted to pH=3 by adding 1M HCl. The mixture was then extracted with EtOAc (3 x 5 mL), dried over anhydrous Na_2SO_4, filtered and concentrated under reduced pressure to afford the crude product as a white solid, (155 mg 84% yield).

The crude product was used directly for the next step with no further purification.

ESI-MS *m/z* 441 $[M+H]^+$, 439 $[M-H]^-$

2-((*S*)-2-(8-Chloro-1-methyl-4-oxo-1,4-dihydroquinoline-3-carboxamido)-4-methylpentanamido)-3-((*S*)-2-oxopyrrolidin-3-yl)propanoic acid ((*S,S,S*) and (*S,R,S*)-24)

For the synthesis of the acid intermediates (*S,S,S*) and (*S,R,S*)-**24** the synthetic protocol adopted has been the same as compounds (*S,S,S*) and (*S,R,S*)-**23**, affording *S,S,*S) and (S*,R,S*-**24** as white solid (95% yield).

The mixture was used directly for the next synthetic step without any further purification.

ESI-MS *m/z* 506 $[M+H]^+$, 504 $[M-H]^-$

***N*-((2*S*)-1-((1-Amino-1-oxo-3-((*S*)-2-oxopyrrolidin-3-yl)propan-2-yl)amino)-4-methyl-1-oxopentan-2-yl)quinoline-8-carboxamide ((*S,S,S*) and (*S,R,S*)-25)**

To a solution of the crude diastereomeric mixture (*S,S,*S) and (S*,R,S)*-**23** (150 mg, 1 eq) in THF (8,5 mL, 0,04 M), 1,1'-carbonyldiimidazole (CDI) (65 mg, 1,2 eq) was added. After 15 min ammonium hydroxide solution (28.0-30.0% NH_3) (0,17 mL, 3,65 eq) was slowly dropped and the resulting reaction mixture was stirred for 3 h. Then H_2O (5 mL) was added and the aqueous phase was extracted with EtOAc (3 x 3 mL);

the combined organic phases were washed with brine (2 x 5 mL), dried over anhydrous Na_2SO_4, filtered and concentrated under high vacuum.

The crude mixture, a pale yellow oil, was used with no further purification (67 mg, 45% yield).

ESI-MS *m/z* 440 $[M+H]^+$, 462 $[M+Na]^+$

^1H NMR (300 MHz, $CDCl_3$) δ 11.75 (dd, *J* = 30.1, 6.3 Hz, 1H), 10.41 (s, 2H), 8.93 – 8.83 (m, 1H), 8.66 (t, *J* = 7.6 Hz, 1H), 8.30 (dd, *J* = 42.2, 7.1 Hz, 1H), 7.90 (dd, *J* = 13.8, 7.1 Hz, 1H), 7.73 (s, 1H), 7.62 – 7.52 (m, 1H), 7.51 – 7.37 (m, 1H), 6.70 (s, 1H), 4.80 – 4.44 (m, 1H), 4.16 – 3.57 (m, 1H), 3.37 – 3.01 (m, 2H), 2.61 – 2.12 (m, 1H), 2.06 – 1.48 (m, 5H), 0.96 (dd, *J* = 17.7, 5.9 Hz, 6H).

_N_-((2_S_)-1-((1-Amino-1-oxo-3-((_S_)-2-oxopyrrolidin-3-yl)propan-2-yl)amino)-4-methyl-1-oxopentan-2-yl)-8-chloro-1-methyl-4-oxo-1,4-dihydroquinoline-3-carboxamide ((_S,S,S/S,R,S_)-26)

The mixture of intermediates (*S,S,S*) and (S,*R,S*)-**26** has been synthesized following the same synthetic reaction as the one used for compounds (*S,S,S/S,R,S*)-**25**.

The mixture of crude products has been used with no further purification (87 mg, 65% yield).

ESI-MS *m/z* 505 $[M+H]^+$, 527 $[M+Na]^+$

^1H NMR (300 MHz, $CDCl_3$) δ 10.46 (d, *J* = 4.9 Hz, 1H), 10.16 (d, *J* = 7.1 Hz, 1H), 9.74 (s, 2H), 8.90 (s, 1H), 8.58 (t, *J* = 9.4 Hz, 1H), 8.48 – 8.34 (m, 1H), 7.41 – 7.28 (m, 1H), 6.71 (s, 1H), 4.67 – 4.37 (m, 2H), 4.29 (s, 3H), 3.21 (s, 2H), 2.48 – 2.05 (m, 3H), 1.76 (t, *J* = 11.0 Hz, 5H), 1.03 – 0.90 (m, 6H).

<u>General procedure (III) for the primary amide conversion in nitrile moiety</u> exemplified with compound _N_-((2_S_)-1-((1-cyano-2-((_S_)-2-oxopyrrolidin-3-yl)ethyl)amino)-4-methyl-1-oxopentan-2-yl)quinoline-8-carboxamide ((_S,S,S_)-27 and (_S,R,S_)-27)

In an oven dried round bottom flask under N_2 atmosphere, the amide intermediate (*S,S,S*) and (*S,R,S*)-**25** (35 mg, 1 eq) has been solubilized in anhydrous DCM (2 mL, 0,04 M), the reaction mixture has been cooled at 0 °C, then anhydrous TEA (0,022 mL, 2 eq) has been slowly added followed by TFAA (0,033 mL, 3 eq). The reaction mixture has been stirred at 0 °C for 2 h, then brine solution (2 mL) has been added, and the reaction mixture was allowed to reach room temperature and extracted with DCM (3 x 2 mL). The collected organic phases were combined, dried over anhydrous Na_2SO_4, filtered and concentrated under reduced pressure. The crude diastereomer mixture was purified by column chromatography, allowing to separate the two diastereomers as colorless amorphous solids. Elution solvent DCM/MeOH (20:1).

N-((*S*)-1-(((*S*)-1-Cyano-2-((*S*)-2-oxopyrrolidin-3-yl)ethyl)amino)-4-methyl-1-oxopentan-2-yl)quinoline-8-carboxamide ((*S,S,S*)-**27**), 7 mg, 21% yield;

ESI-MS *m/z* 421 $[M+H]^+$, 444 $[M+Na]^+$

^{1}H NMR (300 MHz, $CDCl_3$) δ 11.75 (d, *J* = 7.6 Hz, 1H), 8.97 (dd, *J* = 4.2, 1.6 Hz, 1H), 8.76 (d, *J* = 7.4 Hz, 1H), 8.41 (d, *J* = 7.1 Hz, 1H), 8.29 (dd, *J* = 8.3, 1.5 Hz, 1H), 7.97 (d, *J* = 8.1 Hz, 1H), 7.66 (t, *J* = 7.7 Hz, 1H), 7.51 (dd, *J* = 8.3, 4.3 Hz, 1H), 6.45 (s, 1H), 4.98 – 4.81 (m, 2H), 3.38 – 3.15 (m, 2H), 2.53 – 2.26 (m, 3H), 1.99 – 1.64 (m, 5H), 1.00 (dd, *J* = 8.2, 6.3 Hz, 6H).

^{13}C NMR (75 MHz, $CDCl_3$) δ 178.6, 172.9, 166.3, 149.6, 145.5, 137.8, 133.8, 132.4, 128.5, 127.9, 126.4, 121.1, 118.5, 52.3, 40.8, 40.3, 39.1, 37.7, 33.9, 29.7, 28.1, 25.1, 23.1, 22.1.

N-((*S*)-1-(((*R*)-1-Cyano-2-((*S*)-2-oxopyrrolidin-3-yl)ethyl)amino)-4-methyl-1-oxopentan-2-yl)quinoline-8-carboxamide ((*S,R,S*)-**27**), 6 mg, 18% yield.

ESI-MS *m/z* 421 $[M+H]^+$, 444 $[M+Na]^+$

^{1}H NMR (300 MHz, $CDCl_3$) δ 11.69 (d, *J* = 7.5 Hz, 1H), 8.96 (dd, *J* = 4.2, 1.7 Hz, 1H), 8.79 (dd, *J* = 7.4, 1.5 Hz, 1H), 8.29 (dd, *J* = 8.3, 1.7 Hz, 1H), 7.99 (dd, *J* = 8.1, 1.3 Hz, 1H), 7.69 (t, *J* = 7.8 Hz, 1H), 7.51 (dd, *J* = 8.3, 4.3 Hz, 1H), 7.33 (t, *J* = 5.7 Hz, 1H), 6.96 (s, 1H), 4.80 (dd, *J* = 13.8, 8.2 Hz, 1H), 4.37 (t, *J* = 7.5 Hz, 1H), 3.40

(dtt, *J* = 32.4, 13.1, 6.4 Hz, 2H), 2.65 (ddt, *J* = 101.6, 14.2, 8.5 Hz, 1H), 2.20 – 1.96 (m, 2H), 1.96 – 1.56 (m, 5H), 0.99 (dd, *J* = 9.8, 6.2 Hz, 6H).

8-Chloro-*N*-((2*S*)-1-((1-cyano-2-((*S*)-2-oxopyrrolidin-3-yl)ethyl)amino)-4-methyl-1-oxopentan-2-yl)-1-methyl-4-oxo-1,4-dihydroquinoline-3-carboxamide ((*S,S,S*) and (*S,R,S*)-28)

The target molecules (*S,S,S*) and (*S,R,S*)-**28** were obtained from the amide intermediates mixture (*S,S,S*) and (*S,R,S*)-**26** following the general procedure (III) for the primary amide conversion in nitrile moiety. The crude mixture was purified by SiO_2 column chromatography using $CHCl_3$/MeOH (30:1) as elution mixture.

8-Chloro-*N*-((*S*)-1-(((*S*)-1-cyano-2-((*S*)-2-oxopyrrolidin-3-yl)ethyl)amino)-4-methyl-1-oxopentan-2-yl)-1-methyl-4-oxo-1,4-dihydroquinoline-3-carboxamide (*S,S,S*)-**28**), 4 mg, 9% yield.

ESI-MS *m/z* 487 $[M+H]^+$, 509 $[M+Na]^+$

^{1}H NMR (300 MHz, $CDCl_3$) δ 10.14 (d, *J* = 7.1 Hz, 1H), 8.64 (s, 1H), 8.45 (d, *J* = 8.0 Hz, 1H), 7.74 (d, *J* = 7.6 Hz, 1H), 7.37 (t, *J* = 7.8 Hz, 1H), 6.57 (s, 1H), 5.55 (s, 1H), 4.68 – 4.54 (m, 1H), 4.35 (s, 3H), 3.83 – 3.23 (m, 2H), 2.88 – 2.28 (m, 2H), 1.99 – 1.56 (m, 6H), 0.95 (dd, *J* = 15.0, 5.2 Hz, 6H).

^{13}C NMR (75 MHz, CD_3OD) δ 179.5, 175.7, 173.3, 164.9, 152.3, 152.3, 137.7, 136.7, 130.5, 125.9, 125.6, 122.5, 118.4, 110.5, 109.9, 40.9, 40.0, 38.4, 37.7, 33.8, 27.2, 24.8, 22.0, 20.7.

8-Chloro-*N*-((*S*)-1-(((*R*)-1-cyano-2-((*S*)-2-oxopyrrolidin-3-yl)ethyl)amino)-4-methyl-1-oxopentan-2-yl)-1-methyl-4-oxo-1,4-dihydroquinoline-3-carboxamide (*S,R,S*)-**28**), 9 mg, 16% yield.

ESI-MS *m/z* 487 $[M+H]^+$, 509 $[M+Na]^+$

^{1}H NMR (300 MHz, $CDCl_3$) δ 10.09 (d, *J* = 7.2 Hz, 1H), 8.56 (s, 1H), 8.31 (d, *J* = 7.1 Hz, 1H), 7.64 (d, *J* = 7.5 Hz, 1H), 7.24 (t, *J* = 7.8 Hz, 1H), 5.76 (s, 1H), 5.05 – 4.88 (m, 1H), 4.61 (dt, *J* = 9.9, 5.0 Hz, 1H), 4.37 (s, 3H), 3.39 – 3.24 (m, 2H), 2.61 – 2.36 (m, 3H), 2.01 – 1.70 (m, 5H), 0.95 (dd, *J* = 17.9, 5.7 Hz, 6H).

7.1.4 – Synthesis of molecules 27a, 28a and 33a-k

Methyl (*S*)-2-((2*S*,3*R*)-2-((tert-butoxycarbonyl)amino)-3-hydroxybutanamido)-3-((*S*)-2-oxopyrrolidin-3-yl)propanoate (29)

Compound **29** has been prepared following the general procedures (I-II) for Boc-cleavage and coupling reaction, using methyl (tert-butoxycarbonyl)-L-threoninate as the appropriate carboxylic acid. The mixture has been purified by SiO_2 column chromatography using as elution mixture DCM/MeOH (30:1), yielding a colorless oil (43% yield).

Spectroscopic data are in agreement with those reported in literature.

ESI-MS *m/z* 388 $[M+H]^+$, 410 $[M+Na]^+$

Methyl (*S*)-2-((2*S*,3*R*)-3-(benzyloxy)-2-((tert-butoxycarbonyl)amino)butanamido)-3-((*S*)-2-oxopyrrolidin-3-yl)propanoate (30)

Compound **30** has been prepared following general procedures (I-II) for Boc-cleavage and coupling reaction, methyl O-benzyl-*N*-(tert-butoxycarbonyl)-L-threoninate as the appropriate carboxylic acid. The mixture has been purified by SiO_2 column chromatography using as elution mixture DCM/MeOH (30:1), yielding a colorless oil (89% yield).

ESI-MS *m/z* 600 $[M+H]^+$, 622 $[M+Na]^+$

^{1}H NMR (300 MHz, CD_3OD) δ 8.55 (dd, *J* = 30.0, 7.8 Hz, 1H), 7.75 (d, *J* = 7.5 Hz, 2H), 7.71 – 7.54 (m, 2H), 7.43 – 7.14 (m, 9H), 4.67 – 3.99 (m, 6H), 3.64 (s, 3H), 3.20 – 2.92 (m, 2H), 2.46 – 2.02 (m, 3H), 1.85 – 1.53 (m, 2H), 1.21 (dt, *J* = 7.1, 3.6 Hz, 3H).

Methyl (*S*)-2-((*S*)-2-(isoquinoline-8-carboxamido)-4-methylpentanamido)-3-((*S*)-2-oxopyrrolidin-3-yl)propanoate (31a)

Compound **31a** was synthesized according to general procedures (I-II) for Boc-cleavage and coupling reaction, using isoquinoline-8-carboxylic acid as the

appropriate carboxylic acid. The compound was purified by SiO_2 column chromatography DCM/MeOH (30:1), yielding a colorless oil (57%).

ESI-MS *m/z* 455 $[M+H]^+$, 477 $[M+Na]^+$

^1H NMR (300 MHz, $CDCl_3$) δ 9.76 – 9.62 (m, 1H), 8.75 (d, *J* = 7.0 Hz, 1H), 8.50 (dd, *J* = 16.2, 6.0 Hz, 1H), 8.42 (d, *J* = 6.6 Hz, 1H), 7.84 (d, *J* = 8.2 Hz, 1H), 7.73 (t, *J* = 5.6 Hz, 1H), 7.62 (dd, *J* = 10.1, 4.9 Hz, 2H), 7.13 (dd, *J* = 18.6, 8.6 Hz, 1H), 6.94 (d, *J* = 12.1 Hz, 1H), 4.95 (ddd, *J* = 14.4, 11.2, 7.0 Hz, 1H), 4.63 – 4.37 (m, 1H), 3.72 (s, 3H), 3.37 – 3.22 (m, 2H), 2.52 – 2.15 (m, 3H), 1.94 – 1.62 (m, 5H), 1.07 – 0.93 (m, 6H).

Methyl (*S*)-2-((*S*)-2-(isoquinoline-5-carboxamido)-4-methylpentanamido)-3-((*S*)-2-oxopyrrolidin-3-yl)propanoate (31b)

Compound **31b** was synthesized according to general procedures (I-II) for Boc-cleavage and coupling reaction, using isoquinoline-5-carboxylic acid as the appropriate carboxylic acid. The compound was purified by SiO_2 column chromatography DCM/MeOH (30:1), yielding a colorless oil (55% yield).

ESI-MS *m/z* 455 $[M+H]^+$, 477 $[M+Na]^+$

^1H NMR (300 MHz, CD_3OD) δ 9.27 (s, 1H), 8.48 (dd, *J* = 7.3, 3.1 Hz, 1H), 8.27 – 8.13 (m, 2H), 7.99 (dd, *J* = 7.2, 1.0 Hz, 1H), 7.72 (t, 1H), 4.80 – 4.57 (m, 2H), 3.74 (d, *J* = 4.7 Hz, 3H), 3.38 – 3.22 (m, 2H), 2.77 – 2.11 (m, 3H), 1.92 – 1.65 (m, 5H), 1.03 (dd, *J* = 6.4, 2.6 Hz, 6H).

Methyl (*S*)-2-((*S*)-2-(8-chloro-4-hydroxyquinoline-3-carboxamido)-4-methylpentanamido)-3-((*S*)-2-oxopyrrolidin-3-yl)propanoate (31c)

Compound **31c** was synthesized according to general procedures (I-II) for Boc-cleavage and coupling reaction, using 8-chloro-4-hydroxyquinoline-3-carboxylic acid as the appropriate carboxylic acid. The mixture was purified through SiO_2 column chromatography, yielding a colorless oil (65% yield).

^1H NMR (300 MHz, $CDCl_3$) δ 9.34 (dd, *J* = 19.2, 7.9 Hz, 1H), 9.22 (dd, *J* = 17.0, 6.0 Hz, 1H), 8.15 – 8.02 (m, 1H), 7.67 – 7.52 (m, 1H), 7.41 (d, *J* = 8.3 Hz, 1H), 4.75 –

4.46 (m, 2H), 3.66 (d, *J* = 4.2 Hz, 3H), 3.35 – 3.16 (m, 2H), 2.47 – 2.02 (m, 4H), 2.00 – 1.58 (m, 5H), 0.96 – 0.87 (m, 6H).

Methyl (S)-2-((S)-2-(4-hydroxy-8-(trifluoromethoxy)quinoline-3-carboxamido)-4-methylpentanamido)-3-((S)-2-oxopyrrolidin-3-yl)propanoate (31d)

Compound **31d** was synthesized according to general procedures (I-II) for Boc-cleavage and coupling reaction using 8-chloro-1-methyl-4-oxo-1,4-dihydroquinoline-3-carboxylic acid as the appropriate carboxylic acid. The target molecule was purified by column chromatography eluting with a mixture of $CHCl_3$/MeOH (40:1), yielding a colorless oil (67% yield).

ESI-MS *m/z* 555 $[M+H]^+$, 577 $[M+Na]^+$

^{1}H NMR (300 MHz, $CDCl_3$) δ 12.58 (s, 1H), 10.24 (s, 1H), 8.76 (d, *J* = 28.1 Hz, 1H), 8.41 – 8.15 (m, 2H), 7.66 – 7.41 (m, 2H), 4.76 – 4.52 (m, 2H), 3.72 (s, 3H), 3.55 – 3.07 (m, 3H), 2.70 – 2.25 (m, 3H), 2.09 – 1.63 (m, 4H), 1.10 – 0.78 (m, 6H).

Methyl (*S*)-2-((*S*)-4-methyl-2-(1-methyl-4-oxo-8-(trifluoromethoxy)-1,4-dihydroquinoline-3-carboxamido)pentanamido)-3-((*S*)-2-oxopyrrolidin-3-yl)propanoate (31e)

Compound **31e** was synthesized according to general procedures (I-II) for Boc-cleavage and coupling reaction using 8-chloro-1-methyl-4-oxo-1,4-dihydroquinoline-3-carboxylic acid as the appropriate carboxylic acid. The target molecule was purified by column chromatography eluting with a mixture of $CHCl_3$/MeOH (40:1), yielding a colorless oil (78% yield).

ESI-MS *m/z* 569 $[M+H]^+$, 591 $[M+Na]^+$

^{1}H NMR (300 MHz, DMSO-d6) δ 10.00 (d, *J* = 7.7 Hz, 1H), 8.74 (s, 1H), 8.68 (d, *J* = 7.3 Hz, 1H), 8.39 (d, *J* = 8.1 Hz, 1H), 7.88 (d, *J* = 7.6 Hz, 1H), 7.66 – 7.53 (m, 2H), 4.73 – 4.58 (m, 1H), 4.38 – 4.26 (m, 1H), 4.12 (s, 3H), 3.61 (s, 3H), 3.19 – 2.99 (m,, 4H), 2.37 – 1.97 (m, 4H), 1.72 – 1.44 (m, 4H), 0.96 – 0.84 (m, 6H).

Methyl (*S*)-2-((*S*)-2-(4-hydroxy-6-nitroquinoline-3-carboxamido)-4-methylpentanamido)-3-((*S*)-2-oxopyrrolidin-3-yl)propanoate (31f)

Compound **31f** was synthesized according to general procedures (I-II) for Boc-cleavage and coupling reaction using 4-hydroxy-6-nitroquinoline-3-carboxylic acid as the appropriate carboxylic acid. The crude mixture was purified by SiO_2 column chromatography with $CHCl_3$/MeOH (20:1), yielding a bright yellow oil (61%).

ESI-MS *m/z* 516 $[M+H]^+$, 538 $[M+Na]^+$

^1H NMR (300 MHz, CD_3OD) δ 10.23 (dd, *J* = 18.5, 6.9 Hz, 1H), 9.72 (d, *J* = 7.1 Hz, 1H), 9.00 – 8.56 (m, 3H), 8.42 (dd, *J* = 9.1, 2.4 Hz, 1H), 7.78 – 7.65 (m, 1H), 4.69 – 4.42 (m, 2H), 3.73 (s, 3H), 3.26 – 3.02 (m, 2H), 2.70 – 2.09 (m, 3H), 1.94 – 1.67 (m, 5H), 1.02 (dd, *J* = 12.5, 6.1 Hz, 6H).

tert-Butyl 8-bromo-1-(((*S*)-1-(((*S*)-1-methoxy-1-oxo-3-((*S*)-2-oxopyrrolidin-3-yl)propan-2-yl)amino)-4-methyl-1-oxopentan-2-yl)carbamoyl)-3,4-dihydroisoquinoline-2(1H)-carboxylate (31g)

Compound **31g** was synthesized according to the general procedures (I-II) for Boc-cleavage and coupling reaction using 8-bromo-2-(*tert*-butoxycarbonyl)-1,2,3,4-tetrahydroisoquinoline-1-carboxylic acid as the appropriate carboxylic acid. The colorless crude product was purified by column chromatography with DCM/MeOH (30:1) as eluent (71%).

ESI-MS *m/z* 638 $[M+H]^+$

^1H NMR (300 MHz, CD_3OD) δ 7.66 (d, *J* = 17.6 Hz, 1H), 7.41 – 7.29 (m, 1H), 7.10 (t, *J* = 7.3 Hz, 1H), 5.35 (s, 1H), 4.64 – 4.33 (m, 3H), 4.04 – 3.84 (m, 1H), 3.69 (s, 3H), 3.60 – 3.42 (m, 1H), 3.23 – 3.10 (m, 1H), 3.01 – 2.88 (m, 2H), 2.55 – 2.02 (m, 3H), 1.90 – 1.56 (m, 5H), 1.49 (d, *J* = 2.0 Hz, 9H), 0.92 (dd, *J* = 31.6, 25.8 Hz, 6H).

Methyl (*S*)-2-((2*S*,3*S*)-2-(8-chloro-1-methyl-4-oxo-1,4-dihydroquinoline-3-carboxamido)-3-hydroxybutanamido)-3-((*S*)-2-oxopyrrolidin-3-yl)propanoate (31h)

Compound **31h** was synthesized according to the general procedures (I-II) for Boc-cleavage and coupling reaction using 8-chloro-1-methyl-4-oxo-1,4-dihydroquinoline-3-carboxylic acid as the appropriate carboxylic acid. The crude mixture was purified

by SiO_2 column chromatography using DCM/MeOH (30:1) as eluent, yielding a colorless oil (70%).

ESI-MS *m/z* 638 $[M+H]^+$

^1H NMR (300 MHz, CD_3OD) δ 8.55 (s, 1H), 8.28 – 8.19 (m, 1H), 7.70 (ddd, *J* = 15.5, 7.7, 1.4 Hz, 1H), 7.32 (q, *J* = 8.0 Hz, 1H), 4.78 – 4.52 (m, 3H), 4.30 (s, 3H), 3.74 (s, 3H), 2.80 – 2.22 (m, 3H), 1.94 – 1.72 (m, 2H), 1.25 (d, *J* = 6.4 Hz, 3H).

Methyl (*S*)-2-((2*S*,3*S*)-3-(benzyloxy)-2-(8-chloro-1-methyl-4-oxo-1,4-dihydroquinoline-3-carboxamido)butanamido)-3-((*S*)-2-oxopyrrolidin-3-yl)propanoate (31i)

Compound **31i** was synthesized according to general procedures (I-II) for Boc-cleavage and coupling reaction 8-chloro-using 1-methyl-4-oxo-1,4-dihydroquinoline-3-carboxylic acid as the appropriate carboxylic acid. The mixture has been purified by SiO_2 column chromatography, affording the target molecule as a colorless oil (83%).

ESI-MS *m/z* 598 $[M+H]^+$, 621 $[M+Na]^+$

^1H NMR (300 MHz, CD_3OD) δ 10.60 (d, *J* = 8.0 Hz, 1H), 8.63 (s, 1H), 8.40 – 8.26 (m, 1H), 7.82 – 7.70 (m, 1H), 7.32 (ddt, *J* = 22.2, 14.2, 6.9 Hz, 6H), 4.75 – 4.51 (m, 5H), 4.33 (s, 3H), 3.68 (d, *J* = 1.9 Hz, 3H), 3.11 – 2.91 (m, 1H), 2.56 – 2.10 (m, 4H), 1.87 – 1.62 (m, 3H), 1.28 (d, *J* = 4.6 Hz, 3H).

General procedure (IV) for the conversion of the ester intermediates into primary amides exemplified with compound *N*-((*S*)-1-(((*S*)-1-amino-1-oxo-3-((*S*)-2-oxopyrrolidin-3-yl)propan-2-yl)amino)-4-methyl-1-oxopentan-2-yl)quinoline-8-carboxamide ((*S,S,S*)-25)

In an oven dried round bottom flask, the ester intermediate **21** (25 mg, 0,051 mmol) was solubilized in the smallest quantity of MeOH (0,2 mL), then $NH_3$7N in MeOH (0,86 mL) was slowly added and the resulting reaction mixture was stirred at 20 °C for 12 h. The solvent was evaporated under reduced pressure and the crude product, a white amorphous solid, was used directly without any further purification (76%)

ESI-MS *m/z* 440 $[M+H]^+$, 462 $[M+Na]^+$

_N_-((_S_)-1-(((_S_)-1-amino-1-oxo-3-((_S_)-2-oxopyrrolidin-3-yl)propan-2-yl)amino)-4-methyl-1-oxopentan-2-yl)isoquinoline-8-carboxamide (32a)

For the synthesis of compound **32a**, the general procedure (IV) for the primary amide conversion has been followed using **31a** as starting material. The crude product, a white amorphous solid, has been used for the following reaction without any further purification (72% yield)

ESI-MS *m/z* 440 [M+H]+, 462 $[M+Na]^+$

_N_-((_S_)-1-(((_S_)-1-Amino-1-oxo-3-((_S_)-2-oxopyrrolidin-3-yl)propan-2-yl)amino)-4-methyl-1-oxopentan-2-yl)isoquinoline-5-carboxamide (32b)

For the synthesis of compound **32b**, the general procedure (IV) for the primary amide conversion has been followed using **31b** as starting material. The crude product, a white amorphous solid, has been used for the following reaction without any further purification (69% yield)

ESI-MS *m/z* 440 $[M+H]^+$, 462 $[M+Na]^+$

_N_-((_S_)-1-(((_S_)-1-Amino-1-oxo-3-((_S_)-2-oxopyrrolidin-3-yl)propan-2-yl)amino)-4-methyl-1-oxopentan-2-yl)-8-chloro-4-hydroxyquinoline-3-carboxamide (32c)

For the synthesis of compound **32c**, the general procedure (IV) for the primary amide conversion has been followed using **31c** as starting material. The crude product has been used for the following reaction without any further purification, furnishing a white amorphous solid (68% yield).

ESI-MS *m/z* 490 $[M+H]^+$

_N_-((_S_)-1-(((_S_)-1-Amino-1-oxo-3-((_S_)-2-oxopyrrolidin-3-yl)propan-2-yl)amino)-4-methyl-1-oxopentan-2-yl)-8-chloro-1-methyl-4-oxo-1,4-dihydroquinoline-3-carboxamide ((_S,S,S_)-26)

For the synthesis of compound (S)-**26**, the general procedure (IV) for the primary amide conversion has been followed using **22** as starting material. The crude

product, a white amorphous solid (79% yield), has been used for the following reaction without any further purification.

ESI-MS *m/z* 504 $[M+H]^+$

_N_-((_S_)-1-(((_S_)-1-amino-1-oxo-3-((_S_)-2-oxopyrrolidin-3-yl)propan-2-yl)amino)-4-methyl-1-oxopentan-2-yl)-4-hydroxy-8-(trifluoromethoxy)quinoline-3-carboxamide (32d)

For the synthesis of compound **32d**, the general procedure (IV) for the primary amide conversion has been followed using **31d** as starting material. The crude product, a white amorphous solid (66% yield), has been used for the following reaction without any further purification.

ESI-MS *m/z* 540 $[M+H]^+$

_N_-((_S_)-1-(((_S_)-1-amino-1-oxo-3-((_S_)-2-oxopyrrolidin-3-yl)propan-2-yl)amino)-4-methyl-1-oxopentan-2-yl)-1-methyl-4-oxo-8-(trifluoromethoxy)-1,4-dihydroquinoline-3-carboxamide (32e)

For the synthesis of compound **32e**, the general procedure (IV) for the primary amide conversion has been followed using **31e** as starting material. The crude product, a white amorphous solid (76% yield), has been used for the following reaction without any further purification.

ESI-MS *m/z* 553 $[M+H]^+$

_N_-((_S_)-1-(((S)-1-Amino-1-oxo-3-((_S_)-2-oxopyrrolidin-3-yl)propan-2-yl)amino)-4-methyl-1-oxopentan-2-yl)-4-hydroxy-6-nitroquinoline-3-carboxamide (32f)

For the synthesis of compound **32f**, the general procedure (IV) for the primary amide conversion has been followed using **31f** as starting material. The crude product, a bright yellow amorphous solid, has been used for the following reaction without any further purification (64% yield).

ESI-MS *m/z* 501 $[M+H]^+$, 523 $[M+Na]^+$

***tert*-Butyl 1-(((*S*)-1-(((*S*)-1-amino-1-oxo-3-((*S*)-2-oxopyrrolidin-3-yl)propan-2-yl)amino)-4-methyl-1-oxopentan-2-yl)carbamoyl)-8-bromo-3,4-dihydroisoquinoline-2(1*H*)-carboxylate (32g)**

For the synthesis of compound **32g**, the general procedure (IV) for the primary amide conversion has been followed using **31g** as starting material. The crude product has been used for the following reaction without any further purification, furnishing a white amorphous solid (83% yield).

ESI-MS *m/z* 623 $[M+H]^+$, 646 $[M+Na]^+$

***N*-((2*S*,3*S*)-1-(((*S*)-1-Amino-1-oxo-3-((*S*)-2-oxopyrrolidin-3-yl)propan-2-yl)amino)-3-hydroxy-1-oxobutan-2-yl)-8-chloro-1-methyl-4-oxo-1,4-dihydroquinoline-3-carboxamide (32h)**

For the synthesis of compound **32h**, the general procedure (IV) for the primary amide conversion has been followed using **31h** as starting material. The crude product, a white amorphous solid, has been used for the following reaction without any further purification (84% yield).

ESI-MS *m/z* 492 $[M+H]^+$, 515 $[M+Na]^+$

***N*-((2*S*,3*S*)-1-(((S)-1-Amino-1-oxo-3-((*S*)-2-oxopyrrolidin-3-yl)propan-2-yl)amino)-3-(benzyloxy)-1-oxobutan-2-yl)-8-chloro-1-methyl-4-oxo-1,4-dihydroquinoline-3-carboxamide (32i)**

For the synthesis of compound **32i**, the general procedure (IV) for the primary amide conversion has been followed using **31i** as starting material. The crude product, a white amorphous solid, has been used for the following reaction without any further purification (83% yield).

ESI-MS *m/z* 583 $[M+H]^+$, 605 $[M+Na]^+$

General procedure (V) for the primary amide conversion in nitrile moiety exemplified with compound *N*-((*S*)-1-(((*S*)-1-cyano-2-((*S*)-2-oxopyrrolidin-3-yl)ethyl)amino)-4-methyl-1-oxopentan-2-yl)quinoline-8-carboxamide ((S)-27)

In an oven dried round bottom flask under N_2 atmosphere, the amide intermediate (S)-**25** (35 mg, 1 eq) has been solubilized in anhydrous DCM (2 mL, 0,04 M), the reaction mixture has been cooled at 0 °C, then anhydrous TEA (0,022 mL, 2 eq) has been slowly added followed by TFAA (0,033 mL, 3 eq). The reaction mixture has been stirred at 0 °C for 2 h, then brine solution (2 mL) has been added to the mixture, that was allowed to reach room temperature and extracted with DCM (3 x 2 mL). The collected organic phases were combined, dried over anhydrous Na_2SO_4, filtered and concentrated under reduced pressure to afford the crude mixture. The crude mixture was purified by column chromatography, furnishing a colorless amorphous solid. Elution solvent DCM/MeOH (20:1), 7 mg (21% yield)

ESI-MS *m/z* 421 $[M+H]^+$, 444 $[M+Na]^+$

^{1}H NMR (300 MHz, $CDCl_3$) δ 11.75 (d, *J* = 7.6 Hz, 1H), 8.97 (dd, *J* = 4.2, 1.6 Hz, 1H), 8.76 (d, *J* = 7.4 Hz, 1H), 8.41 (d, *J* = 7.1 Hz, 1H), 8.29 (dd, *J* = 8.3, 1.5 Hz, 1H), 7.97 (d, *J* = 8.1 Hz, 1H), 7.66 (t, *J* = 7.7 Hz, 1H), 7.51 (dd, *J* = 8.3, 4.3 Hz, 1H), 6.45 (s, 1H), 4.98 – 4.81 (m, 2H), 3.38 – 3.15 (m, 2H), 2.53 – 2.26 (m, 3H), 1.99 – 1.64 (m, 5H), 1.00 (dd, *J* = 8.2, 6.3 Hz, 6H).

^{13}C NMR (75 MHz, $CDCl_3$) δ 178.6, 172.9, 166.3, 149.6, 145.5, 137.8, 133.8, 132.4, 128.5, 127.9, 126.4, 121.1, 118.5, 52.3, 40.8, 40.3, 39.1, 37.7, 33.9, 29.7, 28.1, 25.1, 23.1, 22.1.

_N_-((_S_)-1-(((_R_)-1-Cyano-2-((_S_)-2-oxopyrrolidin-3-yl)ethyl)amino)-4-methyl-1-oxopentan-2-yl)isoquinoline-8-carboxamide (33a)

The conversion of the primary amide **32a** to the corresponding nitrile derivative **33a** has been carried out following the general procedure (V) for the nitrile warhead formation. The crude mixture has been purified through SiO_2 column chromatography DCM/MeOH (20:1) yielding a colorless oil (23% yield).

ESI-MS *m/z* 422 $[M+H]^+$, 445 $[M+Na]^+$

^{1}H NMR (300 MHz, CD_3OD) δ 9.59 (s, 1H), 8.49 (d, *J* = 5.7 Hz, 1H), 8.07 (d, *J* = 8.2 Hz, 1H), 7.95 – 7.76 (m, 3H), 5.09 (dd, *J* = 13.9, 7.1 Hz, 1H), 4.76 – 4.63 (m, 1H), 3.19 – 2.86 (m, 2H), 2.78 – 2.20 (m, 3H), 2.07 – 1.48 (m, 5H), 1.12 – 0.98 (m, 6H).

^{13}C NMR (75 MHz, $CDCl_3$) δ 180.4, 172.6, 169.2, 145.4, 134.3, 134.2, 129.9, 129.8, 129.2, 128.9, 121.9, 120.2, 54.2, 42.6, 40.5, 39.8, 34.8, 33.5, 25.3, 23.1.

_N_-((_S_)-1-(((_R_)-1-Cyano-2-((_S_)-2-oxopyrrolidin-3-yl)ethyl)amino)-4-methyl-1-oxopentan-2-yl)isoquinoline-5-carboxamide (33b)

The conversion of the primary amide **32b** to the corresponding nitrile derivative **33b** has been carried out following the general procedure (V) for the nitrile warhead formation. The crude mixture has been purified through SiO_2 column chromatography DCM/MeOH (20:1) yielding a colorless oil (37% yield).

ESI-MS *m/z* 422 $[M+H]^+$, 445 $[M+Na]^+$

^{1}H NMR (300 MHz, CD_3OD) δ 9.30 (s, 1H), 8.50 (s, 1H), 8.21 (dd, *J* = 18.2, 7.0 Hz, 1H), 8.02 (dd, *J* = 9.6, 4.8 Hz, 1H), 7.75 (t, *J* = 7.6 Hz, 1H), 5.13 (dd, *J* = 10.3, 5.5 Hz, 1H), 4.60 (dd, *J* = 9.2, 5.5 Hz, 1H), 3.80 – 3.58 (m, 2H), 2.74 – 2.19 (m, 3H), 2.05 – 1.53 (m, 5H), 1.07 – 0.87 (m, 6H).

^{13}C NMR (75 MHz, CD_3OD) δ 179.6, 173.4, 169.5, 142.3, 133.2, 132.5, 131.8, 130.3, 130.2, 128.7, 126.7, 126.7, 118.4, 52.7, 40.0, 39.9, 37.7, 31.6, 27.2, 24.8, 22.3, 21.9, 20.6.

8-Chloro-_N_-((_S_)-1-(((_S_)-1-cyano-2-((_S_)-2-oxopyrrolidin-3-yl)ethyl)amino)-4-methyl-1-oxopentan-2-yl)-4-hydroxyquinoline-3-carboxamide (33c)

The conversion of the primary amide **32c** to the corresponding nitrile derivative **33c** has been carried out following the general procedure (V) for the nitrile warhead formation. The target molecule has been purified through SiO_2 column chromatography DCM/MeOH (20:1) furnishing a colorless oil (11% yield).

ESI-MS *m/z* 473 $[M+H]^+$, 495 $[M+Na]^+$

^{1}H NMR (300 MHz, CD_3OD) δ 8.77 (s, 1H), 8.34 (d, *J* = 8.1 Hz, 1H), 7.89 (d, *J* = 7.8 Hz, 1H), 7.48 (t, *J* = 8.0 Hz, 1H), 5.01 (dd, *J* = 9.4, 4.3 Hz, 1H), 4.65 – 4.48 (m, 1H), 3.70 – 3.47 (m, 2H), 2.79 – 2.11 (m, 3H), 2.00 – 1.69 (m, 5H), 1.00 (dd, *J* = 12.4, 6.3 Hz, 6H).

^{13}C NMR (75 MHz, CD_3OD) δ 179.5, 173.6, 165.4, 144.1, 132.7, 125.2, 124.7, 111.1, 52.0, 40.9, 40.0, 39.4, 38.4, 37.7, 33.7, 33.2, 29.4, 29.3, 27.5, 27.2, 24.8, 22.0, 20.6.

_N_-((_S_)-1-(((_S_)-1-Cyano-2-((_S_)-2-oxopyrrolidin-3-yl)ethyl)amino)-4-methyl-1-oxopentan-2-yl)-4-hydroxy-8-(trifluoromethoxy)quinoline-3-carboxamide (33d)

The conversion of the primary amide **32d** to the corresponding nitrile derivative **33d** has been carried out following the general procedure (V) for the nitrile warhead formation. The target molecule has been purified through SiO_2 column chromatography DCM/MeOH (20:1) furnishing a colorless oil (33% yield)

ESI-MS *m/z* 522 $[M+H]^+$, 544 $[M+Na]^+$

^{1}H NMR (300 MHz, CD_3OD) δ 8.72 (s, 1H), 8.33 (d, *J* = 4.9 Hz, 1H), 7.79 (d, *J* = 7.8 Hz, 1H), 7.54 (t, *J* = 8.1 Hz, 1H), 5.17 – 4.88 (m, 1H), 4.65 – 4.45 (m, 1H), 2.72 – 2.19 (m, 4H), 2.01 – 1.61 (m, 6H), 1.01 (dd, *J* = 12.7, 5.0 Hz, 6H).

^{13}C NMR (75 MHz, CD_3OD) δ 192.1, 179.5, 179.3, 176.5, 176.4, 173.5, 173.2, 143.9, 138.6, 132.3, 128.2, 124.6, 124.4, 123.7, 111.3, 40.9, 40.1, 40.0, 39.4, 38.2, 37.7, 33.2, 27.5, 24.8, 22.0, 20.6.

_N_-((_S_)-1-(((_S_)-1-Cyano-2-((_S_)-2-oxopyrrolidin-3-yl)ethyl)amino)-4-methyl-1-oxopentan-2-yl)-1-methyl-4-oxo-8-(trifluoromethoxy)-1,4-dihydroquinoline-3-carboxamide (33e)

The conversion of the primary amide **32e** to the corresponding nitrile derivative **33e** has been carried out following the general procedure (V) for the nitrile warhead formation. The target molecule has been purified through SiO_2 column chromatography DCM/MeOH (20:1) furnishing a pale yellow oil (24% yield)

ESI-MS *m/z* 536 $[M+H]^+$, 558 $[M+Na]^+$

^{1}H NMR (300 MHz, CD_3OD) δ 8.75 – 8.68 (m, 1H), 8.55 – 8.44 (m, 1H), 7.83 (d, *J* = 8.0 Hz, 1H), 7.58 (dd, *J* = 11.7, 4.4 Hz, 1H), 5.08 – 4.88 (m, 1H), 4.72 – 4.42 (m, 1H), 4.20 (s, 3H), 2.68 – 2.17 (m, 4H), 1.99 – 1.64 (m, 6H), 1.10 – 0.92 (m, 6H).

^{13}C NMR (75 MHz, CD_3OD) δ 175.3, 173.3, 152.0, 133.6, 130.2, 126.5, 125.8, 125.3, 118.9, 118.3, 117.8, 110.8, 40.9, 40.0, 39.3, 38.2, 37.7, 33.2, 27.4, 27.1, 24.8, 22.0, 20.5.

_N_-((_S_)-1-(((_S_)-1-Cyano-2-((_S_)-2-oxopyrrolidin-3-yl)ethyl)amino)-4-methyl-1-oxopentan-2-yl)-4-hydroxy-6-nitroquinoline-2-carboxamide (33f)

The conversion of the primary amide **32f** to the corresponding nitrile derivative **33f** has been carried out following the general procedure (V) for the nitrile warhead formation. The target molecule has been purified through SiO_2 column chromatography DCM/MeOH (20:1) furnishing a bright yellow oil (43% yield)

ESI-MS *m/z* 483 $[M+H]^+$, 505 $[M+Na]^+$

^{1}H NMR (300 MHz, CD_3OD) δ 10.34 (s, 1H), 8.77 (d, *J* = 3.9 Hz, 1H), 8.53 (ddd, *J* = 9.1, 2.4, 1.5 Hz, 1H), 7.78 (dd, *J* = 9.1, 1.6 Hz, 1H), 5.14 – 4.97 (m, 1H), 4.68 – 4.50 (m, 1H), 3.59 (dt, *J* = 113.9, 4.0 Hz, 2H), 2.71 – 2.18 (m, 3H), 1.85 (ddt, *J* = 24.4, 14.9, 7.6 Hz, 5H), 1.02 (ddd, *J* = 9.9, 6.0, 3.0 Hz, 6H).

^{13}C NMR (75 MHz, CD_3OD) δ 179.5, 179.3, 176.6, 173.3, 145.1, 144.6, 142.8, 126.6, 125.9, 125.9, 121.9, 120.4, 111.8, 40.8, 40.1, 37.7, 33.2, 27.5, 27.2, 24.8, 22.1, 20.7, 20.6.

***tert*-Butyl 8-bromo-1-(((_S_)-1-(((_S_)-1-cyano-2-((_S_)-2-oxopyrrolidin-3-yl)ethyl)amino)-4-methyl-1-oxopentan-2-yl)carbamoyl)-3,4-dihydroisoquinoline-2(1H)-carboxylate (33g)**

The conversion of the primary amide **32g** to the corresponding nitrile derivative **33g** has been carried out following the general procedure (V) for the nitrile warhead formation. The crude mixture has been purified through SiO_2 column chromatography DCM/MeOH (20:1) yielding a colorless oil (26% yield).

ESI-MS *m/z* 453 $[M+H]^+$, 476 $[M+Na]^+$

^{1}H NMR (300 MHz, CD_3OD) δ 7.65 (d, *J* = 24.4 Hz, 1H), 7.37 (t, *J* = 8.9 Hz, 1H), 7.11 (dd, *J* = 12.5, 8.9 Hz, 1H), 5.39 – 5.25 (m, 1H), 5.11 – 4.93 (m, 1H), 4.48 – 4.28

(m, 2H), 3.72 (dt, *J* = 28.3, 11.7 Hz, 2H), 3.08 – 2.86 (m, 2H), 2.62 – 2.18 (m, 4H), 2.10 – 1.96 (m, 1H), 1.87 – 1.62 (m, 5H), 1.49 (s, 9H), 1.01 – 0.83 (m, 6H).

^{13}C NMR (75 MHz, CD_3OD) δ 179.5, 172.9, 172.7, 171.9, 135.1, 134.2, 130.3, 130.2, 129.9, 129.9, 119.4, 118.3, 115.4, 51.9, 51.4, 40.2, 39.9, 37.4, 33.6, 29.3, 27.4, 27.2, 27.2, 26.9, 24.7, 24.4, 22.3.

8-Chloro-*N*-((2*S*,3*S*)-1-(((*S*)-1-cyano-2-((*S*)-2-oxopyrrolidin-3-yl)ethyl)amino)-3-hydroxy-1-oxobutan-2-yl)-1-methyl-4-oxo-1,4-dihydroquinoline-3-carboxamide (33h)

The conversion of the primary amide **32h** to the corresponding nitrile derivative **33h** has been carried out following the general procedure (V) for the nitrile warhead formation. The crude mixture was purified through SiO_2 column chromatography DCM/MeOH (30:1) furnishing a colorless oil (27% yield).

ESI-MS *m/z* 474 $[M+H]^+$, 496 $[M+Na]^+$

^{1}H NMR (300 MHz, CD_3OD) δ 10.57 (d, *J* = 7.3 Hz, 1H), 8.68 (s, 1H), 8.41 (dd, *J* = 8.1, 1.5 Hz, 1H), 7.88 – 7.79 (m, 1H), 7.54 – 7.31 (m, 1H), 5.11 (dd, *J* = 10.1, 6.0 Hz, 1H), 4.47 (dd, *J* = 7.3, 3.7 Hz, 1H), 4.38 (s, 3H), 4.34 (dd, *J* = 6.4, 3.6 Hz, 1H), 3.20 (dd, *J* = 14.8, 7.5 Hz, 1H), 2.68 – 2.22 (m, 4H), 2.01 – 1.65 (m, 2H), 1.25 (d, *J* = 6.4 Hz, 3H).

^{13}C NMR (75 MHz, CD_3OD) δ 179.6, 171.6, 165.6, 152.4, 137.7, 136.6, 130.5, 125.9, 125.9, 125.5, 122.5, 118.4, 110.7, 66.8, 64.6, 59.2, 53.4, 40.0, 37.6, 33.8, 27.2, 19.1.

***N*-((2*S*,3*S*)-3-(Benzyloxy)-1-(((*S*)-1-cyano-2-((*S*)-2-oxopyrrolidin-3-yl)ethyl)amino)-1-oxobutan-2-yl)-8-chloro-1-methyl-4-oxo-1,4-dihydroquinoline-3-carboxamide (33i)**

The conversion of the primary amide **32i** to the corresponding nitrile derivative **33i** has been carried out following the general procedure (V) for the nitrile warhead formation. The crude mixture was purified through SiO_2 column chromatography DCM/MeOH (30:1) furnishing a colorless oil (36% yield).

ESI-MS *m/z* 464 $[M+H]^+$, 486 $[M+Na]^+$

^{1}H NMR (300 MHz, CD_3OD) δ 8.73 (s, 1H), 8.46 (dd, *J* = 8.1, 1.6 Hz, 1H), 7.92 – 7.85 (m, 1H), 7.52 – 7.14 (m, 6H), 5.06 (dd, *J* = 10.1, 5.9 Hz, 1H), 4.77 – 4.47 (m, 3H), 4.39 (d, *J* = 3.7 Hz, 3H), 4.30 (dd, *J* = 6.3, 2.9 Hz, 1H), 3.24 – 2.94 (m, 2H), 2.49 – 2.10 (m, 3H), 1.90 – 1.65 (m, 2H), 1.29 (d, *J* = 2.2 Hz, 3H).

^{13}C NMR (75 MHz, CD_3OD) δ 179.4, 175.5, 171.3, 171.1, 170.8, 165.5, 165.4, 165.2, 152.4, 138.4, 137.4, 136.6, 130.2, 127.9, 127.4, 127.1, 127.1, 125.7, 125.4, 122.4, 118.5, 110.5, 74.4, 70.7, 58.1, 39.9, 37.5, 33.6, 26.9, 15.3.

6-Amino-*N*-((*S*)-1-(((*S*)-1-cyano-2-((*S*)-2-oxopyrrolidin-3-yl)ethyl)amino)-4-methyl-1-oxopentan-2-yl)-4-hydroxyquinoline-2-carboxamide (33j)

To a solution of the final compound **33f** (40 mg, 1 eq) in a mixture of EtOH/H_2O (5:1, 0,82 mL, 0,1 M), solid NH_4Cl (15 mg, 3,3 eq) and iron powder (15 mg, 3,3 eq) were added. The reaction mixture was stirred at 55 °C for 30 min, then the solid was filtered on celite®, and washed with EtOH (3 x 1 mL). The solute was concentrated under pressure, solubilized with EtOAc (3 mL) and washed with aqueous $NaHCO_3$ (3 x 2 mL), then the combined organic phase was dried over anhydrous Na_2SO_4, filtered and concentrated under reduced pressure. The final compound has been purified by SiO_2 column chromatography DCM/MeOH (20:1) furnishing a pale yellow oil (95% yield).

ESI-MS *m/z* 453 $[M+H]^+$, 476 $[M+Na]^+$

^{1}H NMR (300 MHz, CD_3OD) δ 8.58 (s, 1H), 7.98 (bs, 1H), 7.87 (t, *J* = 7.2 Hz, 1H), 7.75 – 7.44 (m, 4H), 7.33 – 7.14 (m, 2H), 6.97 (d, *J* = 7.6 Hz, 1H), 4.64 – 4.47 (m, 2H), 3.77 – 3.59 (m, 1H), 3.25 – 3.08 (m, 1H), 2.68 – 2.22 (m, 3H), 2.04 – 1.63 (m, 5H), 1.00 (dd, *J* = 12.7, 6.1 Hz, 6H).

^{13}C NMR (75 MHz, CD_3OD) δ 180.7, 177.1, 172.8, 153.8, 139.7, 139.5, 138.0, 129.3, 128.8, 128.5, 127.3, 119.7, 75.7, 72.0, 58.7, 41.2, 39.8, 39.7, 38.8, 30.7, 28.4, 28.3, 16.7.

8-Bromo-*N*-((*S*)-1-(((*S*)-1-cyano-2-((*S*)-2-oxopyrrolidin-3-yl)ethyl)amino)-4-methyl-1-oxopentan-2-yl)-1,2,3,4-tetrahydroisoquinoline-1-carboxamide (33k)

Final compound **33g** has then been deprotected allowing to obtain final compound **33k**. In a round bottom flask the final compound **33g** (20 mg, 1 eq) has been solubilized in MeOH (0,66 mL, 0,05 M), the solution was cooled at 0 °C then HCl in MeOH (20 eq, 1 M) has been slowly added. The reaction mixture was stirred at the same temperature for 1 h, then the mixture was concentrated under N_2 flux and the crude mixture was purified by SiO_2 column chromatography using $CHCl_3$/MeOH (30:1) as elution mixture furnishing a pale yellow oil (40% yield).

ESI-MS *m/z* 453 $[M+H]^+$, 476 $[M+Na]^+$

^1H NMR (300 MHz, CD_3OD) δ 7.89 (s, 1H), 7.46 (d, *J* = 9.9 Hz, 1H), 7.30 (d, *J* = 8.3 Hz, 1H), 7.09 – 7.00 (m, 1H), 4.69 – 4.32 (m, 3H), 3.00 – 2.68 (m, 4H), 2.57 – 2.43 (m, 2H), 2.33 – 2.07 (m, 3H), 1.98 – 1.50 (m, 5H), 1.09 – 0.74 (m, 6H).

^{13}C NMR (75 MHz, CD_3OD) δ 201.2, 171.9, 171.6, 158.8, 129.3, 128.6, 127.8, 117.8, 108.7, 76.5, 38.6, 30.8, 30.7, 27.8, 27.5, 25.4, 23.1, 20.6, 18.8.

7.1.5 - Synthetic procedure for the preparation of compound 41

Methyl (S)-2-((((9H-fluoren-9-yl)methoxy)carbonyl)amino)-3-azidopropanoate (35)

In an oven dried round bottom flask, the non-natural amino acid methyl (*S*)-2-((((9H-fluoren-9-yl)methoxy)carbonyl)amino)-3-azidopropanoate **34** (500 mg, 1 eq) was suspended in anhydrous MeOH (5,6 mL, 0,25M) and the mixture was cooled at 0 °C, then chlorotrimethylsilane (TMSCl) (340 mg, 2,2 eq) was slowly added and the reaction was allowed to reach room temperature and stirred in these conditions for 12 h. After this time the reaction mixture was cooled at 0 °C and TEA (0,43 mL, 2,2 eq) was slowly added. The reaction mixture was concentrated under N_2 flux and the solid precipitate was filtered off and washed with Et_2O. ~~so~~ The organic phase was dried over Na_2SO_4, filtered and concentrated under vacuum. The compound was purified by SiO_2 column chromatography PetEt/EtOAc (2:1) yielding **35** as a colorless oil (73% yield).

ESI-MS *m/z* 366 $[M+H]^+$

^{1}H NMR (300 MHz, $CDCl_3$) δ 7.77 (d, *J* = 7.4 Hz, 2H), 7.60 (d, *J* = 7.2 Hz, 2H), 7.37 (dt, *J* = 26.1, 7.3 Hz, 4H), 5.63 (dd, *J* = 4.1, 1.3 Hz, 1H), 4.63 – 4.50 (m, 1H), 4.50 – 4.36 (m, 2H), 4.24 (t, *J* = 7.0 Hz, 1H), 3.82 (s, 3H), 3.80 – 3.72 (m, 2H).

Methyl (*S*)-2-((((9*H*-fluoren-9-yl)methoxy)carbonyl)amino)-3-(1*H*-1,2,3-triazol-1-yl)propanoate (36)

In a round bottom flask, to a solution of **36** (200mg, 1 eq) in water/*tert*-butanol/DMSO (1:1:0,01, 20 mL, 0,025 M), sodium ascorbate (32 mg, 0,3 eq) and $CuSO_4$ (9 mg, 0,1 eq) were added at once, then TMS-acetylene (113 mg, 2,1 eq) was slowly added. The reaction mixture was stirred for 96 h, then NBu_4F (129 mg, 1,5 eq) was slowly added. After 4 h, the mixture was washed with EtOAc (3 x 4 mL), and the organic phase was dried over Na_2SO_4, filtered and concentrated under reduced pressure. The resulting residue was purified by SiO_2 column chromatography PetEt/EtOAc (1:1) affording a white amorphous solid (67% yield).

ESI-MS *m/z* 383 $[M+H]^+$, 405 $[M+Na]^+$

^{1}H NMR (300 MHz, $CDCl_3$) δ 7.77 (d, *J* = 7.5 Hz, 2H), 7.66 (s, 1H), 7.57 (d, *J* = 7.3 Hz, 2H), 7.36 (ddd, *J* = 22.1, 14.8, 7.3 Hz, 5H), 5.68 (d, *J* = 6.0 Hz, 1H), 4.98 – 4.71 (m, 3H), 4.57 – 4.37 (m, 2H), 4.21 (t, *J* = 6.5 Hz, 1H), 3.79 (s, 3H).

Methyl (S)-2-amino-3-(1H-1,2,3-triazol-1-yl)propanoate (37)

In a round bottom flask, to a solution of **36** (50 mg, 1 eq) in dry DCM (0,2 mL, 0,6 M), diethylamine (123 mg, 14 eq) was slowly added. The reaction mixture was stirred at 20 °C for 2 h, then after completion of the reaction, monitored by TLC, the mixture was dried under N_2 flux. The crude product was purified by SiO_2 column chromatography using DCM/MeOH (20:1) as eluent, affording a white amorphous solid (73% yield).

ESI-MS *m/z* 171 $[M+H]^+$, 193 $[M+Na]^+$

^{1}H NMR (300 MHz, $CDCl_3$) δ 7.68 (d, *J* = 4.1 Hz, 2H), 4.73 (dd, *J* = 13.8, 4.5 Hz, 1H), 4.57 (dd, *J* = 13.8, 6.7 Hz, 1H), 3.98 (dd, *J* = 6.6, 4.6 Hz, 1H), 3.75 (s, 3H), 1.81 (bs, 2H).

Methyl (S)-2-((S)-2-((*tert*-butoxycarbonyl)amino)-4-methylpentanamido)-3-(1H-1,2,3-triazol-1-yl)propanoate (38)

Compound **38** was synthesized according to the general procedure (II) for coupling reaction using (*tert*-butoxycarbonyl)-*L*-leucine as the appropriate carboxylic acid. The mixture was used without any further purification, affording a colorless oil (89% yield).

ESI-MS *m/z* 384 $[M+H]^+$, 406 $[M+Na]^+$

^{1}H NMR (300 MHz, CD_3OD) δ 7.81 (d, J = 7.5 Hz, 1H), 7.68 (d, J = 7.5 Hz, 1H), 4.67 – 4.56 (m, 3H), 4.27 (m, 6.6 Hz, 1H), 3.79 (s, 3H), 1.93 (t, J = 7.6 Hz, 1H), 1.74 – 1.61 (m, 1H), 1.54 – 1.49 (m, 10H), 1.07 – 0.98 (m, 6H).

Methyl (*S*)-2-((*S*)-2-(8-chloro-1-methyl-4-oxo-1,4-dihydroquinoline-3-carboxamido)-4-methylpentanamido)-3-(1H-1,2,3-triazol-1-yl)propanoate (39)

Compound **39** was synthesized according to the general procedures (I-II) for Boc-cleavage and coupling reaction using 8-chloro-1-methyl-4-oxo-1,4-dihydroquinoline-3-carboxylic acid as the appropriate carboxylic acid. The crude mixture was purified by column chromatography DCM/MeOH (30:1), affording a colorless oil (64% yield).

ESI-MS *m/z* 504 $[M+H]^+$, 526 $[M+Na]^+$

^{1}H NMR (300 MHz, CD_3OD) δ 10.29 (d, *J* = 6.7 Hz, 1H), 8.70 (d, *J* = 2.8 Hz, 1H), 8.40 (d, *J* = 8.1 Hz, 1H), 8.05 (dd, *J* = 8.6, 0.9 Hz, 1H), 7.87 (ddd, *J* = 7.7, 3.4, 1.6 Hz, 1H), 7.74 – 7.64 (m, 1H), 7.44 (td, *J* = 7.9, 2.4 Hz, 1H), 5.13 – 4.72 (m, 3H), 4.57 (dd, *J* = 18.6, 12.9 Hz, 1H), 4.40 (d, *J* = 1.5 Hz, 3H), 3.76 (s, 3H), 1.83 – 1.56 (m, 3H), 0.96 (ddd, *J* = 7.5, 6.3, 2.3 Hz, 6H).

***N*-((*S*)-1-(((*S*)-1-Amino-1-oxo-3-(1H-1,2,3-triazol-1-yl)propan-2-yl)amino)-4-methyl-1-oxopentan-2-yl)-8-chloro-1-methyl-4-oxo-1,4-dihydroquinoline-3-carboxamide (40)**

For the synthesis of compound **40**, the general procedure (IV) for the primary amide conversion has been followed using **39** as starting material. The crude product, a

white amorphous solid, has been used immediately for the following reaction without any further purification (95% yield).

ESI-MS *m/z* 489 $[M+H]^+$, 511 $[M+Na]^+$

8-Chloro-*N*-((*S*)-1-(((*S*)-1-cyano-2-(1H-1,2,3-triazol-1-yl)ethyl)amino)-4-methyl-1-oxopentan-2-yl)-1-methyl-4-oxo-1,4-dihydroquinoline-3-carboxamide (41)

The conversion of the primary amide **40** to the corresponding nitrile derivative **41** has been carried out following the general procedure (V) for the nitrile warhead formation. The crude mixture has been purified by SiO_2 column chromatography DCM/MeOH (20:1) yielding a colorless oil (37%).

ESI-MS *m/z* 470 $[M+H]^+$, 492 $[M+Na]^+$

^{1}H NMR (300 MHz, CD_3OD) δ 10.33 (d, *J* = 5.8 Hz, 1H), 8.71 (d, *J* = 3.6 Hz, 1H), 8.48 – 8.37 (m, 1H), 8.10 (d, *J* = 15.2 Hz, 1H), 7.89 (dd, *J* = 7.7, 1.5 Hz, 1H), 7.74 (d, *J* = 3.7 Hz, 1H), 7.46 (dd, *J* = 9.2, 6.6 Hz, 1H), 5.42 (dd, *J* = 13.4, 6.3 Hz, 1H), 4.95 – 4.87 (m, 2H), 4.50 (dd, *J* = 9.3, 5.2 Hz, 1H), 4.39 (d, *J* = 4.8 Hz, 3H), 1.78 – 1.54 (m, 3H), 1.01 – 0.90 (m, 6H).

^{13}C NMR (75 MHz, CD_3OD) δ 175.7, 173.4, 165.0, 152.4, 137.8, 136.7, 133.3, 130.5, 125.9, 125.6, 125.5, 122.6, 115.5, 110.4, 52.0, 51.9, 49.6, 40.7, 24.7, 21.9, 20.5.

7.1.6 - Synthetic procedure for the preparation of compounds 46a-b and 47

Methyl (*tert*-butoxycarbonyl)-*L*-leucyl-*L*-threoninate (43a)

Compound **43a** was synthesized according to general procedures (I-II) for Boc-cleavage and coupling reaction using (*tert*-butoxycarbonyl)-*L*-leucine as the appropriate carboxylic acid.

MS-ESI and ^{1}H NMR data are in accordance with those reported in literature.

Methyl (*tert*-butoxycarbonyl)-*L*-leucyl-*L*-histidinate (43b)

Compound **43b** was synthesized according to general procedures (I-II) for Boc-cleavage and coupling reaction using (*tert*-butoxycarbonyl)-*L*-leucine as the appropriate carboxylic acid.

MS-ESI and ^{1}H NMR data are in accordance with those reported in literature.

Methyl (8-chloro-1-methyl-4-oxo-1,4-dihydroquinoline-3-carbonyl)-*L*-leucyl-*L*-threoninate (44a)

Compound **44a** was synthesized according to general procedures (I-II) for Boc-cleavage and coupling reaction using 8-chloro-1-methyl-4-oxo-1,4-dihydroquinoline-3-carboxylic acid as the appropriate carboxylic acid. The mixture was purified by SiO_2 column chromatography eluting with DCM/MeOH (30:1) yielding a pale yellow oil (61% yield).

ESI-MS *m/z* 470 $[M+H]^+$, 492 $[M+Na]^+$

^{1}H NMR (300 MHz, Acetone-d6) δ 10.23 (d, *J* = 7.7 Hz, 1H), 8.69 (s, 1H), 8.41 (d, 1H), 7.89 –7.84 (m, 1H), 7.48 (dd, *J* = 7.9, 3.2 Hz, 1H), 4.90 – 4.78 (m, 1H), 4.43 (s, 1H), 4.31 – 4.26 (m, 1H), 3.92 (dq, *J* = 13.2, 6.6 Hz, 1H), 3.69 (s, 1H), 2.05 (dt, *J* = 4.4, 2.2 Hz,1H), 1.86 – 1.68 (m, H), 1.17 (d, *J* = 6.3 Hz, 1H), 0.97 (dd, *J* = 11.3, 5.9 Hz, 3H).

Methyl (8-chloro-1-methyl-4-oxo-1,4-dihydroquinoline-3-carbonyl)-*L*-leucyl-*L*-histidinate (44b)

Compound **44b** was synthesized according to general procedures (I-II) for Boc-cleavage and coupling reaction using 8-chloro-1-methyl-4-oxo-1,4-dihydroquinoline-3-carboxylic acid as the appropriate carboxylic acid. The mixture was purified by SiO_2 column chromatography eluting with DCM/MeOH (30:1) yielding a colorless oil (68% yield).

ESI-MS *m/z* 470 $[M+H]^+$, 492 $[M+Na]^+$

^{1}H NMR (300 MHz, CD_3OD) δ 10.36 (d, *J* = 6.5 Hz, 1H), 8.67 (s, 1H), 8.38 (t, *J* = 6.9 Hz, 1H), 7.90 – 7.76 (m, 1H), 7.43 (t, *J* = 8.2 Hz, 1H), 6.92 (s, 1H), 4.69 (m, 1H),

4.52 (m, 1H), 4.43 – 4.25 (s, 3H), 3.4 (s, 3H), 3.30 (dt, *J* = 3.4, 1.8 Hz, 1H), 3.22 – 2.95 (m, 1H), 1.89 – 1.54 (m, 3H), 1.06 (dt, *J* = 13.9, 7.1 Hz, 6H).

_N_-((_S_)-1-(((2_S_,3_S_)-1-Amino-3-hydroxy-1-oxobutan-2-yl)amino)-4-methyl-1-oxopentan-2-yl)-8-chloro-1-methyl-4-oxo-1,4-dihydroquinoline-3-carboxamide (45a)

For the synthesis of compound **45a**, the general procedure (IV) for the primary amide conversion has been followed using the ester intermediate **44a** as starting material. The crude product, a white amorphous solid, has been used immediately for the following reaction without any further purification (68% yield).

ESI-MS *m/z* 470 $[M+H]^+$, 492 $[M+Na]^+$

_N_-((_S_)-1-(((_S_)-1-Amino-3-(1H-imidazol-4-yl)-1-oxopropan-2-yl)amino)-4-methyl-1-oxopentan-2-yl)-8-chloro-1-methyl-4-oxo-1,4-dihydroquinoline-3-carboxamide (45b)

For the synthesis of compound **45b**, the general procedure (IV) for the primary amide conversion has been followed using the ester intermediate **44b** as starting material. The crude product, a white amorphous solid, has been used for the following reaction without any further purification (88% yield).

ESI-MS *m/z* 470 $[M+H]^+$, 492 $[M+Na]^+$

8-Chloro-_N_-((_S_)-1-(((1_R_,2_S_)-1-cyano-2-hydroxypropyl)amino)-4-methyl-1-oxopentan-2-yl)-1-methyl-4-oxo-1,4-dihydroquinoline-3-carboxamide (46a)

The conversion of the primary amide **45a** to the corresponding nitrile derivative **46a** has been carried out following the general procedure (V) for the nitrile warhead formation. The mixture was purified by SiO_2 column chromatography eluting with DCM/MeOH (30:1) yielding a colorless oil (41% yield).

ESI-MS *m/z* 470 $[M+H]^+$, 492 $[M+Na]^+$

^1H NMR (300 MHz, CD_3OD) δ 10.39 (d, *J* = 6.9 Hz, 1H), 8.70 (s, 1H), 8.43 (dd, *J* = 8.1, 1.5 Hz, 1H), 7.89 (dd, *J* = 7.7, 1.5 Hz, 1H), 7.46 (t, *J* = 7.9 Hz, 1H), 4.63 (d, *J* =

4.1 Hz, 1H), 4.38 (s, 3H), 4.04 (dd, *J* = 11.9, 5.7 Hz, 1H), 1.76 (dt, *J* = 15.0, 9.5 Hz, 3H), 1.28 (d, *J* = 6.3 Hz, 3H), 1.16 (dd, *J* = 15.4, 7.0 Hz, 1H), 1.01 (dd, *J* = 11.8, 6.2 Hz, 6H).

^{13}C NMR (75 MHz, CD_3OD) δ 175.7, 173.4, 165.0, 152.3, 137.7, 136.7, 130.5, 125.9, 125.6, 122.5, 117.2, 110.4, 66.5, 51.9, 40.9, 24.8, 22.1, 20.6, 17.7.

8-Chloro-N-((*S*)-1-(((*S*)-1-cyano-2-(1*H*-imidazol-4-yl)ethyl)amino)-4-methyl-1-oxopentan-2-yl)-1-methyl-4-oxo-1,4-dihydroquinoline-3-carboxamide (46b)

The conversion of the primary amide **45b** to the corresponding nitrile derivative **46b** has been carried out following the general procedure (V) for the nitrile warhead formation. The mixture was purified by SiO_2 column chromatography eluting with DCM/MeOH (30:1) yielding a colorless oil (37% yield).

ESI-MS *m/z* 470 $[M+H]^+$, 492 $[M+Na]^+$

^{1}H NMR (300 MHz, CD_3OD) δ 8.72 (s, 1H), 8.45 (dd, *J* = 8.1, 1.5 Hz, 1H), 7.94 – 7.84 (m, 1H), 7.59 (s, 1H), 7.48 (t, *J* = 7.9 Hz, 1H), 7.02 (s, 1H), 5.05 (t, *J* = 7.4 Hz, 1H), 4.56 (dd, *J* = 9.2, 5.7 Hz, 1H), 4.40 (s, 3H), 3.13 (dd, *J* = 7.3, 4.0 Hz, 1H), 1.84 – 1.54 (m, 4H), 0.98 (dd, *J* = 12.2, 6.3 Hz, 6H).

^{13}C NMR (75 MHz, CD_3OD) δ 175.6, 173.1, 165.0, 152.3, 137.7, 136.7, 130.4, 125.9, 125.6, 122.6, 117.7, 110.4, 78.0, 51.9, 40.9, 40.6, 31.3, 29.3, 24.7, 22.0, 20.6, 12.9.

8-Chloro-*N*-((2*S*)-1-(((1*R*,2*S*)-1-cyano-2-((tetrahydrofuran-2-yl)oxy)propyl)amino)-4-methyl-1-oxopentan-2-yl)-1-methyl-4-oxo-1,4-dihydroquinoline-3-carboxamide (47)

In a glass vial under N_2 atmosphere, the final compound **46a** (10 mg, 1 eq) was solubilized in anhydrous DCM (0,5 mL, 0,04 M), then 2,3-dihydrofuran (3 mg, 1,5 eq) was added, followed by a solution (0,006 M) of PTSA (2 mg, 0,15 eq) in DCM (0,5 mL). The reaction mixture was stirred for 12 h at 20 °C, was dried under N_2 flux. The mixture was directly purified by SiO_2 column chromatography using $CHCl_3$/MeOH (30:1) as elution mixture, affording a white amorphous solid (44% yield).

ESI-MS *m/z* 470 $[M+H]^+$, 492 $[M+Na]^+$

^{1}H NMR (300 MHz, CD_3OD) δ 8.71 (s, 1H), 8.46 (d, *J* = 8.1 Hz, 1H), 7.91 (d, *J* = 7.9 Hz, 1H), 7.48 (t, *J* = 7.9 Hz, 1H), 4.69 – 4.57 (m, 1H), 4.39 (s, 3H), 4.14 – 3.72 (m, 2H), 2.09 – 1.51 (m, 5H), 1.44 – 1.17 (m, 8H), 1.08 – 0.73 (m, 6H).

7.1.7 – Synthetic procedure for the preparation of compound 54

tert-Butyl ((1*R*,2*S*)-2-((_tert_-butyldimethylsilyl)oxy)-1-cyanopropyl)carbamate (52)

Compounds **49-52** were prepared according to literature procedures.

Spectroscopic data are in agreement with those previously reported in literature [291].

Methyl *N*-((_tert_-butoxycarbonyl)-*L*-leucyl)-*O*-(_tert_-butyldimethylsilyl)-*L*-threoninate (53)

Compound **53** was synthesized according to general procedures (I-II) for Boc-cleavage and coupling reaction using (*tert*-butoxycarbonyl)-*L*-leucine as the appropriate carboxylic acid. Intermediate **53** was obtained as a yellow solid after purification through SiO_2 column chromatography using as mobile phase PetEt/EtOAc (4:1), 108 mg (40% yield).

ESI-MS *m/z* 450 $[M+H]^+$.

^{1}H NMR (300 MHz, $CDCl_3$) δ 4.80-4.70 (m, 1H), 4.50-4.38 (m, 1H), 4.20-4.10 (m, 1H), 1.97 (m, 2H), 1.63-0.74 (m, 28H), 0.30-0.21 (m, 6H).

Methyl *O*-(_tert_-butyldimethylsilyl)-*N*-((8-chloro-1-methyl-4-oxo-1,4-dihydroquinoline-3-carbonyl)-*L*-leucyl)-*L*-threoninate (54)

Final compound **54** was synthesized according to the general procedures (I-II) for Boc-cleavage and coupling reaction using 8-chloro-1-methyl-4-oxo-1,4-dihydroquinoline-3-carboxylic acid as the appropriate carboxylic acid. **54** was purified with flash column chromatography, eluent PetEt/EtOAc (1:1) a colorless oil (65% yield).

ESI-MS *m/z* 548 $[M+H]^+$ 570 $[M+Na]^+$, 546 $[M-H]^-$.

^{1}H NMR (300 MHz, CD_3OD) δ 10.05 (d, *J* = 7.3 Hz, 1H), 8.47 – 8.22 (m, 1H), 8.07 (dd, *J* = 8.1, 1.7 Hz, 1H), 7.64 – 7.44 (m, 1H), 7.28 – 7.02 (m, 1H), 4.67 – 4.41 (m, 1H), 4.41 – 4.14 (m, 1H), 4.05 (d, *J* = 2.4 Hz, 1H), 1.62 – 1.30 (m, 3H), 1.21 – 0.75 (m, 8H), 0.79 – 0.22 (m, 14H), -0.11 – -0.42 (m, 6H).

^{13}C NMR (75 MHz, CD_3OD) δ 175.3, 172.9, 164.7, 164.6, 152.0, 137.3, 136.4, 130.1, 125.6, 125.3, 122.2, 116.8, 110.1, 81.5, 67.5, 51.4, 26.7, 24.5, 24.4 (2C), 21.8, 20.3, 18.1, 17.0, -6.2, -6.5.

7.1.8 – Synthetic procedure for the preparation of compound 58

Methyl (6*S*,9*S*,12*S*)-9-isobutyl-6-isopropyl-2,2-dimethyl-4,7,10-trioxo-12-(((*S*)-2-oxopyrrolidin-3-yl)methyl)-3-oxa-5,8,11-triazatridecan-13-oate (55)

Compound **55** was synthesized according to general procedures (I-II) for Boc-cleavage and coupling reaction using (*tert*-butoxycarbonyl)-*L*-valine as the appropriate carboxylic acid, and the previously prepared ester intermediate **20** as starting material.

ESI-MS and 1H NMR data are in accordance with those reported in literature.

Methyl (*S*)-2-((*S*)-2-((*R*)-2-(8-chloro-1-methyl-4-oxo-1,4-dihydroquinoline-3-carboxamido)-3-methylbutanamido)-4-methylpentanamido)-3-((*S*)-2-oxopyrrolidin-3-yl)propanoate (56)

Compound **56** was synthesized according to general procedures (I-II) for Boc-cleavage and coupling reaction using 8-chloro-1-methyl-4-oxo-1,4-dihydroquinoline-3-carboxylic acid as the appropriate carboxylic acid. The mixture was purified by SiO_2 column chromatography eluting with DCM/MeOH (30:1) yielding a colorless oil (61% yield).

ESI-MS *m/z* 618 $[M+H]^+$ 640 $[M+Na]^+$

^{1}H NMR (300 MHz, $CDCl_3$) δ 10.36 (dd, *J* = 16.8, 7.2 Hz, 1H), 8.67 (d, *J* = 19.3 Hz, 1H), 8.40 (d, *J* = 7.8 Hz, 1H), 8.13 (dd, *J* = 36.4, 7.4 Hz, 1H), 7.86 – 7.58 (m, 1H), 7.36 – 7.18 (m, 2H), 6.87 (s, 1H), 4.72 – 4.40 (m, 3H), 4.34 (s, 3H), 3.67 (s, 3H), 3.37 – 3.18 (m, 2H), 2.58 – 2.19 (m, 4H), 1.91 – 1.39 (m, 5H), 1.12 – 0.75 (m, 12H).

_N_-((_S_)-1-(((_S_)-1-(((_S_)-1-Amino-1-oxo-3-((_S_)-2-oxopyrrolidin-3-yl)propan-2-yl)amino)-4-methyl-1-oxopentan-2-yl)amino)-3-methyl-1-oxobutan-2-yl)-8-chloro-1-methyl-4-oxo-1,4-dihydroquinoline-3-carboxamide (57)

For the synthesis of compound **57**, the general procedure (IV) for the primary amide conversion has been followed using the ester intermediate **56** as starting material. The crude product, a white amorphous solid, has been used immediately for the following reaction without any further purification (88% yield).

ESI-MS *m/z* 604 $[M+H]^+$ 626 $[M+Na]^+$

8-Chloro-_N_-((_S_)-1-(((_S_)-1-(((_S_)-1-cyano-2-((S)-2-oxopyrrolidin-3-yl)ethyl)amino)-4-methyl-1-oxopentan-2-yl)amino)-3-methyl-1-oxobutan-2-yl)-1-methyl-4-oxo-1,4-dihydroquinoline-3-carboxamide (58)

The conversion of the primary amide **57** to the corresponding nitrile derivative **58** has been carried out following the general procedure (V) for the nitrile warhead formation. The mixture was purified by SiO_2 column chromatography eluting with DCM/MeOH (30:1) yielding a colorless oil (18% yield).

ESI-MS *m/z* 586 $[M+H]^+$ 608 $[M+Na]^+$

^1H NMR (300 MHz, CD_3OD) δ 10.58 – 10.47 (m, 1H), 8.80 – 8.68 (m, 1H), 8.58 (dd, *J* = 15.2, 8.2 Hz, 1H), 8.47 – 8.39 (m, 1H), 8.23 (d, *J* = 8.5 Hz, 1H), 7.89 (d, *J* = 7.5 Hz, 1H), 7.73 (dd, *J* = 8.8, 4.3 Hz, 1H), 7.47 (t, *J* = 7.9 Hz, 1H), 4.40 (s, 3H), 4.70 – 4.13 (m, 3H), 3.23 – 3.07 (m, 1H), 2.58 – 2.15 (m, 5H), 1.92 – 1.57 (m, 5H), 1.12 – 0.87 (m, 12H).

^{13}C NMR (75 MHz, CD_3OD) δ 175.8, 173.3, 172.5, 152.4, 137.8, 136.7, 130.5, 125.9, 125.6, 122.6, 110.7, 59.0, 51.6, 51.3, 40.1, 38.4, 32.3, 30.7, 29.5, 29.3, 27.9, 27.7, 24.4, 22.3, 21.9, 20.5, 18.7, 16.9.

7.1.9 – Synthetic procedure for the preparation of compounds 62a,b, 63 and 66

Methyl (S)-2-((2S,3S)-2-((_tert_-butoxycarbonyl)amino)-3-methylpentanamido)-3-((S)-2-oxopyrrolidin-3-yl)propanoate (59)

Compound **59** was synthesized according to general procedures (I-II) for Boc-cleavage and coupling reaction using (*tert*-butoxycarbonyl)-*L*-isoleucine as the appropriate carboxylic acid. The crude mixture was purified through SiO_2 column chromatography DCM/MeOH (30:1) affording a colorless oil (91% yield).

ESI-MS *m/z* 400 $[M+H]^+$ 422 $[M+Na]^+$

^1H NMR (300 MHz, $CDCl_3$) δ 7.79 (d, *J* = 7.1 Hz, 1H), 5.25 (d, *J* = 6.3 Hz, 1H), 4.16 – 3.96 (m, 2H), 3.71 (d, *J* = 3.2 Hz, 3H), 3.32 (d, *J* = 6.5 Hz, 2H), 2.55 – 2.28 (m, 2H), 2.22 – 1.72 (m, 5H), 1.40 (s, 9H), 1.28 – 1.20 (m, 1H), 0.92 (dd, *J* = 9.8, 6.4 Hz, 6H).

Methyl (*S*)-2-((2*S*,3*S*)-3-methyl-2-(quinoline-8-carboxamido)pentanamido)-3-((*S*)-2-oxopyrrolidin-3-yl)propanoate (60)

Compound **60** was synthesized according to general procedures (I-II) for Boc-cleavage and coupling reaction using quinoline-8-carboxylic acid as the appropriate carboxylic acid. The mixture was purified by SiO_2 column chromatography eluting with DCM/MeOH (20:1), affording a colorless oil (66% yield)

ESI-MS *m/z* 455 $[M+H]^+$ 477 $[M+Na]^+$

^1H NMR (300 MHz, $CDCl_3$) δ 11.88 (d, *J* = 8.4 Hz, 1H), 8.98 (d, *J* = 3.9 Hz, 1H), 8.78 (d, *J* = 7.4 Hz, 1H), 8.26 (d, *J* = 8.3 Hz, 1H), 7.95 (d, *J* = 8.1 Hz, 1H), 7.64 (t, *J* = 7.7 Hz, 1H), 7.48 (dd, *J* = 7.3, 4.3 Hz, 1H), 7.02 – 6.55 (m, 1H), 5.00 – 4.42 (m, 2H), 3.70 (s, 3H), 3.27 (dt, *J* = 9.4, 7.5 Hz, 2H), 2.54 – 2.01 (m, 4H), 1.95 – 1.59 (m, 2H), 1.47 – 1.13 (m, 2H), 1.14 – 0.90 (m, 6H).

<u>General procedure (VI) for ester reduction to alcohol</u> exemplified with compound *N*-((*S*)-1-(((*S*)-1-hydroxy-3-((*S*)-2-oxopyrrolidin-3-yl)propan-2-yl)amino)-4-methyl-1-oxopentan-2-yl)quinoline-8-carboxamide (61a)

In a round bottom flask the ester intermediate **21** (60 mg, 1 eq) was solubilized in anhydrous MeOH (0,8 mL, 0,15 M) in N_2 atmosphere and cooled at 0 °C. Then sodium borohydride ($NaBH_4$) (40 mg, 8 eq) was carefully added, the reaction mixture was allowed to reach 20 °C and stirred for 10 h. After this time an aqueous solution

of NH_4Cl (1 mL) was slowly added, and the water phase was extracted with EtOAc (3 x 3 mL). The combined organic phase was dried over Na_2SO_4, filtered and concentrated under vacuum. The crude mixture was then purified by SiO_2 column chromatography using DCM/MeOH (20:1) as elution mixture, affording a white amorphous solid (68% yield).

ESI-MS *m/z* 427 $[M+H]^+$ 449 $[M+Na]^+$

^1H NMR (300 MHz, CD_3OD) δ 8.92 (dd, J = 7.5, 1.4 Hz, 1H), 8.23 – 8.03 (m, 1H), 7.91 (dt, J = 7.5, 1.4 Hz, 1H), 7.53 (t, J = 7.5 Hz, 1H), 7.38 (t, J = 7.5 Hz, 1H), 4.54 (t, J = 3.4 Hz, 1H), 3.96 – 3.51 (m, 1H), 3.51 – 3.26 (m, J = 51.7, 12.6, 6.4 Hz, 1H), 2.42 (ddd, J = 14.7, 8.4, 4.7 Hz, 1H), 2.28 – 1.83 (m, 1H), 1.78 – 1.46 (m, 1H), 0.95 (d, J = 6.3 Hz, 1H).

_N_-((2_S_,3_S_)-1-(((_S_)-1-Hydroxy-3-((_S_)-2-oxopyrrolidin-3-yl)propan-2-yl)amino)-3-methyl-1-oxopentan-2-yl)quinoline-8-carboxamide (61b)

Compound **61b** has been synthesized starting from ester intermediate **60** following the general procedure (VI) for ester reduction to alcohol previously reported. The mixture was purified by SiO_2 column chromatography using DCM/MeOH (20:1) as eluent yielding a colorless oil (65% yield).

ESI-MS *m/z* 427 $[M+H]^+$ 449 $[M+Na]^+$

^1H NMR (300 MHz, CD_3OD) δ 11.94 (dd, *J* = 23.2, 7.8 Hz, 1H), 9.02 (dd, *J* = 4.2, 1.7 Hz, 1H), 8.77 – 8.56 (m, 1H), 8.46 (dd, *J* = 8.4, 1.6 Hz, 1H), 8.30 – 8.00 (m, 1H), 7.89 – 7.45 (m, 2H), 5.48 (s, 1H), 4.69 – 4.49 (m, 1H), 4.17 – 3.90 (m, 1H), 3.64 – 3.39 (m, 2H), 3.23 – 3.07 (m, 2H), 2.62 – 2.24 (m, 2H), 2.17 – 1.93 (m, 2H), 1.80 – 1.32 (m, 4H), 1.12 – 0.95 (m, 6H).

General procedure (VII) for the conversion of the alcohol moiety in aldehyde warhead exemplified by compound _N_-((_S_)-4-methyl-1-oxo-1-(((_S_)-1-oxo-3-((_S_)-2-oxopyrrolidin-3-yl)propan-2-yl)amino)pentan-2-yl)quinoline-8-carboxamide (62a)

In a two-necked oven-dried round bottom flask under N_2 atmosphere, the alcohol intermediate **61a** (36 mg, 1 eq) was solubilized in anhydrous DCM (1,2 mL, 0,07 M) and cooled at 0 °C. Then Dess-Martin periodinane (DMP) (286 mg, 8 eq) was added in one portion. The reaction mixture was stirred at 0°C for 30 min then an aqueous solution of $NaHCO_3$ (2 mL) was added and the water phase was extracted with DCM (3 x 2 mL). The combined organic phase was washed with Na_2SO_3 (3 x 1 mL) and brine (3 x 1 mL), dried over anhydrous Na_2SO_4, filtered, and concentrated under vacuum. The crude mixture was purified by SiO_2 column chromatography DCM/MeOH (15:1) as eluent affording a colorless oil (72% yield).

ESI-MS *m/z* 425 $[M+H]^+$ 447 $[M+Na]^+$

^{1}H NMR (300 MHz, $CDCl_3$) δ 11.67 (d, *J* = 7.2 Hz, 1H), 9.56 (s, 1H), 8.96 (d, *J* = 2.5 Hz, 1H), 8.80 (d, *J* = 7.4 Hz, 1H), 8.29 (d, *J* = 8.2 Hz, 1H), 7.98 (d, *J* = 7.9 Hz, 1H), 7.67 (t, *J* = 7.8 Hz, 1H), 7.51 (dd, *J* = 8.2, 4.3 Hz, 1H), 4.96 – 4.81 (m, Hz, 1H), 4.62 – 4.39 (m, 1H), 3.21 (dt, *J* = 15.0, 6.9 Hz, 2H), 2.61 – 1.67 (m, 8H), 1.09 – 0.88 (m, 6H).

^{13}C NMR (75 MHz, $CDCl_3$) δ 199.7, 172.8, 168.7, 166.2, 149.6, 141.4, 137.8, 133.9, 132.6, 131.4, 127.8, 126.5, 121.0, 94.4, 58.9, 57.5, 40.7, 37.2, 28.3, 25.3, 16.0, 15.1, 11.6.

_N_-((2_S_,3_S_)-3-Methyl-1-oxo-1-(((_S_)-1-oxo-3-((_S_)-2-oxopyrrolidin-3-yl)propan-2-yl)amino)pentan-2-yl)quinoline-8-carboxamide (62b)

The final aldehydic compound **62b** has been synthesized starting from the alcohol intermediate **61b**, following the general procedure (VII) for the conversion of the alcohol moiety in aldehyde warhead previously reported. The crude mixture was purified by column chromatography using DCM/MeOH (15:1) as eluting mixture (71% yield).

ESI-MS *m/z* 425 $[M+H]^+$ 447 $[M+Na]^+$

^{1}H NMR (300 MHz, CD_3OD) δ 12.07 – 11.81 (m, 1H), 9.53 (s, 1H), 9.02 (dd, *J* = 4.3, 1.7 Hz, 1H), 8.63 (d, *J* = 7.3 Hz, 1H), 8.47 (dd, *J* = 8.3, 1.4 Hz, 1H), 8.12 (dd, *J* = 11.9, 5.1 Hz, 1H), 7.71 (t, *J* = 7.8 Hz, 1H), 7.62 (dd, *J* = 8.3, 4.3 Hz, 2H), 4.68 – 4.57

(m, 1H), 4.57 – 4.43 (m, 1H), 4.08 – 3.95 (m, 1H), 3.24 – 3.03 (m, 2H), 2.59 – 2.01 (m, 3H), 1.84 – 1.33 (m, 4H), 1.16 – 0.95 (m, 6H).

^{13}C NMR (75 MHz, CD_3OD) δ 181.3, 172.8, 166.6, 149.9, 145.3, 137.8, 132.8, 132.5, 128.7, 128.0, 126.0, 121.3, 98.2, 59.1, 51.5, 40.0, 38.0, 37.3, 29.1, 27.4, 24.9, 14.9, 10.4.

_N_-((2_S_,3_R_)-1-(((2_S_)-1-Cyano-1-hydroxy-3-((_S_)-2-oxopyrrolidin-3-yl)propan-2-yl)amino)-3-methyl-1-oxopentan-2-yl)quinoline-8-carboxamide (63)

In a round bottom flask the final compound **62b** (30 mg, 1 eq) was solubilized in DCM (1,3 mL, 0,05 M), then an aqueous solution (8 M) of $NaHSO_3$ (10 mg, 1,3 eq) was added drop-by-drop. The reaction mixture was stirred at 20 °C for 30 min, after this time an aqueous solution (1,6 M) of KCN (5,5 mg, 1,2 eq) was slowly added. The reaction mixture, closed with a rubber stopper, was stirred at 20 °C for 12 h, and then was extracted with DCM (3 x 2 mL). The combined organic phase was dried over Na_2SO_4, filtered and concentrated under vacuum. The crude mixture was purified by SiO_2 column chromatography using DCM/MeOH (20:1) as eluting mixture, affording a colorless oil (63% yield).

ESI-MS *m/z* 452 $[M+H]^+$ 474 $[M+Na]^+$

^{1}H NMR (300 MHz, CD_3OD) δ 9.02 (d, *J* = 4.0 Hz, 1H), 8.65 (d, *J* = 6.8 Hz, 1H), 8.47 (d, *J* = 7.0 Hz, 1H), 8.14 (d, *J* = 8.0 Hz, 1H), 7.72 (t, *J* = 7.8 Hz, 1H), 7.62 (dd, *J* = 8.3, 4.3 Hz, 1H), 4.70 – 4.43 (m, 1H), 4.29 – 4.16 (m, 1H), 3.26 – 3.06 (m, 2H), 2.67 – 1.99 (m, 4H), 1.88 – 1.36 (m, 4H), 1.17 – 0.95 (m, 6H).

^{13}C NMR (75 MHz, CD_3OD) δ 181.3, 180.9, 173.2, 172.8, 166.6, 149.9, 145.3, 137.9, 132.9, 132.6, 128.7, 126.0, 121.3, 98.2, 59.2, 40.0, 38.0, 37.3, 29.3, 29.1, 27.4, 24.9, 15.0, 10.3.

***tert*-Butyl ((_S_)-1-(((_S_)-1-hydroxy-3-((_S_)-2-oxopyrrolidin-3-yl)propan-2-yl)amino)-4-methyl-1-oxopentan-2-yl)carbamate (64)**

Compound **64** has been synthesized starting from ester intermediate **20** following the general procedure (VI) for ester reduction to alcohol previously reported. The

mixture was purified by SiO_2 column chromatography DCM/MeOH (20:1) yielding a colorless oil (46% yield).

ESI-MS *m/z* 372 $[M+H]^+$ 394 $[M+Na]^+$

^1H NMR (300 MHz, CD_3OD) δ 4.68 (t, J = 7.4 Hz, 1H), 3.87 (dt, J = 18.4, 6.6 Hz, 2H), 3.54 – 3.40 (m, 2H), 3.35 (dt, J = 12.6, 6.4 Hz, 1H), 2.44 – 2.29 (m, 1H), 2.23 – 2.12 (m, 1H), 2.02 – 1.84 (m, 1H), 1.84 – 1.62 (m, 4H), 1.54 – 1.46 (m, 1H), 1.42 (s, 9H), 1.08 – 0.92 (m, 6H).

8-Chloro-*N*-((*S*)-1-(((*S*)-1-hydroxy-3-((*S*)-2-oxopyrrolidin-3-yl)propan-2-yl)amino)-4-methyl-1-oxopentan-2-yl)-1-methyl-4-oxo-1,4-dihydroquinoline-3-carboxamide (65)

Compound **65** was synthesized according to general procedures (I-II) for Boc-cleavage and coupling reaction using 8-chloro-1-methyl-4-oxo-1,4-dihydroquinoline-3-carboxylic acid as the appropriate carboxylic acid. The mixture was purified by SiO_2 column chromatography eluting with DCM/MeOH (30:1) yielding a colorless oil (41% yield).

ESI-MS *m/z* 492 $[M+H]^+$ 514 $[M+Na]^+$

^1H NMR (300 MHz, CD_3OD) δ 8.85 (s, 1H), 8.49 (d, *J* = 9.4 Hz, 1H), 8.00 (d, *J* = 7.7 Hz, 1H), 7.56 (t, *J* = 7.9 Hz, 1H), 4.66 – 4.50 (m, 1H), 4.46 (s, 3H), 4.09 – 3.92 (m, 1H), 3.61 – 3.37 (m, 2H), 3.03 – 2.91 (m, 1H), 2.57 – 2.20 (m, 3H), 2.09 – 1.46 (m, 6H), 1.06 – 0.85 (m, 6H).

8-Chloro-1-methyl-*N*-((*S*)-4-methyl-1-oxo-1-(((*S*)-1-oxo-3-((S)-2-oxopyrrolidin-3-yl)propan-2-yl)amino)pentan-2-yl)-4-oxo-1,4-dihydroquinoline-3-carboxamide (66)

The final aldehydic compound **66** has been synthesized starting from the alcohol intermediate **65**, following the general procedure (VII) for the conversion of the alcohol moiety in aldehyde warhead previously reported. The crude mixture was purified by column chromatography using DCM/MeOH (30:1) as eluting mixture (36% yield).

ESI-MS *m/z* 490 $[M+H]^+$ 512 $[M+Na]^+$

^{1}H NMR (300 MHz, CD_3OD) δ 10.34 (d, *J* = 7.2 Hz, 1H), 9.50 (s, 1H), 8.71 (d, *J* = 3.1 Hz, 1H), 8.45 (d, *J* = 8.3 Hz, 1H), 7.84 (d, *J* = 8.1 Hz, 1H), 7.71 – 7.60 (m, 1H), 7.47 (t, *J* = 7.9 Hz, 1H), 7.34 (d, *J* = 8.8 Hz, 1H), 4.67 – 4.43 (m, *J* = 18.3, 15.9 Hz, 2H), 4.39 (s, 3H), 3.26 – 3.16 (m, 2H), 2.36 (ddd, *J* = 34.8, 16.7, 10.6 Hz, 3H), 1.91 – 1.47 (m, 5H), 1.00 (dd, *J* = 12.6, 6.2 Hz, 6H).

^{13}C NMR (75 MHz, CD_3OD) δ 202.1, 192.1, 175.7, 152.3, 137.8, 136.7, 131.4, 130.5, 129.6, 125.9, 125.6, 122.6, 120.8, 78.0, 41.1, 40.1, 39.0, 37.9, 27.3, 24.7, 22.3, 22.0, 20.9, 20.9.

7.2 – EXPERIMENTAL SMALL MOLECULES SARS-CoV-2

7.2.1 – Synthetic protocol for the synthesis of compounds 67-69

methyl (*S*)-2-(6-bromonicotinamido)-3-((*S*)-2-oxopyrrolidin-3-yl)propanoate (76a)

Compound **76a** has been synthesized following the coupling reaction procedure using 6-bromonicotinic acid. The crude mixture has been purified through SiO_2 flash chromatography eluting with a mixture of DCM/MeOH (20:1), yielding a pale brown oil (46% yield).

ESI-MS *m/z* 371 $[M+H]^+$

^1H NMR (300 MHz, $CDCl_3$) δ 9.33 (d, *J* = 4.8 Hz, 1H), 8.94 (d, *J* = 2.3 Hz, 1H), 8.20 – 7.91 (m, 1H), 7.55 (d, *J* = 8.3 Hz, 1H), 6.47 (s, 1H), 4.53 (dt, *J* = 11.7, 4.5 Hz, 1H), 3.77 (s, 3H), 3.49 – 3.32 (m, 2H), 2.67 – 2.39 (m, 2H), 2.27 – 1.82 (m, 3H).

methyl (S)-2-((1*S*,4*R*)-4-((*tert*-butoxycarbonyl)amino)cyclohexane-1-carboxamido)-3-((*S*)-2-oxopyrrolidin-3-yl)propanoate (76b)

For the synthesis of intermediate **76b** the general procedure (II) for the coupling reaction reported previously has been followed, using (1s,4s)-4-((*tert*-butoxycarbonyl)amino)cyclohexane-1-carboxylic acid. The mixture has been purified by SiO_2 cloumn chromatography using a mixture of DCM/MeOH (20:1), yielding a colorless oil (51% yield).

ESI-MS *m/z* 411 $[M+H]^+$

^1H NMR (300 MHz, $CDCl_3$) δ 5.93 (s, 1H), 4.92 (s, 1H), 3.80 (s, 3H), 3.75 – 3.54 (m, J = 9.3, 3.8 Hz, 1H), 3.25 – 3.04 (m, 6H), 2.31 – 2.17 (m, 1H), 1.77 – 1.47 (m, 8H), 1.38 (s, 9H).

<u>General procedure (VIII) for the reduction reaction using DIBAL</u> exemplified through 6-bromo-*N*-((*S*)-1-oxo-3-((*S*)-2-oxopyrrolidin-3-yl)propan-2-yl)nicotinamide (67)

The target molecule has been prepared through reduction of intermediate **76a**. In an oven dried double-neck flask, under N_2 atmosphere, intermediate **76a** (20 mg, 0,06 mmol) has been solubilized with anhydrous DCM (1,35 mL) and cooled at -78 °C, successively diisobutylaluminium hydride 1M in THF (DIBAL) (0,08 mL, 0,08 mmol) has been slowly added drop-by-drop. The reaction mixture has been stirred at the same temperature for 3 h, then MeOH (1 mL) has been added followed by NH_4Cl (2 mL), and the mixture has been extracted with DCM (3 x 2 mL), dried over Na_2SO_4, filtered and concentrated under vacuum. The target molecule has been purified through SiO_2 column chromatography with $CHCl_3$/MeOH (15:1), yielding a colorless oil (36% yield).

ESI-MS *m/z* 341 $[M+H]^+$

^1H NMR (300 MHz, CD_3OD) δ 9.56 (s, 1H), 8.77 (d, J = 2.4 Hz, 1H), 8.09 (dd, J = 8.3, 2.5 Hz, 1H), 7.69 (d, J = 8.4 Hz, 1H), 4.66 – 4.51 (m, 1H), 4.16 (m, 1H), 3.40 – 3.30 (m, 3H), 2.61 (d, J = 18.4 Hz, 1H), 2.32 (d, J = 40.3 Hz, 1H), 1.82 (d, J = 3.3 Hz, 2H), 1.67 (d, J = 4.2 Hz, 1H).

^{13}C NMR (75 MHz, CD_3OD) δ 181.2, 149.0, 144.3, 137.9, 127.6, 60.1, 53.3, 52.6, 52.5, 40.2, 38.3, 30.1, 29.9.

tert-butyl ((1*R*,4*S*)-4-(((*S*)-1-oxo-3-((*S*)-2-oxopyrrolidin-3-yl)propan-2-yl)carbamoyl)cyclohexyl)carbamate (68)

The target molecule has been prepared starting from the alcohol intermediate **76b** following the general procedure (VIII) for the reduction reaction using DIBAL, the mixture has been stirred at the same temperature for 3 h, then MeOH (1 mL) has been added followed by NH_4Cl (2 mL), and the mixture has been extracted with DCM (3 x 2 mL). The organic phase was, dried over anhydrous Na_2SO_4, filtered and concentrated under vacuum. The target molecule has been purified through SiO_2 column chromatography with $CHCl_3$/MeOH (15:1) as eluent, yielding a colorless oil (33% yield).

ESI-MS *m/z* 382 $[M+H]^+$

^{1}H NMR (300 MHz, CD_3OD) δ 9.48 (s, 1H), 7.62 (d, *J* = 8.8 Hz, 1H), 6.58 (d, *J* = 4.7 Hz, 1H), 4.47 (dd, *J* = 7.8, 3.9 Hz, 1H), 4.13 – 3.87 (m, 1H), 3.71 – 3.60 (m, 1H), 2.38 – 2.19 (m, 3H), 2.03 – 1.87 (m, 1H), 1.74 (d, *J* = 9.9 Hz, 4H), 1.60 (d, *J* = 10.8 Hz, 6H), 1.44 (s, 9H).

(1*S*,4*R*)-4-amino-*N*-((*S*)-1-oxo-3-((*S*)-2-oxopyrrolidin-3-yl)propan-2-yl)cyclohexane-1-carboxamide (69)

To a solution of **68** (10 mg, 1eq) in MeOH (1 mL) at 0 °C, the freshly prepared solution of HCl in MeOH (20 eq) was slowly added. The mixture was stirred at 0 °C for 1 h, then the solvent was removed under N_2 flux. The target molecule was characterized without any further purification (>95% yield).

ESI-MS *m/z* 312 $[M+H]^+$

7.3 – EXPERIMENTAL HDACi PREVENTION SARS-CoV-2

Methyl 4-((7-chloro-4-oxoquinazolin-3(4*H*)-yl)methyl)benzoate (78)

To a well-stirred solution of **77** (250 mg, 1.26 mmol) in acetone (15 mL), methyl 4-(bromomethyl)benzoate, K_2CO_3 (867 mg, 6.28 mmol) and NaI (188 mg, 1.26 mmol) were added. The mixture was stirred at 55 °C for 12 h. After this time the mixture was filtered, and the solvent was removed under vacuum. The crude mixture was purified by crystallization from n-hexane affording a yellow solid (96% yield).

ESI-MS *m/z* 329 $[M+H]^+$, 351 $[M+Na]^+$.

^{1}H NMR (300 MHz, DMSO-d6) δ 8.63 (s, 1 H), 8.11 (d, *J*=8.5 Hz, 1 H), 8.00 – 7.85 (m, 2 H), 7.76 (d, *J* = 2.0 Hz, 1 H), 7.58 (d, *J* = 2.0 Hz, 1H), 7.46 (d, *J* = 8.4 Hz, 2 H), 5.25 (s, 2 H), 3.81 (s, 3 H).

4-((7-Chloro-4-oxoquinazolin-3(4*H*)-yl)methyl)-*N*-hydroxybenzamide (79)

To a suspension of $NH_2OH{\cdot}HCl$ (500 mg, 7.2 mmol) in MeOH (5 mL), a solution of KOH (648 mg, 11.5 mmol) in MeOH (5 mL) was added at 0 °C, then the resulting mixture was allowed to room temperature and stirred in these conditions for 30 min The solid residue (KCl) was filtered off and the filtrate was added to a solution of **78** (250 mg, 0.76 mmol) in MeOH (5 mL). The resulting solution was stirred at 25 °C for 12 h. After that, pH was neutralized by adding aqueous 6 N HCl. Solvents were removed under reduced pressure and the target compound was purified through silica gel column chromatography, using a mixture of $CHCl_3$/MeOH/NH4OH (20:1:0.1) as the eluent affording an orange solid (24% yield).

ESI-MS *m/z* 330 $[M+H]^+$.

^{1}H NMR (300 MHz, DMSO-d6) δ 11.18 (s, 1 H), 8.63 (s, 1 H), 8.12 (d, *J* =8.6 Hz, 1 H), 7.87 – 7.52 (m, 4 H), 7.40 (d, *J* = 8.2 Hz, 2 H), 5.21 (s, 2 H).

^{13}C NMR (75 MHz, DMSO-d6) δ 164.2, 160.0, 149.9, 149.5, 140.0,139.5, 132.6, 129.1, 128.0, 127.6, 126.9, 120.9, 49.3.

N-(2-aminophenyl)-4-((7-chloro-4-oxoquinazolin-3(4*H*)-yl)methyl)benzamide (80)

To a well-stirred solution of **78** (395 mg, 1.20 mmol) in THF (20 mL), aqueous NaOH (192 mg, 4.80 mmol) was added. The mixture was stirred at 25 °C for 12 h, then, was neutralized with 6N HCl and extracted with EtOAc. The organic layer was dried over anhydrous Na_2SO_4, filtered and evaporated under vacuum. Without any further purification, the carboxylic acid (380 mg, 1.21 mmol) was solubilized in dry DMF (15 mL) and o-phenylendiamine (0.8 eq.), HBTU (551 mg, 1.45 mmol), and TEA (673 µL, 4.84 mmol) were added. The resulting mixture was stirred at 25 °C for 12 h. Then, it was treated with a saturated solution of NH_4Cl and extracted with EtOAc. The pure compound was obtained after flash-column chromatography eluting with $CHCl_3$:MeOH (20:1) and subsequent crystallization from ethanol.

ESI-MS *m/z* 405 $[M+H]^+$

^1H 300 MHz, DMSO-d6) δ 9.62 (s, 1 H), 8.66 (s, 1 H), 8.13 (d, *J* = 8.6 Hz, 1 H), 7.93 (d, *J*=8.1 Hz, 2 H), 7.78 (d, *J*=2.0 Hz, 1 H), 7.59 (dd, *J*= 8.6, 2.1 Hz, 1 H), 7.47 (d, *J* = 8.1 Hz, 2 H), 7.12 (d, *J* = 7.7 Hz, 1 H), 7.05 – 6.85 (m, 1 H), 6.75 (dd, *J* = 8.0, 1.4 Hz, 1 H), 6.57 (t, *J* = 7.8 Hz, 1 H), 5.25 (s, 2 H), 4.87 (s, 2 H).

^{13}C NMR (75 MHz, DMSO-d6) δ 161.6, 160.0, 149.9, 149.5, 143.6, 140.3, 139.6, 134.5, 128.6, 127.9, 127.1, 123.5, 120.9, 116.7, 49.7.

7.4 – EXPERIMENTAL MPXV VP37 INHIBITORS

Synthetic protocol for the preparation of the target compounds 89a-e.

ethyl 4-(trifluoromethyl)benzoate (87)

Intermediate **87** has been prepared starting from 4-(trifluoromethyl)benzoic acid **(86)** (1000 mg, 1 eq) which was solubilized in a round bottom flask with H_2SO_4 (0,561 mL, 1 eq) in EtOH (40 mL, 0,25 M) and then refluxed for 18 h. After this time the reaction mixture was allowed to reach room temperature and concentrated under N_2 flux. Successively the reaction mixture was partitioned between EtOAc (10 mL) and $NaHCO_3$ *s.s.* (5 mL), the organic phase was dried over Na_2SO_4, filtered and concentrated under high vacuum, allowing to obtain a colorless oil (89% yield) which was used without any further purification.

ESI-MS *m/z* 219 $[M+H]^+$

^1H NMR (300 MHz, DMSO-d6) δ 8.12 (d, *J* = 8.2 Hz, 2H), 7.87 (d, *J* = 8.2 Hz, 2H), 4.34 (q, *J* = 7.1 Hz, 2H), 1.32 (dd, *J* = 8.7, 5.4 Hz, 3H).

4-(trifluoromethyl)benzohydrazide (88)

In a round bottom flask intermediate **87** (2043 mg, 1eq) and hydrazine hydrate (3884 mg, 10 eq), were solubilized in EtOH (4 mL, 2,5 M) and heated to reflux for 12 h. Successively the mixture was warmed at room temperature and partly concentrated under N_2 flux, then NH_4Cl *s.s.* (5 mL) was added and the organic phase was extracted with DCM (3 x 5 mL). The organic phase was then dried over Na_2SO_4, filtered and dried in vacuum.

Important to note, any contamination of the glassware with acetone will afford the formation of the enaminic byproduct, N'-(propan-2-ylidene)-4-(trifluoromethyl)benzohydrazide, as white crystals.

The crude product was purified by crystallization from ethanol, affording a translucent white crystal (90% yield).

ESI-MS *m/z* 205 $[M+H]^+$

^{1}H NMR (300 MHz, DMSO-d6) δ 10.01 (s, 1H), 7.99 (d, *J* = 8.0 Hz, 2H), 7.82 (d, *J* = 8.1 Hz, 1H), 4.59 (s, 1H).

General procedure (IX) for the conversion of the hydrazide intermediates (88) to the imide target compounds exemplified with *N*-((3a*R*,4*R*,7*S*,7a*S*)-1,3-dioxo-1,3,3a,4,7,7a-hexahydro-2H-4,7-methanoisoindol-2-yl)-4-(trifluoromethyl)benzamide (89a)

To a suspension of (3a*R*,4*R*,7*S*,7a*S*)-3a,4,7,7a-tetrahydro-4,7-methanoisobenzofuran-1,3-dione (50 mg, 1 eq) in anhydrous toluene (2,45 mL, 0,01 M), the intermediate **(88)** (27 mg, 1 eq), pTSA (4 mg, 0,01 eq) and 4 Å molecular sieves (~20 sieves were added) were added. The reaction mixture was refluxed for 12 h, then dried under N_2 flux. The resulting residue was suspended in EtOAc and filtered to remove the solid, then the organic phase was washed with $NaHCO_3$ (*s.s.*) and dried over Na_2SO_4. The crude mixture was purified by SiO_2 column chromatography using $CHCl_3$/MeOH (15:1) as eluent affording a white crystal (64% yield).

ESI-MS *m/z* 351 $[M+H]^+$

^{1}H NMR (400 MHz, $CDCl_3$) δ 8.30 (s, 1H), 7.87 (d, J = 8.2 Hz, 2H), 7.64 (d, J = 8.2 Hz, 2H), 6.20 (s, 2H), 3.46 (s, 2H), 3.40 (s, 2H), 1.78 (d, J = 9.0 Hz, 1H), 1.65 – 1.53 (m, 1H).

***N*-(2,4-dioxo-3-azabicyclo[3.1.0]hexan-3-yl)-4-(trifluoromethyl)benzamide (89b)**

For the synthesis of the target compound **89b** the general procedure (IX) previously reported for compound **89a** has been followed using the appropriate cyclic anhydride: 3-oxabicyclo[3.1.0]hexane-2,4-dione. The crude mixture was purified through column chromatography eluting with $CHCl_3$/MeOH (15:1) to give a white crystal solid (66% yield).

ESI-MS *m/z* 299 $[M+H]^+$

^{1}H NMR (400 MHz, $CDCl_3$) δ 8.88 (s, 1H), 7.79 (d, J = 8.2 Hz, 2H), 7.57 (d, J = 8.3 Hz, 2H), 2.67 – 2.46 (m, 2H), 1.84 – 1.55 (m, 2H).

^{13}C NMR (101 MHz, $CDCl_3$) δ 172.2, 164.0, 134.1, 133.2, 127.9, 125.7, 125.6, 20.7, 20.5, 19.1, 18.8.

***N*-(6,6-dimethyl-2,4-dioxo-3-azabicyclo[3.1.0]hexan-3-yl)-4-(trifluoromethyl)benzamide (89c)**

The final molecule **89c** has been achieved following the reported general procedure (IX) using 6,6-dimethyl-3-oxabicyclo[3.1.0]hexane-2,4-dione. The crude mixture was purified through SiO_2 column chromatography with a solution of $CHCl_3$/MeOH (15:1) affording a beige crystal (47% yield).

ESI-MS *m/z* 327 $[M+H]^+$

^{1}H NMR (400 MHz, $CDCl_3$) δ 8.13 (s, 1H), 7.91 (t, J = 9.2 Hz, 2H), 7.69 (d, J = 8.2 Hz, 2H), 2.15 (s, 2H), 1.24 (s, 6H).

^{13}C NMR (101 MHz, MeOD) δ 170.8, 128.2, 125.3, 31.5, 28.9, 24.9.

***N*-(2,5-dioxopyrrolidin-1-yl)-4-(trifluoromethyl)benzamide (89d)**

The final molecule **89d** has been achieved following the reported general procedure (IX) using succinic anhydride as starting material. The crude mixture was purified through SiO_2 column chromatography with a solution of $CHCl_3$/MeOH (15:1) affording a beige crystal (17% yield).

ESI-MS *m/z* 287 [M+H]+

^{1}H NMR (300 MHz, DMSO-d6) δ 11.33 (s, 1H), 8.10 (d, J = 8.1 Hz, 2H), 7.93 (d, J = 8.1 Hz, 2H), 2.85 (s, 4H)

^{13}C NMR (75 MHz, DMSO-d6) δ 174.6, 164.1, 135.2, 132.9, 132.5, 129.1, 126.3, 126.2, 122.4, 26.8

Synthetic protocol for the synthesis of target compound 93

2,2,6,6-tetramethyl-1-nitrosopiperidine (91)

To a solution of 2,2,6,6-tetramethylpiperidine (100 mg, 1 eq) in acetic acid/acetic anhydride (1:2, 1,2 mL) cooled at 0 °C, $NaNO_2$ (489 mg, 10 eq) was added in one portion at the same temperature. The reaction mixture was stirred vigorously for 30 min at 0 °C, then another portion of $NaNO_2$ was added (489 mg, 10eq), and the reaction mixture was stirred at 0 °C for 3 h. After this time it was allowed to reach room temperature and stirred for 72 h. The reaction was monitored by TLC; differently from the precursor, the desired intermediate is visible on TLC under 254 UV, and does not burn in ninhydrin. After this time the mixture was concentrated under N_2 flux and quenched by slow addition of $NaHCO_3$ *s.s.*, until pH=8. The aqueous phase was extracted with Et_2O (2 x 2 mL), then it was acidified with HCl 1N until pH=2 and extracted with Et_2O (2 x 2 mL) once again. The combined organic phases were dried over Na_2SO_4, filtered and dried under vacuum. The crude mixture (80 % yield) was used without any further purification for the next synthetic step.

2,2,6,6-tetramethylpiperidin-1-amine (92)

In a round bottom flask, to a solution of the nitroso intermediate **91** (65 mg, 1 eq) in acetic acid (0,4 mL) and water (0,4 mL) cooled at 0 °C, Zn powder (99 mg, 4 eq) was added. The mixture was stirred at the same temperature for 4 h, then after completion of the reaction monitored by TLC, the mixture was filtered on celite, and concentrated under N_2 flux. Successively the crude mixture was solubilized in EtOAc and stirred at 25 °C for 30 min, filtered once again, and the filtrate was dried over Na_2SO_4, filtered and solvent was removed under vacuum. The crude product was used without any further purification affording a slightly volatile colorless liquid (92% yield).

ESI-MS *m/z* 157 [M+H]+

^{1}H NMR (300 MHz, $CDCl_3$) δ 3.30 (s, 2H), 2.03 (s, 3H), 1.79 – 1.67 (m, 3H), 1.67 – 1.53 (m, 2H), 1.42 (s, 2H), 1.23 (s, 8H).

***N*-(2,2,6,6-tetramethylpiperidin-1-yl)-4-(trifluoromethyl)benzamide (93)**

To a solution of the azido intermediate **92** (65 mg, 1 eq) in anhydrous DCM (4,2 mL) cooled at 0 °C, TEA (126 mg, 3 eq) and 4-(trifluoromethyl)benzoyl chloride (131 mg,

1,5 eq) were slowly added. The reaction mixture was allowed to reach room temperature over 12 h. After this time the mixture was diluted with DCM (4 mL) and the organic phase was washed with HCl 1N (2 x 2 mL), brine (2 x 2 mL) and water (2 x 2 mL). The crude mixture was purified through column chromatography eluting with DCM/MeOH (20:1) affording a white crystal (44% yield).

ESI-MS *m/z* 329 [M+H]+

^{1}H NMR (300 MHz, $CDCl_3$) δ 7.85 (d, *J* = 8.1 Hz, 2H), 7.71 (d, *J* = 8.1 Hz, 2H), 6.75 (s, 1H), 1.84 – 1.48 (m, 6H), 1.11 (d, *J* = 21.0 Hz, 12H).

^{13}C NMR (101 MHz, $CDCl_3$) δ 169.9, 137.35, 133.07, 130.02, 125.24, 122.53, 45.65, 8.54.

4-(trifluoromethyl)benzohydrazide (95)

In a round-bottom flask ethyl 4-(trifluoromethyl)benzoate (1690 mg, 1 eq) was solubilized in EtOH (3 mL, 2,5M) and hydrazine hydrate (3884 mg, 10 eq) was added. The reaction mixture was stirred at 120 °C for 12 h, then the mixture was concentrated under vacuum and the desired compound was purified by crystallization in EtOH affording a white crystal (50% yield).

ESI-MS *m/z* 205 [M+H]+ 227 [M+Na]+

^{1}H NMR (300 MHz, DMSO-d6) δ 10.00 (s, 1H), 7.99 (d, J = 8.1 Hz, 1H), 7.81 (d, J = 8.2 Hz, 1H), 4.58 (s, 1H)

***N*-(1,3-dioxoisoindolin-2-yl)-4-(trifluoromethyl)benzamide (96)**

In a round-bottom flask a suspension of intermediate **95** (100 mg, 1 eq) and phatlic anhydride (109 mg, 1,5 eq) in xylene (5 mL, 0,1M) was refluxed for 24 h. After this time the mixture was cooled at 0 °C and the formed white precipitate was filtered on thin paper filter. The white solid was washed with cold EtOH (2x 1mL) and the final compound was achieved without any further purification (11% yield).

ESI-MS *m/z* 335 [M+H]+ 357 [M+Na]+

^{1}H NMR (300 MHz, DMSO-d6) δ 11.61 (s, 1H), 8.16 (d, J = 7.9 Hz, 2H), 8.06 – 7.87 (m, 6H)

^{13}C NMR (75 MHz, DMSO-d6) δ 165.6, 164.8, 135.9, 134.9, 133.1, 132.6, 129.8, 129.2, 126.3, 126.3, 125.9, 124.4.

(3aR,4R,7S,7aS)-1,3-dioxo-1,3,3a,4,7,7a-hexahydro-2H-4,7-methanoisoindol-2-yl 4-(trifluoromethyl)benzoate (98)

To a solution of 4-(trifluoromethyl)benzoic acid (106 mg, 1 eq) in anhydrous DCM (1 mL, 0,6M), TEA (56 mg, 1 eq) and EDC.HCl (107 mg, 1 eq) were added and the mixture was stirred at 25 °C for 10 min. After this time (3aR,4R,7S,7aS)-2-hydroxy-3a,4,7,7a-tetrahydro-1H-4,7-methanoisoindole-1,3(2H)-dione (100 mg, 1 eq) was added in one portion, and the reaction mixture was stirred for additional 4 h at 25 °C, then $NaHCO_3$ *s.s.* (2 mL) was added, and the reaction mixture was partitioned in DCM (3 x 2 mL). The combined organic phases were washed with brine (2 x 1 mL), dried over Na_2SO_4, filtered and dried under vacuum. The crude mixture was purified through SiO_2 column chromatography eluting with PetEt/EtOAc (4:1) affording a yellow oil (17% yield).

ESI-MS *m/z* 374 [M+H]+

^{1}H NMR (300 MHz, Acetone-d6) δ 8.31 (d, J = 8.3 Hz, 1H), 8.00 (d, J = 8.3 Hz, 1H), 6.22 (s, 1H), 3.59 (s, 1H), 3.43 (s, 1H), 1.71 (dd, J = 20.0, 8.8 Hz, 1H).

^{13}C NMR (75 MHz, Acetone-d6) δ 205.1, 169.5, 134.7, 130.8, 126.2, 126.1, 50.9, 44.5.

3-amino-3-azaspiro[5.5]undecane-2,4-dione (100)

To a stirred suspension of NaH (46 mg, 1,05 eq) in DMF (2,3 mL, 0,5M for NaH suspension) a solution of 3-azaspiro[5.5]undecane-2,4-dione (200 mg, 1 eq) in anhydrous DMF (3 mL, 0,35M for SM solution) has been added slowly. After 1h, a solution of HOSA (250 mg, 12 eq) in DMF (9 mL, 0,25M) was slowly added. The reaction mixture was then heated at 110 °C and stirred for an additional 3 h, after this time NH_4Cl (5 mL) *s.s*. was added, and the reaction mixture was extracted with

DCM (3 x 5 mL). The combined organic phase was washed with $NaHCO_3$ (2 x 3 mL) and brine (2 x 3 mL), and dried over Na_2SO_4 . The crude mixture was purified through column chromatography eluent: DCM/MeOH (100:1) affording an off-white solid (11% yield).

ESI-MS *m/z* 197 [M+H]+

^{1}H NMR (300 MHz, acetone) δ 5.11 (s, 2H), 2.63 (s, 4H), 1.60 – 1.34 (m, 10H)

General procedure (X) for coupling reaction exemplified with compound *N*-(2,4-dioxo-3-azaspiro[5.5]undecan-3-yl)-4-(trifluoromethyl)benzamide (101)

To a solution of intermediate **100** (25 mg, 1 eq) in dry DMF (0,254 mL, 0,5M), 4-(trifluoromethyl)benzoic acid (29 mg, 1,2 eq), HATU (48 mg, 1 eq) and NMM (26 mh, 2 eq) were added. The mixture was stirred at 25 °C for 12 h, then NH_4Cl (1 mL) was added, and the organic phase was partitioned with EtOAC (3 x 1 mL). The organic phase was dried over Na_2SO_4, filtered and evaporated under vacuum. The crude mixture was purified through SiO_2 column chromatography eluting with PetEt/EtOAc (4:1) affording a white solid (53% yield).

ESI-MS *m/z* 391 [M+H]+

^{1}H NMR (300 MHz, Acetone-d6) δ 10.00 (s, 1H), 8.15 (d, J = 8.1 Hz, 2H), 7.89 (d, J = 8.2 Hz, 2H), 2.93 – 2.68 (m, 2H), 1.72 (d, J = 6.0 Hz, 2H), 1.62 – 1.40 (m, 8H)

^{13}C NMR (75 MHz, acetone-6) δ 205.2, 168.9, 128.4, 125.6, 125.5, 43.3, 36.2, 34.4, 32.0, 25.5, 21.3, 21.2.

General procedure (XI) for the hydantoin synthesis exemplified through compound 1,3-diazaspiro[4.5]decane-2,4-dione (103)

To a solution of cyclohexanone (200 mg, 1 eq) in MeOH/H_2O (2,5 mL, 2:3) in a MW vials, $(NH_4)_2CO_3$ (588 mg, 3 eq) and KCN (200 mg, 1,5 eq) were added. The vial was sealed and irradiated in a MW for 10 min (100 W, 90 °C). After this time solvent was removed under N_2 flux, and the yellow residue was washed with H_2O (3 x 5 mL). The compound was used without any further purification (99% yield).

ESI-MS *m/z* 169 [M+H]+

^{1}H NMR (300 MHz, DMSO-d6) δ 10.50 (s, 1H), 8.35 (s, 1H), 1.53 (dt, J = 22.5, 10.1 Hz, 10H).

3-amino-1,3-diazaspiro[4.5]decane-2,4-dione (104)

For the preparation of **104**, intermediate **103** (100 mg, 1 eq) was refluxed in $NH_2NH_2.H_2O$ (197 mg, 6,7 eq) for 1 h. After this time 0,5 mL of H_2O were additionally added and the mixture was stirred at the same temperature for 4 h. Then the mixture was allowed to reach 25 °C, and SiO_2 was added directly to absorb the excess $NH_2NH_2.H_2O$, and the so-obtained slurry was dried and used directly for the purification through SiO_2 column eluting with DCM/MeOH (100:1). The desired compound was obtained as a white solid (68% yield).

ESI-MS *m/z* 206 $[M+H]^+$

^{1}H NMR (300 MHz, DMSO-d6) δ 8.54 (s, 1H), 4.65 (s, 2H), 1.78 – 0.96 (m, 10H).

***N*-(2,4-dioxo-1,3-diazaspiro[4.5]decan-3-yl)-4-(trifluoromethyl)benzamide (105)**

Following the general procedure (X) for coupling reaction described for **101**, the target compound **105** has been prepared. The purification of the compound has been carried out through SiO_2 chromatography PetEt/EtOAc (4:1) affording a white solid (53% yield).

ESI-MS *m/z* 391 $[M+Na]^+$

^{1}H NMR (300 MHz, DMSO-d6) δ 11.32 (s, 1H), 9.05 (s, 1H), 8.09 (d, J = 8.2 Hz, 2H), 7.94 (d, J = 8.3 Hz, 2H), 1.60 (dt, J = 82.7, 43.3 Hz, 10H)

^{13}C NMR (75 MHz, DMSO-d6) δ 174.8, 164.5, 153.6, 135.0, 132.9, 129.0, 126.2, 126.2, 60.5, 34.0, 33.8, 24.6, 20.9.

3-(4-(trifluoromethyl)benzoyl)-1,3-diazaspiro[4.5]decane-2,4-dione (106)

To a solution of intermediate **103a** (100 mg, 1 eq), in anhydrous THF (2,5 mL, 0,25M) TEA (120mg, 2 eq) was added. TH mixture was stirred at 25 °C for 1 h, then 4-(trifluoromethyl)benzoyl chloride was slowly added drop-by-drop. The reaction

mixture was stirred at the same temperature for 12 h, after this time NH_4Cl (3 mL) was added, and the mixture was extracted with DCM (3 x 3 mL). The combined organic phase was dried over Na_2SO_4, filtered and solvent was removed under vacuum at 25 °C. The crude mixture was purified through SiO_2 column chromatography eluent: DCM/Acetone (20:1), affording a white solid (11% yield).

ESI-MS *m/z* 341 [M+H]+

^{1}H NMR (300 MHz, acetone-d6) δ 8.12 (s, 1H), 8.08 (d, J = 8.3 Hz, 2H), 7.88 (d, J = 8.3 Hz, 2H), 1.98 – 1.33 (m, 10H).

(2*S*)-2-chlorobicyclo[2.2.2]oct-5-ene-2-carbonitrile (108)

In a round-bottom flask a solution of HQ (5 mg, 0,008 eq), (1Z,3Z)-cycloocta-1,3-diene (500 mg, 1 eq) and 2-chloroacrylonitrile (600 mg, 1 eq) in anhydrous toluene (2 mL, 3M) were heated at 80 °C for 12 h under N_2, in a sealed tube. After this time solvent was evaporated and the crude mixture was used for the further step without any purification.

(1*R*,4*R*)-bicyclo[2.2.2]oct-5-en-2-one (109)

For the synthesis of intermediate **109**, derivative **108** was solubilized in DMSO, then a solution of KOH was slowly added. The reaction mixture was stirred at the same temperature for 48 h. After this time HCl 1N was added, and the mixture was partitioned in pentane (3 x 3 mL). The solvent was removed under N_2 flux and the product, white crystals, was used without any further purification (53% yield).

^{1}H NMR (300 MHz, $CDCl_3$) δ 6.49 – 6.40 (m, 1H), 6.23 – 6.11 (m, 1H), 3.15 – 3.03 (m, 1H), 3.01 – 2.89 (m, 1H), 1.91 – 1.40 (m, 5H), 1.25 (dd, J = 15.6, 4.6 Hz, 1H).

(1*S*,4*R*)-3-oxobicyclo[2.2.2]oct-5-ene-2-carbaldehyde (110)

In a two-necked round bottom flask, to a pre-cooled suspension of NaH 60% w/w (88 mg, 1,5 eq) in anhydrous THF (3 mL, 0,5M), EtOH (10 drops) was added drop-by-drop. Then intermediate **109** (180 mg, 1 eq) and ethylformate (164 mg, 1,5 eq) were added slowly. The mixture was slowly allowed to reach 25 °C and stirred for 12 h. After this time EtOH (10 drops) was added to the mixture, that was stirred 1

additional hour. After this time H_2O (2 mL) was slowly added, and the mixture was concentrated under N_2 flux, successively the residual aqueous mixture was partitioned with Et_2O (2 x 2mL), acidified at pH=2 and partitioned one again with Et_2O (2 x 2 mL), then the organic phase was dried over Na_2SO_4. The crude mixture was used for the next step without any further purification (169 mg).

ESI-MS *m/z* 151 $[M+H]^+$, 149 [M-H]

(4*S*,7*R*)-4,7-dihydro-2*H*-4,7-ethanoindazole (111)

To a solution of intermediate **110** (169 mg, 1 eq), in MeOH (1,2 mL, 1M), $NH_2NH_2.H_2O$ (62 mg, 1,1 eq) was slowly added. The reaction mixture was stirred at 25 °C for 12h, after which solvent and residual hydrazine were removed under N_2 flux. Successively NH_4Cl was added and the mixture was partitioned with EtOAc (3 x 3 mL), the combined organic phase was dried over anhydrous Na_2SO_4, filtered and concentrated under vacuum. The residue was washed with HCl 1N (2 x 2 mL) to remove impurities, and was used as it was, a white solid (58% yield) without any further purification.

ESI-MS *m/z* 147 $[M+H]^+$

^1H NMR (300 MHz, $CDCl_3$) δ 7.11 (s, 1H), 6.55 – 6.43 (m, 2H), 3.98 (dd, J = 31.3, 2.9 Hz, 2H), 1.67 – 1.32 (m, 4H).

<u>General procedure (XII) for the amination reaction</u> of the indazole-derivative exemplified through compounds (4*S*,7*R*)-4,7-dihydro-1/2*H*-4,7-ethanoindazol-2-amine (112,114)

In a two necked-round bottom flask, to a solution of intermediate **111** (20 mg, 1 eq) in anhydrous DMF (0,3 mL, 0,5M) under N_2 flux, NaH 60%mw (7 mg, 1,2 eq) was added in one portion. The mixture was stirred at the same temperature for 1 h, after this time freshly prepared NH_2Cl was added slowly (1 mL, 0,15 M in Et_2O). The reaction mixture was stirred at 25 °C for 12 h, then $Na_2S_2O_3$ (2 mL) was added, and the mixture was extracted with Et_2O (3 x 3 mL). The combined organic phase was dried over Na_2SO_4, filtered and dried under vacuum. The mixture of the two

regioisomers was purified by SiO_2 column chromatography, affording an overall yield of 64%.

(4*S*,7*R*)-4,7-dihydro-2*H*-4,7-ethanoindazol-2-amine (**112**)

ESI-MS *m/z* 162 $[M+H]^+$

^1H NMR (300 MHz, $CDCl_3$) δ 6.95 (s, 1H), 6.51 (t, J = 6.8 Hz, 1H), 6.37 (t, J = 6.8 Hz, 1H), 5.08 (s, 2H), 4.01 (dd, J = 74.1, 5.5 Hz, 2H), 1.76 – 1.12 (m, 4H).

(4*S*,7*R*)-4,7-dihydro-1*H*-4,7-ethanoindazol-2-amine (**114**)

ESI-MS *m/z* 162 $[M+H]^+$

^1H NMR (300 MHz, $CDCl_3$) δ 7.03 – 6.90 (m, 1H), 6.53 – 6.29 (m, 2H), 5.22 (s, 2H), 3.88 (ddd, J = 7.4, 4.8, 2.1 Hz, 2H), 1.78 – 1.20 (m, 4H).

_N_-((4*S*,7*R*)-4,7-dihydro-2*H*-4,7-ethanoindazol-2-yl)-4-(trifluoromethyl)benzamide (113)

The target molecule **113** has been synthesized according to the coupling reaction procedure used for **101**. The crude product has been purified through column chromatography eluting with PetEt/EtOAc (4:1), furnishing a dark yellow oil (46% yield).

ESI-MS *m/z* 334 $[M+H]^+$

^1H NMR (300 MHz, $CDCl_3$) δ 8.03 (d, J = 7.3 Hz, 2H), 7.64 (d, J = 7.5 Hz, 2H), 7.00 (s, 1H), 6.54 (t, J = 6.7 Hz, 1H), 6.36 (t, J = 6.5 Hz, 1H), 3.95 (d, J = 6.0 Hz, 2H), 1.49 (dd, J = 41.4, 18.6 Hz, 4H).

^{13}C NMR (75 MHz, $CDCl_3$) δ 137.8, 134.4, 133.6, 132.8, 128.2, 125.5, 125.3, 121.7, 33.5, 33.1, 26.5, 25.6.

_N_-((4*S*,7*R*)-4,7-dihydro-1*H*-4,7-ethanoindazol-1-yl)-4-(trifluoromethyl)benzamide (115)

The target molecule **115** has been synthesized according to the coupling reaction procedure used for **101**. The crude product has been purified through column

chromatography eluting with PetEt/EtOAc (4:1), furnishing a dark yellow oil (46% yield).

ESI-MS *m/z* 334 $[M+H]^+$

^1H NMR (300 MHz, $CDCl_3$) δ 11.10 (s, 1H), 7.95 (s, 2H), 7.62 (d, J = 7.9 Hz, 2H), 7.08 (s, 1H), 6.46 (t, J = 6.8 Hz, 1H), 6.34 (s, 1H), 3.89 (d, J = 4.3 Hz, 1H), 3.73 (s, 1H), 1.77 – 1.14 (m, 4H).

^{13}C NMR (75 MHz, $CDCl_3$) δ 155.6, 136.3, 134.5, 134.0, 128.1, 125.5, 122.7, 121.7, 33.7, 32.0, 26.5, 25.9.

7.5 – EXPERIMENTAL MODULATORS VIRULENCE FACTORS PA

Synthetic protocol for the synthesis of compounds 127, 128 and 132.

General procedure (XIII) for the synthesis of differently substituted quinazolinone core exemplified through compound 7-chloroquinazolin-4(3H)-one (124a)

2-amino-4-chlorobenzoic acid **123a** (2000 mg, 1 eq.) was diluted in formamide (4 mL). The reaction was heated at 150 °C for 20 h. Then, ice (2.0 g) was added to the reaction to favor the precipitation of the product, which was filtered and washed with water. Then, it was dried at 50 °C for 2 h. The crude mixture was used without any further purification (93% yield).

Sppectroscopic data are in agreement with those reported in literature [201]

6-chloroquinazolin-4(3H)-one (124b)

For the synthesis of quinazolinone **124b** 2-amino-5-chlorobenzoic acid (**123b**) has been used, following the general procedure (XIII) reported previously. The mixture was used without any further purification (90% yield).

ESI-MS *m/z*: 179 $[M-H]^-$

^{1}H NMR (300 MHz, DMSO) δ 12.39 (s, 1H), 8.25 – 7.92 (m, 2H), 7.71 (d, *J* = 2.0 Hz, 1H), 7.54 (dd, *J* = 8.6, 2.1 Hz, 1H).

General procedure (XIV) for the synthesis of the alkylation rection affording the 4-nitro derivatives exemplified with compound 7-chloro-3-(4-nitrobenzyl)quinazolin-4(3H)-one (125a)

To a suspension of **124a** (207 mg, 1 eq.) in acetone (13 mL), 1-(chloromethyl)-4-nitrobenzene (178 mg, 1 eq.), K_2CO_3 (718 mg, 5 eq.) and NaI (155 mg, 1 eq.) were added. The mixture was stirred at 50 °C for 24 h. After this time, the reaction was partitioned between brine and EtOAc and the aqueous layer was washed again with EtOAc (3 x 10 mL). The combined organic layers were dried over Na_2SO_4, filtered and evaporated in vacuo. The title compound was purified through silica gel column chromatography, eluent PetEt/EtOAc (3:1) affording a yellow solid (60% yield).

ESI-MS *m/z*: 316 $[M+H]^+$

^{1}H NMR (300 MHz, DMSO) δ 8.65 (s, 1H), 8.14 (dd, *J* = 23.0, 8.6 Hz, 3H), 7.76 (d, *J* = 1.9 Hz, 1H), 7.57 (dd, *J* = 12.5, 5.4 Hz, 3H), 5.30 (s, 2H).

^{13}C NMR (75 MHz, DMSO) δ 160.0, 149.8, 149.4, 147.3, 144.6, 139.6, 129.1, 128.6, 128.0, 126.9, 124.1, 120.8, 49.2, 40.7, 40.4, 40.1, 39.9, 39.6, 39.3, 39.0.

6-chloro-3-(4-nitrobenzyl)quinazolin-4(3H)-one (125b)

Intermediate **125b** has been obtained following the general procedure (XIV) reported previously, starting from the quinazolinone derivative **124b**. The crude mixture has been purified through silica gel column chromatography, eluent PetEt/EtOAc (3:1) affording a yellow solid (66% yield).

ESI-MS *m/z*: 316 $[M+H]^+$

^{1}H NMR (300 MHz, DMSO-d6) δ 8.63 (s, 1H), 8.18 (d, *J* = 8.6 Hz, 2H), 8.05 (d, *J* = 2.3 Hz, 1H), 7.86 (dd, *J* = 8.7, 2.4 Hz, 1H), 7.73 (d, *J* = 8.7 Hz, 1H), 7.59 (d, *J* = 8.6 Hz, 2H), 5.32 (s, 2H).

^{13}C NMR (75 MHz, DSMO-d6) δ 159.7, 148.9, 147.4, 147.1, 144.5, 135.1, 132.0, 130.0, 129.2, 125. 5, 124.2, 123.3, 49.3

General procedure (XV) for the reduction reaction of nitro moiety to amino to obtain the aniline intermediate exemplified with compound 3-(4-aminobenzyl)-7-chloroquinazolin-4(3H)-one 126a

To a suspension of **125a** (182 mg, 1 eq.) in EtOH (6 mL), heated at 55 °C, saturated NH_4Cl (6 mL) was added. After that, iron powder (330 mg, 10 eq.) was added and the mixture was heated at 70°C for 2 h. Solvent was removed, the mixture was diluted in EtOAc and filtered on Celite®, then pH was adjusted to 8 by adding saturated $NaHCO_3$ solution. The mixture was then partitioned between water and EtOAc. The organic layer was dried over anhydrous Na_2SO_4, filtered and evaporated under reduced pressure to afford the final product without further purification (95% yield).

ESI-MS *m/z*: 286 $[M+H]^+$

^{1}H NMR (300 MHz, DMSO-d6) δ 8.55 (s, 1H), 8.12 (d, *J* = 8.6 Hz, 1H), 7.73 (d, *J* = 1.9 Hz, 1H), 7.53 (dt, *J* = 30.1, 15.1 Hz, 1H), 7.03 (t, *J* = 19.0 Hz, 2H), 6.48 (d, *J* = 8.4 Hz, 2H), 5.11 (s, 2H), 4.96 (s, 2H)

3-(4-aminobenzyl)-6-chloroquinazolin-4(3H)-one (126b)

The aniline intermediate **126b** has been synthesized through reduction of the intermediate **125b**; the crude mixture was used without any further purification affording a white solid (54% yield).

ESI-MS *m/z*: 286 $[M+H]^+$

^{1}H NMR (300 MHz, DMSO-d6) δ 8.53 (s, 1H), 8.07 (d, *J* = 2.4 Hz, 1H), 7.82 (dd, *J* = 8.7, 2.5 Hz, 1H), 7.68 (d, *J* = 8.7 Hz, 1H), 7.07 (d, *J* = 8.3 Hz, 2H), 6.48 (d, *J* = 8.3 Hz, 2H), 5.09 (s, 2H), 4.97 (s, 2H)

General procedure for the reductive amination reaction exemplified with compound 7-chloro-3-(4-((furan-2-ylmethyl)amino)benzyl)quinazolin-4(3H)-one (127)

To a well-stirred solution of **126a** (180 mg, 1 eq.) in MeOH (5 mL), the appropriate aldehyde (1 eq.) and AcOH (5 drops) were added. The mixture was heated at 50 °C for 12 h. After this time, the reaction was cooled to 25 °C and $NaBH_3CN$ (60 mg, 1.5 eq.) was added. The mixture was stirred for additional 2 h. Then, pH was adjusted to 8 by adding saturated $NaHCO_3$ aqueous solution. The crude was partitioned between H_2O and EtOAc; the aqueous layer was extracted with EtOAc (3 x 10 mL). The title compound was purified through silica gel column chromatography, eluent PetEt/EtOAc (3:1) affording a white solid (70% yield).

ESI-MS *m/z*: 366 $[M+H]^+$

^{1}H NMR (300 MHz, Acetone) δ 8.41 (s, 1H), 8.19 (d, *J* = 8.6 Hz, 1H), 7.64 (d, *J* = 1.9 Hz, 1H), 7.50 (dd, *J* = 8.6, 2.0 Hz, 1H), 7.42 (s, 1H), 7.25 (d, *J* = 8.5 Hz, 3H), 6.69 (d, *J* = 8.5 Hz, 3H), 6.27 (dd, *J* = 17.7, 2.4 Hz, 2H), 5.47 (t, *J* = 5.3 Hz, 1H), 5.10 (s, 3H), 4.30 (d, *J* = 5.9 Hz, 3H).

^{13}C NMR (75 MHz, Acetone-d6) δ 159.7, 153.3, 149.4, 148.7, 148.3, 141.7, 139.3, 129.4, 128.2, 127.1, 126.6, 124.5, 121.0, 112.6, 110.2, 106.6, 48.8, 40.3

6-Chloro-3-(4-((ferrocene-2-ylmethyl)amino)benzyl)quinazolin-4(3H)-one (128)

The final compound **128** has been synthesized according to the general procedure previously reported, The crude mixture has been purified through SiO_2 column chromatography eluent: PetEt/EtOAc (3:1) affording a red solid (70% yield).

ESI-MS *m/z*: 484 $[M+H]^+$

^{1}H NMR (300 MHz, $CDCl_3$) δ 8.29 (d, *J* = 2.6 Hz, 1H), 8.09 (d, *J* = 6.1 Hz, 1H), 7.71 – 7.55 (m, 3H), 7.18 (dd, *J* = 17.4, 7.8 Hz, 2H), 6.61 (d, *J* = 8.5 Hz, 2H), 5.07 (s, 3H), 4.22 (s, 3H), 4.17 (s, 6H), 4.14 (s, 2H), 3.93 (s, 2H)

^{13}C NMR (75 MHz, $CDCl_3$) δ 160.1, 148.3, 146.5, 135.3, 134.6, 133.0, 129.8, 129.1, 126.2, 123.8, 123.3, 113.0, 86.0, 70.3, 69.5, 69.1, 68.3, 49.6, 43.2. **6-chloro-2-methyl-4H-benzo[d][1,3]oxazin-4-one (129)**

2-amino-5-chlorobenzoic acid (500 mg, 1 eq.) was heated at 140 °C in acetic anhydride (2.8 mL, 10 eq.) for 2 h. The reaction was warmed to room temperature and pH adjusted to 7 by adding solid $NaHCO_3$. Then, the mixture was partitioned between water and DCM. The organic layer was dried over anhydrous Na_2SO_4, filtered and evaporated under reduced pressure, to obtain the crude mixtures as solid (90% yield).

^{1}H NMR (300 MHz, DMSO-d6) δ 8.02 (d, *J* = 2.3 Hz, 1H), 7.91 (dd, *J* = 8.6, 2.4 Hz, 1H), 7.56 (d, *J* = 8.6 Hz, 1H), 2.38 (s, 3H)

6-chloro-2-methylquinazolin-4(3H)-one (130)

To a solution of **129** (200 mg, 1 eq.) in EtOH (7 mL) 28% NH_3 was added (2 mL). The mixture was refluxed for 15 h, then the solvent was removed under reduced pressure to furnish the crude product as a white solid, that was used without further purification (70% yield).

ESI-MS *m/z*: 195 $[M+H]^+$

^{1}H NMR (300 MHz, DMSO-d6) δ 8.04 (d, *J* = 8.5 Hz, 2H), 7.63 (dd, *J* = 12.8, 5.1 Hz, 2H), 7.47 (dd, *J* = 8.5, 1.9 Hz, 2H), 2.48 (s, 6H), 2.33 (s, 3H).

6-chloro-2-methyl-3-(prop-2-yn-1-yl)quinazolin-4(3H)-one (131)

To a mixture of **130** (200 mg, 1 eq.) and propargyl chloride (80 µL, 1.1 eq.) in dry DMF (5 mL), potassium *tert*-butoxide (188 mg, 1.65 eq.) was added. The mixture was stirred under nitrogen atmosphere for 24 h. After that, the reaction was neutralized by adding 1N HCl and partitioned between H_2O and EtOAc (3 x 10 mL). The combined organic layers were dried with anhydrous Na_2SO_4, filtered and evaporated under reduced pressure. The title intermediate was purified through silica gel column chromatography, eluent: PetEt/EtOAc (3:1) furnishing a white solid (52% yield).

ESI-MS *m/z*: 233 $[M+H]^+$.

^{1}H NMR (300 MHz, $CDCl_3$) δ 8.19 (d, *J* = 2.4 Hz, 1H), 7.64 (dd, *J* = 8.7, 2.4 Hz, 1H), 7.54 (d, *J* = 8.7 Hz, 1H), 4.90 (d, *J* = 2.4 Hz, 2H), 2.74 (s, 3H), 2.32 (t, *J* = 2.4 Hz, 1H).

methyl 5-((4-((6-chloro-2-methyl-4-oxoquinazolin-3(4H)-yl)methyl)-1H-1,2,3-triazol-1-yl)methyl)furan-2-carboxylate (132)

To a solution of **131** (100 mg, 1 eq.) in a 1:1 mixture of H_2O:*tert*-butanol (10 mL) methyl 5-formylfuran-2-carboxylate (57 mg, 1 eq.) was added, followed by the addition of sodium ascorbate (5 mg, 0.06 eq) and copper(II) sulfate (2 mg, 0.03 eq.). The reaction mixture was stirred at 25 °C for 72 h, then it was concentrated in vacuo, diluted with water and extracted with EtOAc (3 x 10 mL). The combined organic layers were dried over anhydrous Na_2SO_4, filtered and evaporated under reduced pressure. The title compound was purified by SiO_2 gel column chromatography, eluent: PetEt/EtOAc (2:1), affording a white solid (87% yield).

ESI-MS *m/z*: 414 M+H]$^+$.

^{1}H NMR (300 MHz, $CDCl_3$) δ 8.12 (d, *J* = 2.6 Hz, 1H), 7.81 (s, 1H), 7.74 – 7.57 (m, 1H), 7.52 (t, *J* = 9.3 Hz, 1H), 7.09 (d, *J* = 3.5 Hz, 1H), 6.49 (d, *J* = 3.5 Hz, 1H), 5.52 (s, 3H), 5.31 (s, 2H), 3.84 (s, 4H), 2.86 (s, 4H).

BIBLIOGRAPHY

(1) Mindra, G.; Wortham, J. M.; Haddad, M. B.; Powell, K. M. Tuberculosis Outbreaks in the United States, 2009-2015. *http://dx.doi.org/10.1177/0033354916688270* **2017**, *132* (2), 157–163.

(2) Baicus, A. History of Polio Vaccination. *World J. Virol.* **2012**, *1* (4), 108. https://doi.org/10.5501/WJV.V1.I4.108.

(3) Mehndiratta, M. M.; Mehndiratta, P.; Pande, R. Poliomyelitis. *http://dx.doi.org/10.1177/1941874414533352* **2014**, *4* (4), 223–229.

(4) Wood, C. L.; McInturff, A.; Young, H. S.; Kim, D.; Lafferty, K. D. Human Infectious Disease Burdens Decrease with Urbanization but Not with Biodiversity. *Philos. Trans. R. Soc. B Biol. Sci.* **2017**, *372* (1722). https://doi.org/10.1098/RSTB.2016.0122.

(5) Cohen, M. L. Changing Patterns of Infectious Disease. *Nat. 2000 4066797* **2000**, *406* (6797), 762–767. https://doi.org/10.1038/35021206.

(6) Feldmann, H.; Czub, M.; Jones, S.; Dick, D.; Garbutt, M.; Grolla, A.; Artsob, H. Emerging and Re-Emerging Infectious Diseases. *Med. Microbiol. Immunol.* **2002**, *191* (2), 63–74. https://doi.org/10.1007/S00430-002-0122-5.

(7) Chala, B.; Hamde, F. Emerging and Re-Emerging Vector-Borne Infectious Diseases and the Challenges for Control: A Review. *Front. Public Heal.* **2021**, *9*, 715759. https://doi.org/10.3389/FPUBH.2021.715759.

(8) Mancuso, G.; Midiri, A.; Gerace, E.; Biondo, C. Bacterial Antibiotic Resistance: The Most Critical Pathogens. *Pathogens* **2021**, *10* (1310), 1–14.

(9) Vora, N. M.; Hannah, L.; Walzer, C.; Vale, M. M.; Lieberman, S.; Emerson, A.; Jennings, J.; Alders, R.; Bonds, M. H.; Evans, J.; Chilukuri, B.; Cook, S.; Sizer, N. C.; Epstein, J. H. Interventions to Reduce Risk for Pathogen Spillover and Early Disease Spread to Prevent Outbreaks, Epidemics, and Pandemics. *Emerg. Infect. Dis.* **2023**, *29* (3), E1–E9. https://doi.org/10.3201/EID2903.221079.

(10) Alexander, K. A.; Carlson, C. J.; Lewis, B. L.; Getz, W. M.; Marathe, M. V; Eubank, S. G.; Sanderson, C. E.; Blackburn, J. K.; Alexander, K. A.; Sanderson, C. E.; Carlson, C. J.; Getz, · W M; Lewis, B. L.; Marathe, M. V; Eubank, · S G; Blackburn, J. K. The Ecology of Pathogen Spillover and Disease Emergence at the Human-Wildlife-Environment Interface. **2018**, 267–298. https://doi.org/10.1007/978-3-319-92373-4_8.

(11) Abd El-Ghany, W. A. Pseudomonas Aeruginosa Infection of Avian Origin: Zoonosis and One Health Implications. **2021**. https://doi.org/10.14202/vetworld.2021.2155-2159.

(12) Baker, R. E.; Mahmud, A. S.; Miller, I. F.; Rajeev, M.; Rasambainarivo, F.; Rice, B. L.; Takahashi, S.; Tatem, A. J.; Wagner, C. E.; Wang, L. F.; Wesolowski, A.; Metcalf, C. J. E. Infectious Disease in an Era of Global Change. *Nat. Rev. Microbiol.* **2022**, *20* (4), 193–205. https://doi.org/10.1038/s41579-021-00639-z.

(13) McArthur, D. B. Emerging Infectious Diseases. *Nurs. Clin. North Am.* **2019**, *54* (2), 297–311. https://doi.org/10.1016/j.cnur.2019.02.006.

(14) Cannalire, R.; Cerchia, C.; Beccari, A. R.; Di Leva, F. S.; Summa, V. Targeting SARS-CoV-2 Proteases and Polymerase for COVID-19 Treatment: State of the Art and Future Opportunities. *J. Med. Chem.* **2020**, acs.jmedchem.0c01140. https://doi.org/10.1021/acs.jmedchem.0c01140.

(15) Simpson, S.; Kaufmann, M. C.; Glozman, V.; Chakrabarti, A. Disease X: Accelerating the Development of Medical Countermeasures for the next Pandemic. *Lancet Infect. Dis.* **2020**, *20* (5), e108–e115. https://doi.org/10.1016/S1473-3099(20)30123-7.

(16) Mehand, M. S.; Al-Shorbaji, F.; Millett, P.; Murgue, B. The WHO R&D Blueprint: 2018 Review of Emerging Infectious Diseases Requiring Urgent Research and Development Efforts. *Antiviral Res.* **2018**, *159*, 63–67. https://doi.org/10.1016/J.ANTIVIRAL.2018.09.009.

(17) Tompa, D. R.; Immanuel, A.; Srikanth, S.; Kadhirvel, S.; Rao Tompa, D.; Immanuel, A.; Srikanth, S.; Kadhirvel, S. Trends and Strategies to Combat Viral Infections: A Review on FDA Approved Antiviral Drugs. *Int. J. Biol. Macromol.* **2021**, *172*, 524–541. https://doi.org/10.1016/j.ijbiomac.2021.01.076.

(18) Aminov, R. History of Antimicrobial Drug Discovery: Major Classes and Health Impact. **2016**. https://doi.org/10.1016/j.bcp.2016.10.001.

(19) Aminov, R. I. A Brief History of the Antibiotic Era: Lessons Learned and Challenges for the Future. *Article* **2010**, *1* (1). https://doi.org/10.3389/fmicb.2010.00134.

(20) Payne, D. J.; Gwynn, M. N.; Holmes, D. J.; Pompliano, D. L. Drugs for Bad Bugs: Confronting the Challenges of Antibacterial Discovery. *Nat. Rev. Drug Discov. 2006 61* **2006**, *6* (1), 29–40. https://doi.org/10.1038/nrd2201.

(21) Shinu, P.; Al Mouslem, A. K.; Nair, A. B.; Venugopala, K. N.; Attimarad, M.; Singh, V. A.; Nagaraja, S.; Alotaibi, G.; Deb, P. K. Progress Report: Antimicrobial Drug Discovery in the Resistance Era. *Pharmaceuticals* **2022**, *15* (4). https://doi.org/10.3390/ph15040413.

(22) Pacios, O.; Blasco, L.; Bleriot, I.; Fernandez-Garcia, L.; Bardanca, M. G.; Ambroa, A.; López, M.; Bou, G.; Tomás, M. Strategies to Combat Multidrug-Resistant and Persistent Infectious Diseases. *Antibiot. 2020, Vol. 9, Page 65* **2020**, *9* (2), 65. https://doi.org/10.3390/ANTIBIOTICS9020065.

(23) Wagner, E. K.; Maynard, J. A. Engineering Therapeutic Antibodies to Combat Infectious Diseases. *Curr. Opin. Chem. Eng.* **2018**, *19*, 131–141. https://doi.org/10.1016/J.COCHE.2018.01.007.

(24) Matić, Z.; Šantak, M. Current View on Novel Vaccine Technologies to Combat Human Infectious Diseases. *Appl. Microbiol. Biotechnol. 2021 1061* **2021**, *106* (1), 25–56. https://doi.org/10.1007/S00253-021-11713-0.

(25) Pantaleo, G.; Correia, B.; Fenwick, C.; Joo, V. S.; Perez, L. Antibodies to Combat Viral Infections: Development Strategies and Progress. https://doi.org/10.1038/s41573-022-00495-3.

(26) Domingo, E.; Garcia-Crespo, C.; Perales, C. Historical Perspective on the Discovery of the

Quasispecies Concept. *Annu. Rev. Virol.* **2021**, *8* (Volume 8, 2021), 51–72. https://doi.org/10.1146/ANNUREV-VIROLOGY-091919-105900.

(27) Ghorbani, A.; Samarfard, S.; Ramezani, A.; Izadpanah, K.; Afsharifar, A.; Eskandari, M. H.; Karbanowicz, T. P.; Peters, J. R. Quasi-Species Nature and Differential Gene Expression of Severe Acute Respiratory Syndrome Coronavirus 2 and Phylogenetic Analysis of a Novel Iranian Strain. *Infect. Genet. Evol.* **2020**, *85*, 104556. https://doi.org/10.1016/J.MEEGID.2020.104556.

(28) Batool, S.; Chokkakula, S.; Song, M. S. Influenza Treatment: Limitations of Antiviral Therapy and Advantages of Drug Combination Therapy. *Microorg. 2023, Vol. 11, Page 183* **2023**, *11* (1), 183. https://doi.org/10.3390/MICROORGANISMS11010183.

(29) von Kleist, M.; Menz, S.; Stocker, H.; Arasteh, K.; Schütte, C.; Huisinga, W. HIV Quasispecies Dynamics during Pro-Active Treatment Switching: Impact on Multi-Drug Resistance and Resistance Archiving in Latent Reservoirs. *PLoS One* **2011**, *6* (3). https://doi.org/10.1371/JOURNAL.PONE.0018204.

(30) Domingo, E. *Trends in Antiviral Strategies*; 2020. https://doi.org/10.1016/b978-0-12-816331-3.00009-x.

(31) Lou, Z.; Sun, Y.; Rao, Z. Current Progress in Antiviral Strategies. *Trends Pharmacol. Sci.* **2014**, *35* (2), 86–102. https://doi.org/10.1016/j.tips.2013.11.006.

(32) Danis-Wlodarczyk, K.; Dąbrowska, K.; Abedon, S. T. Phage Therapy: The Pharmacology of Antibacterial Viruses. *Curr. Issues Mol. Biol. 2021, Vol. 40, Pages 81-164* **2020**, *40* (1), 81–164. https://doi.org/10.21775/CIMB.040.081.

(33) Rahman, M. U.; Wang, W.; Sun, Q.; Shah, J. A.; Li, C.; Sun, Y.; Li, Y.; Zhang, B.; Chen, W.; Wang, S. Endolysin, a Promising Solution against Antimicrobial Resistance. *Antibiot. 2021, Vol. 10, Page 1277* **2021**, *10* (11), 1277. https://doi.org/10.3390/ANTIBIOTICS10111277.

(34) Baldelli, V.; D'Angelo, F.; Pavoncello, V.; Fiscarelli, E. V.; Visca, P.; Rampioni, G.; Leoni, L. Identification of FDA-Approved Antivirulence Drugs Targeting the Pseudomonas Aeruginosa Quorum Sensing Effector Protein PqsE. *Virulence* **2020**, *11* (1), 652–668. https://doi.org/10.1080/21505594.2020.1770508.

(35) Cattoir, V.; Felden, B. Future Antibacterial Strategies: From Basic Concepts to Clinical Challenges. *J. Infect. Dis.* **2019**, *220* (3), 350–360. https://doi.org/10.1093/infdis/jiz134.

(36) Song, J. H. Introduction: The Goals of Antimicrobial Therapy. *Int. J. Infect. Dis.* **2003**, *7* (SUPPL. 1). https://doi.org/10.1016/S1201-9712(03)90064-6.

(37) Plotniece, A.; Sobolev, A.; Supuran, C. T.; Carta, F.; Björkling, F.; Franzyk, H.; Yli-Kauhaluoma, J.; Augustyns, K.; Cos, P.; De Vooght, L.; Govaerts, M.; Aizawa, J.; Tammela, P.; Žalubovskis, R. Selected Strategies to Fight Pathogenic Bacteria. *J. Enzyme Inhib. Med. Chem.* **2023**, *38* (1). https://doi.org/10.1080/14756366.2022.2155816.

(38) Medina, E.; Pieper, D. H. Tackling Threats and Future Problems of Multidrug-Resistant Bacteria. *Curr. Top. Microbiol. Immunol.* **2016**, *398*, 3–33. https://doi.org/10.1007/82_2016_492.

(39) Shen, Y.; Gao, S.; Fan, Q.; Zuo, J.; Wang, Y.; Yi, L.; Wang, Y. New Antibacterial Targets: Regulation of Quorum Sensing and Secretory Systems in Zoonotic Bacteria. *Microbiol. Res.* **2023**, *274*, 127436. https://doi.org/10.1016/J.MICRES.2023.127436.

(40) Kunz Coyne Amer El Ghali Dana Holger Nicholas Rebold Michael J Rybak, A. J. Therapeutic Strategies for Emerging Multidrug-Resistant Pseudomonas Aeruginosa. *Infect. Dis. Ther. 11*. https://doi.org/10.1007/s40121-022-00591-2.

(41) Langendonk, R. F.; Neill, D. R.; Fothergill, J. L. The Building Blocks of Antimicrobial Resistance in Pseudomonas Aeruginosa: Implications for Current Resistance-Breaking Therapies. https://doi.org/10.3389/fcimb.2021.665759.

(42) Yang, H.; Rao, Z. Structural Biology of SARS-CoV-2 and Implications for Therapeutic Development. *Nat. Rev. Microbiol. 2021 1911* **2021**, *19* (11), 685–700. https://doi.org/10.1038/s41579-021-00630-8.

(43) Ayittey, F. K.; Dhar, B. K.; Anani, G.; Chiwero, N. B. Gendered Burdens and Impacts of SARS-CoV-2: A Review. *Health Care Women Int.* **2020**, *41* (11–12), 1210–1225. https://doi.org/10.1080/07399332.2020.1809664.

(44) V'kovski, P.; Kratzel, A.; Steiner, S.; Stalder, H.; Thiel, V. Coronavirus Biology and Replication: Implications for SARS-CoV-2. *Nat. Rev. Microbiol. 2020 193* **2020**, *19* (3), 155–170. https://doi.org/10.1038/s41579-020-00468-6.

(45) Baric, R. S. SARS-CoV: Lessons for Global Health. *Virus Res.* **2008**, *133* (1), 1. https://doi.org/10.1016/J.VIRUSRES.2007.03.024.

(46) Fung, I. C. H.; Fu, K. W.; Ying, Y.; Schaible, B.; Hao, Y.; Chan, C. H.; Tse, Z. T. H. Chinese Social Media Reaction to the MERS-CoV and Avian Influenza A(H7N9) Outbreaks. *Infect. Dis. Poverty* **2013**, *2* (1), 1–12. https://doi.org/10.1186/2049-9957-2-31.

(47) Fontanet, A.; Autran, B.; Lina, B.; Kieny, M. P.; Karim, S. S. A.; Sridhar, D. SARS-CoV-2 Variants and Ending the COVID-19 Pandemic. *Lancet* **2021**, *397* (10278), 952–954. https://doi.org/10.1016/S0140-6736(21)00370-6.

(48) Kadam, S. B.; Sukhramani, G. S.; Bishnoi, P.; Pable, A. A.; Barvkar, V. T. SARS-CoV-2, the Pandemic Coronavirus: Molecular and Structural Insights. *J. Basic Microbiol.* **2021**, *61* (3), 180–202. https://doi.org/10.1002/JOBM.202000537.

(49) Silva, L. R.; da Silva Santos-Júnior, P. F.; de Andrade Brandão, J.; Anderson, L.; Bassi, Ê. J.; Xavier de Araújo-Júnior, J.; Cardoso, S. H.; da Silva-Júnior, E. F. Druggable Targets from Coronaviruses for Designing New Antiviral Drugs. *Bioorganic Med. Chem.* **2020**, *28* (22), 115745. https://doi.org/10.1016/j.bmc.2020.115745.

(50) Harvey, W. T.; Carabelli, A. M.; Jackson, B.; Gupta, R. K.; Thomson, E. C.; Harrison, E. M.; Ludden, C.; Reeve, R.; Rambaut, A.; Peacock, S. J.; Robertson, D. L. SARS-CoV-2 Variants, Spike Mutations and Immune Escape. *Nat. Rev. Microbiol. 2021 197* **2021**, *19* (7), 409–424. https://doi.org/10.1038/s41579-021-00573-0.

(51) Markov, P. V; Ghafari, M.; Beer, M.; Lythgoe, K.; Simmonds, P.; Stilianakis, N. I.; Katzourakis, A. The Evolution of SARS-CoV-2. *Nat. Rev. Microbiol.* | **2023**, *21*, 361–379. https://doi.org/10.1038/s41579-023-00878-2.

(52) Yan, W.; Zheng, Y.; Zeng, X.; He, B.; Cheng, W. Structural Biology of SARS-CoV-2: Open the Door for Novel Therapies. *Signal Transduct. Target. Ther. 2022 71* **2022**, *7* (1), 1–28. https://doi.org/10.1038/s41392-022-00884-5.

(53) Yadav, R.; Chaudhary, J. K.; Jain, N.; Chaudhary, P. K.; Khanra, S.; Dhamija, P.; Sharma, A.; Kumar, A.; Handu, S. Role of Structural and Non-Structural Proteins and Therapeutic Targets of SARS-CoV-2 for COVID-19. *Cells 2021, Vol. 10, Page 821* **2021**, *10* (4), 821. https://doi.org/10.3390/CELLS10040821.

(54) Raj, R. Analysis of Non-Structural Proteins, NSPs of SARS-CoV-2 as Targets for Computational Drug Designing. *Biochem. Biophys. Reports* **2021**, *25*, 100847. https://doi.org/10.1016/J.BBREP.2020.100847.

(55) Zhu, J.; Zhang, H.; Lin, Q.; Lyu, J.; Lu, L.; Chen, H.; Zhang, X.; Zhang, Y.; Chen, K. Progress on SARS-CoV-2 3CLpro Inhibitors: Inspiration from SARS-CoV 3CLpro Peptidomimetics and Small-Molecule Anti-Inflammatory Compounds. *Drug Des. Devel. Ther.* **2022**, *16*, 1067–1082. https://doi.org/10.2147/DDDT.S359009.

(56) Halford, B. The Path to Paxlovid. *ACS Cent. Sci.* **2022**, *8* (4), 405–407. https://doi.org/10.1021/ACSCENTSCI.2C00369.

(57) Reguera, J.; Santiago, C.; Mudgal, G.; Ordoño, D.; Enjuanes, L.; Casasnovas, J. M. Structural Bases of Coronavirus Attachment to Host Aminopeptidase N and Its Inhibition by Neutralizing Antibodies. *PLOS Pathog.* **2012**, *8* (8), e1002859. https://doi.org/10.1371/JOURNAL.PPAT.1002859.

(58) Pöhlmann, S.; Gramberg, T.; Wegele, A.; Pyrc, K.; Van Der Hoek, L.; Berkhout, B.; Hofmann, H. Interaction between the Spike Protein of Human Coronavirus NL63 and Its Cellular Receptor ACE2. *Adv. Exp. Med. Biol.* **2006**, *581*, 281–284. https://doi.org/10.1007/978-0-387-33012-9_47.

(59) Li, W.; Sui, J.; Huang, I. C.; Kuhn, J. H.; Radoshitzky, S. R.; Marasco, W. A.; Choe, H.; Farzan, M. The S Proteins of Human Coronavirus NL63 and Severe Acute Respiratory Syndrome Coronavirus Bind Overlapping Regions of ACE2. *Virology* **2007**, *367* (2), 367–374. https://doi.org/10.1016/J.VIROL.2007.04.035.

(60) Li, Y.; Zhang, Z.; Yang, L.; Xin, S.; Cao, P.; Lu, J. The MERS-CoV Receptor DPP4 as a Candidate Binding Target of the SARS-CoV-2 Spike. https://doi.org/10.1016/j.isci.2020.101160.

(61) Cevik, M.; Kuppalli, K.; Kindrachuk, J.; Peiris, M. Virology, Transmission, and Pathogenesis of SARS-CoV-2. *BMJ* **2020**, *371*. https://doi.org/10.1136/BMJ.M3862.

(62) Mazinani, M.; Rude, B. J. The Novel Zoonotic Coronavirus Disease 2019 (COVID-19) Pandemic: Health Perspective on the Outbreak PALABRAS CLAVE. *J. Healthc. Qual. Res.* **2021**, *36*, 47–51. https://doi.org/10.1016/j.jhqr.2020.09.004.

(63) V'kovski, P.; Kratzel, A.; Steiner, S.; Stalder, H.; Thiel, V. Coronavirus Biology and Replication: Implications for SARS-CoV-2. *Nat. Rev. Microbiol.* **2021**, *19* (3), 155–170. https://doi.org/10.1038/s41579-020-00468-6.

(64) Hillen, H. S.; Kokic, G.; Farnung, L.; Dienemann, C.; Tegunov, D.; Cramer, P. Structure of Replicating SARS-CoV-2 Polymerase. *Nat. 2020 5847819* **2020**, *584* (7819), 154–156. https://doi.org/10.1038/s41586-020-2368-8.

(65) Romano, M.; Ruggiero, A.; Squeglia, F.; Maga, G.; Berisio, R. A Structural View of SARS-CoV-2 RNA Replication Machinery: RNA Synthesis, Proofreading and Final Capping. *Cells 2020, Vol. 9, Page 1267* **2020**, *9* (5), 1267. https://doi.org/10.3390/CELLS9051267.

(66) Gussow, A. B.; Auslander, N.; Faure, G.; Wolf, Y. I.; Zhang, F.; Koonin, E. V. Genomic Determinants of Pathogenicity in SARS-CoV-2 and Other Human Coronaviruses. *Proc. Natl. Acad. Sci. U. S. A.* **2020**, *117* (26), 15193–15199. https://doi.org/10.1073/PNAS.2008176117.

(67) Huang, J.; Teoh, J. Y. C.; Wong, S. H.; Wong, M. C. S. The Potential Impact of Previous Exposure to SARS or MERS on Control of the COVID-19 Pandemic. *Eur. J. Epidemiol.* **2020**, *35* (11), 1099–1103. https://doi.org/10.1007/S10654-020-00674-9.

(68) Song, P.; Li, W.; Xie, J.; Hou, Y.; You, C. Cytokine Storm Induced by SARS-CoV-2. *Clin. Chim. Acta* **2020**, *509*, 280–287. https://doi.org/10.1016/J.CCA.2020.06.017.

(69) Liu, J.; Li, Y.; Liu, Q.; Yao, Q.; Wang, X.; Zhang, H.; Chen, R.; Ren, L.; Min, J.; Deng, F.; Yan, B.; Liu, L.; Hu, Z.; Wang, M.; Zhou, Y. SARS-CoV-2 Cell Tropism and Multiorgan Infection. *Cell Discov. 2021 71* **2021**, *7* (1), 1–4. https://doi.org/10.1038/s41421-021-00249-2.

(70) Cagno, V. SARS-CoV-2 Cellular Tropism. *The Lancet Microbe* **2020**, *1* (1), e2–e3. https://doi.org/10.1016/s2666-5247(20)30008-2.

(71) Heisch, R. B. Zoonoses as a Study in Ecology. *Br. Med. J.* **1956**, *2* (4994), 669. https://doi.org/10.1136/BMJ.2.4994.669.

(72) Otte, J.; Pica-Ciamarra, U. Emerging Infectious Zoonotic Diseases: The Neglected Role of Food Animals. *One Heal.* **2021**, *13*, 100323. https://doi.org/10.1016/J.ONEHLT.2021.100323.

(73) The European Union One Health 2022 Zoonoses Report. *EFSA J.* **2023**, *21* (12). https://doi.org/10.2903/J.EFSA.2023.8442.

(74) Mackenstedt, U.; Jenkins, D.; Romig, T. The Role of Wildlife in the Transmission of Parasitic Zoonoses in Peri-Urban and Urban Areas. *Int. J. Parasitol. Parasites Wildl.* **2015**, *4* (1), 71–79. https://doi.org/10.1016/J.IJPPAW.2015.01.006.

(75) Carlson, C. J.; Albery, G. F.; Merow, C.; Trisos, C. H.; Zipfel, C. M.; Eskew, E. A.; Olival, K. J.; Ross, N.; Bansal, S. Climate Change Increases Cross-Species Viral Transmission Risk. *Nat. 2022 6077919* **2022**, *607* (7919), 555–562. https://doi.org/10.1038/s41586-022-04788-w.

(76) O'Brien, B.; Goodridge, L.; Ronholm, J.; Nasheri, N. Exploring the Potential of Foodborne

Transmission of Respiratory Viruses. *Food Microbiol.* **2021**, *95*, 103709. https://doi.org/10.1016/J.FM.2020.103709.

(77) Pandey, R. K.; Dubey, A. K.; Sharma, S.; Rani, C. Climate Change and Zoonotic Diseases: Malaria, Plague, Dengue, and Encephalitis. *Emerg. Pandemics Connect. with Environ. Clim. Chang.* **2023**, 81–97. https://doi.org/10.1201/9781003288732-6.

(78) Ain-Najwa, M. Y.; Yasmin, A. R.; Arshad, S. S.; Omar, A. R.; Abu, J.; Kumar, K.; Mohammed, H. O.; Natasha, J. A.; Mohammed, M. N.; Bande, F.; Abdullah, M. L.; Rovie-Ryan, J. J. Exposure to Zoonotic West Nile Virus in Long-Tailed Macaques and Bats in Peninsular Malaysia. *Anim. 2020, Vol. 10, Page 2367* **2020**, *10* (12), 2367. https://doi.org/10.3390/ANI10122367.

(79) Mead, P. Epidemiology of Lyme Disease. *Infect. Dis. Clin.* **2022**, *36* (3), 495–521. https://doi.org/10.1016/J.IDC.2022.03.004.

(80) González-Barrio, D. Zoonoses and Wildlife: One Health Approach. *Animals* **2022**, *12* (4). https://doi.org/10.3390/ani12040480.

(81) Mubareka, S.; Amuasi, J.; Banerjee, A.; Carabin, H.; Jack, J. C.; Jardine, C.; Jaroszewicz, B.; Keefe, G.; Kotwa, J.; Kutz, S.; McGregor, D.; Mease, A.; Nicholson, L.; Nowak, K.; Pickering, B.; Reed, M. G.; Saint-Charles, J.; Simonienko, K.; Smith, T.; Weese, J. S.; Parmley, E. J. Strengthening a One Health Approach to Emerging Zoonoses. *Facets* **2023**, *8*, 16–79.

(82) Rupasinghe, R.; Chomel, B. B.; Martínez-López, B. Climate Change and Zoonoses: A Review of the Current Status, Knowledge Gaps, and Future Trends. *Acta Trop.* **2022**, *226*, 106225. https://doi.org/10.1016/j.actatropica.2021.106225.

(83) Murphy, F. Emerging Zoonoses. *Emerg. Infect. Dis.* **1998**, *4* (3), 429.

(84) Carroll, D.; Watson, B.; Togami, E.; Daszak, P.; Mazet, J. A. K.; Chrisman, C. J.; Rubin, E. M.; Wolfe, N.; Morel, C. M.; Gao, G. F.; Burci, G. L.; Fukuda, K.; Auewarakul, P.; Tomori, O. Building a Global Atlas of Zoonotic Viruses. *Bull. World Health Organ.* **2018**, *96* (4), 292–294. https://doi.org/10.2471/BLT.17.205005.

(85) Khalafalla, A. I. Zoonotic Diseases Transmitted from the Camels. *Front. Vet. Sci.* **2023**, *10*, 1244833. https://doi.org/10.3389/FVETS.2023.1244833.

(86) Kane, Y.; Wong, G.; Gao, G. F. Animal Models, Zoonotic Reservoirs, and Cross-Species Transmission of Emerging Human-Infecting Coronaviruses. *Annu. Rev. Anim. Biosci.* **2023**, *11* (Volume 11, 2023), 1–31. https://doi.org/10.1146/ANNUREV-ANIMAL-020420-025011/1.

(87) Bahari, A.; Azami, S.; Goudarztalejerdi, A.; Karimi, S.; Esmaeili, S.; Chomel, B. B.; Sazmand, A. Focus: Zoonotic Disease: Molecular Detection of Zoonotic Pathogens in the Blood and Tissuesof Camels (Camelus Dromedarius) in Central Desert Of. *Yale J. Biol. Med.* **2021**, *94* (2), 249.

(88) Sit, T. H. C.; Sun, W.; Tse, A. C. N.; Brackman, C. J.; Cheng, S. M. S.; Yan Tang, A. W.; Cheung, J. T. L.; Peiris, M.; Poon, L. L. M. Novel Zoonotic Avian Influenza A(H3N8) Virus in Chicken, Hong Kong, China. *Emerg. Infect. Dis.* **2022**, *28* (10), 2009. https://doi.org/10.3201/EID2810.221067.

(89) Petersen, L. R.; Nett, R. J. West Nile Virus: From Africa to Europe, America, and Beyond. *Zoonoses Infect. Affect. Humans Anim.* **2022**, 1–44. https://doi.org/10.1007/978-3-030-85877-3_38-1.

(90) Ruiz-Aravena, M.; McKee, C.; Gamble, A.; Lunn, T.; Morris, A.; Snedden, C. E.; Yinda, C. K.; Port, J. R.; Buchholz, D. W.; Yeo, Y. Y.; Faust, C.; Jax, E.; Dee, L.; Jones, D. N.; Kessler, M. K.; Falvo, C.; Crowley, D.; Bharti, N.; Brook, C. E.; Aguilar, H. C.; Peel, A. J.; Restif, O.; Schountz, T.; Parrish, C. R.; Gurley, E. S.; Lloyd-Smith, J. O.; Hudson, P. J.; Munster, V. J.; Plowright, R. K. Ecology, Evolution and Spillover of Coronaviruses from Bats. *Nat. Rev. Microbiol. 2021 205* **2021**, *20* (5), 299–314. https://doi.org/10.1038/s41579-021-00652-2.

(91) Recht, J.; Schuenemann, V. J.; Sánchez-Villagra, M. R. Host Diversity and Origin of Zoonoses: The Ancient and the New. https://doi.org/10.3390/ani10091672.

(92) Moratelli, R.; Calisher, C. H. Bats and Zoonotic Viruses: Can We Confidently Link Bats with Emerging Deadly Viruses? *Mem. Inst. Oswaldo Cruz* **2015**, *110* (1), 1–22. https://doi.org/10.1590/0074-02760150048.

(93) Chauhan, S. Comprehensive Review of Coronavirus Disease 2019 (COVID-19). *Biomed. J.* **2020**, *43* (4), 334–340. https://doi.org/10.1016/J.BJ.2020.05.023.

(94) Wang, Z.; Huang, G.; Huang, M.; Dai, Q.; Hu, Y.; Zhou, J.; Wei, F. Global Patterns of Phylogenetic Diversity and Transmission of Bat Coronavirus. **2023**, *66* (4), 861–874. https://doi.org/10.1007/s11427-022-2221-5.

(95) Temmam, S.; Vongphayloth, K.; Baquero, E.; Munier, S.; Bonomi, M.; Regnault, B.; Douangboubpha, B.; Karami, Y.; Chrétien, D.; Sanamxay, D.; Xayaphet, V.; Paphaphanh, P.; Lacoste, V.; Somlor, S.; Lakeomany, K.; Phommavanh, N.; Pérot, P.; Dehan, O.; Amara, F.; Donati, F.; Bigot, T.; Nilges, M.; Rey, F. A.; Van Der Werf, S.; Brey, P. T.; Eloit, M. Bat Coronaviruses Related to SARS-CoV-2 and Infectious for Human Cells. *330 | Nat. |* **2022**, *604*. https://doi.org/10.1038/s41586-022-04532-4.

(96) Pavan, M.; Bassani, D.; Sturlese, M.; Moro, S. Bat Coronaviruses Related to SARS-CoV-2: What about Their 3CL Proteases (MPro)? *J. Enzyme Inhib. Med. Chem.* **2022**, *37* (1), 1077–1082. https://doi.org/10.1080/14756366.2022.2062336.

(97) Zhao, J.; Cui, W.; Tian, B. P. The Potential Intermediate Hosts for SARS-CoV-2. *Front. Microbiol.* **2020**, *11*, 580137. https://doi.org/10.3389/FMICB.2020.580137.

(98) Zhang, J.; Xiao, T.; Cai, Y.; Chen, B. Structure of SARS-CoV-2 Spike Protein. *Curr. Opin. Virol.* **2021**, *50*, 173–182. https://doi.org/10.1016/J.COVIRO.2021.08.010.

(99) Beniac, D. R.; Andonov, A.; Grudeski, E.; Booth, T. F. Architecture of the SARS Coronavirus Prefusion Spike. *Nat. Struct. Mol. Biol. 2006 138* **2006**, *13* (8), 751–752. https://doi.org/10.1038/nsmb1123.

(100) Essalmani, R.; Jain, J.; Susan-Resiga, D.; Andréo, U.; Evagelidis, A.; Derbali, R. M.; Huynh, D. N.; Dallaire, F.; Laporte, M.; Delpal, A.; Sutto-Ortiz, P.; Coutard, B.; Mapa, C.; Wilcoxen, K.; Decroly, E.; NQ Pham, T.; Cohen, É. A.; Seidah, N. G. Distinctive Roles of Furin and TMPRSS2 in SARS-CoV-2 Infectivity. *J. Virol.* **2022**, *96* (8). https://doi.org/10.1128/JVI.00128-22.

(101) Wang, Y.; Anirudhan, V.; Du, R.; Cui, Q.; Rong, L. RNA-Dependent RNA Polymerase of SARS-CoV-2 as a Therapeutic Target. *J. Med. Virol.* **2021**, *93* (1), 300–310. https://doi.org/10.1002/JMV.26264.

(102) Martin, R.; Li, J.; Parvangada, A.; Perry, J.; Cihlar, T.; Mo, H.; Porter, D.; Svarovskaia, E. Genetic Conservation of SARS-CoV-2 RNA Replication Complex in Globally Circulating Isolates and Recently Emerged Variants from Humans and Minks Suggests Minimal Pre-Existing Resistance to Remdesivir. *Antiviral Res.* **2021**, *188*, 105033. https://doi.org/10.1016/J.ANTIVIRAL.2021.105033.

(103) Chen, J.; Wang, Q.; Malone, B.; Llewellyn, E.; Pechersky, Y.; Maruthi, K.; Eng, E. T.; Perry, J. K.; Campbell, E. A.; Shaw, D. E.; Darst, S. A. Ensemble Cryo-EM Reveals Conformational States of the Nsp13 Helicase in the SARS-CoV-2 Helicase Replication–Transcription Complex. *Nat. Struct. Mol. Biol. 2022 293* **2022**, *29* (3), 250–260. https://doi.org/10.1038/s41594-022-00734-6.

(104) Kokic, G.; Hillen, H. S.; Tegunov, D.; Dienemann, C.; Seitz, F.; Schmitzova, J.; Farnung, L.; Siewert, A.; Höbartner, C.; Cramer, P. Mechanism of SARS-CoV-2 Polymerase Stalling by Remdesivir. *Nat. Commun. 2021 121* **2021**, *12* (1), 1–7. https://doi.org/10.1038/s41467-020-20542-0.

(105) McClain, C. B.; Vabret, N. SARS-CoV-2: The Many Pros of Targeting PLpro. *Signal Transduct. Target. Ther. 2020 51* **2020**, *5* (1), 1–2. https://doi.org/10.1038/s41392-020-00335-z.

(106) Osipiuk, J.; Azizi, S. A.; Dvorkin, S.; Endres, M.; Jedrzejczak, R.; Jones, K. A.; Kang, S.; Kathayat, R. S.; Kim, Y.; Lisnyak, V. G.; Maki, S. L.; Nicolaescu, V.; Taylor, C. A.; Tesar, C.; Zhang, Y. A.; Zhou, Z.; Randall, G.; Michalska, K.; Snyder, S. A.; Dickinson, B. C.; Joachimiak, A. Structure of Papain-like Protease from SARS-CoV-2 and Its Complexes with Non-Covalent Inhibitors. *Nat. Commun. 2021 121* **2021**, *12* (1), 1–9. https://doi.org/10.1038/s41467-021-21060-3.

(107) Gao, X.; Qin, B.; Chen, P.; Zhu, K.; Hou, P.; Wojdyla, J. A.; Wang, M.; Cui, S. Crystal Structure of SARS-CoV-2 Papain-like Protease. *Acta Pharm. Sin. B* **2021**, *11* (1), 237–245. https://doi.org/10.1016/J.APSB.2020.08.014.

(108) Sohag, A. A. M.; Hannan, M. A.; Rahman, S.; Hossain, M.; Hasan, M.; Khan, M. K.; Khatun, A.; Dash, R.; Uddin, M. J. Revisiting Potential Druggable Targets against SARS-CoV-2 and Repurposing Therapeutics under Preclinical Study and Clinical Trials: A Comprehensive Review. *Drug Dev. Res.* **2020**, No. June, 1–23. https://doi.org/10.1002/ddr.21709.

(109) Lan, J.; Ge, J.; Yu, J.; Shan, S.; Zhou, H.; Fan, S.; Zhang, Q.; Shi, X.; Wang, Q.; Zhang, L.; Wang, X. Structure of the SARS-CoV-2 Spike Receptor-Binding Domain Bound to the ACE2 Receptor. *Nat. 2020 5817807* **2020**, *581* (7807), 215–220. https://doi.org/10.1038/s41586-020-2180-5.

(110) Newman, J. A.; Douangamath, A.; Yadzani, S.; Yosaatmadja, Y.; Aimon, A.; Brandão-Neto, J.; Dunnett, L.; Gorrie-stone, T.; Skyner, R.; Fearon, D.; Schapira, M.; von Delft, F.; Gileadi, O. Structure, Mechanism and Crystallographic Fragment Screening of the SARS-CoV-2 NSP13 Helicase. *Nat. Commun. 2021 121* **2021**, *12* (1), 1–11. https://doi.org/10.1038/s41467-021-25166-6.

(111) Ullrich, S.; Nitsche, C. The SARS-CoV-2 Main Protease as Drug Target. *Bioorganic Med. Chem. Lett.* **2020**, *30* (17), 127377. https://doi.org/10.1016/j.bmcl.2020.127377.

(112) Anand, K.; Ziebuhr, J.; Wadhwani, P.; Mesters, J. R.; Hilgenfeld, R. Coronavirus Main Proteinase (3CLpro) Structure: Basis for Design of Anti-SARS Drugs. *Science (80-.).* **2003**, *300* (5626), 1763–1767. https://doi.org/10.1126/science.1085658.

(113) Li, X.; Song, Y. Structure and Function of SARS-CoV and SARS-CoV-2 Main Proteases and Their Inhibition: A Comprehensive Review. *Eur. J. Med. Chem.* **2023**, *260*, 115772. https://doi.org/10.1016/j.ejmech.2023.115772.

(114) Liu, Y.; Liang, C.; Xin, L.; Ren, X.; Tian, L.; Ju, X. The Development of Coronavirus 3C-Like Protease (3CLpro) Inhibitors from 2010 to 2020. *Eur. J. Med. Chem.* **2020**, No. January.

(115) Ullrich, S.; Nitsche, C. The SARS-CoV-2 Main Protease as Drug Target. *Bioorg. Med. Chem. Lett.* **2020**, *30* (17), 127377. https://doi.org/10.1016/J.BMCL.2020.127377.

(116) Hu, Q.; Xiong, Y.; Zhu, G. H.; Zhang, Y. N.; Zhang, Y. W.; Huang, P.; Ge, G. B. The SARS-CoV-2 Main Protease (Mpro): Structure, Function, and Emerging Therapies for COVID-19. *MedComm* **2022**, *3* (3), e151. https://doi.org/10.1002/MCO2.151.

(117) Suárez, D.; Díaz, N. SARS-CoV-2 Main Protease: A Molecular Dynamics Study. *J. Chem. Inf. Model.* **2020**, *60* (12), 5815–5831. https://doi.org/10.1021/ACS.JCIM.0C00575.

(118) Pathak, N.; Chen, Y. T.; Hsu, Y. C.; Hsu, N. Y.; Kuo, C. J.; Tsai, H. P.; Kang, J. J.; Huang, C. H.; Chang, S. Y.; Chang, Y. H.; Liang, P. H.; Yang, J. M. Uncovering Flexible Active Site Conformations of SARS-CoV-2 3CL Proteases through Protease Pharmacophore Clusters and COVID-19 Drug Repurposing. *ACS Nano* **2021**, *15* (1), 857–872. https://doi.org/10.1021/ACSNANO.0C07383.

(119) Ramos-Guzmán, C. A.; Ruiz-Pernía, J. J.; Tuñón, I. Unraveling the SARS-CoV-2 Main Protease Mechanism Using Multiscale Methods. *ACS Catal.* **2020**, *10* (21), 12544–12554. https://doi.org/10.1021/ACSCATAL.0C03420.

(120) Citarella, A.; Scala, A.; Piperno, A.; Micale, N. Sars-Cov-2 Mpro: A Potential Target for Peptidomimetics and Small-Molecule Inhibitors. *Biomolecules* **2021**, *11* (4), 607. https://doi.org/10.3390/biom11040607.

(121) Zhao, Y.; Fang, C.; Zhang, Q.; Zhang, R.; Zhao, X.; Duan, Y.; Wang, H.; Zhu, Y.; Feng, L.; Zhao, J.; Shao, M.; Yang, X.; Zhang, L.; Peng, C.; Yang, K.; Ma, D.; Rao, Z.; Yang, H. Crystal Structure of SARS-CoV-2 Main Protease in Complex with Protease Inhibitor PF-07321332. *Protein Cell* **2022**, *13* (9), 689–693. https://doi.org/10.1007/S13238-021-00883-2.

(122) de Vries, M.; Mohamed, A. S.; Prescott, R. A.; Valero-Jimenez, A. M.; Desvignes, L.; O'Connor, R.; Steppan, C.; Devlin, J. C.; Ivanova, E.; Herrera, A.; Schinlever, A.; Loose, P.; Ruggles, K.; Koralov, S. B.; Anderson, A. S.; Binder, J.; Dittmann, M. A Comparative Analysis of SARS-CoV-2 Antivirals Characterizes 3CL pro Inhibitor PF-00835231 as a Potential New Treatment for COVID-19 . *J. Virol.* **2021**, *95* (10). https://doi.org/10.1128/JVI.01819-20.

(123) Khan, S.; Fakhar, Z.; Hussain, A.; Ahmad, A.; Jairajpuri, D. S.; Alajmi, M. F.; Hassan, M. I. Structure-Based Identification of Potential SARS-CoV-2 Main Protease Inhibitors. *J. Biomol. Struct. Dyn.* **2022**,

40 (8), 3595–3608. https://doi.org/10.1080/07391102.2020.1848634.

(124) Nur, A.; Ansori, M.; Sabilil, M. S.; Arif, A.; Muhammad, N. Candidate Inhibitors of SARS-CoV-2 Main Protease with 3D Structures Similar to N3. *Artic. Res. J. Biotechnol.* **2020**, *15* (11).

(125) Jin, Z.; Du, X.; Xu, Y.; Deng, Y.; Liu, M.; Zhao, Y.; Zhang, B.; Li, X.; Zhang, L.; Peng, C.; Duan, Y.; Yu, J.; Wang, L.; Yang, K.; Liu, F.; Jiang, R.; Yang, X.; You, T.; Liu, X.; Yang, X.; Bai, F.; Liu, H.; Liu, X.; Guddat, L. W.; Xu, W.; Xiao, G.; Qin, C.; Shi, Z.; Jiang, H.; Rao, Z.; Yang, H. Structure of Mpro from SARS-CoV-2 and Discovery of Its Inhibitors. *Nature* **2020**, *582* (7811), 289–293. https://doi.org/10.1038/s41586-020-2223-y.

(126) Ma, C.; Sacco, M. D.; Hurst, B.; Townsend, J. A.; Hu, Y.; Szeto, T.; Zhang, X.; Tarbet, B.; Marty, M. T.; Chen, Y.; Wang, J. Boceprevir , GC-376 , and Calpain Inhibitors II , XII Inhibit SARS-CoV-2 Viral Replication by Targeting the Viral Main Protease. *Cell Res.* **2020**, No. May. https://doi.org/10.1038/s41422-020-0356-z.

(127) Fu, L.; Ye, F.; Feng, Y.; Yu, F.; Wang, Q.; Wu, Y.; Zhao, C.; Sun, H.; Huang, B.; Niu, P.; Song, H.; Shi, Y.; Li, X.; Tan, W.; Qi, J.; Gao, G. F. Both Boceprevir and GC376 Efficaciously Inhibit SARS-CoV-2 by Targeting Its Main Protease. *Nat. Commun. 2020 111* **2020**, *11* (1), 1–8. https://doi.org/10.1038/s41467-020-18233-x.

(128) Vuong, W.; Fischer, C.; Khan, M. B.; van Belkum, M. J.; Lamer, T.; Willoughby, K. D.; Lu, J.; Arutyunova, E.; Joyce, M. A.; Saffran, H. A.; Shields, J. A.; Young, H. S.; Nieman, J. A.; Tyrrell, D. L.; Lemieux, M. J.; Vederas, J. C. Improved SARS-CoV-2 Mpro Inhibitors Based on Feline Antiviral Drug GC376: Structural Enhancements, Increased Solubility, and Micellar Studies. *Eur. J. Med. Chem.* **2021**, 113584. https://doi.org/10.1016/j.ejmech.2021.113584.

(129) Jiang, X.; Su, H.; Shang, W.; Zhou, F.; Zhang, Y.; Zhao, W.; Zhang, Q.; Xie, H.; Jiang, L.; Nie, T.; Yang, F.; Xiong, M.; Huang, X.; Li, M.; Chen, P.; Peng, S.; Xiao, G.; Jiang, H.; Tang, R.; Zhang, L.; Shen, J.; Xu, Y. Structure-Based Development and Preclinical Evaluation of the SARS-CoV-2 3C-like Protease Inhibitor Simnotrelvir. *Nat. Commun.* **2023**, *14* (1). https://doi.org/10.1038/s41467-023-42102-y.

(130) Ghazaiean, M.; Aliasgharian, A.; Karami, H.; Darvishi-Khezri, H. Ebselen: A Promising Therapy Protecting Cardiomyocytes from Excess Iron in Iron-Overloaded Thalassemia Patients. *Open Med.* **2023**, *18* (1). https://doi.org/10.1515/MED-2023-0733.

(131) Sahoo, P.; Lenka, D. R.; Batabyal, M.; Pain, P. K.; Kumar, S.; Manna, D.; Kumar, A. Detailed Insights into the Inhibitory Mechanism of New Ebselen Derivatives against Main Protease (Mpro) of Severe Acute Respiratory Syndrome Coronavirus-2 (SARS-CoV-2). *ACS Pharmacol. Transl. Sci.* **2023**, *6* (1), 171–180. https://doi.org/10.1021/ACSPTSCI.2C00203

(132) Sies, H.; Parnham, M. J. Potential Therapeutic Use of Ebselen for COVID-19 and Other Respiratory Viral Infections. *Free Radic. Biol. Med.* **2020**, *156*, 107–112. https://doi.org/10.1016/j.freeradbiomed.2020.06.032.

(133) Stille, J. K.; Tjutrins, J.; Wang, G.; Venegas, F. A.; Hennecker, C.; Rueda, A. M.; Sharon, I.; Blaine, N.;

Miron, C. E.; Pinus, S.; Labarre, A.; Plescia, J.; Burai Patrascu, M.; Zhang, X.; Wahba, A. S.; Vlaho, D.; Huot, M. J.; Schmeing, T. M.; Mittermaier, A. K.; Moitessier, N. Design, Synthesis and in Vitro Evaluation of Novel SARS-CoV-2 3CLpro Covalent Inhibitors. *Eur. J. Med. Chem.* **2022**, *229*, 114046. https://doi.org/10.1016/j.ejmech.2021.114046.

(134) Pang, X.; Xu, W.; Liu, Y.; Li, H.; Chen, L. The Research Progress of SARS-CoV-2 Main Protease Inhibitors from 2020 to 2022. *Eur. J. Med. Chem.* **2023**, *257*, 115491. https://doi.org/10.1016/J.EJMECH.2023.115491.

(135) Unoh, Y.; Uehara, S.; Nakahara, K.; Nobori, H.; Yamatsu, Y.; Yamamoto, S.; Maruyama, Y.; Taoda, Y.; Kasamatsu, K.; Suto, T.; Kouki, K.; Nakahashi, A.; Kawashima, S.; Sanaki, T.; Toba, S.; Uemura, K.; Mizutare, T.; Ando, S.; Sasaki, M.; Orba, Y.; Sawa, H.; Sato, A.; Sato, T.; Kato, T.; Tachibana, Y. Discovery of S-217622, a Noncovalent Oral SARS-CoV-2 3CL Protease Inhibitor Clinical Candidate for Treating COVID-19. *J. Med. Chem.* **2022**, *2022*, 6499–6512. https://doi.org/10.1021/ACS.JMEDCHEM.2C00117.

(136) Lee, J.; Kenward, C.; Worrall, L. J.; Vuckovic, M.; Gentile, F.; Ton, A. T.; Ng, M.; Cherkasov, A.; Strynadka, N. C. J.; Paetzel, M. X-Ray Crystallographic Characterization of the SARS-CoV-2 Main Protease Polyprotein Cleavage Sites Essential for Viral Processing and Maturation. *Nat. Commun. 2022 131* **2022**, *13* (1), 1–13. https://doi.org/10.1038/s41467-022-32854-4.

(137) Göhl, M.; Zhang, L.; El Kilani, H.; Sun, X.; Zhang, K.; Brönstrup, M.; Hilgenfeld, R. From Repurposing to Redesign: Optimization of Boceprevir to Highly Potent Inhibitors of the SARS-CoV-2 Main Protease†. *Molecules* **2022**, *27* (13), 4292. https://doi.org/10.3390/MOLECULES27134292/S1.

(138) Marjomäki, V.; Kalander, K.; Hellman, M.; Permi, P. Enteroviruses and Coronaviruses: Similarities and Therapeutic Targets. *Expert Opin. Ther. Targets* **2021**, *25* (6), 479–489. https://doi.org/10.1080/14728222.2021.1952985.

(139) Dai, W.; Jochmans, D.; Xie, H.; Yang, H.; Li, J.; Su, H.; Chang, D.; Wang, J.; Peng, J.; Zhu, L.; Nian, Y.; Hilgenfeld, R.; Jiang, H.; Chen, K.; Zhang, L.; Xu, Y.; Neyts, J.; Liu, H. Design, Synthesis, and Biological Evaluation of Peptidomimetic Aldehydes as Broad-Spectrum Inhibitors against Enterovirus and Sars-Cov-2. *J. Med. Chem.* **2021**. https://doi.org/10.1021/acs.jmedchem.0c02258.

(140) Debing, Y.; Neyts, J.; Delang, L. The Future of Antivirals: Broad-Spectrum Inhibitors. *Curr. Opin. Infect. Dis.* **2015**, *28* (6), 596–602. https://doi.org/10.1097/QCO.0000000000000212.

(141) Kumar, V.; Shin, J. S.; Shie, J. J.; Ku, K. B.; Kim, C.; Go, Y. Y.; Huang, K. F.; Kim, M.; Liang, P. H. Identification and Evaluation of Potent Middle East Respiratory Syndrome Coronavirus (MERS-CoV) 3CLPro Inhibitors. *Antiviral Res.* **2017**, *141*, 101–106. https://doi.org/10.1016/j.antiviral.2017.02.007.

(142) Amblard, F.; Zhou, S.; Liu, P.; Yoon, J.; Cox, B.; Muzzarelli, K.; Kuiper, B. D.; Kovari, L. C.; Schinazi, R. F. Synthesis and Antiviral Evaluation of Novel Peptidomimetics as Norovirus Protease Inhibitors. *Bioorganic Med. Chem. Lett.* **2018**, *28* (12), 2165–2170. https://doi.org/10.1016/j.bmcl.2018.05.012.

(143) Ghosh, A. K.; Xi, K.; Ratia, K.; Santarsiero, B. D.; Fu, W.; Harcourt, B. H.; Rota, P. A.; Baker, S. C.; Johnson, M. E.; Mesecar, A. D. Design and Synthesis of Peptidomimetic Severe Acute Respiratory

Syndrome Chymotrypsin-like Protease Inhibitors. *J. Med. Chem.* **2005**, *48* (22), 6767–6771. https://doi.org/10.1021/jm050548m.

(144) Stefanelli, I.; Corona, A.; Cerchia, C.; Cassese, E.; Improta, S.; Costanzi, E.; Pelliccia, S.; Morasso, S.; Esposito, F.; Paulis, A.; Scognamiglio, S.; Di Leva, F. S.; Storici, P.; Brindisi, M.; Tramontano, E.; Cannalire, R.; Summa, V. Broad-Spectrum Coronavirus 3C-like Protease Peptidomimetic Inhibitors Effectively Block SARS-CoV-2 Replication in Cells: Design, Synthesis, Biological Evaluation, and X-Ray Structure Determination. *Eur. J. Med. Chem.* **2023**, *253*, 115311. https://doi.org/10.1016/J.EJMECH.2023.115311.

(145) Sacco, M. D.; Ma, C.; Lagarias, P.; Gao, A.; Townsend, J. A.; Meng, X.; Dube, P.; Zhang, X.; Hu, Y.; Kitamura, N.; Hurst, B.; Tarbet, B.; Marty, M. T.; Kolocouris, A.; Xiang, Y.; Chen, Y.; Wang, J. Structure and Inhibition of the SARS-CoV-2 Main Protease Reveal Strategy for Developing Dual Inhibitors against Mpro and Cathepsin L. *Sci. Adv.* **2020**, *6* (50), 1–20. https://doi.org/10.1126/sciadv.abe0751.

(146) Hoffman, R. L.; Kania, R. S.; Brothers, M. A.; Davies, J. F.; Ferre, R. A.; Gajiwala, K. S.; He, M.; Hogan, R. J.; Kozminski, K.; Li, L. Y.; Lockner, J. W.; Lou, J.; Marra, M. T.; Mitchell, L. J.; Murray, B. W.; Nieman, J. A.; Noell, S.; Planken, S. P.; Rowe, T.; Ryan, K.; Smith, G. J.; Solowiej, J. E.; Steppan, C. M.; Taggart, B. Discovery of Ketone-Based Covalent Inhibitors of Coronavirus 3Cl Proteases for the Potential Therapeutic Treatment of Covid-19. *J. Med. Chem.* **2020**. https://doi.org/10.1021/acs.jmedchem.0c01063.

(147) Richter, S.; Parolin, C.; Palumbo, M.; Palù, G. Antiviral Properties of Quinolone-Based Drugs. *Curr. Drug Targets-Infectious Disord.* **2004**, *4*, 111–116.

(148) Shin, Y. S.; Lee, J. Y.; Jeon, S.; Myung, S.; Gong, H. J.; Kim, S.; Kim, H. R.; Jeong, L. S.; Park, C. M. Discovery of 2-Aminoquinolone Acid Derivatives as Potent Inhibitors of SARS-CoV-2. *Bioorg. Med. Chem. Lett* **2023**, *85*, 129214. https://doi.org/10.1016/j.bmcl.2023.129214.

(149) Zhai, Y.; Zhao, X.; Cui, Z.; Wang, M.; Wang, Y.; Li, L.; Sun, Q.; Yang, X.; Zeng, D.; Liu, Y.; Sun, Y.; Lou, Z.; Shang, L.; Yin, Z. Cyanohydrin as an Anchoring Group for Potent and Selective Inhibitors of Enterovirus 71 3C Protease. *J. Med. Chem.* **2015**, *58* (23), 9414–9420. https://doi.org/10.1021/acs.jmedchem.5b01013.

(150) Hanessian, S.; Margarita, R. 1,3-Asymmetric Induction in Dianionic Allylation Reactions of Amino Acid Derivatives-Synthesis of Functionally Useful Enantiopure Glutamates, Pipecolates and Pyroglutamates. *Tetrahedron Lett.* **1998**, *39* (33), 5887–5890. https://doi.org/10.1016/S0040-4039(98)00900-9.

(151) Wolfgang, B. Y. Hydrogenation of Basic Nitriles with Raney Nickel. **1944**, *66* (1), 876–879.

(152) Harrington, P. E.; Croghan, M. D.; Fotsch, C.; Frohn, M.; Lanman, B. A.; Pennington, L. D.; Pickrell, A. J.; Reed, A. B.; Sham, K. K. C.; Tasker, A.; Arnett, H. A.; Fiorino, M.; Lee, M. R.; McElvain, M.; Morrison, H. G.; Xu, H.; Xu, Y.; Zhang, X.; Wong, M.; Cee, V. J. Optimization of a Potent, Orally Active S1P1 Agonist Containing a Quinolinone Core. *ACS Med. Chem. Lett.* **2012**, *3* (1), 74–78. https://doi.org/10.1021/ML200252B.

(153) Ganesan, M.; Nagaraaj, P. Recent Developments in Dehydration of Primary Amides to Nitriles. *Org. Chem. Front.* **2020**, *7* (22), 3792–3814. https://doi.org/10.1039/D0QO00843E.

(154) Bai, B.; Arutyunova, E.; Khan, M. B.; Lu, J.; Joyce, M. A.; Saffran, H. A.; Shields, J. A.; Kandadai, A. S.; Belovodskiy, A.; Hena, M.; Vuong, W.; Lamer, T.; Young, H. S.; Vederas, J. C.; Tyrrell, D. L.; Lemieux, M. J.; Nieman, J. A. Peptidomimetic Nitrile Warheads as SARS-CoV-2 3CL Protease Inhibitors. *RSC Med. Chem.* **2021**, *12* (10), 1722–1730. https://doi.org/10.1039/D1MD00247C.

(155) Jackson, C. B.; Farzan, M.; Chen, B.; Choe, H. Mechanisms of SARS-CoV-2 Entry into Cells. https://doi.org/10.1038/s41580-021-00418-x.

(156) Jackson, C. B.; Farzan, M.; Chen, B.; Choe, H. Mechanisms of SARS-CoV-2 Entry into Cells. *Nat. Rev. Mol. Cell Biol. 2021 231* **2021**, *23* (1), 3–20. https://doi.org/10.1038/s41580-021-00418-x.

(157) Shang, J.; Wan, Y.; Luo, C.; Ye, G.; Geng, Q.; Auerbach, A.; Li, F. Cell Entry Mechanisms of SARS-CoV-2. *Proc. Natl. Acad. Sci. U. S. A.* **2020**, *117* (21), 11727–11734. https://doi.org/10.1073/PNAS.2003138117/SUPPL_FILE/PNAS.2003138117.SD01.XLSX.

(158) Lin, J. Y.; Huang, H. I. Autophagy Is Induced and Supports Virus Replication in Enterovirus A71-Infected Human Primary Neuronal Cells. *Sci. Rep.* **2020**, *10* (1). https://doi.org/10.1038/s41598-020-71970-3.

(159) Zhuang, M. W.; Cheng, Y.; Zhang, J.; Jiang, X. M.; Wang, L.; Deng, J.; Wang, P. H. Increasing Host Cellular Receptor—Angiotensin-Converting Enzyme 2 Expression by Coronavirus May Facilitate 2019-NCoV (or SARS-CoV-2) Infection. *J. Med. Virol.* **2020**, *92* (11), 2693–2701. https://doi.org/10.1002/JMV.26139.

(160) Lamers, M. M.; Haagmans, B. L. SARS-CoV-2 Pathogenesis. *Nat. Rev. Microbiol.* **2022**, *20* (5), 270–284. https://doi.org/10.1038/s41579-022-00713-0.

(161) Gusev, E.; Sarapultsev, A.; Solomatina, L.; Chereshnev, V. Sars-Cov-2-Specific Immune Response and the Pathogenesis of COVID-19. *Int. J. Mol. Sci.* **2022**, *23* (3). https://doi.org/10.3390/ijms23031716.

(162) Sahu, U.; Biswas, D.; Singh, A. K.; Khare, P. Mechanism Involved in the Pathogenesis and Immune Response against SARS-CoV-2 Infection. *VirusDisease* **2021**, *32* (2), 211–219. https://doi.org/10.1007/S13337-021-00687-2.

(163) Turner, A. J. ACE2 Cell Biology, Regulation, and Physiological Functions. *Prot. Arm Renin Angiotensin Syst.* **2015**, 185. https://doi.org/10.1016/B978-0-12-801364-9.00025-0.

(164) Guo, Z.; Niu, Q.; Mi, X.; Yang, B.; Cai, M.; Liang, Y. Sirt1 Activation Prevents High Glucose-Induced Angiotensin Converting Enzyme 2 Downregulation in Renal Tubular Cells by Regulating the TIMP3/ADAM17 Pathway. *Mol. Biol. Rep.* **2024**, *51* (1), 1–8. https://doi.org/10.1007/S11033-023-08957-6.

(165) Sato, T.; Suzuki, T.; Watanabe, H.; Kadowaki, A.; Fukamizu, A.; Liu, P. P.; Kimura, A.; Ito, H.;

Penninger, J. M.; Imai, Y.; Kuba, K. Apelin Is a Positive Regulator of ACE2 in Failing Hearts. *J. Clin. Invest.* **2013**, *123* (12), 5203–5211. https://doi.org/10.1172/JCI69608.

(166) Schurink, B.; Roos, E.; Vos, W.; Breur, M.; van der Valk, P.; Bugiani, M. ACE2 Protein Expression During Childhood, Adolescence, and Early Adulthood. *Pediatr. Dev. Pathol.* **2022**, *25* (4), 404–408. https://doi.org/10.1177/10935266221075312.

(167) Hikmet, F.; Méar, L.; Edvinsson, Å.; Micke, P.; Uhlén, M.; Lindskog, C. The Protein Expression Profile of ACE2 in Human Tissues. *Mol. Syst. Biol.* **2020**, *16* (7), 9610. https://doi.org/10.15252/MSB.20209610.

(168) Onabajo, O. O.; Banday, A. R.; Stanifer, M. L.; Yan, W.; Obajemu, A.; Santer, D. M.; Florez-Vargas, O.; Piontkivska, H.; Vargas, J. M.; Ring, T. J.; Kee, C.; Doldan, P.; Tyrrell, D. L.; Mendoza, J. L.; Boulant, S.; Prokunina-Olsson, L. Interferons and Viruses Induce a Novel Truncated ACE2 Isoform and Not the Full-Length SARS-CoV-2 Receptor. *Nat. Genet. 2020 5212* **2020**, *52* (12), 1283–1293. https://doi.org/10.1038/s41588-020-00731-9.

(169) Scialo, F.; Daniele, A.; Amato, F.; Pastore, L.; Matera, M. G.; Cazzola, M.; Castaldo, G.; Bianco, A. ACE2: The Major Cell Entry Receptor for SARS-CoV-2. *Lung* **2020**, *198* (6), 867–877. https://doi.org/10.1007/s00408-020-00408-4.

(170) Moore, L. D.; Le, T.; Fan, G. DNA Methylation and Its Basic Function. *Neuropsychopharmacol. 2013 381* **2012**, *38* (1), 23–38. https://doi.org/10.1038/npp.2012.112.

(171) Razin, A.; Cedar, H. DNA Methylation and Gene Expression. *Microbiol. Rev.* **1991**, *37* (4), 173–175. https://doi.org/10.1128/MR.55.3.451-458.1991.

(172) He, H.; Lehming, N. Global Effects of Histone Modifications. *Brief. Funct. Genomics* **2003**, *2* (3), 234–243. https://doi.org/10.1093/BFGP/2.3.234.

(173) Shvedunova, M.; Akhtar, A. Modulation of Cellular Processes by Histone and Non-Histone Protein Acetylation. *Nat. Rev. Mol. Cell Biol. 2022 235* **2022**, *23* (5), 329–349. https://doi.org/10.1038/s41580-021-00441-y.

(174) Zhang, Y.; Sun, Z.; Jia, J.; Du, T.; Zhang, N.; Tang, Y.; Fang, Y.; Fang, D. Overview of Histone Modification. *Adv. Exp. Med. Biol.* **2021**, *1283*, 1–16. https://doi.org/10.1007/978-981-15-8104-5_1/COVER.

(175) Saxton, D. S.; Rine, J. Nucleosome Positioning Regulates the Establishment, Stability, and Inheritance of Heterochromatin in Saccharomyces Cerevisiae. *Proc. Natl. Acad. Sci. U. S. A.* **2020**, *117* (44), 27493–27501. https://doi.org/10.1073/PNAS.2004111117.

(176) HAT/HDAC: The epigenetic regulators of inflammatory gene expression (Review) https://www.spandidos-publications.com/10.3892/ije.2021.5.

(177) Wu, D.; Qiu, Y.; Jiao, Y.; Qiu, Z.; Liu, D. Small Molecules Targeting HATs, HDACs, and BRDs in Cancer Therapy. *Front. Oncol.* **2020**, *10*, 560487. https://doi.org/10.3389/FONC.2020.560487.

(178) Chan, J. C.; Maze, I. Nothing Is Yet Set in (Hi)Stone: Novel Post-Translational Modifications Regulating Chromatin Function. *Trends Biochem. Sci.* **2020**, *45* (10), 829–844. https://doi.org/10.1016/J.TIBS.2020.05.009.

(179) Fontana, A.; Cursaro, I.; Carullo, G.; Gemma, S.; Butini, S.; Campiani, G. A Therapeutic Perspective of HDAC8 in Different Diseases: An Overview of Selective Inhibitors. *Int. J. Mol. Sci.* **2022**, *23* (17). https://doi.org/10.3390/ijms231710014.

(180) Brindisi, M.; Saraswati, A. P.; Brogi, S.; Gemma, S.; Butini, S.; Campiani, G. Old but Gold: Tracking the New Guise of Histone Deacetylase 6 (HDAC6) Enzyme as a Biomarker and Therapeutic Target in Rare Diseases. *J. Med. Chem.* **2020**, *63* (1), 23–39. https://doi.org/10.1021/ACS.JMEDCHEM.9B00924.

(181) Ghosh, S.; Snehlata; Hussain, S.; Makkar, H.; Mukherjee, B. Role of Chromatin Modulation in the Establishment of Protozoan Parasite Infection for Developing Targeted Chemotherapeutics. *Nucl. 2021 643* **2021**, *64* (3), 401–413. https://doi.org/10.1007/S13237-021-00356-1.

(182) Saccoccia, F.; Brindisi, M.; Gimmelli, R.; Relitti, N.; Guidi, A.; Saraswati, A. P.; Cavella, C.; Brogi, S.; Chemi, G.; Butini, S.; Papoff, G.; Senger, J.; Herp, D.; Jung, M.; Campiani, G.; Gemma, S.; Ruberti, G. Screening and Phenotypical Characterization of Schistosoma Mansoni Histone Deacetylase 8 (SmHDAC8) Inhibitors as Multistage Antischistosomal Agents. *ACS Infect. Dis.* **2020**, *6* (1), 100–113. https://doi.org/10.1021/ACSINFECDIS.9B00224.

(183) Campiani, G.; Cavella, C.; Osko, J. D.; Brindisi, M.; Relitti, N.; Brogi, S.; Saraswati, A. P.; Federico, S.; Chemi, G.; Maramai, S.; Carullo, G.; Jaeger, B.; Carleo, A.; Benedetti, R.; Sarno, F.; Lamponi, S.; Rottoli, P.; Bargagli, E.; Bertucci, C.; Tedesco, D.; Herp, D.; Senger, J.; Ruberti, G.; Saccoccia, F.; Saponara, S.; Gorelli, B.; Valoti, M.; Kennedy, B.; Sundaramurthi, H.; Butini, S.; Jung, M.; Roach, K. M.; Altucci, L.; Bradding, P.; Christianson, D. W.; Gemma, S.; Prasse, A. Harnessing the Role of HDAC6 in Idiopathic Pulmonary Fibrosis: Design, Synthesis, Structural Analysis, and Biological Evaluation of Potent Inhibitors. *J. Med. Chem.* **2021**, *64* (14), 9960–9988. https://doi.org/10.1021/ACS.JMEDCHEM.1C00184.

(184) Hess, L.; Moos, V.; Lauber, A. A.; Reiter, W.; Schuster, M.; Hartl, N.; Lackner, D.; Boenke, T.; Koren, A.; Guzzardo, P. M.; Gundacker, B.; Riegler, A.; Vician, P.; Miccolo, C.; Leiter, S.; Chandrasekharan, M. B.; Vcelkova, T.; Tanzer, A.; Jun, J. Q.; Bradner, J.; Brosch, G.; Hartl, M.; Bock, C.; Bürckstümmer, T.; Kubicek, S.; Chiocca, S.; Bhaskara, S.; Seiser, C. A Toolbox for Class I HDACs Reveals Isoform Specific Roles in Gene Regulation and Protein Acetylation. *PLOS Genet.* **2022**, *18* (8), e1010376. https://doi.org/10.1371/JOURNAL.PGEN.1010376.

(185) Park, S. Y.; Kim, J. S. A Short Guide to Histone Deacetylases Including Recent Progress on Class II Enzymes. *Exp. Mol. Med. 2020 522* **2020**, *52* (2), 204–212. https://doi.org/10.1038/s12276-020-0382-4.

(186) Saraswati, A. P.; Relitti, N.; Brindisi, M.; Osko, J. D.; Chemi, G.; Federico, S.; Grillo, A.; Brogi, S.; McCabe, N. H.; Turkington, R. C.; Ibrahim, O.; O'Sullivan, J.; Lamponi, S.; Ghanim, M.; Kelly, V. P.; Zisterer, D.; Amet, R.; Hannon Barroeta, P.; Vanni, F.; Ulivieri, C.; Herp, D.; Sarno, F.; Di Costanzo, A.;

Saccoccia, F.; Ruberti, G.; Jung, M.; Altucci, L.; Gemma, S.; Butini, S.; Christianson, D. W.; Campiani, G. Spiroindoline-Capped Selective HDAC6 Inhibitors: Design, Synthesis, Structural Analysis, and Biological Evaluation. *ACS Med. Chem. Lett.* **2020**, *11* (11), 2268–2276. https://doi.org/10.1021/ACSMEDCHEMLETT.0C00395.

(187) Di Bello, E.; Noce, B.; Fioravanti, R.; Mai, A. Current HDAC Inhibitors in Clinical Trials. *Chimia (Aarau).* **2022**, *76* (5), 448–453. https://doi.org/10.2533/chimia.2022.448.

(188) Singh, T.; Kaur, P.; Singh, P.; Singh, S.; Munshi, A. Differential Molecular Mechanistic Behavior of HDACs in Cancer Progression. *Med. Oncol. 2022 3911* **2022**, *39* (11), 1–26. https://doi.org/10.1007/S12032-022-01770-4.

(189) Ramaiah, M. J.; Tangutur, A. D.; Manyam, R. R. Epigenetic Modulation and Understanding of HDAC Inhibitors in Cancer Therapy. *Life Sci.* **2021**, *277*, 119504. https://doi.org/10.1016/J.LFS.2021.119504.

(190) Khatun, S.; Amin, S. A.; Choudhury, D.; Chowdhury, B.; Jha, T.; Gayen, S. Advances in Structure-Activity Relationships of HDAC Inhibitors as HIV Latency-Reversing Agents. *Expert Opin. Drug Discov.* **2024**, *19* (3). https://doi.org/10.1080/17460441.2024.2305730.

(191) Zwinderman, M. R. H.; Cao, F.; Dekker, F. J. Acetylation and Methylation in Asthma, COPD, and Lung Cancer. *Top. Med. Chem.* **2020**, *33*, 429–453. https://doi.org/10.1007/7355_2019_81/COVER.

(192) Bondarev, A. D.; Attwood, M. M.; Jonsson, J.; Chubarev, V. N.; Tarasov, V. V.; Schiöth, H. B. Recent Developments of HDAC Inhibitors: Emerging Indications and Novel Molecules. *Br. J. Clin. Pharmacol.* **2021**, *87* (12), 4577–4597. https://doi.org/10.1111/bcp.14889.

(193) Lu, Y.; Zhao, Y.; Gao, C.; Suresh, S.; Men, J.; Sawyers, A.; Correspondence, G. L. S.; Smith, G. L. In Brief HDAC5 Enhances TRIF-Mediated IRF3 Activation and Restricts Several Orthopoxviruses. Lu et Al. Show That the C6 Protein of These Orthopoxviruses Induces Degradation of HDAC5 and Interacts Directly with HDAC5 via the HDAC5 N-Terminal Dimerization D. https://doi.org/10.1016/j.celrep.2024.113788.

(194) Yin, J.; Wang, S.; Ren, S.; Liang, Z.; Ge, J.; Sun, Y.; Yin, X.; Wang, X. TMP269, a Small Molecule Inhibitor of Class IIa HDAC, Suppresses RABV Replication in Vitro. *Front. Microbiol.* **2023**, *14* (December), 1–11. https://doi.org/10.3389/fmicb.2023.1284439.

(195) Qu, M.; Zhang, H.; Cheng, P.; Wubshet, A. K.; Yin, X.; Wang, X.; Sun, Y. Histone Deacetylase 6's Function in Viral Infection, Innate Immunity, and Disease: Latest Advances. *Front. Immunol.* **2023**, *14* (August), 1–14. https://doi.org/10.3389/fimmu.2023.1216548.

(196) Correia da Costa, L.; Maciel Bomfim, L.; Victoria Torres Dittz, U.; de Almeida Velozo, C.; Delvecchio da Cunha, R.; Tanuri, A. Repression of HIV-1 Reactivation Mediated by CRISPR/DCas9-KRAB in Lymphoid and Myeloid Cell Models. **2022**, *19*, 12. https://doi.org/10.1186/s12977-022-00600-9.

(197) Gao, S.; Zhang, L. ACE2 Partially Dictates the Host Range and Tropism of SARS-CoV-2. *Comput. Struct. Biotechnol. J.* **2020**, *18*, 4040–4047. https://doi.org/10.1016/J.CSBJ.2020.11.032.

(198) Bhat, S.; Rishi, P.; Chadha, V. D. Understanding the Epigenetic Mechanisms in SARS CoV-2 Infection

and Potential Therapeutic Approaches. *Virus Res.* **2022**, *318* (February), 198853. https://doi.org/10.1016/j.virusres.2022.198853.

(199) El Baba, R.; Herbein, G. Management of Epigenomic Networks Entailed in Coronavirus Infections and COVID-19. *Clin. Epigenetics* **2020**, *12* (1), 1–12. https://doi.org/10.1186/s13148-020-00912-7.

(200) Takahashi, Y.; Hayakawa, A.; Sano, R.; Fukuda, H.; Harada, M.; Kubo, R.; Okawa, T.; Kominato, Y. Histone Deacetylase Inhibitors Suppress ACE2 and ABO Simultaneously, Suggesting a Preventive Potential against COVID-19. *Sci. Rep.* **2021**, *11* (1), 1–9. https://doi.org/10.1038/s41598-021-82970-2.

(201) Carullo, G.; Di Bonaventura, G.; Rossi, S.; Lupetti, V.; Tudino, V.; Brogi, S.; Butini, S.; Campiani, G.; Gemma, S.; Pompilio, A. Development of Quinazolinone Derivatives as Modulators of Virulence Factors of Pseudomonas Aeruginosa Cystic Fibrosis Strains. *Molecules* **2023**, *28* (18). https://doi.org/10.3390/molecules28186535.

(202) Rossi, S.; Tatangelo, V.; Dichiara, M.; Butini, S.; Gemma, S.; Brogi, S.; Pasquini, S.; Cappello, M.; Vincenzi, F.; Varani, K.; Lopresti, L.; Malchiodi, M.; Carrara, C.; Gozzetti, A.; Bocchia, M.; Marotta, G.; Patrussi, L.; Carullo, G.; Baldari, C. T.; Campiani, G. A Novel Potent Class I HDAC Inhibitor Reverses the STAT4/P66Shc Apoptotic Defect in B Cells from Chronic Lymphocytic Leukemia Patients. *Biomed. Pharmacother.* **2024**, *174*, 116537. https://doi.org/10.1016/J.BIOPHA.2024.116537.

(203) Bragazzi, N. L.; Kong, J. D.; Mahroum, N.; Tsigalou, C.; Khamisy-Farah, R.; Converti, M.; Wu, J. Epidemiological Trends and Clinical Features of the Ongoing Monkeypox Epidemic: A Preliminary Pooled Data Analysis and Literature Review. *J. Med. Virol.* **2023**, *95* (1), e27931. https://doi.org/10.1002/JMV.27931.

(204) Bhagavathula, A. S.; Raubenheimer, J. E. A Real-Time Infodemiology Study on Public Interest in Mpox (Monkeypox) Following the World Health Organization Global Public Health Emergency Declaration. *Inf.* **2023**, *14* (1), 5. https://doi.org/10.3390/INFO14010005/S1.

(205) Al-Gburi, S.; Namuq, Z. A Review of the Recent Monkeypox Outbreak in 2022. *Cureus* **2022**, *14* (8), 8–11. https://doi.org/10.7759/cureus.27880.

(206) Hantz, S.; Mafi, S.; Pinet, P.; Deback, C. [Monkeypox to Mpox or the Re-Emergence of an Old Zoonosis]. *Rev. Francoph. des Lab. RFL* **2023**, *2023* (553), 25–37. https://doi.org/10.1016/S1773-035X(23)00132-6.

(207) Benites-Zapata, V. A.; Ulloque-Badaracco, J. R.; Alarcon-Braga, E. A.; Hernandez-Bustamante, E. A.; Mosquera-Rojas, M. D.; Bonilla-Aldana, D. K.; Rodriguez-Morales, A. J. Clinical Features, Hospitalisation and Deaths Associated with Monkeypox: A Systematic Review and Meta-Analysis. *Ann. Clin. Microbiol. Antimicrob.* **2022**, *21* (1), 1–18. https://doi.org/10.1186/S12941-022-00527-1.

(208) Sharma, A.; Priyanka; Fahrni, M. L.; Choudhary, O. P. Monkeypox Outbreak: New Zoonotic Alert after the COVID-19 Pandemic. *Int. J. Surg.* **2022**, *104*, 106812. https://doi.org/10.1016/J.IJSU.2022.106812.

(209) Kaler, J.; Hussain, A.; Flores, G.; Kheiri, S.; Desrosiers, D. Monkeypox: A Comprehensive Review of Transmission, Pathogenesis, and Manifestation. **2022**. https://doi.org/10.7759/cureus.26531.

(210) 2022 Mpox Outbreak Global Map | Mpox | Poxvirus | CDC https://www.cdc.gov/poxvirus/mpox/response/2022/world-map.html (accessed Mar 13, 2024).

(211) Marennikova, S. S.; Moyer, R. W. Classification of Poxviruses and Brief Characterization of the Genus Orthopoxvirus. *Orthopoxviruses Pathog. Humans* **2005**, 11–18. https://doi.org/10.1007/0-387-25306-8_2.

(212) Breman, J. G.; Kalisa-Ruti; Steniowski, M. V.; Zanotto, E.; Gromyko, A. I.; Arita, I. Human Monkeypox, 1970-79. *Bull. World Health Organ.* **1980**, *58* (2), 165.

(213) Shchelkunov, S. N.; Totmenin, A. V.; Babkin, I. V.; Safronov, P. F.; Ryazankina, O. I.; Petrov, N. A.; Gutorov, V. V.; Uvarova, E. A.; Mikheev, M. V.; Sisler, J. R.; Esposito, J. J.; Jahrling, P. B.; Moss, B.; Sandakhchiev, L. S. Human Monkeypox and Smallpox Viruses: Genomic Comparison. *FEBS Lett.* **2001**, *509* (1), 66–70. https://doi.org/10.1016/S0014-5793(01)03144-1.

(214) N, D.; K, D. Independent Evolution of Monkeypox and Variola Viruses. *J. Virol.* **1992**, *66* (12), 7565–7567. https://doi.org/10.1128/JVI.66.12.7565-7567.1992.

(215) Shafaati, M.; Zandi, M. State-of-the-Art on Monkeypox Virus: An Emerging Zoonotic Disease. *Infection* **2022**, *50* (6), 1425–1430. https://doi.org/10.1007/S15010-022-01935-3.

(216) Karagoz, A.; Tombuloglu, H.; Alsaeed, M.; Tombuloglu, G.; AlRubaish, A. A.; Mahmoud, A.; Smajlović, S.; Ćordić, S.; Rabaan, A. A.; Alsuhaimi, E. Monkeypox (Mpox) Virus: Classification, Origin, Transmission, Genome Organization, Antiviral Drugs, and Molecular Diagnosis. *J. Infect. Public Health* **2023**, *16* (4), 531–541. https://doi.org/10.1016/J.JIPH.2023.02.003.

(217) Wikel, S. K.; Ranjan, R.; Kumar Biswal, J. Monkeypox: Re-Emerging Zoonotic Threat. *Zoonotic Dis. 2022, Vol. 2, Pages 234-246* **2022**, *2* (4), 234–246. https://doi.org/10.3390/ZOONOTICDIS2040019.

(218) Comparative Proteomics of Human Monkeypox and Vaccinia Intracellular Mature and Extracellular Enveloped Virions | Journal of Proteome Research https://pubs.acs.org/doi/abs/10.1021/pr070432.

(219) Lum, F. M.; Torres-Ruesta, A.; Tay, M. Z.; Lin, R. T. P.; Lye, D. C.; Rénia, L.; Ng, L. F. P. Monkeypox: Disease Epidemiology, Host Immunity and Clinical Interventions. *Nat. Rev. Immunol. 2022 2210* **2022**, *22* (10), 597–613. https://doi.org/10.1038/s41577-022-00775-4.

(220) Ortiz-Martínez, Y.; Rodríguez-Morales, A. J.; Franco-Paredes, C.; Chastain, D. B.; Gharamti, A. A.; Vargas Barahona, L.; Henao-Martínez, A. F. Monkeypox – a Description of the Clinical Progression of Skin Lesions: A Case Report from Colorado, USA. *Ther. Adv. Infect. Dis.* **2022**, *9*. https://doi.org/10.1177/20499361221117726.

(221) Chowdhury, P. P. D.; Haque, M. A.; Ahamed, B.; Tanbir, M.; Islam, M. R. A Brief Report on Monkeypox Outbreak 2022: Historical Perspective and Disease Pathogenesis. *Clin. Pathol.* **2022**, *15*. https://doi.org/10.1177/2632010X221131660.

(222) Shuvo, P. A.; Roy, A.; Dhawan, M.; Chopra, H.; Emran, T. Bin. Recent Outbreak of Monkeypox: Overview of Signs, Symptoms, Preventive Measures, and Guideline for Supportive Management. *Int. J. Surg.* **2022**, *105*. https://doi.org/10.1016/J.IJSU.2022.106877.

(223) Huang, Y.; Mu, L.; Wang, W. Monkeypox: Epidemiology, Pathogenesis, Treatment and Prevention. *Signal Transduct. Target. Ther. 2022 71* **2022**, *7* (1), 1–22. https://doi.org/10.1038/s41392-022-01215-4.

(224) Gieryńska, M.; Szulc-Dąbrowska, L.; Struzik, J.; Gregorczyk-Zboroch, K. P.; Mielcarska, M. B.; Toka, F. N.; Schollenberger, A.; Biernacka, Z. Orthopoxvirus Zoonoses—Do We Still Remember and Are Ready to Fight? *Pathog. 2023, Vol. 12, Page 363* **2023**, *12* (3), 363. https://doi.org/10.3390/PATHOGENS12030363.

(225) Subbaram, K.; Shaik, P.; Ali, S.; Ali, S. Monkeypox: Epidemiology, Mode of Transmission, Clinical Features, Genetic Clades and Molecular Properties. **1980**. https://doi.org/10.26355/eurrev_202208_29540.

(226) Okwor, T.; Mbala, P. K.; Evans, D. H.; Kindrachuk, J. A Contemporary Review of Clade-Specific Virological Differences in Monkeypox Viruses. *Clin. Microbiol. Infect.* **2023**, *29* (12), 1502–1507. https://doi.org/10.1016/J.CMI.2023.07.011.

(227) Shannon Keckler, M.; Salzer, J. S.; Patel, N.; Townsend, M. B.; Akazawa, Y. J.; Doty, J. B.; Gallardo-Romero, N. F.; Satheshkumar, P. S.; Carroll, D. S.; Karem, K. L.; Damon, I. K. IMVAMUNE® and ACAM2000® Provide Different Protection against Disease When Administered Postexposure in an Intranasal Monkeypox Challenge Prairie Dog Model. *Vaccines 2020, Vol. 8, Page 396* **2020**, *8* (3), 396. https://doi.org/10.3390/VACCINES8030396.

(228) Kandeel, M.; Morsy, M. A.; Abd El-Lateef, H. M.; Marzok, M.; El-Beltagi, H. S.; Al Khodair, K. M.; Albokhadaim, I.; Venugopala, K. N. Efficacy of the Modified Vaccinia Ankara Virus Vaccine and the Replication-Competent Vaccine ACAM2000 in Monkeypox Prevention. *Int. Immunopharmacol.* **2023**, *119*, 110206. https://doi.org/10.1016/J.INTIMP.2023.110206.

(229) Meo, S. A.; Al-Masri, A. A.; Klonoff, D. C.; Alshahrani, A. N.; Al-khlaiwi, T. Comparison of Biological, Pharmacological Characteristics, Indications, Contraindications and Adverse Effects of JYNNEOS and ACAM2000 Monkeypox Vaccines. *Vaccines 2022, Vol. 10, Page 1971* **2022**, *10* (11), 1971. https://doi.org/10.3390/VACCINES10111971.

(230) Singhvi, N.; Chandni Talwar, ·; Utkarsha Mahanta, ·; Kaur, J.; Mondal, K.; Ahmad, N.; Tyagi, I.; Sharma, · Gaurav; Gupta, V. Comparative Genomics and Integrated System Biology Approach Unveiled Undirected Phylogeny Patterns, Mutational Hotspots, Functional Patterns, and Molecule Repurposing for Monkeypox Virus. **2023**, *23*, 231. https://doi.org/10.1007/s10142-023-01168-z.

(231) Baker, R. O.; Bray, M.; Huggins, J. W. Potential Antiviral Therapeutics for Smallpox, Monkeypox and Other Orthopoxvirus Infections. *Antiviral Res.* **2003**, *57* (1–2), 13–23. https://doi.org/10.1016/S0166-3542(02)00196-1.

(232) Imran, M.; Abida; Alotaibi, N. M.; Thabet, H. K.; Alruwaili, J. A.; Eltaib, L.; Alshehri, A.; Alsaiari, A. A.; Kamal, M.; Alshammari, A. M. A. Repurposing Anti-Dengue Compounds against Monkeypox Virus Targeting Core Cysteine Protease. *Biomedicines* **2023**, *11* (7). https://doi.org/10.3390/BIOMEDICINES11072025.

(233) Ali, Y.; Imtiaz, H.; Tahir, M. M.; Gul, F.; Saddozai, U. A. K.; ur Rehman, A.; Ren, Z. G.; Khattak, S.; Ji, X. Y. Fragment-Based Approaches Identified Tecovirimat-Competitive Novel Drug Candidate for Targeting the F13 Protein of the Monkeypox Virus. *Viruses 2023, Vol. 15, Page 570* **2023**, *15* (2), 570. https://doi.org/10.3390/V15020570.

(234) DeLaurentis, C. E.; Kiser, J.; Zucker, J. New Perspectives on Antimicrobial Agents: Tecovirimat for Treatment of Human Monkeypox Virus. *Antimicrob. Agents Chemother.* **2022**, *66* (12). https://doi.org/10.1128/AAC.01226-22.

(235) Almehmadi, M.; Allahyani, M.; Alsaiari, A. A.; Alshammari, M. K.; Alharbi, A. S.; Hussain, K. H.; Alsubaihi, L. I.; Kamal, M.; Alotaibi, S. S.; Alotaibi, A. N.; Aldhafeeri, A. A.; Imran, M. A Glance at the Development and Patent Literature of Tecovirimat: The First-in-Class Therapy for Emerging Monkeypox Outbreak. *Viruses*. 2022, p 1870. https://doi.org/10.3390/v14091870.

(236) Russo, A. T.; Grosenbach, D. W.; Chinsangaram, J.; Honeychurch, K. M.; Long, P. G.; Lovejoy, C.; Maiti, B.; Meara, I.; Hruby, D. E. An Overview of Tecovirimat for Smallpox Treatment and Expanded Anti-Orthopoxvirus Applications. *Expert Rev. Anti. Infect. Ther.* **2021**, *19* (3), 331–344. https://doi.org/10.1080/14787210.2020.1819791.

(237) Russo, A. T.; Grosenbach, D. W.; Chinsangaram, J.; Honeychurch, K. M.; Long, P. G.; Lovejoy, C.; Maiti, B.; Meara, I.; Hruby, D. E. An Overview of Tecovirimat for Smallpox Treatment and Expanded Anti-Orthopoxvirus Applications. *Expert Rev. Anti. Infect. Ther.* **2021**, *19* (3), 331–344. https://doi.org/10.1080/14787210.2020.1819791.

(238) Duraffour, S.; Lorenzo, M. M.; Zöller, G.; Topalis, D.; Grosenbach, D.; Hruby, D. E.; Andrei, G.; Blasco, R.; Meyer, H.; Snoeck, R. ST-246 Is a Key Antiviral to Inhibit the Viral F13L Phospholipase, One of the Essential Proteins for Orthopoxvirus Wrapping. *J. Antimicrob. Chemother.* **2015**, *70* (5), 1367–1380. https://doi.org/10.1093/JAC/DKU545.

(239) Hudu, S. A.; Alshrari, A. S.; Al Qtaitat, A.; Imran, M. VP37 Protein Inhibitors for Mpox Treatment: Highlights on Recent Advances, Patent Literature, and Future Directions. **2023**, *11* (4), 1106. https://doi.org/10.3390/BIOMEDICINES11041106.

(240) Siegrist, E. A.; Sassine, J. Antivirals With Activity Against Mpox: A Clinically Oriented Review. *Clin. Infect. Dis.* **2023**, *76* (1), 155–164. https://doi.org/10.1093/CID/CIAC622.

(241) Shiryaev, V. A.; Skomorohov, M. Y.; Leonova, M. V.; Bormotov, N. I.; Serova, O. A.; Shishkina, L. N.; Agafonov, A. P.; Maksyutov, R. A.; Klimochkin, Y. N. Adamantane Derivatives as Potential Inhibitors of P37 Major Envelope Protein and Poxvirus Reproduction. Design, Synthesis and Antiviral Activity. *Eur. J. Med. Chem.* **2021**, *221*, 113485. https://doi.org/10.1016/J.EJMECH.2021.113485.

(242) Sokolova; Kovaleva; Kuranov; Bormotov; Borisevich; Zhukovets; Yaovaya; Serova; Nawrozkij; Vernigora; Davidenko; Khamitov; Peshkov; Shishkina; Maksuytov; Salakhutdinov. Design Synthesis and Biological Evaluation of -Camphor- and -Fenchone-Based. *ChemMedChem* **2022**.

(243) Wang, J.; Shahed-Al-Mahmud, M.; Chen, A.; Li, K.; Tan, H.; Joyce, R. An Overview of Antivirals against Monkeypox Virus and Other Orthopoxviruses. *J. Med. Chem.* **2023**, *66* (7), 4468–4490.

https://doi.org/10.1021/ACS.JMEDCHEM.3C00069.

(244) Rani, I.; Joshi, H.; Sharma, U.; Kaur, J.; Sood, S.; Ramniwas, S.; Chauhan, A.; Abdulabbas, H. S.; Tuli, H. S. Potential Use of Cidofovir, Brincidofovir, and Tecovirimat Drugs in Fighting Monkeypox Infection: Recent Trends and Advancements. *Naunyn. Schmiedebergs. Arch. Pharmacol.* **2023**, *397* (4), 2055–2065. https://doi.org/10.1007/S00210-023-02769-Y/METRICS.

(245) Rabaan, A. A.; Abas, A. H.; Tallei, T. E.; Al-Zaher, M. A.; Al-Sheef, N. M.; Fatimawali; Al-Nass, E. Z.; Al-Ebrahim, E. A.; Effendi, Y.; Idroes, R.; Alhabib, M. F.; Al-Fheid, H. A.; Adam, A. A.; Bin Emran, T. Monkeypox Outbreak 2022: What We Know so Far and Its Potential Drug Targets and Management Strategies. *J. Med. Virol.* **2023**, *95* (1), e28306. https://doi.org/10.1002/JMV.28306.

(246) Bárcena, J.; Lorenzo, M. M.; Sánchez-Puig, J. M.; Blasco, R.; Ba, J.; Lorenzo, M. M.; Sa, J. M.; Blasco, R. Sequence and Analysis of a Swinepox Virus Homologue of the Vaccinia Virus Major Envelope Protein P37 (F13L). *J. Gen. Virol.* **2000**, *81* (4), 1073–1085. https://doi.org/10.1099/0022-1317-81-4-1073.

(247) Roch, M.; Sierra, R.; Andrey, D. O. Antibiotic Heteroresistance in ESKAPE Pathogens, from Bench to Bedside. *Clin. Microbiol. Infect.* **2023**, *29* (3), 320–325. https://doi.org/10.1016/J.CMI.2022.10.018.

(248) Ma, Y. X.; Wang, C. Y.; Li, Y. Y.; Li, J.; Wan, Q. Q.; Chen, J. H.; Tay, F. R.; Niu, L. N. Considerations and Caveats in Combating ESKAPE Pathogens against Nosocomial Infections. *Adv. Sci.* **2020**, *7* (1), 1901872. https://doi.org/10.1002/ADVS.201901872.

(249) Mulani, M. S.; Kamble, E. E.; Kumkar, S. N.; Tawre, M. S.; Pardesi, K. R. Emerging Strategies to Combat ESKAPE Pathogens in the Era of Antimicrobial Resistance: A Review. *Front. Microbiol.* **2019**, *10* (APR), 539. https://doi.org/10.3389/FMICB.2019.00539.

(250) Murray, C. J.; Ikuta, K. S.; Sharara, F.; Swetschinski, L.; Robles Aguilar, G.; Gray, A.; Han, C.; Bisignano, C.; Rao, P.; Wool, E.; Johnson, S. C.; Browne, A. J.; Chipeta, M. G.; Fell, F.; Hackett, S.; Haines-Woodhouse, G.; Kashef Hamadani, B. H.; Kumaran, E. A. P.; McManigal, B.; Agarwal, R.; Akech, S.; Albertson, S.; Amuasi, J.; Andrews, J.; Aravkin, A.; Ashley, E.; Bailey, F.; Baker, S.; Basnyat, B.; Bekker, A.; Bender, R.; Bethou, A.; Bielicki, J.; Boonkasidecha, S.; Bukosia, J.; Carvalheiro, C.; Castañeda-Orjuela, C.; Chansamouth, V.; Chaurasia, S.; Chiurchiù, S.; Chowdhury, F.; Cook, A. J.; Cooper, B.; Cressey, T. R.; Criollo-Mora, E.; Cunningham, M.; Darboe, S.; Day, N. P. J.; De Luca, M.; Dokova, K.; Dramowski, A.; Dunachie, S. J.; Eckmanns, T.; Eibach, D.; Emami, A.; Feasey, N.; Fisher-Pearson, N.; Forrest, K.; Garrett, D.; Gastmeier, P.; Giref, A. Z.; Greer, R. C.; Gupta, V.; Haller, S.; Haselbeck, A.; Hay, S. I.; Holm, M.; Hopkins, S.; Iregbu, K. C.; Jacobs, J.; Jarovsky, D.; Javanmardi, F.; Khorana, M.; Kissoon, N.; Kobeissi, E.; Kostyanev, T.; Krapp, F.; Krumkamp, R.; Kumar, A.; Kyu, H. H.; Lim, C.; Limmathurotsakul, D.; Loftus, M. J.; Lunn, M.; Ma, J.; Mturi, N.; Munera-Huertas, T.; Musicha, P.; Mussi-Pinhata, M. M.; Nakamura, T.; Nanavati, R.; Nangia, S.; Newton, P.; Ngoun, C.; Novotney, A.; Nwakanma, D.; Obiero, C. W.; Olivas-Martinez, A.; Olliaro, P.; Ooko, E.; Ortiz-Brizuela, E.; Peleg, A. Y.; Perrone, C.; Plakkal, N.; Ponce-de-Leon, A.; Raad, M.; Ramdin, T.; Riddell, A.; Roberts, T.; Robotham, J. V.; Roca, A.; Rudd, K. E.; Russell, N.; Schnall, J.; Scott, J. A. G.; Shivamallappa, M.; Sifuentes-Osornio, J.; Steenkeste, N.; Stewardson, A. J.; Stoeva,

T.; Tasak, N.; Thaiprakong, A.; Thwaites, G.; Turner, C.; Turner, P.; van Doorn, H. R.; Velaphi, S.; Vongpradith, A.; Vu, H.; Walsh, T.; Waner, S.; Wangrangsimakul, T.; Wozniak, T.; Zheng, P.; Sartorius, B.; Lopez, A. D.; Stergachis, A.; Moore, C.; Dolecek, C.; Naghavi, M. Global Burden of Bacterial Antimicrobial Resistance in 2019: A Systematic Analysis. *Lancet* **2022**, *399* (10325), 629–655. https://doi.org/10.1016/S0140-6736(21)02724-0.

(251) Abban, M. K.; Ayerakwa, E. A.; Mosi, L.; Isawumi, A. The Burden of Hospital Acquired Infections and Antimicrobial Resistance. *Heliyon* **2023**, *9* (10), 2405–8440. https://doi.org/10.1016/J.HELIYON.2023.E20561.

(252) Aloke, C.; Achilonu, I. Coping with the ESKAPE Pathogens: Evolving Strategies, Challenges and Future Prospects. *Microb. Pathog.* **2023**, *175*, 105963. https://doi.org/10.1016/j.micpath.2022.105963.

(253) Santajit, S.; Indrawattana, N. Mechanisms of Antimicrobial Resistance in ESKAPE Pathogens. *Biomed Res. Int.* **2016**, *2016*. https://doi.org/10.1155/2016/2475067.

(254) De Oliveira, D. M. P.; Forde, B. M.; Kidd, T. J.; Harris, P. N. A.; Schembri, M. A.; Beatson, S. A.; Paterson, D. L.; Walker, M. J. Antimicrobial Resistance in ESKAPE Pathogens. *Clin. Microbiol. Rev.* **2020**, *33* (3). https://doi.org/10.1128/CMR.00181-19.

(255) Hall, B. G.; Barlow, M. Revised Ambler Classification of β-Lactamases. *J. Antimicrob. Chemother.* **2005**, *55* (6), 1050–1051. https://doi.org/10.1093/JAC/DKI130.

(256) Akhtar, A.; Fatima, N.; Khan, H. M. Beta-Lactamases and Their Classification: An Overview. *Beta-Lactam Resist. Gram-Negative Bact. Threat. Challenges* **2022**, 25–33. https://doi.org/10.1007/978-981-16-9097-6_3.

(257) Joji, R. M.; Al-Mahmeed, A.; Dar, F. K.; Shahid, M. Trends in Beta-Lactamase Classification. *Beta-Lactam Resist. Gram-Negative Bact. Threat. Challenges* **2022**, 17–24. https://doi.org/10.1007/978-981-16-9097-6_2.

(258) Fernández, L.; Hancock, R. E. W. Adaptive and Mutational Resistance: Role of Porins and Efflux Pumps in Drug Resistance. *Clin. Microbiol. Rev.* **2012**, *25* (4), 661–681. https://doi.org/10.1128/CMR.00043-12/ASSET/CBE4B115-0D1B-4807-BCA7-7DE726E1B10B/ASSETS/GRAPHIC/ZCM9990923970002.

(259) Ciofu, O.; Tolker-Nielsen, T. Tolerance and Resistance of Pseudomonas Aeruginosabiofilms to Antimicrobial Agents-How P. AeruginosaCan Escape Antibiotics. *Front. Microbiol.* **2019**, *10* (MAY), 453354. https://doi.org/10.3389/FMICB.2019.00913.

(260) Patil, A.; Banerji, R.; Kanojiya, P.; Saroj, S. D. Foodborne ESKAPE Biofilms and Antimicrobial Resistance: Lessons Learned from Clinical Isolates. *Pathog. Glob. Health* **2021**, *115* (6), 339–356. https://doi.org/10.1080/20477724.2021.1916158.

(261) Parkins, M. D.; Somayaji, R.; Waters, V. J. Epidemiology, Biology, and Impact of Clonal Pseudomonas Aeruginosa Infections in Cystic Fibrosis. *Clin. Microbiol. Rev.* **2018**, *31* (4). https://doi.org/10.1128/CMR.00019-18.

(262) Tolker-Nielsen, T. Pseudomonas Aeruginosa Biofilm Infections: From Molecular Biofilm Biology to New Treatment Possibilities. *APMIS* **2014**, *122* (s138), 1–51. https://doi.org/10.1111/APM.12335.

(263) Galán-Vásquez, E.; Luna, B.; Martínez-Antonio, A. The Regulatory Network of Pseudomonas Aeruginosa. *Microb. Informatics Exp. 2011 11* **2011**, *1* (1), 1–11. https://doi.org/10.1186/2042-5783-1-3.

(264) El Zowalaty, M. E.; Al Thani, A. A.; Webster, T. J.; El Zowalaty, A. E.; Schweizer, H. P.; Nasrallah, G. K.; Marei, H. E.; Ashour, H. M. Pseudomonas Aeruginosa: Arsenal of Resistance Mechanisms, Decades of Changing Resistance Profiles, and Future Antimicrobial Therapies. *http://dx.doi.org/10.2217/fmb.15.48* **2015**, *10* (10), 1683–1706. https://doi.org/10.2217/FMB.15.48.

(265) Bonyadi, P.; Saleh, N. T.; Dehghani, M.; Yamini, M.; Amini, K. Prevalence of Antibiotic Resistance of Pseudomonas Aeruginosa in Cystic Fibrosis Infection: A Systematic Review and Meta-Analysis. *Microb. Pathog.* **2022**, *165*, 105461. https://doi.org/10.1016/J.MICPATH.2022.105461.

(266) Okoliegbe, I. N.; Hijazi, K.; Cooper, K.; Ironside, C.; Gould, I. M. Trends of Antimicrobial Resistance and Combination Susceptibility Testing of Multidrug-Resistant Pseudomonas Aeruginosa Isolates from Cystic Fibrosis Patients: A 10-Year Update. *Antimicrob. Agents Chemother.* **2021**, *65* (6). https://doi.org/10.1128/AAC.02483-20/ASSET/278A2584-ACB8-4304-9120-AC5511AA5E01.

(267) Feng, W.; Huang, Q.; Wang, Y.; Yuan, Q.; Li, X.; Xia, P.; Sun, F. Changes in the Resistance and Epidemiological Characteristics of Pseudomonas Aeruginosa during a Ten-Year Period. *J. Microbiol. Immunol. Infect.* **2021**, *54* (2), 261–266. https://doi.org/10.1016/J.JMII.2019.08.017.

(268) Laborda, P.; Hernando-Amado, S.; Martínez, J. L.; Sanz-García, F. Antibiotic Resistance in Pseudomonas. *Adv. Exp. Med. Biol.* **2022**, *1386*, 117–143. https://doi.org/10.1007/978-3-031-08491-1_5.

(269) Pseudomonas aeruginosa - Sorveglianza dell'Antibiotico-Resistenza - AR-ISS https://www.epicentro.iss.it/antibiotico-resistenza/ar-iss-rapporto-pseudomonas-aeruginosa (accessed Mar 14, 2024).

(270) Lee, T. W. R.; Brownlee, K. G.; Conway, S. P.; Denton, M.; Littlewood, J. M. Evaluation of a New Definition for Chronic Pseudomonas Aeruginosa Infection in Cystic Fibrosis Patients. *J. Cyst. Fibros.* **2003**, *2* (1), 29–34. https://doi.org/10.1016/S1569-1993(02)00141-8.

(271) Ong, T.; Ramsey, B. W. Cystic Fibrosis: A Review. *JAMA* **2023**, *329* (21), 1859–1871. https://doi.org/10.1001/JAMA.2023.8120.

(272) Allen, L.; Allen, L.; Carr, S. B.; Davies, G.; Downey, D.; Egan, M.; Forton, J. T.; Gray, R.; Haworth, C.; Horsley, A.; Smyth, A. R.; Southern, K. W.; Davies, J. C. Future Therapies for Cystic Fibrosis. *Nat. Commun. 2023 141* **2023**, *14* (1), 1–13. https://doi.org/10.1038/s41467-023-36244-2.

(273) Fonseca, C.; Bicker, J.; Alves, G.; Falcão, A.; Fortuna, A. Cystic Fibrosis: Physiopathology and the Latest Pharmacological Treatments. *Pharmacol. Res.* **2020**, *162*, 105267. https://doi.org/10.1016/J.PHRS.2020.105267.

(274) Bell, S. C.; Mall, M. A.; Gutierrez, H.; Macek, M.; Madge, S.; Davies, J. C.; Burgel, P. R.; Tullis, E.; Castaños, C.; Castellani, C.; Byrnes, C. A.; Cathcart, F.; Chotirmall, S. H.; Cosgriff, R.; Eichler, I.; Fajac, I.; Goss, C. H.; Drevinek, P.; Farrell, P. M.; Gravelle, A. M.; Havermans, T.; Mayer-Hamblett, N.; Kashirskaya, N.; Kerem, E.; Mathew, J. L.; McKone, E. F.; Naehrlich, L.; Nasr, S. Z.; Oates, G. R.; O'Neill, C.; Pypops, U.; Raraigh, K. S.; Rowe, S. M.; Southern, K. W.; Sivam, S.; Stephenson, A. L.; Zampoli, M.; Ratjen, F. The Future of Cystic Fibrosis Care: A Global Perspective. *Lancet Respir. Med.* **2020**, *8* (1), 65–124. https://doi.org/10.1016/S2213-2600(19)30337-6.

(275) Thi, M. T. T.; Wibowo, D.; Rehm, B. H. A. Pseudomonas Aeruginosa Biofilms. *Int. J. Mol. Sci. 2020, Vol. 21, Page 8671* **2020**, *21* (22), 8671. https://doi.org/10.3390/IJMS21228671.

(276) Venkateswaran, P.; Vasudevan, S.; David, H.; Shaktivel, A.; Shanmugam, K.; Neelakantan, P.; Solomon, A. P. Revisiting ESKAPE Pathogens: Virulence, Resistance, and Combating Strategies Focusing on Quorum Sensing. *Front. Cell. Infect. Microbiol.* **2023**, *13* (June), 1–30. https://doi.org/10.3389/fcimb.2023.1159798.

(277) Lamont, I. L.; Konings, A. F.; Reid, D. W. Iron Acquisition by Pseudomonas Aeruginosa in the Lungs of Patients with Cystic Fibrosis. *BioMetals* **2009**, *22* (1), 53–60. https://doi.org/10.1007/s10534-008-9197-9.

(278) Martin, L. W.; Reid, D. W.; Sharples, K. J.; Lamont, I. L. Pseudomonas Siderophores in the Sputum of Patients with Cystic Fibrosis. *BioMetals* **2011**, *24* (6), 1059–1067. https://doi.org/10.1007/s10534-011-9464-z.

(279) De Kievit, T. R. Quorum Sensing in Pseudomonas Aeruginosa Biofilms. *Environ. Microbiol.* **2009**, *11* (2), 279–288. https://doi.org/10.1111/J.1462-2920.2008.01792.X.

(280) Whiteley, M.; Bangera, M. G.; Bumgarner, R. E.; Parsek, M. R.; Teitzel, G. M.; Lory, S.; Greenberg, E. P. Gene Expression in Pseudomonas Aeruginosa Biofilms. *Nat. 2001 4136858* **2001**, *413* (6858), 860–864. https://doi.org/10.1038/35101627.

(281) de Kievit, T. R.; Kakai, Y.; Register, J. K.; Pesci, E. C.; Iglewski, B. H. Role of the Pseudomonas Aeruginosa Las and Rhl Quorum-Sensing Systems in RhlI Regulation. *FEMS Microbiol. Lett.* **2002**, *212* (1), 101–106. https://doi.org/10.1111/J.1574-6968.2002.TB11251.X.

(282) Chakraborty, A.; Kabashi, A.; Wilk, S.; Rahme, L. G. Quorum-Sensing Signaling Molecule 2-Aminoacetophenone Mediates the Persistence of Pseudomonas Aeruginosa in Macrophages by Interference with Autophagy through Epigenetic Regulation of Lipid Biosynthesis. *MBio* **2023**, *14* (2). https://doi.org/10.1128/MBIO.00159-23/ASSET/2AF6EA31-F94F-431D-AF61-11E47A7C7A16.

(283) Ahmed, S. A. K. S.; Rudden, M.; Smyth, T. J.; Dooley, J. S. G.; Marchant, R.; Banat, I. M. Natural Quorum Sensing Inhibitors Effectively Downregulate Gene Expression of Pseudomonas Aeruginosa Virulence Factors. *Appl. Microbiol. Biotechnol.* **2019**, *103* (8), 3521–3535. https://doi.org/10.1007/S00253-019-09618-0.

(284) Erickson, D. L.; Endersby, R.; Kirkham, A.; Stuber, K.; Vollman, D. D.; Rabin, H. R.; Mitchell, I.; Storey, D. G. Pseudomonas Aeruginosa Quorum-Sensing Systems May Control Virulence Factor Expression

in the Lungs of Patients with Cystic Fibrosis. *Infect. Immun.* **2002**, *70* (4), 1783–1790. https://doi.org/10.1128/IAI.70.4.1783-1790.2002/ASSET/42E6E087-A2A7-4EE0-A4E5-1E22A7613CA7.

(285) Karruli, A.; Catalini, C.; D'Amore, C.; Foglia, F.; Mari, F.; Harxhi, A.; Galdiero, M.; Durante-Mangoni, E. Evidence-Based Treatment of Pseudomonas Aeruginosa Infections: A Critical Reappraisal. *Antibiot. (Basel, Switzerland)* **2023**, *12* (2). https://doi.org/10.3390/ANTIBIOTICS12020399.

(286) Grossman, S.; Soukarieh, F.; Richardson, W.; Liu, R.; Mashabi, A.; Emsley, J.; Williams, P.; Cámara, M.; Stocks, M. J. Novel Quinazolinone Inhibitors of the Pseudomonas Aeruginosa Quorum Sensing Transcriptional Regulator PqsR. *Eur. J. Med. Chem.* **2020**, *208*. https://doi.org/10.1016/j.ejmech.2020.112778.

(287) Soukarieh, F.; Mashabi, A.; Richardson, W.; Oton, E. V.; Romero, M.; Roberston, S. N.; Grossman, S.; Sou, T.; Liu, R.; Halliday, N.; Kukavica-Ibrulj, I.; Levesque, R. C.; Bergstrom, C. A. S.; Kellam, B.; Emsley, J.; Heeb, S.; Williams, P.; Stocks, M. J.; Cámara, M. Design and Evaluation of New Quinazolin-4(3 H)-One Derived PqsR Antagonists as Quorum Sensing Quenchers in Pseudomonas Aeruginosa. *ACS Infect. Dis.* **2021**, *7* (9), 2666–2685. https://doi.org/10.1021/ACSINFECDIS.1C00175.

(288) Ilangovan, A.; Fletcher, M.; Rampioni, G.; Pustelny, C.; Rumbaugh, K.; Heeb, S.; Cámara, M.; Truman, A.; Chhabra, S. R.; Emsley, J.; Williams, P. Structural Basis for Native Agonist and Synthetic Inhibitor Recognition by the Pseudomonas Aeruginosa Quorum Sensing Regulator PqsR (MvfR). *PLoS Pathog.* **2013**, *9* (7). https://doi.org/10.1371/JOURNAL.PPAT.1003508.

(289) Michaud, C. M. Global Burden of Infectious Diseases. *Encycl. Microbiol.* **2009**, 444. https://doi.org/10.1016/B978-012373944-5.00185-1.

(290) Brogi, S.; Rossi, S.; Ibba, R.; Butini, S.; Calderone, V.; Campiani, G.; Gemma, S. In Silico Analysis of Peptide-Based Derivatives Containing Bifunctional Warheads Engaging Prime and Non-Prime Subsites to Covalent Binding SARS-CoV-2 Main Protease (Mpro). *Comput. 2022, Vol. 10, Page 69* **2022**, *10* (5), 69. https://doi.org/10.3390/COMPUTATION10050069.

(291) McLaughlin, M.; Mohareb, R. M.; Rapoport, H. An Efficient Procedure for the Preparation of 4-Substituted 5-Aminoimidazoles. *J. Org. Chem.* **2003**, *68* (1), 50–54. https://doi.org/10.1021/JO026257S.